MESO-MECHANICAL MODEL OF THE STRUCTURAL INTEGRITY OF ADVANCED COMPOSITE LAMINATES

A THESIS SUBMITTED TO
FACULTY OF ENGINEERING, UNIVERSITY OF PORTO

BY

MIGUEL BESSA

IN PARTIAL FULFILLMENT OF THE REQUIREMENTS
FOR
THE DEGREE OF MASTER OF SCIENCE
IN
MECHANICAL ENGINEERING

JULY 2010

Approval of the thesis:

MESO-MECHANICAL MODEL OF THE STRUCTURAL INTEGRITY OF ADVANCED COMPOSITE LAMINATES

submitted by **MIGUEL BESSA** in partial fulfillment of the requirements for the degree of **Master of Science in Mechanical Engineering Department, Faculty of Engineering, University of Porto** by,

Prof. Dr. Sebastião Feyo de Azevedo _____
Dean, **Faculty of Engineering, University of Porto**

Prof. Dr. António Torres Marques _____
Head of Department, **Mechanical Engineering**

Prof. Dr. Pedro P. Camanho _____
Supervisor, **Mechanical Engineering Department, FEUP**

Examining Committee Members:

Prof. Dr. Paulo Tavares de Castro
Mechanical Engineering, FEUP _____

Prof. Dr. Pedro P. Camanho
Mechanical Engineering, FEUP _____

Dr. Cláudio Saúl Lopes
Aerospace Engineering, INEGI _____

Date: _____

I hereby declare that all information in this document has been obtained and presented in accordance with academic rules and ethical conduct. I also declare that, as required by these rules and conduct, I have fully cited and referenced all material and results that are not original to this work.

Name, Last Name: MIGUEL BESSA

Signature :

ABSTRACT

MESO-MECHANICAL MODEL OF THE STRUCTURAL INTEGRITY OF ADVANCED COMPOSITE LAMINATES

Bessa, Miguel

M.S., Department of Mechanical Engineering

Supervisor : Prof. Dr. Pedro P. Camanho

July 2010, 204 pages

The mechanical behavior of composite materials is very complex. With this thesis, it is intended to provide an insight on the physical principles that explain the material's behavior and its possible failure modes.

The most significant analytical models for predicting the behavior of composite materials were used for the simulations of fracture of notched composites.

Meso-mechanical numerical models which have the ability of modeling composite materials at the laminae level were used and developed in order to model accurately their constitutive behavior.

An eperimental program was carried out, in order to compare the results with the analytical and numerical predictions.

Keywords: continuum damage mechanics, fracture, FRP, meso-mechanics

RESUMO

MODELAÇÃO MESO-MECÂNICA DA INTEGRIDADE ESTRUTURAL DE LAMINADOS COMPÓSITOS AVANÇADOS

Bessa, Miguel
Me., Engenharia Mecânica
Orientador : Prof. Pedro P. Camanho

Julho de 2010, 204 páginas

O comportamento mecânico dos materiais compósitos é bastante complexo. Com esta tese pretende-se fornecer uma visão sobre os princípios físicos fundamentais que explicam o comportamento deste tipo de materiais e os seus modos de fractura.

Os modelos analíticos mais importantes de previsão do comportamento mecânico destes materiais foram usados na simulação da fractura dos materiais compósitos na presença de concentrações de tensão.

Foram desenvolvidos e utilizados modelos numéricos meso-mecânicos de forma a prever com precisão o comportamento constitutivo dos materiais compósitos.

Finalmente, foi realizado um programa experimental de forma a comparar os resultados experimentais obtidos com as previsões analíticas e numéricas elaboradas.

Palavras-Chave: mecânica do dano dos meios contínuos, fractura, FRP, meso-mecânica

À minha família, amigos e amigas. Por me relembrarem constantemente que há vida para além dos livros, sem nunca me pedirem para os largar.

ACKNOWLEDGMENTS

To Dr. **Pedro Camanho**, supervisor of this thesis, for all the support, for his contribution, for his patience and availability even at the most occupied times. I sincerely could not ask for more from a research adviser, who has not only an outstanding expertise but also the ability to encourage and motivate his colleagues and students.

To **António Melro**, PhD candidate, for his help and cooperation since the very first day I joined Dr. Pedro's research group. For his mischance of sitting right in front of me, being the first to notice when I was facing a problem and, especially, for being the first to offer his help. His contribution went from the smallest and trivial day to day events, to the most challenging problems, always giving a new insight to the question and most of the times providing the answer. More than a research partner, a true friend.

To **Hannes Koerber**, PhD candidate, for his outstanding help in the experimental work, always with great method and precision, for his kindness and his friendship. Hannes, along with António, helped me since the first day. Again, more than a co-worker, a true friend.

To **Giuseppe Catalanotti**, PhD candidate, for his enormous contribution in several parts of this work, for his patience and availability.

To Dr. **Cláudio Lopes**, for his expertise in numerical modeling and his invaluable help in this matter.

To Dr. **Francisco Pires**, for continuous encouraging and guidance.

To Dr. **Michael Sutcliffe**, for sharing the CCSM computer software.

To **Hilal Ercin**, PhD candidate, for the support with the Latex tool (METU template), for her patience and friendship.

To **Dimitra Ramantani**, PhD candidate, for her support in the experimental work.

TABLE OF CONTENTS

LIST OF TABLES

TABLES

LIST OF FIGURES

FIGURES

CHAPTER 1

INTRODUCTION

Advanced composite materials were early identified as key materials for high performance and low weight structures. The continuous development of these materials has been outstanding. The number of different applications in which composite materials are used has increased significantly over the years and in particular for aerospace and aeronautical structures. The recently unveiled Boeing 787 is made mostly of carbon fiber reinforced polymers: composites make up to 50% of the structural weight of the airplane, which is approximately 80% of its volume. By comparison, the Boeing 777 uses just 11% of composites by weight, which demonstrates the incredible growth of composites in the Aeronautical industry.

The growth of composite materials in advanced structures has three primary limitations:

1. Manufacturing processes;
2. Inherent material complexity and propensity to stress concentrations, contributing to a significant scatter in the material's measured properties and strength;
3. Lack of accurate analytical or numerical tools to solve general structural problems.

The main objective of this thesis is the development of analytical and numerical tools which will allow for a better modeling of the mechanical behavior of advanced composite materials in the presence of stress concentrations and the associated effect of size on the structural strength. Nevertheless, understanding the material's behavior is the first step towards an accurate material modeling. Therefore, Chapter 2 will present several material tests performed by different researchers in order to provide a better insight to the particular behavior of these materials and the major practical difficulties faced by those who need to handle them. No

dynamic problems will be addressed in this thesis. The second part of Chapter 2 will consist on a review of the most significant analytical tools available to predict the strength of notched and unnotched composite laminates.

Chapter 3 presents the numerical models developed and used in this work. In the beginning of this chapter, the state of the art of the knowledge about the mechanical behavior of composite materials will be provided. Currently, researchers are using advanced techniques in order to understand failure mechanisms at the microscale. A particularly challenging topic is the longitudinal compressive failure of these materials, as demonstrated in this chapter. The remaining of the chapter will be dedicated to explain the theory behind the numerical models developed.

Chapter 4 provides information about all the experimental work performed during this thesis. Performing experimental work is useful because it allows to actually establish contact with the material, from the manufacturing process until the final testing. Observing and realizing different tests facilitated the understanding of basic composite materials' mechanisms.

A comparison between the experimental results and the analytical and numerical models is presented in Chapter 5. The thesis will wrap up in Chapters 6 and 7, with the main conclusions and suggestions for further developments.

CHAPTER 2

LITERATURE REVIEW

This chapter aims to describe the behavior in tension and in compression of unnotched and notched Carbon Fiber Reinforced Plastics (CFRP). In order to introduce this subject, a review of the most relevant experimental work performed by different researchers will be presented in the first section. Understanding the particular characteristics of fracture in composite materials, the interactive nature of their failure mechanisms and how the latter affect the material's performance differently according to numerous factors, are the main objectives of the referred section.

The strength prediction of composite materials using analytical methods will be addressed in the second section. Here, Open-Hole Tension and Open-Hole Compression strength predictions were emphasized, due to the current importance of these tests for the aerospace industry.

2.1 Experimental Observations: Size effects on Carbon/Epoxy composites

A **size effect** is defined as a change in strength with specimen dimensions [1]. This phenomenon of composite materials is known for quite some time, yet poorly understood and usually not accounted for, explicitly, in design of composite structures [2]. Not accounting the size effect when a composite structure is designed can lead to its premature failure, possibly with catastrophic human and financial consequences, if the part is several times larger than the small test specimens normally used to obtain the material's mechanical properties.

Size effects have been reported in tension [2]-[5], bending [6, 7] and compression tests [13]-[16] for **unnotched and notched unidirectional composites** and also for **unnotched and notched multidirectional laminates**. Several difficulties in testing these materials have been

found, being the most usually reported **the difficulty in loading specimens without causing significant stress concentrations** due to the high fiber strength. This is an important fact because it may induce some erroneous conclusions, e.g., [8]-[10]. Another example of the practical difficulty of testing composite materials was found by **Bing and Sun** [13]. These authors performed off-axis compression tests in Fiber Reinforced Plastics (FRP) in which it was proven that friction at the specimen's end surface can produce size effects, that otherwise would be negligible (if the friction between the specimen and the loading elements was minimized).

The previous paragraph shows the reasons why in some cases there is significant scatter when measuring the composite materials' strength, although it is becoming easier to obtain good measurements' repeatability due to the constant improvement of the available standards.

With this literature review it were identified 3 types of size effects:

1. **Volume effect** (three-dimensional scaling)
2. **In-plane dimensions effect** (two-dimensional scaling);
3. **Thickness effect** (one-dimensional scaling);

In the following subsections it will be shown the 3 types of size effects in CFRPs, although the Volume and Thickness effects were the most extensively reported in the literature.

2.1.1 Tensile Strength of Carbon Fiber/Epoxy Composites

2.1.1.1 Unnotched specimens in tension

Volume effect

Wisnom *et al.* presented results showing size effects in unnotched tensile strength of unidirectional and multidirectional (quasi-isotropic) carbon/epoxy composites of the material IM7/8552 [2] (the same material used for the in-house tests that will be presented in Chapter 4). Table 2.1 summarizes the results obtained for unidirectional specimens.

Table 2.1: Results for unidirectional unnotched specimens loaded in tension. Material: IM7/8552. [2]

Thickness (mm)	Gauge length (mm)	Width (mm)	No. of specimens	Mean failure stress (MPa)	CV (%)
0.5	30	5	12	2806	4.2
1	60	10	12	2687	2.5
2	120	20	9	2553	3.8
4	240	40	6	2410	6.0

The authors concluded that the larger specimens showed a progressive reduction in strength with increasing size, with **the largest having strength and strain both 14% lower than the smallest**. In Figure 2.1 the strengths are plotted against gauge section[1] volume [2].

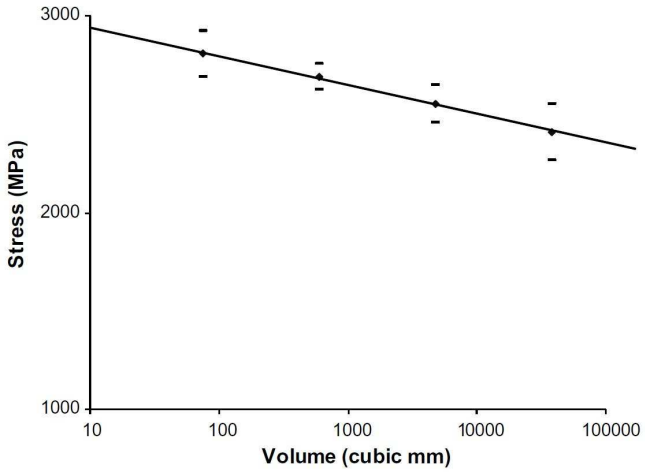

Figure 2.1: Size effect in scaled unidirectional unnotched specimens. Material: IM7/8552. [2]

[1] Gauge section: clean section with constant thickness, i.e., excluding the ends of the specimen

Wisnom and co-workers [2] have also analyzed the size effect for **quasi-isotropic** (unnotched) specimens. **This effect is much more complex in laminates** because there are different failure mechanisms which contribute differently according to many distinct factors such as material's nature, stacking sequence, geometry, load, etc.. Moreover, there's the possibility of interaction of matrix cracking and delamination with fiber longitudinal failure.

In a laminate there are two different ways of scaling the thickness:

1. **Sublaminate-level Scaling**: repeating blocks of plies;
2. **Ply-level Scaling**: increasing the number of plies of the same fiber orientation blocked together.

The authors studied the size effects in tension of the referred multidirectional unnotched laminates with these two types of scaling.

Sublaminate-level scaled specimens were investigated first. Table 2.2 summarizes the results obtained for lay-ups of 8, 16 and 32 plies of the previously referred material (IM7/8552) with stacking sequence $[45/90/\text{-}45/0]_{n\text{S}}$ (sublaminate-level scaling), where $n = 1, 2, 4$ respectively. The stacking sequence was chosen to minimize the risk of delamination by using small angle differences between the plies. The mean thicknesses were 1.09, 2.00 and 4.18mm.

Table 2.2: Results for quasi-isotropic unnotched specimens loaded in tension – sublaminate-level scaling. Material: IM7/8552. [2]

Case	Lay-up	Gauge length (mm)	Width (mm)	No. of specimens	Failure stress (MPa)	CV (%)
$n = 1$	$[45/90/\text{-}45/0]_{\text{S}}$	30	8	11	842	7.6
$n = 2$	$[45/90/\text{-}45/0]_{2\text{S}}$	60	16	6	911	2.0
$n = 4$	$[45/90/\text{-}45/0]_{4\text{S}}$	120	32	10	929	3.9

Figure 2.2(a) shows the typical failure for the smallest $n = 1$ specimen. All the specimens performed similarly, although for $n = 1$ a more severe delamination was observed extending away from the fiber breaks, but no damage was visible during the tests.

The results provided in Table 2.2 reveal a **trend opposite** to the observed in the unidirectional material: **the largest specimens failed at a 10% higher stress than the smallest**.

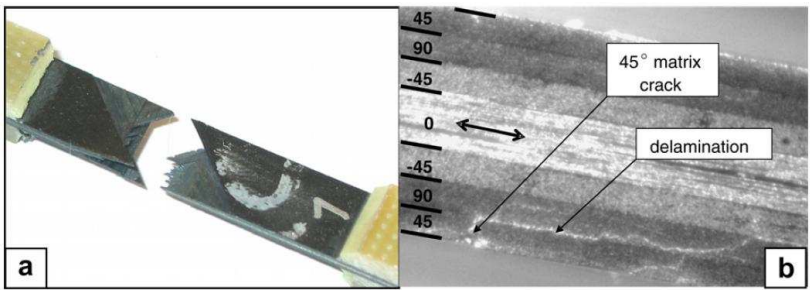

Figure 2.2: Typical failure (a) and edge of specimen away from fracture location (b) for $n = 1$ sublaminate-level scaled specimen $[45/90/\text{-}45/0]_S$. [2]

The authors justified these results by looking carefully to the failure region and noticing that the surface 45° plies were completely delaminated. The edges of the specimens were also examined using a dye penetrant away from the fracture location and clear evidence of transverse cracking and delamination of the surface ply was found, as shown in Figure 2.2(b) for the smallest specimen. The authors investigated this last fact and considered that it occurred before fiber failure, which was proved to be reasonable because they calculated the expected strength removing the contribution of these plies to the laminate modulus and resulted in very close values to the ones experimentally obtained (although no details of the calculations were given nor the analytical results).

Ply-level scaling of the same laminate was also investigated. The previous $n = 1$ specimens were scaled up by factors of 2, 4 and 8 by increasing the number of plies blocked together. The lay-ups were $[45_m/90_m/\text{-}45_m/0_m]_S$ where $m = 1, 2, 4$ and 8. All dimensions and the loading rate were scaled, and the mean thicknesses were 1.09, 2.11, 4.16 and 8.36mm. The curve for $m = 4$ is shown in Figure 2.3, this is an interesting plot because it establishes a relation between the failure mechanisms and the corresponding effect in the stress-displacement curve.

The specimens presented different behavior: delamination occurred sooner and for more plies as the thickness increased. For the detailed discussion of the behavior of each specimen it's recommended to see the complete work [2].

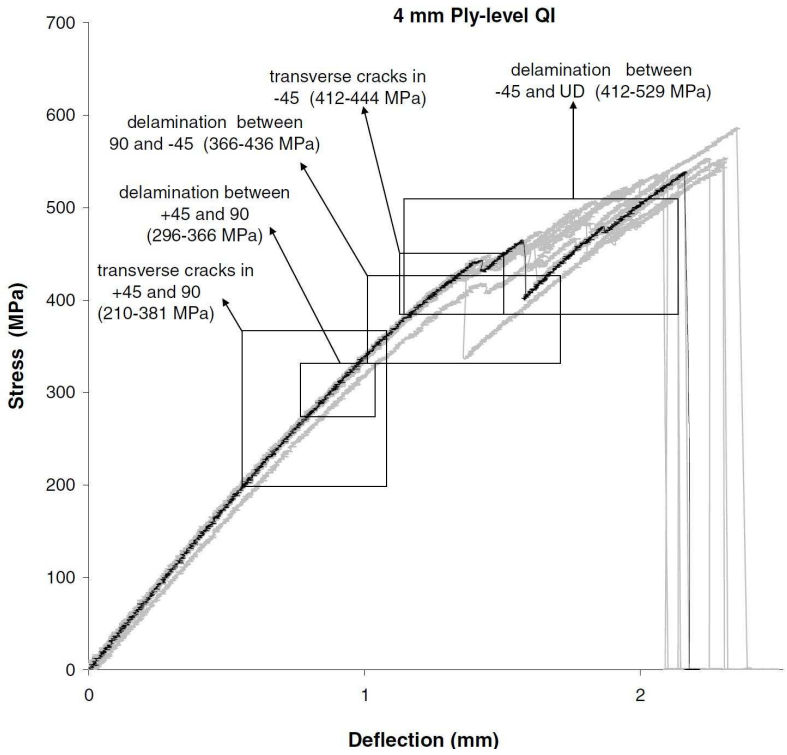

Figure 2.3: Sequence of damage events in $m = 4$ ply-level scaled specimens, $[45_4/90_4/-45_4/0_4]_S$. Material: IM7/8552. [2]

The results for the failure stress are summarized in Table 2.3, and Table 2.4 shows the relationship between the failure mechanism and the corresponding stress.

Table 2.3: Results for quasi-isotropic unnotched specimens loaded in tension – ply level scaling. Material: IM7/8552. [2]

Case	Lay-up	Gauge length (mm)	Width (mm)	No. of specimens	Failure stress (MPa)	CV (%)
m=1	$[45/90/-45/0]_S$	30	8	11	842	7.6
m=2	$[45_2/90_2/-45_2/0_2]_S$	60	16	8	660	3.3
m=4	$[45_4/90_4/-45_1/0_4]_S$	120	32	11	458	5.8
m=8	$[45_8/90_8/-45_8/0_8]_S$	240	64	10	321	2.9

Table 2.3 shows that **the ply level scaled specimens showed a 62% drop in strength by a factor of 8**. Authors claimed that failures on the larger sizes were controlled by complete delamination of the 45°, 90° and −45° plies from the 0° material [2].

Table 2.4: Different failure events of the previous specimens – ply level scaling. Material: IM7/8552. [2]

Case	45°/90° delam. stress (MPa)	CV (%)	−45°/0° delam. stress (MPa)	CV (%)	Fiber failure stress (MPa)	CV (%)
m=1	-		-		842	7.6
m=2	403	13.8	-		660	3.3
m=4	316	11.4	458	5.8	541	5.2
m=8	222	10.3	321	2.9	458	7.2

This particular work from Wisnom *et al.* was presented first because in the experimental work described in Chapter 4 it was used the same material (IM7/8552). However, the behavior in tension for other unnotched carbon/epoxy materials has been characterized by several other authors.

Jackson et. al also performed experiments changing all three dimensions together in order to investigate the Volume effect on AS4/3502 carbon fiber/epoxy specimens with cross-ply, angle-ply and quasi-isotropic lay-ups [7]. One of the tests performed by them included ply--level scaling of the specimens with the stacking sequence $[45_m/\text{-}45_m/0_m/90_m]_S$, with m varying from 1 to 4. **A significant size effect was found, with strength reducing by 28% over a factor of four increase in linear dimensions**. However, the failure strains increased and there was also a change in the failure mode from a localized fracture for the smaller specimens to more extensive fracturing throughout the specimen for the larger ones.

O'Brien [11] analyzed the ply scaling of another carbon fiber/epoxy material, T300/5208, with the same stacking sequence used by Jackson *et al.* ($[45_m/\text{-}45_m/0_m/90_m]_S$, with m) varying from 1 to 3, and concluded that this stacking sequence is susceptible to **free edge delamination** when loaded in tension.

Johnson *et al.* used the AS4/3502 carbon fiber/epoxy to investigate the sublaminate scaling in cross-ply, angle-ply and quasi-isotropic laminates including the same stacking sequence $[45/\text{-}45/0/90]_{nS}$ with n varying from 1 to 4 [12]. **The results showed an increase in strength from the smallest to the other sizes** (the latter gave quite similar results) because, according to the authors, the smallest specimens are more susceptible to the effects of free edge delamination. It was interesting to verify that similar scaled specimens using carbon fiber/PEEK (tougher matrix and therefore less prone to delamination) showed little scaling effect.

Notched specimens

Notched tensile strength is one of the design drivers for composite structures used in the aerospace industry because it is an easy way to simulate stress concentrations as a result of the use of mechanical fasteners or as the result of damaged areas in consequence of different kinds of impact (e.g. tool drop, bird impact, etc.), among other possible causes of stress concentrations (e.g. geometry of the component, etc.). Stress concentrations around a hole and the corresponding behavior in tension and in compression are particularly important compared to any other type of notch because the large majority of stress concentrations are circular: think again about the mechanical fasteners and the damaged areas resulting of a bird impact or a tool drop. For this purpose, aircraft companies have included **Open-Hole Tensile Tests** and **Open-Hole Compressive Tests** as part of their qualification procedure.

In the next section some results for several open-hole tensile tests performed by different authors will be presented, proving that the size effect phenomenon occurs also at the **macro--mechanical level** for composite materials.

2.1.1.2 Open-Hole Tensile tests (OHT)

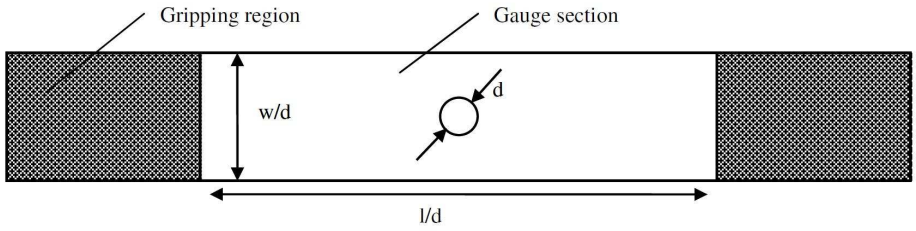

Figure 2.4: Open-Hole Tensile test specimen. [24]

The presence of a stress concentration, in this case a circular hole, **leads to enhanced complex damage and failure mechanisms**, causing a wide range of effects not present in unnotched components. The mechanical performance of a laminate to a notch is sensible to many factors, including: material [25, 27], laminate size and thickness [24, 32], notch size and geometry (in this case: hole diameter) [24, 28], lay-up and stacking sequence [24, 29, 30], ply orientation and thickness [30, 31] and machining quality. A typical specimen used in Open-Hole Tensile tests is presented in Figure 2.4.

Hole diameter effect (in-plane dimensions scaling)

Camanho *et al.* [23] performed open-hole tensile tests, using Hexcel's IM7/8552 quasi-isotropic CFRP laminates with the stacking sequence of $[90/0/\pm 45]_{3S}$, in order to quantify the size effect. Specimens with five different hole diameters, d=2, 4, 6, 8 and 10mm, and with a width-to-diameter ratio w/d equal to 6 were tested in a MTS servo-hydraulic machine following the ASTM D-5766 standard [40] according to the test matrix shown in Table 2.5. Five specimens were tested for each geometry.

Table 2.5: Open hole tension test matrix. [23]

Specimen ref.	d (mm)	w (mm)	w/d
OHT11	2	12	6
OHT10	4	24	6
OHT3	6	36	6
OHT6	8	48	6
OHT9	10	60	6

The remote failure stress is defined using the failure load measured in the tests ($\bar{P}$) and the measured values of the specimen thickness (t_L) and width (w) as: $\overline{\sigma}_t^{\infty} = \frac{\bar{P}}{wt_L}$. The remote failure stresses obtained for the different geometries are summarized in Table 2.6.

Table 2.6: Results of OHT tests. Material: IM7/8552. [23]

Hole diameter (mm)	$\overline{\sigma}_t^{\infty}$(MPa)	STDV (MPa)	CV(%)
2	555.7	15.3	2.8
4	480.6	21.4	4.5
6	438.7	25.3	5.8
8	375.7	15.1	4.0
10	373.7	14.1	3.8

The failure mode observed in all specimens was net-section tension, as shown in Figure 2.5.

Camanho *et al.* concluded that the experimental results presented in Table 2.6 clearly identify a size effect: **an increase in the hole diameter from 2mm to 10mm results in a 32.8% reduction in the strength**. Moreover, it was stated that the observed size effect is caused by the development of the fracture process zone identified in the Acoustic Emission results, which re-distributes the stresses.

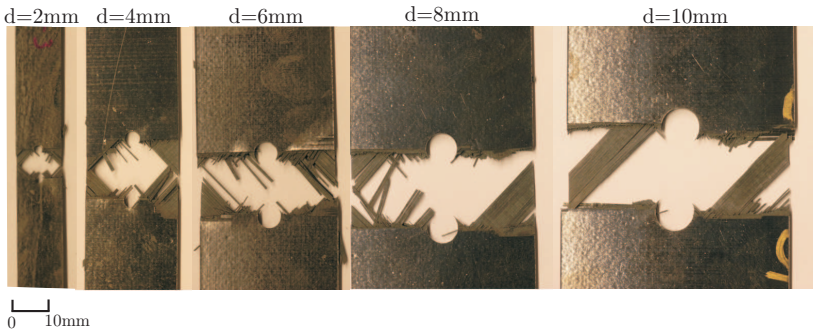

Figure 2.5: Net-section tension failures in specimens with $w/d = 6$. Material: IM7/8552. [23]

Another significant work was done by **Iarve *et al.*** [33]. The authors also studied the influence of changing the in-plane dimensions of quasi-isotropic carbon fiber laminates with two different stacking sequences $[45/0/-45/90]_S$ and $[0/45/90/-45]_S$ with three different hole sizes of 2.54, 6.35 and 12.7mm. The material used was IM7/5250-4 and the nominal thickness of the specimens was 1.1mm. The experimental results are listed below.

Table 2.7: Experimental results for OHT quasi-isotropic specimens. Material: IM7/5250-4. [33]

Hole diameter	$\overline{\sigma}_t^{\infty}$ (MPa)	
	$[45/0/-45/90]_S$	$[0/45/90/-45]_S$
2.54mm	565.4 (c.v. 5.1%)	677.1 (c.v. 7.8%)
6.35mm	468.5 (c.v. 3.9%)	560.7 (c.v. 5.6%)
12.7mm	436.0 (c.v. 9.4%)	479.2 (c.v. N/A)

In this work was also observed the existence of a size effect in OHT tests with carbon/epoxy specimens. An increase in the hole diameter from 2.54mm to 12.7mm results in **a 22.9% reduction in strength for the $[45/0/-45/90]_S$ laminate** and results in a **29.2% reduction for the $[0/45/90/-45]_S$**. Besides, the authors observed that **the laminate with outside** $0°$ **plies showed significantly higher tensile strength for all hole sizes**. They attributed such difference to fiber direction stress relaxation due to **matrix cracking in the form of splitting**[2] and **delamination** affecting the referred stacking sequence. X-radiography and sectioning studies to evaluate the state of matrix damage precipitating fiber failure were performed, which led to the conclusion that no delaminations were observed for the $[45/0/-45/90]_S$ laminate and only small delaminations, not in the high stress concentration area, were observed in the $[0/45/90/-45]_S$ laminate. The length of the splitting of the $0°$ ply and the cracking in the $45°$ plies neighboring with the $0°$ ply were tabulated by the authors with the extent of de-

[2] Longitudinal matrix cracks that cause the fibers' separation.

lamination, leading to the conclusion [39] that the size of the area around the hole that was affected by matrix damage was more important for the lay-up with external 0° ply. Thus, as a consequence of more extensive matrix cracking and accompanying stress relaxations, **the lay-up $[\mathbf{0/45/90/\text{-}45}]_S$ was able to sustain higher loads**.

Ogihara *et al.* confirmed in [27] the major role played by the 0° plies and the importance of their position in the lay-up. They investigated the following two lay-ups: $[0/45/90/\text{-}45]_{S2}$ and $[0/45/90/\text{-}45]_S$. According to [39] the authors showed that the existence of two 0° plies grouped together at the center of the laminate reduced its notch sensitivity, and they also pointed out that splitting in the 0° ply at the hole edge was the first occurring damage, triggering delaminations at the $0/45°$ interface.

Lagace [37] found that for $[0/90_2]_S$ laminates with a center hole loaded in tension the **failure mode changed from fiber-dominated to matrix-dominated with decreasing hole diameter**, and that change was accompanied by an increase in delamination and much less change in strength with hole size than expected on the basis of the Whitney-Nuismer or Mar-Lin hole size models (an overview on the current main analytical models to predict the strength of composites loaded in tension and compression will be presented in the next section). The author attributed this change of the failure mode to the interlaminar stresses in the region around the hole boundary, which decrease in importance with increasing hole radius to laminate thickness ratio.

Thickness effect

Hallett *et al.* performed a ply-level scaling investigation for two different stacking sequences of open-hole tensile composite specimens [30]. The IM7/8552 material was used to make quasi-isotropic laminates with the following stacking sequences: $[45/-45/90/0]_S$ and $[90/45/0/-45]_S$. The geometry of the specimens is the same presented in Figure 2.4, with $d = 3.175mm$, $w = 16mm$ and $l = 64mm$. The specimens were 1mm thick and the corresponding ply level scaled specimens were 2mm thick. The results are summarized in Table 2.8 with t being the laminate thickness and $\overline{\sigma}_t^{\infty}$ the mean average failure stress.

Table 2.8: Results of open-hole tensile tests – ply level scaling. Material: IM7/8552. [30]

Lay-up	t (mm)	$\overline{\sigma}_t^{\infty}$(MPa)	Failure mode
$[-45/45/90/0]_S$	1	563	Fiber dominated failure
$[-45_2/45_2/90_2/0_2]_S$	2	474	Delamination
$[90/45/0/-45]_S$	1	481	Fiber dominated failure
$[90_2/45_2/0_2/-45_2]_S$	2	499	Fiber dominated failure

Therefore if the ply thickness is increased from 0.125mm to 0.25mm for the case of the $[-45/45/90/0]_S$ stacking sequence **there is a change in failure mode from fiber failure to delamination accompanied by a decrease in strength of 15.8%**, but for the stacking sequence $[90/45/0/-45]_S$ there is **no change in failure mode and there is a negligible change in strength**.

The previous work demonstrated that delamination can play a key role in laminate strength in open-hole tensile tests. **In fact delamination is often a crucial failure mechanism for composites due to the generally low interlaminar strength** [34]. Hence, this failure mechanism is not only responsible for the well-known poor response of composites to out-of-plane loading but also can have a major role in laminate failure subjected to in-plane loading. There are several works related to the effect of delamination on notched tensile strength [35]-[38]. **Awerbuch and Madhukar** concluded that notch sensitivity is related to the damage occurring at the notch prior to failure [35]. **Kortschot *et al.*** proved in 1991 that delamination occurs in combination with splitting at the notch, relieving the stress concentration [36].

Vaidya *et al.* investigated the effect of ply thickness on unnotched and notched strength of fiber-dominated laminates [38]. In this study the material used was the AS4/3501-6. It was observed that ply block thickness has a significant effect on notched strength of cross-ply and quasi-isotropic laminates, although it was clearly stated that the quasi-isotropic were less affected. The experimentally observed crack-tip damage was in the form of axial splitting in the 0° plies and delamination. The authors also concluded that **the amount of delamination increased with ply thickness**, and for the quasi-isotropic specimens the failure mode switched from fiber failure to delamination when 4 plies were blocked together.

Volume, In-plane dimensions (hole diameter) & Thickness effects

Green *et al.* [24] performed an extensive experimental program to investigate the effect of

scaling the **hole diameter**, the **ply thickness** and the **laminate thickness** in an open hole tensile test. Therefore, in this research were studied the Volume effect (3D), In-plane dimensions effect or Hole diameter effect (2D) and Thickness effect (1D). For the thickness effect it were used the two scaling techniques previously referred in this work: sublaminate- and ply-level scaling. The ratios of hole diameter to width and length were kept constant, over a scaling range of 8 from the baseline size. The material used was the IM7/8552 with nominal thickness of 0.125mm and the stacking sequence was $[45_m/90_m/-45_m/0_m]_{nS}$. Notice that 0° is in the direction of the loading and that the subscripts *m* and *n* refer to the number of plies of each orientation present, and represent two different ways of increasing the thickness of the laminate. Also note that in this case the authors chose the specimens in a way that the product of *m* and *n* is equal to the laminate thickness. As previously referred in this text in the unnotched subsection, ply-level scaling is managed by changing *m* and sublaminate-level scaling by changing *n*. The specimen is represented is Figure 2.4.

Figure 2.6 shows the testing matrix. The dimensions of the baseline specimen were scaled by a factor of 2 each time up to a maximum of 8.

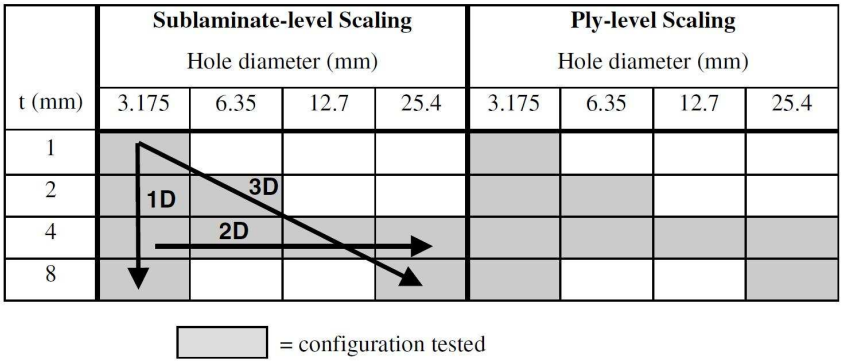

Figure 2.6: Testing program matrix. [24]

The authors used three different routines: one-dimensional, two-dimensional and three-dimensional scaling. In the case of **one-dimensional scaling** only the thickness of the laminate is increased; in **two-dimensional scaling**, the in-plane dimensions (hole diameter, and hence width and length) are increased but the thickness kept the same; and in **three-dimensional scaling** all dimensions are scaled simultaneously. Gauge section dimensions for the different hole diameters used are given in Table 2.9.

The test results obtained by the authors are shown in Table 2.10 with $\overline{\sigma}_t^{\infty}$ being the average

Table 2.9: Gauge section dimensions for different hole diameters. [24]

Hole diameter (mm)	Specimen width (mm)	Gauge length (mm)
3.175	16	64
6.35	32	128
12.7	64	256
25.4	128	512

mean tensile stress. Notice that failure was taken as being the first significant load drop on the load-displacement curve (greater than 5%).

Table 2.10 also shows that the authors examined the specimens failure mechanisms. Three distinct types of failure were identified: **Pull-out** (fiber dominated failure with extensive sub-critical damage), **Brittle** (fiber dominated failure with little sub-critical damage) and **Delamination** (matrix dominated failure).

Table 2.10: OHT results for sublaminate- and ply-level scaling. Material: IM7/8552. [24]

$\overline{\sigma}_t^{\infty}$ for sublaminate-level scaled specimens (MPa) (cv, %)					
t (mm)	Lay-up	Hole diameter (mm)			
		3.175	6.35	12.7	25.4
1	$[45/90/-45/0]_S$	**570 (7.69)**			
2	$[45/90/-45/0]_{2S}$	**500 (3.95)**	**438 (2.44)**		
4	$[45/90/-45/0]_{4S}$	**478 (3.09)**	**433 (2.03)**	**374 (1.01)**	**331 (2.98)**
8	$[45/90/-45/0]_{8S}$	**476 (5.06)**			**332 (1.31)**
$\overline{\sigma}_t^{\infty}$ for ply-level scaled specimens (MPa) (cv, %)					
t (mm)	Lay-up	Hole diameter (mm)			
		3.175	6.35	12.7	25.4
1	$[45/90/-45/0]_S$	**570 (7.69)**			
2	$[45_2/90_2/-45_2/0_2]_S$	**396 (5.18)**	**498 (6.45)** [1]		
4	$[45_4/90_4/-45_4/0_4]_S$	**275 (5.56)**	**285 (5.17)**	**362 (2.60)**	**417 (4.10)** [2]
8	$[45_8/90_8/-45_8/0_8]_S$	**202 (7.90)**			**232 (1.87)**

Pull-out type failure
Brittle type failure
Delamination type failure

[1] *Pull-out failure: 5 specimens; Delamination failure: 1 specimen.*
[2] *Delamination failure: 4 specimens; Pull-out failure: 2 specimens.*

Figure 2.7 shows examples of pictures for each of the types of failure that were identified.

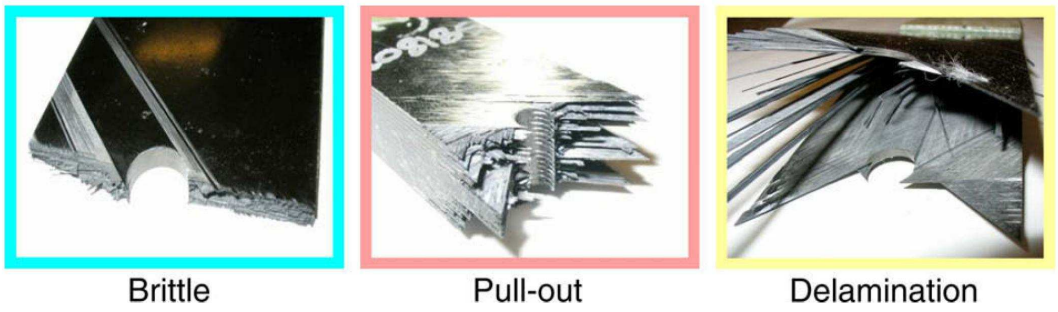

Figure 2.7: Different failure mechanisms in open hole tension tests. [34]

The failure types are related to the stress-strain curves. Green *et al.* also showed the typical load vs. displacement curves associated to each failure mode – Figure 2.8.

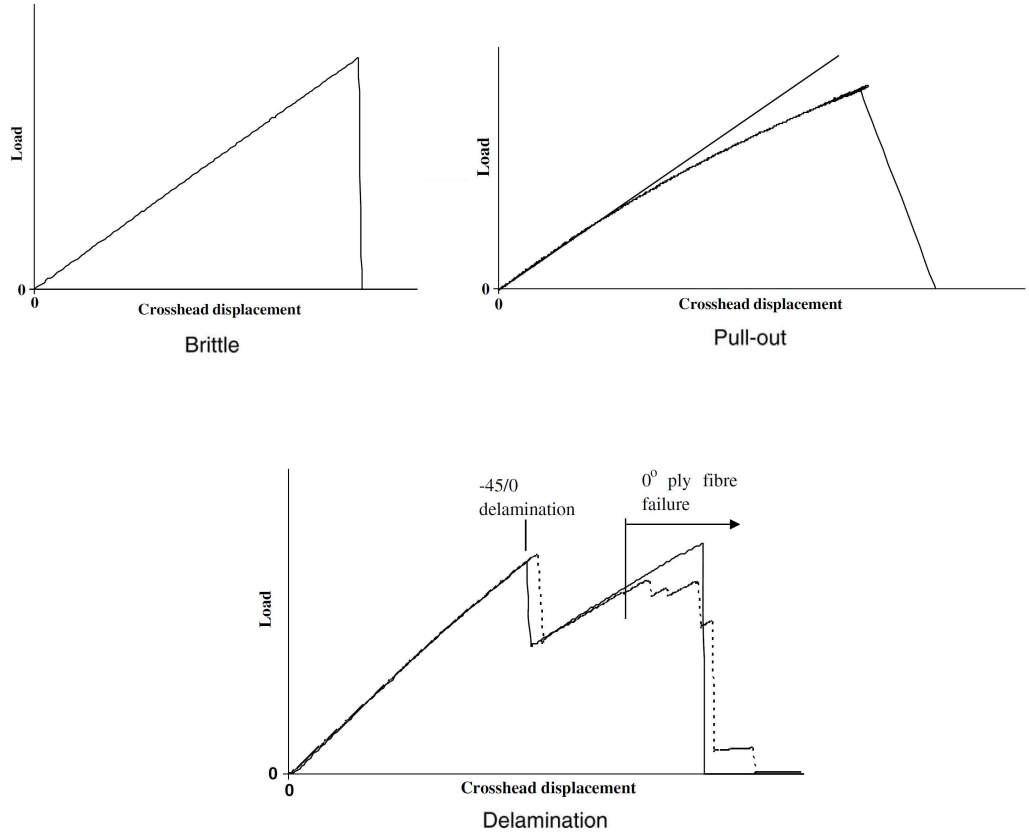

Figure 2.8: Load vs. Displacement curves associated to each failure type. [24]

These experimental results are quite interesting, proving that the size effect occurs not only with the increase of the thickness of the specimen but also with the hole diameter (and the combination of both) for the two types of scaling analyzed: sublaminate- and ply-level scaling. For sublaminate-level scaling of the stacking sequence $[45/90/-45/0]_S$:

- the increase by a factor of 8 in all dimensions (3-D) results in a 42% reduction in strength; and the failure mode changes from pull-out to brittle when the scale factor is 4;

- the increase by a factor of 8 in in-plane dimensions (2-D: hole diameter) leads to a 31% decrease in strength; and the failure mode changes from pull-out to delamination when the scale factor is 4;

- the decrease of thickness (1-D) by a factor of 8 implies a 17% decrease in strength; and pull-out remains always the failure mode;

For ply-level scaling:

- the increase by a factor of 8 in all dimensions (3-D) results in a 59% reduction in strength; and the failure mode changes from pull-out to delamination when the scale factor is 4;

- the increase by a factor of 8 in in-plane dimensions (2-D: the hole diameter) leads, notably, **to a 51% increase in strength**; and delamination remains always the failure mode;

- the decrease of thickness (1-D) by the same factor implies a 64% decrease in strength; and the failure mode changes from pull-out to delamination since the scale factor is 2;

2.1.2 Compressive Strength of Carbon Fiber/Epoxy Composites

2.1.2.1 Unnotched specimens in compression

Volume effect

Lee and Soutis [44] analyzed, in the first part of this study, the size effects for unnotched unidirectional and multidirectional specimens made of the referred IM7/8552 material.

The authors performed tests for three different **unnotched unidirectional** (UD) specimens under compressive loads. The test program is shown in Table 2.11, note that an end-tab material was used in the tests. This detail is important because this end-tab causes a stress concentration (in the transition region from the end-tab to the gauge section).

Table 2.11: Compression test program for the UD specimens (Unit: mm). [44]

Material	Lay-up	Specimen Thickness	Specimen Width × Gauge Length	Tab Length*
Pre-preg IM7/8552	UD	2	10×10	50
		4	20×20	50
		8	40×40	50

(No. of tested specimens = 6, *End-tab material: Woven glass fiber-epoxy reinforcement)*

The authors minimized successfully the bending due to misalignment (confirmed by evaluating the strain given from two back-to-back strain gages). The stress-strain curves showed similar behavior for all three geometries being essentially linear up to a strain level of approximately 0.5% and then nonlinear with softening, which increases with increasing strain. The obtained compressive modulus were independent of specimen volumes (around 155 GPa).

It was observed that the compressive failure of the unidirectional specimens was **instantaneous and catastrophic** and no cracking sound occurred prior to failure. When failure occurred, the test specimen parted into two pieces with fracture surfaces inclined at typical angles of between $\beta = 5^\circ \sim 30^\circ$ in the width direction, with β being the kinkband inclination angle – Figure 2.9. This is denominated as **kinkband formation** type of failure. In the same figure it's possible to see that failure was located near the tab ends with part of the material ejected, which suggests that stress concentration may be partly responsible for the failure (as referred previously). Besides kinkband formation, post failure examination showed that

failure combined also **longitudinal splitting** and **fiber breakage** for all specimens' size.

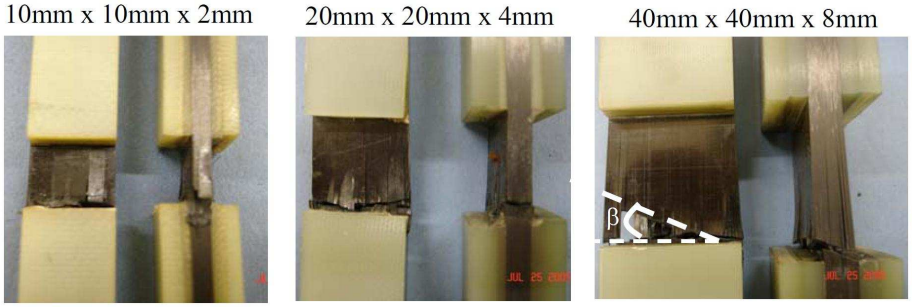

Figure 2.9: Comparison of the overall failure mode of the unidirectional specimens. Front view and side view are shown for different thicknesses (Specimen width × gauge length × thickness) [44]

Table 2.12 summarizes the results for the mean average compressive strength of IM7/8552 unidirectional laminates. The results show that the larger specimens showed a progressive reduction in strength with increasing size. **The strength of the IM7/8552 unidirectional laminates dropped by 45% in going from 2mm to 8mm.**

Table 2.12: Results for unidirectional unnotched specimens loaded in compression. Material: IM7/8552. [44]

Specimen dimensions (mm)	Mean Average Comp. Strength $\overline{\sigma_c^{\infty}}$ (MPa)	CV (%)
$10 \times 10 \times 2$	1570	4.51
$20 \times 20 \times 4$	1253	6.60
$40 \times 40 \times 8$	869	6.03

Failure Mode: combined longitudinal splitting, fiber breakage and kinkband formation

The authors also performed tests for **unnotched multidirectional** (MD) specimens loaded in compression, as previously stated, using sublaminate- and ply-level scaling. The lay-up tested was $[45/90/-45/0]_S$ with the same material as the unidirectional specimens (IM7/8552). Two different ply thicknesses were used: 0.125mm and 0.25mm. The test program is presented in Table 2.13 and Table 2.14.

The typical stress-strain curves were published [44] for both scaling techniques: the curves are linear up to a strain of approximately 0.5% with softening behavior to failure after that. **The**

Table 2.13: Compression test program for the unnotched MD specimens (Ply thickness: 0.125mm; Units: mm). [44]

Material	Lay-up: $[45/90/-45/0]_S$	Specimen Thickness	Specimen Width × Gauge Length	Tab Length*
Pre-preg	Sublaminate-level	2	30×30 *	50
IM7/8552	scaling/Ply-level	4	60×60 *	50
(0.125mm)	scaling	8	120×120 *	50

(No. of tested specimens = 6, *End-tab material: Woven glass fiber-epoxy reinforcement)*
*: Anti-buckling device

Table 2.14: Compression test program for the unnotched MD specimens (Ply thickness: 0.25mm; Units: mm). [44]

Material	Lay-up: $[45/90/-45/0]_S$	Specimen Thickness	Specimen Width × Gauge Length	Tab Length*
Pre-preg	Sublaminate-level	2	16×16 and 30×30*	50
IM7/8552	scaling/Ply-level	4	32×32 and 60×60*	50
(0.25mm)	scaling	8	64×64	50

(No. of tested specimens = 6, *End-tab material: Woven glass fiber-epoxy reinforcement)*
*: Anti-buckling device

nonlinearity of the multidirectional specimens was higher than that for unidirectional ones, which was attributed to matrix nonlinearity of the off-axis layers. The mean average **failure strains** of the multidirectional specimens were also **generally higher**, justified by the fact that the off-axis layers provide lateral support to the 0° axial plies and delay initiation of a kink band. Once again the measured elastic moduli were independent of the specimens' volume (approximately 58 GPa).

The test results for all volumes are shown in Table 2.15 and Table 2.16. In the case of the multidirectional specimens using the **sublaminate-level scaling** technique ($[45/90/\text{-}45/0]_{nS}$), **failure was sudden** and immediately prior to catastrophic fracture distinct cracking sounds were heard. Compressive **failure** of the multidirectional **ply-level scaled** specimens ($[45_m/90_m/\text{-}45_m/0_m]_S$) was **instantaneous and catastrophic** and was accompanied by an audible acoustic event without cracking sound prior to the catastrophic failure.

Table 2.15 shows that the strengths of the multidirectional specimens using the sublaminate--level scaling technique ($[45/90/-45/0]_{nS}$) are almost independent of the specimens' volume. For the ply-level scaled specimens ($[45_m/90_m/-45_m/0_m]_S$) it can not be stated that a size

Table 2.15: Unnotched mean average compressive strength obtained from sublaminate-level scaled specimens ($[45/90/-45/0]_{nS}$) and ply-level scaled specimens ($[45_m/90_m/-45_m/0_m]_S$). **Ply-thickness: 0.125mm**. Material: IM7/8552. [44]

Stacking sequence	Thickness (mm)	$\overline{\sigma_c^\infty}$, MPa (CV, %) Width × Length (mm × mm)		
		30 × 30	60 × 60	120 × 120
$[45/90/-45/0]_{nS}$	2	658 (3.15)	-	-
	4	-	675 (6.6)	-
	8	-	-	644 (14.0)
$[45_m/90_m/-45_m/0_m]_S$	2	666 (19.6)	-	-
	4	-	642 (19.0)	-
	8	-	-	472 (13.4)

effect occurred from the 2mm to the 4mm thick laminate but a 29% drop in strength was observed from the 4mm to the 8mm thick one (marked with a gray background). **This sharp strength drop was attributed to the thermal stress effect during curing process** (for more details it is advised to read the complete work [44]) and no change in the failure mechanisms was observed.

Table 2.16: Unnotched mean average compressive strength obtained from sublaminate-level scaled specimens ($[45/90/-45/0]_{nS}$). **Ply-thickness: 0.25mm**. Material: IM7/8552. [44]

Stacking sequence	Thickness (mm)	$\overline{\sigma_c^\infty}$, MPa (CV, %) Width × Length (mm × mm)				
		16 × 16	30 × 30	32 × 32	60 × 60	64 × 64
$[45/90/-45/0]_{nS}$	2	588 (8.71)	655 (2.03)	-	-	-
	4	-	-	603 (1.73)	588 (4.36)	-
	8	-	-	-	-	541 (4.9)

Table 2.16 shows that for thicker ply specimens (ply thickness: 0.25mm) the average failure strengths are unexpectedly lower than the failure strengths of thinner ply specimens, which was caused by manufacturing defects because the thicker prepreg (0.25mm) was obtained by squeezing the thinner prepregs (0.125mm) seriously waving the fibers and plies.

Post failure examination demonstrates that the **sublaminate-level scaled** specimens ($[45/90/\text{-}45/0]_{nS}$) showed **similar failure characteristics regardless of the specimen volume** and that the failure involved a combination of **kink band formation** in the 0° plies, **delamination** between 0° and ±45° plies, **splitting parallel** to the fibers at 0° and ±45° plies and **matrix cracking and crushing** in the 90° plies. It was also referred that failure seemed

to occur in a crushing failure mode without a global buckling influence at the area where the failure occurred as shown at the side view in Figure 2.10(a).

In relation to the **ply-level scaled specimens** ($[45_m/90_m/-45_m/0_m]_S$) it was stated that the failure modes identified were the same identified for the sublaminate-level scaled specimens, but in a more pronounced way (all of them).

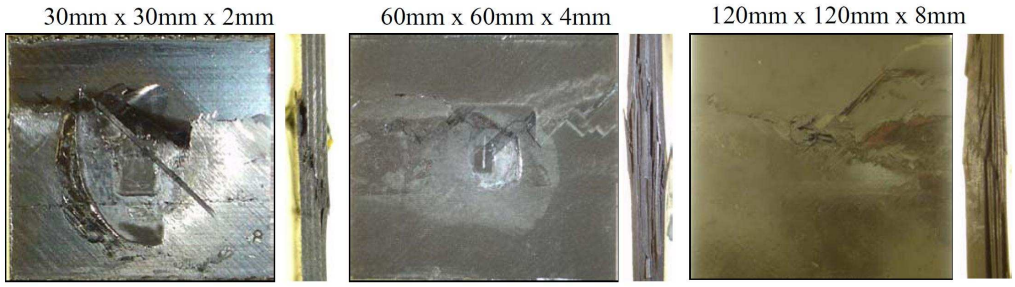

(a) Sublaminate Level Scaled Specimens ($[45/90/-45/0]_{ns}$)

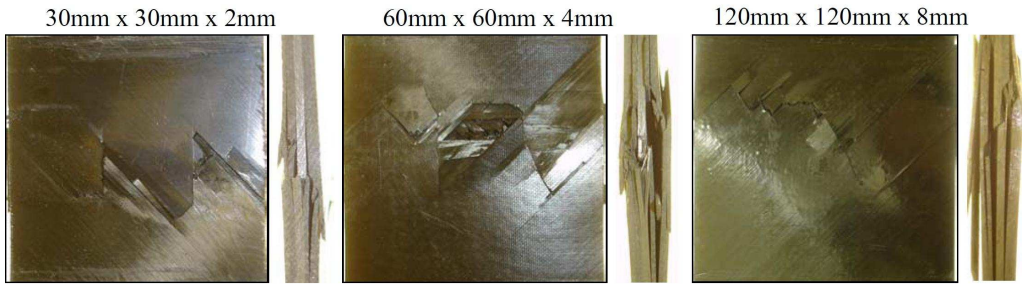

(b) Ply Level Scaled Specimens ($[45_n/90_n/-45_n/0_n]_s$)

Figure 2.10: Comparison of the overall failure mode of the multidirectional specimens. Front view and side view are shown for different thicknesses (Specimen width × gauge length × thickness). Material: IM7/8552. [44]

Stacking sequence influence

Soutis *et al.* [17] investigated the stacking sequence influence on compressive strength of unnotched T800/924C carbon-epoxy panels. The material used for this study was the T800/924C. The results are summarized in Table 2.17.

Post-failure examination of the fracture surfaces using scanning electron microscope revealed that failure is by **kink band formation** in the 0° plies. The fibers break at two points and create a kink band inclined at an angle, $\beta \approx 15°$, to the transverse direction – Figure 2.11. The fibers within the band rotate by an angle $\phi = 30°$ from the initial fiber direction, and the kink width $w = 50 - 60\mu m$ is approximately equal to 10 fiber diameters ($d = 5.5\mu m$) [17].

Table 2.17: Unnotched compressive strength and properties (Ply thickness: 0.25mm; Units: mm). Material: T800/924C. [17]

Lay-up	Ply orientation	% of 0° plies	$\overline{\sigma}^{\infty}_{c,un}$ (MPa)	E_{yy} [c] (GPa)	G_{xy} [d] (GPa)	ε_f (%)	K_c ($MPa.m^{1/2}$)	$[K_c/\overline{\sigma}^{\infty}_{c,un}]^2$ (mm)
L0	$[0_8]_S$	100	1615	160	6	1.10	–	–
L1	$[\pm 45/0_4]_{2S}$	67	1010 (1136)[a]	109	17.76	1.04	50.5	2.50
L2	$[\pm 45/0_2]_{3S}$	50	810 (904)[a]	88	23.5	1.10	46.5	3.29
L3	$[0/90_2/0]_{3S}$	50	670[b] (847)[a]	78	6.0	0.96	40.6	2.30
L4	$[\pm 45/0_2/90_2/0_2/90_2/0_2]_S$	50	820 (865)[a]	84	12.0	1.05	40.0	2.38
L5	$[\pm 45/0/90]_{3S}$	25	568 (523)[a]	58	23.6	1.07	42.5	5.60
L6	$[(\pm 45)_2/0/(\pm 45)_2/0/\pm 45]_S$	17	428 (442)[a]	41	35.4	1.35	35.0	6.68

[a] Predicted values, assuming elastic laminate plate theory and $\varepsilon_r = 1.1\%$.

[b] Premature failure due to out-of-plane microbuckling.

[c] E_{yy} is the laminate stiffness in the loading direction.

[d] G_{xy} is the shear stiffness obtained from the laminate plate theory.

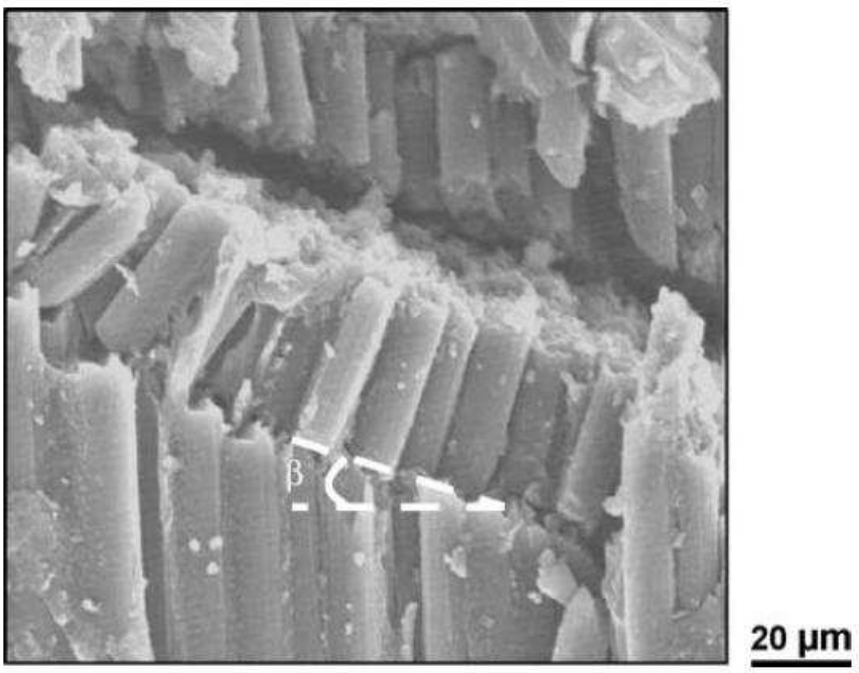

Figure 2.11: SEM micrograph of fiber kinking in a unidirectional T800/924C laminate. [18]

It was interesting to observe that all the tested multidirectional laminates, L1-L6, failed by kink band formation in the 0° plies which led to delamination between the off-axis and 0° plies (the next subsection will show that a similar phenomenon was observed for the open-hole compression specimens). Plastic deformation in the off-axis plies was also observed.

Less than 10% of scatter in strength was obtained and the failure strain ε_f = 1% is almost independent of the lay-up and comparable to the unidirectional laminate. The authors stated that this fact suggests that the off-axis plies have little influence upon the strain for **microbuckling**[3] of the 0° fibers, perhaps because the 0° plies are much stiffer than the off-axis plies and carry most of the load.

Therefore, the **critical event** in these laminates is the **kink band formation in the 0° plies** leading to failure after propagation of the kink band at an angle β = 5-20°.

Two last comments on the results summarized in Table 2.17:

1. **laminate L3**, $[0/90_2/0]_{3S}$, contains 0° outer layers which fail by **out-of-plane microbuckling**. On the contrary **laminate L4**, $[\pm 45/0_2/90_2/0_2/90_2/0_2]_S$, possesses ±45° outer plies which support the 0° inner layers allowing them to fail only by **kink band formation**[4], which is a higher stain failure event. This should be the reason to the low compressive strength observed for the L3 laminate;

2. **laminate L6**, $[(\pm 45)_2/0/(\pm 45)_2/0/\pm 45]_S$, showed a **non-linear stress-strain response** and failed at a higher strain ε_f = 1.35%. The L6 laminate is mainly composed by ±45° plies which have low axial stiffness and the higher strain is expected because the 100% ±45° material exhibits a strain of ε_f = 6%, however the presence of a small portion of 0° plies is responsible for a sharp decrease in strain, very close to the value of the other laminates.

[3] Microbuckling: an instability at the micro-level, characterized by in-phase fiber waviness, dependent on initial defects and common in composites subjected to compressive loadings with strong matrix and fibers [84]. This phenomenon (among others) will be discussed further (Chapter 3).

[4] The authors of the cited work [17] considered that in-plane microbuckling occurred instead of kink band formation. There is some controversy surrounding these two concepts. This topic will be discussed further in this work (Chapter 3). In this thesis the term "kink band" is used when a band of fibers kink in a way that it is created a band that has an orientation defined by a fixed angle (β, in Figure 2.11). Therefore, in this work the "microbuckling" term is reserved for single fiber's bending instability or for a bunch of fibers' bending instability resulting in a non-rotated band of fibers (β = 0°).

Thickness effect

Lee and Soutis [18] did yet another study on the size effect in compressive strength. This time the thickness effect on T800/924C unnotched unidirectional and multidirectional specimens was investigated.

Scaling the thickness of laminates led some other authors to some unreliable results [19, 20], where premature failure (end crushing) had a major role on that uncertainty [19, 21]. However, Lee and Soutis obtained good results for unidirectional and multidirectional unnotched specimens. The specimen geometry is shown in Figure 2.12.

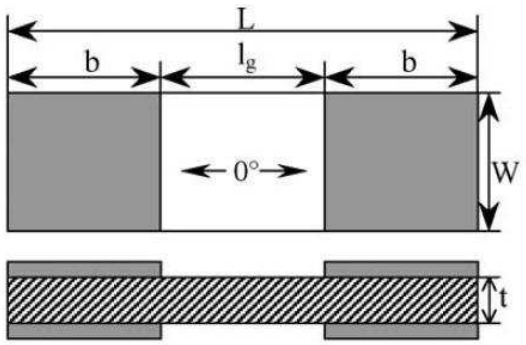

Figure 2.12: Unnotched CFRP specimen dimensions. W (Specimen Width) $\times$ l_g (Gauge Length) = $10mm \times 10mm$ for Unidirectional specimen and W (Specimen Width) $\times$ l_g (Gauge Length) = $30mm \times 30mm$ for Multidirectional specimen. [18]

The results for the **unnotched unidirectional specimens** are summarized in the Figure 2.13. The strains observed at failure were 0.97%, 0.95% and 0.72%, respectively for the 2, 4 and 8mm thick specimens.

Figure 2.13 shows that the compressive strength of unidirectional specimens decreases 34.2% as the thickness increases by a factor of 4. The authors refer an important fact: **failure was observed near the grip** in the thicker specimens which most likely affected the latter's compressive strength (due to stress concentrations). For this reason the results obtained by the referred authors for the unidirectional specimens should be considered with great caution, because it is possible that the size effect for the unidirectional material is not so pronounced.

For the case of the **unnotched multidirectional specimens** the authors did two types of scaling: sublaminate- and ply-level scaling. The results for the unnotched multidirectional

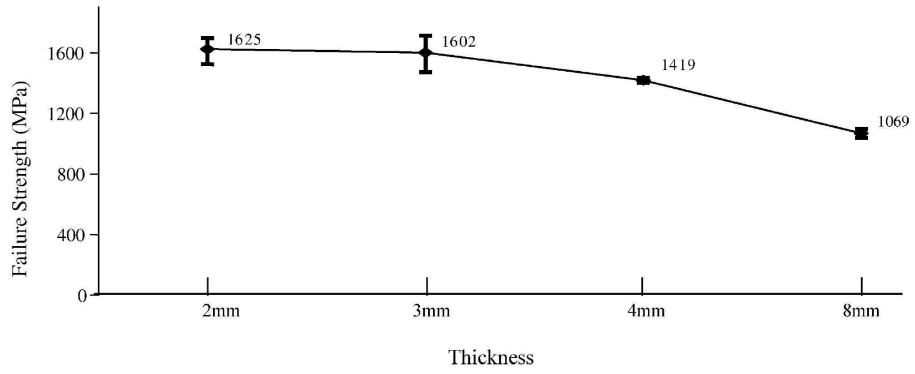

Figure 2.13: Average compressive strength as a function of specimen thickness for unidirectional laminates. Material: T800/924C [18]

specimens are summarized in the Figure 2.14. These tests were all valid, reproducible and all specimens regardless of the specimen thickness failed within the gauge length. In the case of the multidirectional specimens using the sublaminate-level technique ($[45/0/-45/90]_{nS}$), failure was sudden and immediately prior to catastrophic fracture distinct cracking sounds were heard. On the contrary, for the ply-level scaled specimens ($[45_n/0_n/-45_n/90_n]_S$) no cracking sound was heard prior to failure.

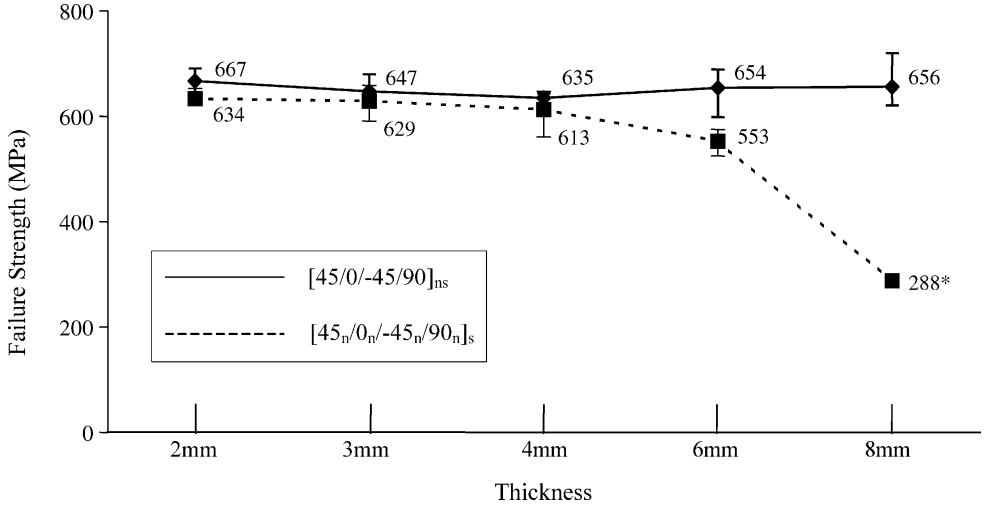

Figure 2.14: Average compressive strength as a function of specimen thickness for multidirectional laminates (*Matrix cracks in the 8mm thick specimens due to material age). Material: T800/924C [18]

One important detail of Figure 2.14 is that for the 8mm thick specimen the failure strength is very low but this is due to brittleness caused by aging of the pre-preg material (over 6 years old). Moreover, residual thermal stresses also contribute to strength reduction (as was

observed for the UD specimens). So the 8mm thick laminate won't be considered in further observations.

The overall failure mode for all specimens was delamination. Post-failure examination of the **sublaminate-level scaled specimens** ($[45/0/\text{-}45/90]_{nS}$) showed similar failure characteristics regardless of the specimen thickness, involving a combination of **kink band formation** in the 0° plies, **delamination** between 0 and ±45° plies, **splitting** parallel to the fibers at 0 and ±45° plies, and **matrix cracking and crushing** in the 90° plies. In addition, the failure seemed to occur in a crushing failure mode without a global buckling influence. **The ply--level scaled specimens** ($[45_n/0_n/\text{-}45_n/90_n]_S$) also showed the above failure characteristics in macroscale, but in a **more pronounced way**. This includes clearer fiber splitting in the 0° and ±45° plies, more delamination between 0° and ±45° plies and more clear matrix cracking and crushing in the 90° plies.

Finally, analyzing Figure 2.14 it is possible to conclude that for unnotched multidirectional specimens:

- the average failure strength values of the specimens using the **sublaminate-level scaling technique** ($[45/0/-45/90]_{nS}$) are almost constant regardless of the specimen thickness, indicating that **no significant thickness effect exists**;
- the compressive strength of the **ply-level scaled specimens** ($[45_n/0_n/-45_n/90_n]_S$) is almost unaffected by thickness changes up to 4mm, but **drops by 10% in going from 4mm to 6mm, showing thickness effect**. The 8mm thick specimen's average strength reduces drastically but this is due to material aging (as was already referred), so this result will be ignored.

2.1.2.2 Open-Hole Compressive (OHC) tests

OHC important failure mechanisms

Suemasu *et al.* published a work that helps understanding the failure mechanisms of composite laminates with an open hole subjected to the compressive load [46]. The authors state that the stress in a composite material around a circular hole is very complex due to the effect of the inhomogeneous material properties as well as the stress concentration. In the same work,

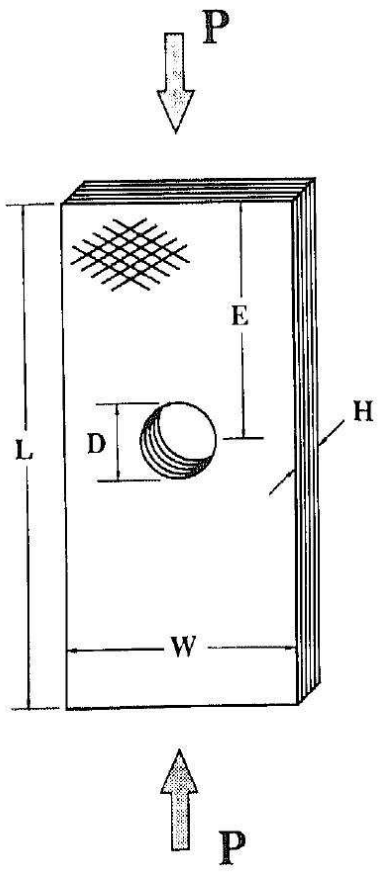

Figure 2.15: Open Hole Compression specimen. [45]

it was cited that the singularity of the interlaminar stress [47, 48] is of a very small power when compared to one half of a typical crack, which makes the problem difficult to estimate.

Quasi-isotropic laminates ($[45/0/\text{-}45/90]_{2S}$) of two different materials (T800H/3633 and TR30/#340) were used. The T800H/3633 laminate has a comparatively tougher interface than the TR30/#340. The specimen dimensions were D = 6.35mm, L = 118.0mm, W = 38.1mm and H = 2.2mm – see Figure 2.15. The OHC specimen was loaded very slowly (0.1mm/min) in order to identify the damage initiation and to track its propagation.

For the material TR30/#340 the authors observed that the specimen failed suddenly without visible damage due to the low interfacial toughness. The load vs. displacement curve of the T800H/3633 is provided in Figure 2.17. During the OHC test for the latter material the damage accumulation process was observed with the digital microscope – Figure 2.18. The close up view of the hole surface of the unloaded T800H/3633 specimen is shown in Figure 2.16.

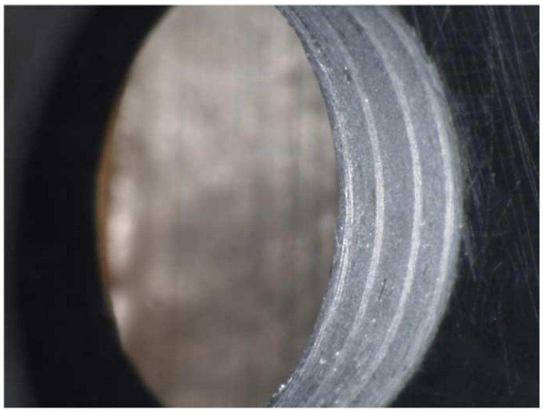

Figure 2.16: Close up view of the hole surface of the unloaded T800H/3633 specimen. Lay-up: $[45/0/\text{-}45/90]_{2S}$. Note that the 0° layers are 'shinning'. [46]

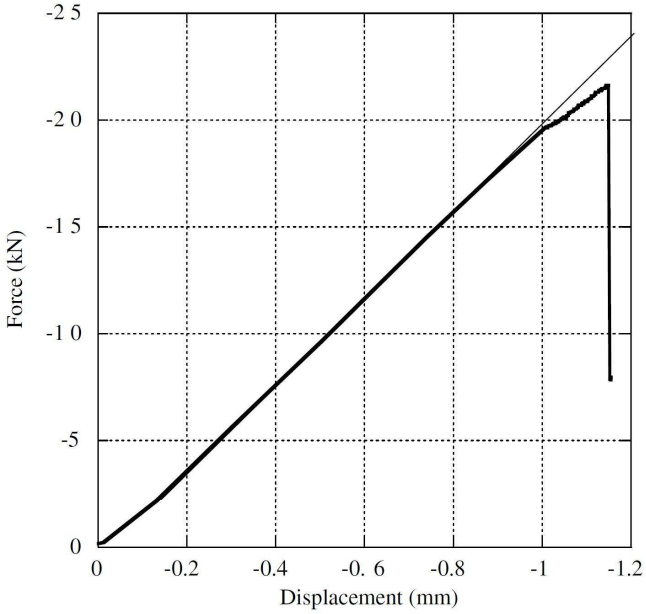

Figure 2.17: OHC: Applied load against the displacement of the fixture for the material T800H/3633. [46]

Figure 2.17 shows that there was some reduction of the compressive stiffness around 17.5kN and further reduction was found at about 19kN. In fact by looking to Figure 2.18(b) it is not observed any damage at the hole surface but because of the first drop in stiffness that occurred at around 17.5kN it is believed that fiber microbuckling started to occur in the 0° layers. Although it is not completely certain when the fiber microbuckling started, there is no doubt that the most noticed **stiffness reduction found at about 19kN is due to fiber microbuckling** – Figure 2.18(c). The damage portions continued to grow and it is clearly observed in Figure 2.18(d), particularly in the magnified image, that the small portion of the 0° layer buckled out

from the hole surface. Consequently, just a small load increase caused delamination, leading to the conclusion that **fiber microbuckling triggered the delamination**, Figure 2.18(e), which led to the final failure of the laminate shown in Figure 2.18(f).

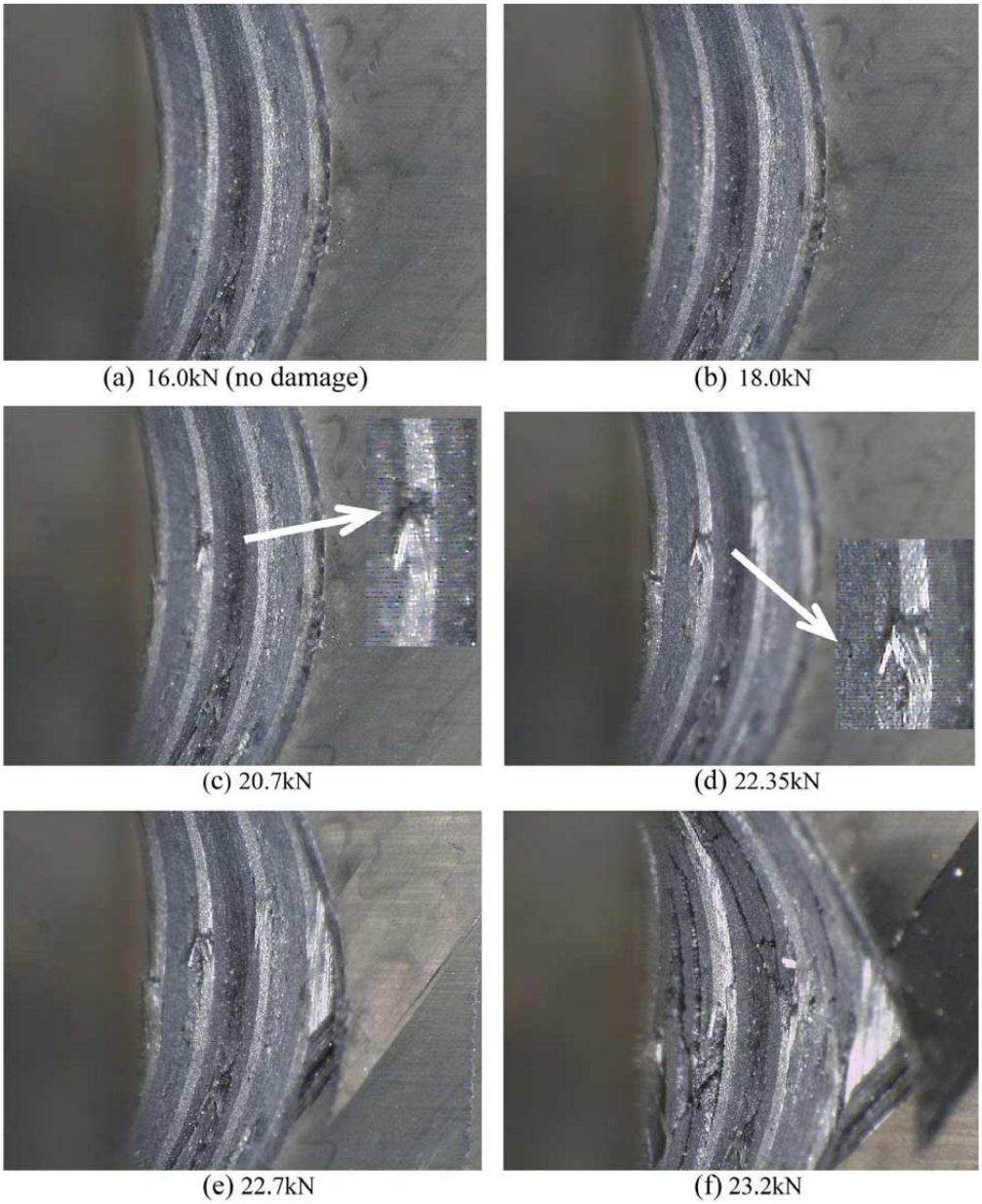

Figure 2.18: Damage process during OHC test taken by a digital microscope. Material: T800H/3633. [46]

The authors also took a photograph of the radial cross-section and a C-scan image of T800H/ /3633 damaged specimen by removing it from the fixture before rupture – Figure 2.19. It was observed the existence of **transverse cracks** in all 0° layers at the hole surface and **significant delaminations** emanating from the damages of the 0° layers at the interfaces between the 0°

and ±45° layers near surface. The overview of the delaminations are observed around the damage site also in Figure 2.19(b).

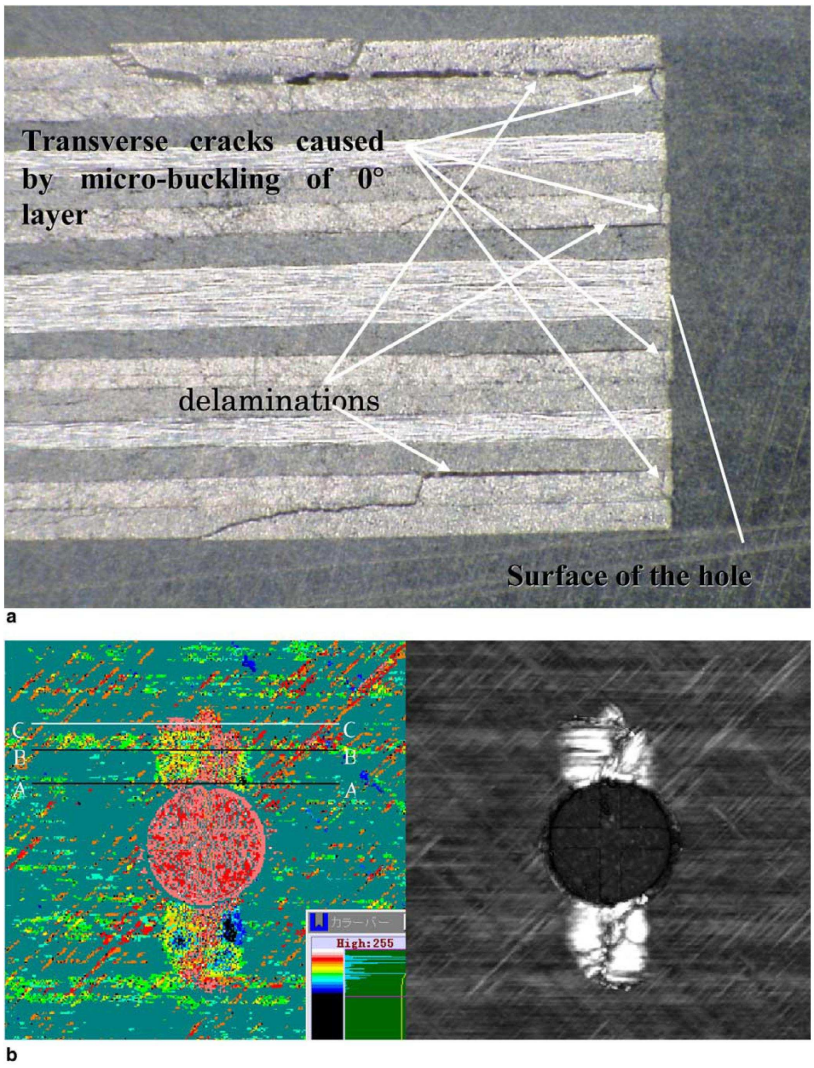

Figure 2.19: Damage stage near the hole for quasi-isotropic laminates ($[45/0/-45/90]_{2S}$) before final failure under the OHC test: (a) micrographs of damage at a radial cross-section; (b) C-scan image of damage. Material: T800H/3633. [46]

With the presented experimental work and with other experimental data collected by the authors in the referred study [46] it was concluded that **the final failure load for laminates with low interface toughness is governed by the compressive strength of the** 0° **layers** of those laminates; and that **the delamination size governs the strength of the laminates with toughened interfaces**.

Thickness effect

Lee and Soutis [18] tested OHC specimens with a 3mm diameter hole in order to investigate thickness effects on notched compressive strength. The material used for this study was the T800/924C and the stacking sequence was [45/0/-45/90]. Sublaminate-level scaled ($[45/0/\text{-}45/90]_{nS}$) and ply-level scaled ($[45_n/0_n/\text{-}45_n/90_n]_S$) specimens were used. The first difference noticed between the behavior of the specimens scaled by these two techniques was that the sublaminate-level scaled specimens emitted a distinct cracking type sound just prior to catastrophic failure, unlike the ply-level scaled ones. From post-failure investigation, the authors concluded that the overall final failure mode was found very similar for each stacking sequence type regardless of specimen thickness. Moreover, the failure modes were common to both scaling techniques, although more localized around the hole for the sublaminate-level scaled specimens. Thus, the ply-level scaled specimens exhibited more clear delamination, fiber splitting, matrix cracks and fiber microbuckling.

One important thing to notice is that the failure mode of the 8m thick specimen was different compared to that of other specimens because the material used was more than 6 years old, so it was observed extensive delamination of the outer plies which lead to premature failure. Figure 2.20 shows the measured average compressive strengths as a function of specimen thickness.

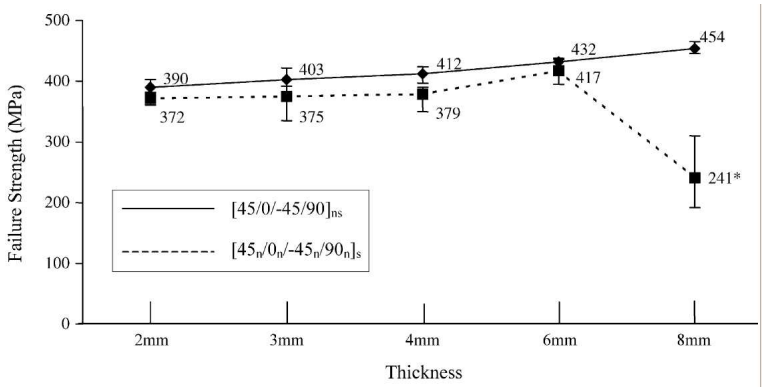

Figure 2.20: Open hole average compressive strength as a function of the specimen thickness for multidirectional laminates ($D/W = 0.1$). Material: T800/924C. (*Premature failing of the 8mm thick specimens due to material aging) [18]

The obtained results of the thickness scaling lead to the following conclusions:

- The average strengths obtained from both scaling techniques increase with increasing

thickness (except for the 8mm thick specimens which fail prematurely due to material aging);

- The OHC strength of the sublaminate-level scaled specimens is slightly higher than the strength of the specimens produced by using the ply-level scaling technique (this was also observed in the unnotched multidirectional specimens tested also in the same cited work and presented in Figure 2.14).

Effect of Stacking sequence & In-plane dimensions variation in OHC strength

Lessard and Chang [45] presented in 1989 an extensive experimental investigation to study the compression response of composite plates containing holes. The material used was the T300/976 (carbon fiber/epoxy pre-preg). The authors tested five different stacking sequences and for each of them different geometries were chosen varying always the in-plane dimensions and keeping the thickness constant, giving a total of over 30 different test configurations. Besides that extensive testing, two of the lay-ups were ply-level scaled. The test matrix of the lay-ups and the geometries of T300/976 samples tested are presented in Table 2.18. Please note that all results here presented were **converted to S.I. units**.

Table 2.18: Test matrix of the lay-ups and geometries of T300/976 samples tested. [45]

Matrix of W/D ratios tested		
Lay-up	W/D ratio with D = 6.35mm	W/D ratio with D = 12.7mm
$[0/90]_{6S}$	3, 4, 5, 6	2, 3
$[\pm 30]_{6S}$	3, 4, 5, 6	2, 3
$[\pm 45]_{6S}$	3, 4, 5, 6	2, 3
$[0/\pm 45/90]_{3S}$	3, 4, 5, 6	2, 3
$[0/\pm 45]_{4S}$	3, 4, 5, 6	2, 3
Ply-level scaled Lay-up	W/D ratio with D = 6.35mm	W/D ratio with D = 12.7mm
$[0_6/90_6]_S$	4	2, 4
$[0_3/(\pm 45)_3/90_3]_S$	4	2, 4

Note that all lay-ups have 24 layers of plies and therefore the same nominal thickness, $H \approx 3.43mm$

A summary of the results is presented in Tables 2.19 to 2.25.

Table 2.19 refers to the $[0/90]_{6S}$ lay-up. Delamination was the observed failure mode. From this table it can be concluded that:

- the mean average compressive strength, $\overline{\sigma}_c^{\infty}$, increased 7.4% when the width was increased by a factor of 2 for D = 6.35mm;
- $\overline{\sigma}_c^{\infty}$ increased 18.0% for the 12.7mm hole diameter when the width increased by a factor of 1.5;
- for the same W/D ratio a decrease of 15.4% in the mean average compressive strength was observed when the hole diameter was doubled – hole size effect.

Table 2.19: Summary of experimental results for $[0/90]_{6S}$. [45]

$[\mathbf{0}/\mathbf{90}]_{\mathbf{6S}}$			
H = 3.43mm, E/D = 4, L/D = 8			
D (mm)	W/D	$\overline{\sigma}_c^{\infty}$ (MPa)	σ_c^{∞} range (MPa)
6.35	3	402.1	384.7-415.1
6.35	4	425.9	408.6-454.8
6.35	5	429.8	413.2-447.6
6.35	6	431.8	398.7-465.8
H = 3.43mm, E/D = 2, L/D = 4			
12.7	2	288.3	284.9-291.7
12.7	3	340.3	336.4-344.3

Failure Mode: **Delamination** (all layers; symmetric fashion); catastrophic

Table 2.20 shows that despite the fact that the failure mode of the $[\pm 30]_{6S}$ lay-up (brittle) was different from the previous laminate (delamination) the strength variation with in-plane dimensions scaling is very similar:

- $\overline{\sigma}_c^{\infty}$ increased 7.3% when the width was increased by a factor of 2 for D = 6.35mm;
- $\overline{\sigma}_c^{\infty}$ increased 23.7% for the 12.7mm hole diameter when the width increased by a factor of 1.5;
- doubling the hole diameter, for the same W/D ratio, results in a mean average compressive strength decrease of 18.4% – hole size effect.

Table 2.20: Summary of experimental results for $[\pm 30]_{6S}$. [45]

$[\pm\mathbf{30}]_{\mathbf{6S}}$			
H = 3.43mm, E/D = 4, L/D = 8			
D (mm)	W/D	$\overline{\sigma}_c^{\infty}$ (MPa)	σ_c^{∞} range (MPa)
6.35	3	205.8	204.3-207.8
6.35	4	214.8	210.3-219.3
6.35	5	218.2	216.4-220.7
6.35	6	220.9	212.2-232.6
H = 3.43mm, E/D = 2, L/D = 4			
12.7	2	135.8	127.9-144.3
12.7	3	168.0	159.7-179.0

Failure Mode: **Brittle** (fracture angle: 30°).

Table 2.21: Summary of experimental results for $[\pm 45]_{6S}$. [45]

$[\pm\mathbf{45}]_{\mathbf{6S}}$			
H = 3.43mm, E/D = 4, L/D = 8			
D (mm)	W/D	$\overline{\sigma}_c^{\infty}$ (MPa)	σ_c^{∞} range (MPa)
6.35	3	134.2	125.7-137.0
6.35	4	160.0	156.4-162.4
6.35	5	169.5	168.2-170.2
6.35	6	177.1	176.0-178.3
H = 3.43mm, E/D = 2, L/D = 4			
12.7	2	105.8	99.8-109.8
12.7	3	141.0	140.7-141.3

Failure Mode: Appears to be dominated by **Matrix Cracking** (fracture angle: 45°).

Note: Stress-strain curve highly nonlinear, even in early stages of loading. Failure without warning.

Scaling the width for the $[\pm 45]_{6S}$ lay-up affects much more the compressive strength of the composite than the previous two lay-ups: $[\pm 30]_{6S}$ and $[0/90]_{6S}$, as can be seen in Table 2.21. On the contrary, **the results for the hole size effect showed the opposite trend compared with all other laminates tested** by the authors: it was noticed a small increase with the increase of diameter. Table 2.21 shows that:

- $\overline{\sigma}_c^{\infty}$ increased 32.0% for the 6.35mm hole diameter when the width was increased by a factor of 2;

- $\overline{\sigma}_c^{\infty}$ increased 33.3% for the 12.7mm hole diameter when the width increased by a factor of 1.5;

- for the same W/D ratio it was observed, notably, that the mean average compressive strength **increased** 5.1% when the hole diameter was doubled.

Table 2.22 shows that the $[0/\pm45/90]_{3S}$ lay-up is not very sensible to the width scaling, particularly when observing the values for the 12.7mm of hole diameter. This laminate (and the next) showed the already referred important compressive failure mechanism: **microbuckling**. From the table it can be seen that:

- $\overline{\sigma}_c^{\infty}$ increased 10.4% for the 6.35mm hole diameter when the width was increased by a factor of 2;

- $\overline{\sigma}_c^{\infty}$ increased 4.0% for the 12.7mm hole diameter when the width increased by a factor of 1.5;

- doubling the hole diameter, for the same W/D ratio, results in a mean average compressive strength decrease of 26.6%.

Table 2.22: Summary of experimental results for $[0/\pm45/90]_{3S}$. [45]

$[\mathbf{0}/\pm\mathbf{45}/\mathbf{90}]_{\mathbf{3S}}$			
H = 3.43mm, E/D = 4, L/D = 8			
D (mm)	W/D	$\overline{\sigma}_c^{\infty}$ (MPa)	σ_c^{∞} range (MPa)
6.35	3	309.7	309.7
6.35	4	315.8	308.1-323.6
6.35	5	311.4	309.8-313.9
6.35	6	341.8	340.5-344.5
H = 3.43mm, E/D = 2, L/D = 4			
12.7	2	218.6	218.6
12.7	3	227.3	217.1-237.3

Failure Mode: **Delamination**, triggered by **Microbuckling** in 0° plies at ≈ 95% of failure load.
Note: Failure was less sudden than the $[0/90]_{6S}$ lay-up.

The next table should be analyzed with caution – Table 2.23. The lay-up $[0/\pm45]_{4S}$ may seem to have an opposite trend for the compressive strength after scaling of the in-plane

dimensions when compared to the previous lay-ups for the 6.35m hole diameter, but that is not likely the case. In fact, for $W/D = 6$ the failure load was smaller than the rest but until there the compressive strength increased with the width of the specimen. Moreover, for the $W/D = 6$ ratio it was only used one specimen so it is not statistically viable to conclude that the compressive strength for this ratio is less than for the others. After understanding the reason why **the specimen used to test the $W/D = 6$ geometry will not be accounted**, it is important to notice that it was not clearly observed a strength variation with the increase of the width for this lay-up (for the 6.35m hole diameter).

Table 2.23: Summary of experimental results for $[0/\pm45]_{4S}$. [45]

$[\mathbf{0}/\pm\mathbf{45}]_{\mathbf{4S}}$			
$H = 3.43$mm, $E/D = 4$, $L/D = 8$			
D (mm)	W/D	$\overline{\sigma}_c^{\infty}$ (MPa)	σ_c^{∞} range (MPa)
6.35	3	354.3	349.2-363.9
6.35	4	363.8	351.8-377.5
6.35	5	360.0	337.5-363.6
6.35	6	305.2	305.2
$H = 3.43$mm, $E/D = 2$, $L/D = 4$			
12.7	2	231.0	222.6-239.4
12.7	3	286.7	285.7-287.6

Failure Mode: Similar to the $[0/\pm45/90]_{3S}$ lay-up. **Delamination**, triggered by **Microbuckling** in 0° plies at ≈ 95% of failure load.

Therefore, the table analysis leads to the following conclusions:

- the compressive strength remained approximately constant when the width was increased by a factor of 1.67 for the 6.35mm hole diameter;
- $\overline{\sigma}_c^{\infty}$ increased 24.1% for the 12.7mm hole diameter when the width increased by a factor of 1.5;
- doubling the hole diameter, for the same W/D ratio, results in a mean average compressive strength decrease of 19.1%.

Tables 2.24 and 2.25 provide the results for the ply-level scaled specimens. Both lay-ups, $[0_6/90_6]_S$ and $[0_3/(\pm45)_3/90_3]_S$, have the same failure mode: premature delamination antic-

ipated by extensive longitudinal matrix cracking, but the compressive strength behavior is different.

Table 2.24 shows some interesting results, some of them need to be compared with Table 2.19:

- the mean average compressive strength of the ply-level scaled laminate, $[0_6/90_6]_S$, is 3.1% **higher** than the compressive strength of the laminate $[0/90]_{6S}$ for the hole diameter of 6.35mm (W/D=4) and it is 1.7% **higher** for the 12.7mm hole diameter (W/D=2). **This is quite interesting** (and maybe a bit unexpected) because the authors stated that premature delamination occurred. Also it is the opposite behavior obtained in open-hole tensile tests (see Table 2.10);
- $\overline{\sigma}_c^{\infty}$ increased 38.3% for the 12.7mm hole diameter when the width increased by a factor of 2;
- doubling the hole diameter, for the same W/D ratio, results in a mean average compressive strength decrease of 7.7%.

Table 2.24: Summary of experimental results for $[0_6/90_6]_S$. [45]

$[\mathbf{0_6/90_6}]_S$ (Ply-level scaled)			
H = 3.43mm, E/D = 4, L/D = 8			
D (mm)	W/D	$\overline{\sigma}_c^{\infty}$ (MPa)	σ_c^{∞} range (MPa)
6.35	4	439.7	385.4-502.6
H = 3.43mm, E/D = 2, L/D = 4			
12.7	2	293.4	265.2-309.6
12.7	4	405.8	305.0-459.7

Failure Mode: Extensive **longitudinal cracks** along 0° lines emanating from hole boundaries leading to premature **Delamination**.

Note: Premature delamination caused a wide variation of the failure load.

Table 2.25 is related with the $[0_3/(\pm45)_3/90_3]_S$ lay-up (compare with Table 2.20). For this laminate it was not obtained the same trend of the previous one, so the results are not unexpected:

- the mean average compressive strength of the ply-level scaled laminate, $[0_3/(\pm45)_3/90_3]_S$,

is 20.8% **lower** than the compressive strength of the laminate $[0/90]_{6S}$ for the hole diameter of 6.35mm and it is 2.7% **lower** for the 12.7mm hole diameter ($W/D = 4$). This is the result expected because of the premature delamination;

- $\overline{\sigma}_c^{\infty}$ increased 8.4% for the 12.7mm hole diameter when the width increased by a factor of 2;
- doubling the hole diameter, for the same W/D ratio, results in a mean average compressive strength decrease of 11.8%.

Table 2.25: Summary of experimental results for $[0_3/(\pm 45)_3/90_3]_S$. [45]

$[\mathbf{0_3}/(\pm\mathbf{45})_\mathbf{3}/\mathbf{90_3}]_S$ (Ply-level scaled) H = 3.43mm, $E/D = 4$, $L/D = 8$			
D (mm)	W/D	$\overline{\sigma}_c^{\infty}$ (MPa)	σ_c^{∞} range (MPa)
6.35	4	261.5	237.4-276.5
H = 3.43mm, $E/D = 2$, $L/D = 4$			
12.7	2	212.9	197.4-232.0
12.7	4	230.7	201.0-270.4

Failure Mode: Similar to the $[0_6/90_6]_S$ lay-up. Extensive **longitudinal cracks** along 0° lines emanating from hole boundaries leading to premature **Delamination**.

Note: Premature delamination caused a wide variation of the failure load. Pre-cracks existed before testing which was incurred during the manufacturing process.

To summarize this extensive study it was made a plot of the compressive strength of the OHC specimens tested with the D/W ratio to show the hole size effect for each laminate. Figure 2.21 was obtained only for the specimens with D = 6.35mm.

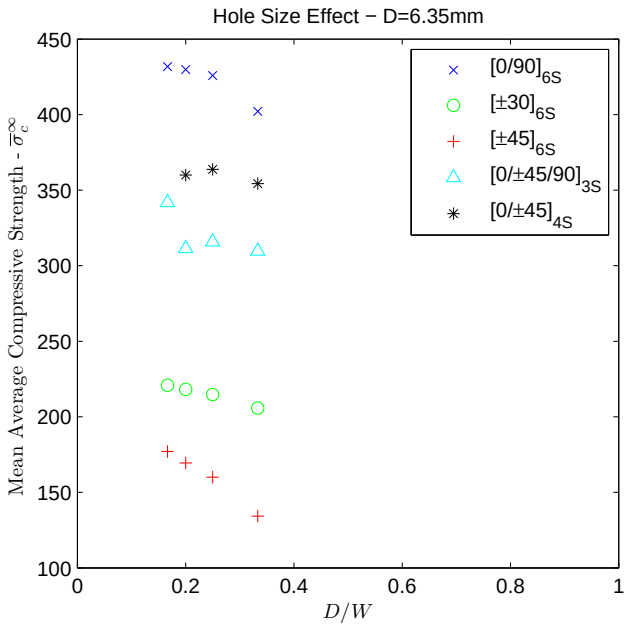

Figure 2.21: Summary of experimental results for specimens with $D = 6.35$mm.

In resemblance with this study of Lessard and Chang [45], **Soutis *et al.*** [17] also performed a study concerning the effect of *stacking sequence and in-plane dimensions variation in the OHC strength*. Soutis *et al.* obtained results for 6 different stacking sequences using the material T800/924C. This work was already mentioned to show the results obtained for unnotched specimens – see Table 2.17. The specimens used had the dimensions $245 \times 50 \times 3\text{mm}^3$ and the layups **L1-L6** shown in Table 2.17 and repeated for convenience in Table 2.26. Aluminum tabs were bonded onto the ends of the specimens resulting in a gauge section of $115 \times 50\text{mm}^2$ and the range of hole diameters drilled at the center of the specimens was from 4 to 25mm.

Table 2.26: Layups of the OHC specimens tested by Soutis *et al.* (Ply thickness: 0.25mm; Units: mm). Material: T800/924C. [17]

Lay-up	Ply orientation	% of 0° plies
L0	$[0_8]_S$	100
L1	$[\pm 45/0_4]_{2S}$	67
L2	$[\pm 45/0_2]_{3S}$	50
L3	$[0/90_2/0]_{3S}$	50
L4	$[\pm 45/0_2/90_2/0_2/90_2/0_2]_S$	50
L5	$[\pm 45/0/90]_{3S}$	25
L6	$[(\pm 45)_2/0/(\pm 45)_2/0/\pm 45]_S$	17

All specimens failed from the hole in a direction transverse to the loading axis. The remote failure stress σ_n normalized by the unnotched failure stress σ_{un} of the laminate is shown in Figure 2.22 as a function of the hole radius R normalized by the semi-width W of the specimen. The following observations were written by the authors:

1. In broad terms the failure strength of the notched laminates is approximately half that of the unnotched material;

2. The data for laminates comprising a large proportion of ±45° plies (by descending order: **L6**, **L5**, **L2**, **L1** and **L4**) lie above that for laminates consisting mainly of 0° plies. Thus, is concluded that **the presence of ±45° plies reduces the notch sensitivity** of the material.

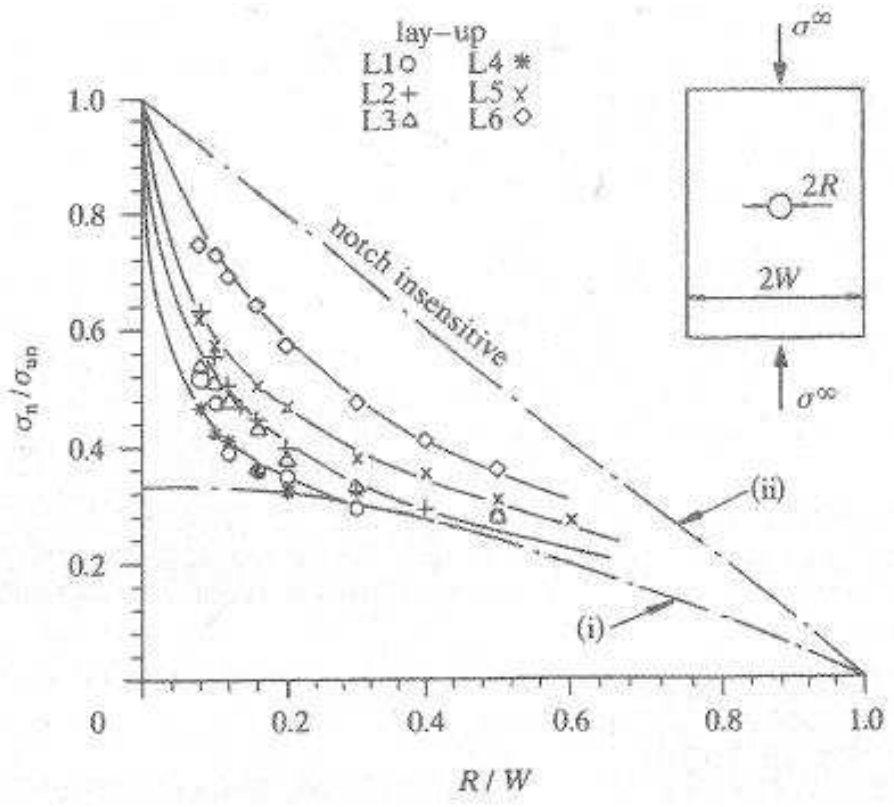

Figure 2.22: Effect of hole diameter on the compressive strength of T800/924C multidirectional laminates. The stress concentration factor k_t, which defines the notch sensitivity curve, depends upon the degree of orthotropy. The notch sensitive curve (i) shown is for the quasi-isotropic laminate **L5**; $\sigma_n/sigma_{un} = 1/k_t$. (ii) $\sigma_n/sigma_{un} = (1 - R/W)$. [17]

The authors also monitored the damage development for all laminates. From this monitorization it were identified 3 stages common to all laminates:

1. A damage zone starts to form at the edge of the hole under increasing remote load;

2. At approximately 75% of the failure load, **longitudinal splits** occur in the 0° layers at the top and bottom of the hole. Although these splits degrade the transverse stiffness of the laminate by a small amount, they have a negligible effect upon further damage development and upon the failure load;

3. At approximately 75-80% of the failure load, **microbuckling** of the 0° plies nucleates at the sides of the hole and is **accompanied by matrix cracking of the off-axis plies** and **delamination between the plies**.

After the referred microbuckling nucleation of 0° plies the damage zone propagates. The extension of the damage zone is the main difference between the damage development of the different laminates. In the case of laminates containing high proportion of ±45° plies **the damage zone is more extensive**. On the contrary, for laminates containing a large volume fraction of 0° plies **the damage zone is more crack-like in nature**. Two final comments related to the **L2** and **L3** laminates were made by the authors:

- For the $[\pm 45/0_2]_{3S}$ laminate (**L2**) the local axial strain (strain measured by a strain gage inside the hole) for the initiation of the microbuckling was 25% higher than the failure strain of the unnotched specimens. The authors believe that the higher strain for triggering of microbuckling from a hole is associated with the existence of a strain gradient from the hole: undamaged material surrounds the microbuckled zone and supports it;

- The $[0/90_2/0]_{3S}$ laminate (**L3**) differed from the other laminates in so far as it had 0° outer plies. This caused out-of-plane microbuckling in these outer plies at an earlier strain level than the strain level observed when in-plane microbuckling developed for the other lay-ups at.

IM7/8552: Thickness, In-plane size and Volume scaling effects

Lee and Soutis [44] performed more OHC tests, but this time the material chosen was the IM7/8552 and the lay-up was $[45/90/\text{-}45/0]_S$. The aim of the study was to investigate **thickness**, **in-plane size** and **volume scaling** effects of multidirectional (MD) specimens which have the same hole diameter to specimen width ratio, D/W=0.2 (W/D=5). The test program is presented in Tables 2.27 and 2.28.

Table 2.27: OHC test program for the MD specimens (Ply thickness: 0.125mm; Units: mm). [44]

Material	Lay-up: $[45/90/\text{-}45/0]_S$	Specimen Thickness	Hole Diameter (D)		
Pre-preg IM7/8552 (0.125mm)	Sublaminate-level scaling/Ply-level scaling	2	6.35*	-	-
		4	6.35	12.7*	25.4*
		8	-	-	25.4*
Specimen Width (W) × Gauge Length			31.8 × 31.8	63.5 × 63.5	127 × 127
D/W			0.2	0.2	0.2
Tab Length*			50	50	50

(No. of tested specimens = 6, *End-tab material: Woven glass fiber-epoxy reinforcement)*
*: Anti-buckling device

Table 2.28: OHC test program for the MD specimens (Ply thickness: 0.25mm; Units: mm). [44]

Material	Lay-up: $[45/90/-45/0]_S$	Specimen Thickness	Hole Diameter (D)		
Pre-preg IM7/8552 (0.25mm)	Sublaminate-level scaling	2	6.35*	-	-
		4	6.35	12.7*	25.4*
		8	-	12.7*	-
		16	6.35	12.7*	25.4*
Specimen Width (W) × Gauge Length			31.8 × 31.8	63.5 × 63.5	127 × 127
D/W			0.2	0.2	0.2
Tab Length*			50	50	50

(No. of tested specimens = 6, *End-tab material: Woven glass fiber-epoxy reinforcement)*
*: Anti-buckling device

After performing the tests the obtained results were summarized in Tables 2.29 and 2.30 for ply thicknesses of 0.125mm and 0.25mm, respectively.

Table 2.29: OHC results for sublaminate-level scaling and for ply-level scaling – **Ply thickness: 0.125mm**. [44]

$\overline{\sigma}_c^{\infty}$ for sublaminate-level scaled specimens (MPa) (cv, %)				
H (mm)	Lay-up	Hole diameter (mm)		
		6.35	12.7	25.4
2	$[45/90/-45/0]_{2S}$	**347 (5.52)**		
4	$[45/90/-45/0]_{4S}$	**351 (2.87)** [1]	**301 (3.64)**	**285 (2.22)**
8	$[45/90/-45/0]_{8S}$			**284 (4.09)**
$\overline{\sigma}_c^{\infty}$ for ply-level scaled specimens (MPa) (cv, %)				
t (mm)	Lay-up	Hole diameter (mm)		
		6.35	12.7	25.4
2	$[45_2/90_2/-45_2/0_2]_S$	**373 (9.20)**		
4	$[45_4/90_4/-45_4/0_4]_S$	**424 (7.53)** [1]	**348 (12.6)**	**288 (8.41)**
8	$[45_8/90_8/-45_8/0_8]_S$			**263 (4.19)**

Different failure mode: Premature damage due to thermal stress

[1] *Specimens without Anti-buckling device.*

Table 2.30: OHC results for sublaminate-level scaling – **Ply thickness: 0.25mm**. [44]

$\overline{\sigma}_c^{\infty}$ for sublaminate-level scaled specimens (MPa) (cv, %)				
H (mm)	Lay-up	Hole diameter (mm)		
		6.35	12.7	25.4
2	$[45/90/-45/0]_S$	**331 (15.5)**		
4	$[45/90/-45/0]_{2S}$	**354 (1.92)** [1]	**300 (5.13)**	**273 (5.91)**
8	$[45/90/-45/0]_{4S}$		**319 (0.65)**	
16	$[45/90/-45/0]_{8S}$	**351 (0.88)** [1]	**312 (1.77)**	**276 (2.22)**

[1] *Specimens without Anti-buckling device.*

From the observation of these two tables it can be concluded that:

- The strength of the specimens in which was not used an anti-buckling device was higher than the strength of the others (and curiously this effect is more pronounced for the ply--level scaled specimens). This produced some scatter in the results which has two consequences: 1) it can lead to the **wrong** conclusion that the laminate thickness influences the compressive strength; 2) it magnifies the decrease in compressive strength due to the hole diameter increase (so the **real** decrease in strength should be calculated considering the compressive strength for the laminate with thickness of 2mm for the 6.35mm

diameter, which had the anti-buckling device – the next calculations will consider this to obtain the compressive strength decrease);

- the average strengths, for both scaling techniques, decrease with increasing hole size and for both ply thicknesses;

- For the **0.125mm ply thickness** using the **sublaminate-level scaling** technique with a hole diameter increase by a factor of 4 it is produced a decrease of 17.9%[5] in compressive strength and with the **ply-level scaling** technique the decrease is of 22.8%;

- For the **0.25mm ply thickness** and using the sublaminate-level scaling technique with a hole diameter increase by a factor of 4 it is produced a decrease of 17.5% ($H = 4mm$) and 16.6% ($H = 16mm$) in compressive strength – which shows the **independence of the hole size effect with thickness in compression**;

So it can be concluded that **the compression of a notched composite material with this stacking sequence only is affected by the hole diameter and is independent of the laminate thickness and negligibly dependent of the scaling technique** (sublaminate-level or ply-level). Until this point it was not stated anything about the failure modes of these OHC specimens, but even before analyzing the failure modes it is logical to assume that they will not differ to much because the compressive strength was proven to be quite independent with the referred scaling methods. This was actually demonstrated by the authors.

From post failure investigation it was concluded that the overall final failure mode, regardless of the specimen size, was found to be very similar for each scaling technique although it was noticed some small differences from the sublaminate- to the ply-level scaled specimens. The fractured specimens are shown in Figure 2.23(a) and (b).

It was observed that sublaminate-level scaled specimens ($[45/90/-45/0]_{nS}$) failed from the hole in a direction almost perpendicular to the loading axis while emitting a distinct cracking type sound just prior to catastrophic failure. The specimens using ply-level scaling technique ($[45_m/90_m/-45_m/0_m]_S$) failed without the cracking sound before catastrophic failure. But more importantly, the authors noted that while **the fractured sublaminate-level scaled specimens**, Figure 2.23(a), showed much **delamination** and **fiber microbuckling** along the

[5] The compressive strength calculated here and further use the value of the strength of the 2 mm thick laminate as if it was the 4mm one because of the referred independence with thickness variation and because the 4mm value was affected by not using an anti-buckling device

plane of fracture but little damage away from the hole, **the fractured ply-level scaled specimens**, Figure 2.23(b), exhibited **more clear delamination**, **fiber splitting**, **matrix cracks and crushing**, and **fiber microbuckling** at large scale.

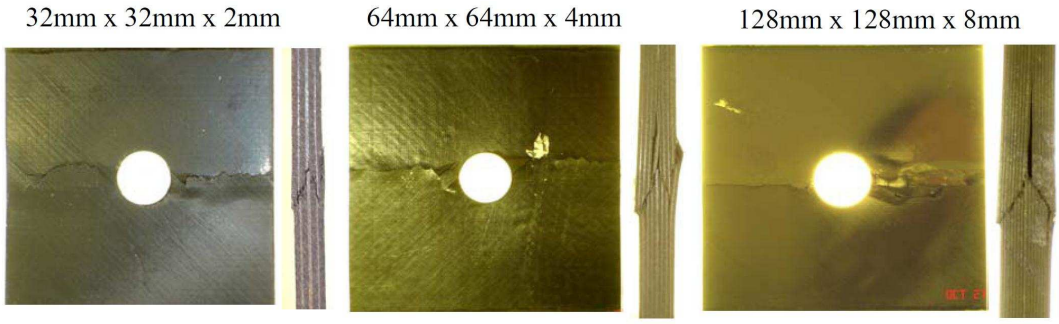

(a) Sublaminate Level Scaled Specimens ($[45/90/-45/0]_{ns}$)

(b) Ply Level Scaled Specimens ($[45_n/90_n/-45_n/0_n]_s$)

Figure 2.23: Comparison of the overall failure mode of the notched multidirectional specimens (ply thickness: 0.125mm). Front view and side view are shown for different thicknesses. [44]

To finalize this section it is important to compare the OHT results obtained by Green *et al.* [24] and the OHC results obtained by Lee and Soutis [44] because in these two articles it was tested exactly the same material and the same stacking sequence subjected to tension and compression, respectively – see Tables 2.10 and 2.29. By observing the two tables we can conclude that:

- **notched composites have higher strength in tension than in compression**, as the unnotched ones, **but when loaded in tension are much more sensible to the hole size effect**;
- **the behavior of notched composites in compression was proven to be almost independent of thickness**;
- there are three main failure modes present in OHT specimens: 1) **Pull-out** type failure;

2) **Brittle** type failure; 3) **Delamination** type failure. And more importantly: **for the OHT specimens the failure modes can change after scaling the specimens causing sharp variations of strength** which increases the unpredictability of these tests;

- On the contrary, the failure modes present in the OHC specimens are similar for any type of scaling, with fiber microbuckling and delamination playing a key-role;

2.2 Analytical Models for Strength Prediction of OHT & OHC tests

After presenting different experimental results for scaled notched and unnotched CFRPs statically loaded it is crucial to have an overview of the most important analytical methods available to predict the behavior of these materials. A great emphasis will be given to the open-hole tension and compression tests in this section due to their importance for the aerospace industry, and to the current difficulty in modeling accurately this tests for FRPs.

A review of the current most important FRP analytical models for strength prediction of OHT specimens was presented by **Camanho *et al.*** [23].

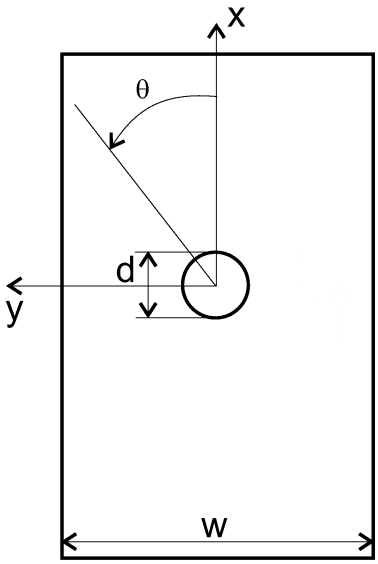

Figure 2.24: Open-Hole specimen.

2.2.1 Maximum stress failure criteria

Strength prediction methods uniquely based on stress or strain failure criteria are unable to predict the size effects observed in notched specimens. Consider for example the calculation of the final failure of a specimen with a central hole using the value of the longitudinal stress in the fiber direction (maximum stress criterion). The distribution of the longitudinal stress in the critical plies, the 0° plies along the fracture plane, defined by $\theta = 0°$ in Figure 2.24, can be calculated using an approximate closed-form solution as:

$$\sigma_{11} = \sigma_{xx}(0, y)(\overline{Q}_{11}a^*_{11} + \overline{Q}_{12}a^*_{12}) \tag{2.1}$$

where a^*_{ij} are the components of the laminate compliance matrix defined as:

$$[a^*] = t_L\,[A]^{-1} \tag{2.2}$$

where the matrix $[A]$ relates the in-plane forces per unit length to the mid-plane strains. $\overline{Q}_{ij}$ are the components of the plane stress transformed reduced stiffness matrix of the 0° plies, and t_L is the thickness of the laminate.

The through-the-thickness averaged normal stress in the fracture plane for a quasi-isotropic laminate is calculated as:

$$\sigma_{xx}(0, y) = \frac{2 + (1 - d/w)^3}{6(1 - d/w)}\left[2 + \left(\frac{d}{2y}\right)^2 + 3\left(\frac{d}{2y}\right)^4\right]\sigma^{\infty}_{xx},\ y \geq d/2 \tag{2.3}$$

where σ^{∞}_{xx} is the remote tensile stress.

From equations (2.1) and (2.3) it is clear that for the same material and stacking sequence the stress concentration factor, and hence the maximum longitudinal stress in the 0° ply, depends on the ratio between the specimen hole diameter and width. Applying the maximum stress criterion and using equations (2.1) and (2.3):

$$\frac{\sigma_{11}}{X_T} = 1 \Rightarrow \overline{\sigma}^{\infty} = \frac{(1 - d/w)X_T}{[2 + (1 - d/w)^3](\overline{Q}_{11}a^*_{11} + \overline{Q}_{12}a^*_{12})} \tag{2.4}$$

Equation (2.4) demonstrates that the application of the maximum stress criterion results in the same strength prediction for different hole diameters when the d/w ratio is held constant. The lack of size effect on the predicted strength contradicts the experimental observations presented in the previous Section.

2.2.2 Two-parameter methods: Point-Stress Model (PSM)

The Point-Stress Model (PSM) proposed by **Whitney and Nuismer** [121], considers that ultimate failure occurs when the stress at a given distance from the hole boundary, r_{ot} or r_{ot}, reaches the unnotched strength of the laminate, X^L_T or X^L_C. An alternative version of the point

stress model uses the ply stresses and strengths, so that it is not necessary to measure the strength for every different laminate. However, the use of ply stresses is only appropriate for fiber-dominated laminates because the criteria to predict laminate failure is based on fracture of the ply in the longitudinal (fiber) direction.

Using equations (2.1) and (2.3), the strength predicted using the ply-level PSM is:

$$\overline{\sigma}^{\infty} = X_T \left\{ \frac{2 + \left(1 - \frac{d}{w}\right)^3}{6\left(1 - \frac{d}{w}\right)} \left[2 + \left(\frac{d}{d + 2r_{ot}} \right)^2 + 3\left(\frac{d}{d + 2r_{ot}} \right)^4 \right] (\overline{Q}_{11} a_{11}^* + \overline{Q}_{12} a_{12}^*) \right\}^{-1} \tag{2.5}$$

Failure is predicted using two parameters: the characteristic distance in tension r_{ot} or in compression r_{ot}, and the respective longitudinal tensile or compressive strength of the ply, X_T or X_C.

2.2.3 Combined methods

Combined methods use the concept of characteristic distance together with ply failure criteria. This method has the advantage of using mainly ply properties, although the characteristic distances still need to be measured at laminate level.

In combined methods, the **Yamada-Sun failure criterion** [122] is typically applied together with a proposed characteristic curve. The Yamada-Sun [122] failure criterion is based on the assumptions that just prior to laminate failure every ply has failed due to cracks along the fibers, and that the shear strength of a symmetric cross-ply laminate, with the same number of plies as the laminate under consideration, represents the substantially higher shear strength of a lamina when it is in a laminate. This criterion has the form:

$$\left(\frac{\sigma_{11}}{X_{T,C}} \right)^2 + \left(\frac{\sigma_{12}}{S_c} \right)^2 - 1 \leq 0 \tag{2.6}$$

where the stresses are either calculated at or averaged over characteristic distances. S_c is the ply shear strength measured from a cross-ply laminate. Since the ply shear stress are likely to not affect the tensile fracture of the laminate, the criterion may be modified as [23]:

$$\left(\frac{\sigma_{11}}{X_T}\right) - 1 \leq 0, \sigma_{11} \geq 0$$
$$\left(\frac{\sigma_{11}}{X_C}\right)^2 + \left(\frac{\sigma_{12}}{S_c}\right)^2 - 1 \leq 0, \sigma_{11} < 0 \tag{2.7}$$

2.2.4 Fracture Mechanics

2.2.4.1 Linear-Elastic Fracture Mechanics (LEFM)

Using Linear-Elastic Fracture Mechanics (LEFM) it is assumed that the length a of a pre--existing crack in the laminate is scaled in the same proportion of the hole diameter and specimen width and that the critical value of the laminate's stress intensity factor, K_{Ic}, is independent of the crack length. Consider two specimens with hole diameters d_1 and d_2. The stress intensity factor at failure is:

$$K_{Ic} = \overline{\sigma}_1^{\infty} F\left(\frac{w_1}{d_1}, \frac{a_1}{d_1}\right)\sqrt{\pi a_1} = \overline{\sigma}_2^{\infty} F\left(\frac{w_2}{d_2}, \frac{a_2}{d_2}\right)\sqrt{\pi a_2} \tag{2.8}$$

Taking into account the fact that the crack length is proportional to the hole diameter and that the finite width correction factors, $F(w/d, a/d)$, are equal for scaled geometries, the failure stress of a specimen with a hole diameter d_2 can be calculated from the failure stress of the specimen with a hole diameter d_1:

$$\overline{\sigma}_2^{\infty} = \overline{\sigma}_1^{\infty}\sqrt{\frac{d_1}{d_2}} \tag{2.9}$$

2.2.4.2 Inherent Flaw Model (IFM)

The inherent flaw model (IFM) proposed by **Waddoups *et al.*** [123] considers that the non--critical damage mechanisms occurring before ultimate failure of a composite laminate can be lumped into a constant "region of intense energy", or "inherent flaw", of length a. The critical value of the stress intensity factor of a plate with a hole of radius R is given by:

$$K_{Ic} = f(a, R)\,\overline{\sigma}^{\infty}\sqrt{\pi a} \tag{2.10}$$

where $f(a, R)$ is Bowie's solution for the calculation of the stress intensity factor of two cracks emanating from a circular hole, given as:

$$f(a, R) = 0.5\left(3 - \frac{a}{d/2 + a}\right)\left[1 + 1.243\left(1 - \frac{a}{d/2 + a}\right)^3\right] \tag{2.11}$$

Waddoups *et al.* [123] considered that the strength of an unnotched specimen can be predicted by taking into account that the hole radius tends to zero, in which case the function $f(a, R)$ tends to one, leaving:

$$K_{Ic} = X^L_{T,\,C}\sqrt{\pi a} \tag{2.12}$$

where X^L_T or X^L_C are the tensile strength or the compressive strength of the unnotched laminate, respectively.

From (2.10) and (2.12), the equation proposed by Waddoups *et al.* [123] is obtained:

$$\overline{\sigma}^{\infty} = X^L_{T,\,C}/f(a, R) \tag{2.13}$$

The strength of the laminate containing an open-hole is predicted using two parameters: the length of the inherent flaw, a, that needs to be calculated from a baseline specimen, and the unnotched tensile or compressive strength of the laminate, X^L_T or X^L_C, respectively.

2.2.5 Budiansky-Fleck-Soutis (BFS) compressive criterion

After conducting some OHC tests on carbon/epoxy laminates using the T800/924C material and the stacking sequence $[\pm 45/0_2]_{3S}$ **Soutis *et al.*** [49] proposed a failure prediction technique that led to the BFS compressive criterion (Budiansky-Fleck-Soutis). From the referred tests the authors concluded that the 0° plies carry most of the compressive load due to their greater axial stiffness and hence **it is the failure of these laminae by localized microbuckling which results in the laminate fracture**. However, other failure mechanisms were observed: fiber splitting of the top and bottom layers (first mechanism, which initiated at approximately 75% of the peak load); matrix cracking and delamination between the 0° and ±45° layers. It should be noted that the role of microbuckling in the 0° fibers of the laminate fracture was observed

previously to this work [45] and posteriorly [17], [44], [46] by several authors for other stacking sequences and with other carbon/epoxy materials, as shown in Chapter 2.

It was the observation of the composite plate failure by unstable microbuckle growth at a determined microbuckle length (at about 2mm from the hole edge for the analyzed laminate) that led the authors to the idea of **modeling this type of damage as a through-thickness crack loaded on its faces**. Although the idea of comparing the microbuckled zone to an equivalent crack was not pioneered by the referred authors [41], the big improvement of the prediction technique of Soutis *et al.* resides in considering a linear relationship between the normal traction σ on the crack flanks and the crack normal displacement $2v$ instead of a constant cohesive stress zone. Therefore, the authors merged the work from Guynn [41] which replaced the microbuckled zone by a crack suffering a constant normal traction σ at its flanks, and the work of Newman [42] which took the equations for the stress intensity factor and the crack surface displacement $v(x)$ of a crack subjected to various loadings in an infinite plate from Tada's analysis [43] and modified them for cracks emanating from a circular hole in a finite plate.

The model is summarized in a report written by Soutis [50] after the publication of the original paper. The following description was extracted from there, although it is advised to read the original paper [49] for a more detailed explanation.

It was already referred that in this model the microbuckle emanating from each side of the hole is mathematically replaced by an equivalent crack. The model assumes that microbuckling initiates when the local compressive stress parallel to the 0° fibers at the hole edge equals the unnotched strength of the laminate X_C^L, i.e.,

$$k_t \sigma^{\infty} = X_C^L \tag{2.14}$$

where k_t is the stress concentration factor and σ^{∞} is the applied stress.

Damage development is represented by replacing the damage zone by an **equivalent crack** (overlapping mode I crack), with normal crack bridging compressive stresses that **drop linearly with crack overlap** from a maximum value of the unnotched compressive strength – Figure 2.25. It is assumed that the length of the equivalent crack, l, represents the length of the microbuckle. When the remote load is increased the equivalent crack grows in length,

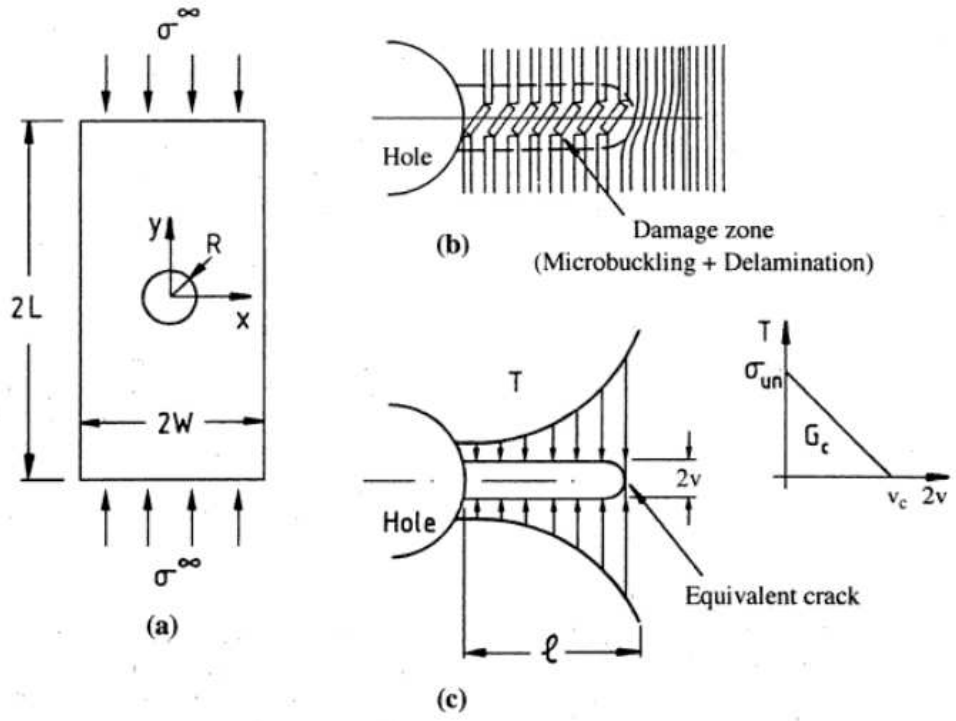

Figure 2.25: Microbuckled zone at a hole and the equivalent crack used to model the damaged zone. (a) Schematic of compression-loaded specimen with hole; (b) Damage zone (microbuckling and delamination); (c) Equivalent crack: normal traction T, closing displacement $2v$. [50]

thus representing microbuckling growth. The evolution of microbuckling is determined by requiring that the total stress intensity factor at the tip of the equivalent crack, K_{tot}, equals to zero,

$$K_{tot} = K^{\infty} + K_T = 0 \tag{2.15}$$

where K^{∞} is the stress intensity factor due to the remote stress σ^{∞}, and K_T is the stress intensity factor due to the local bridging traction T across the faces of the equivalent crack.

When this condition is satisfied, the stresses remain finite everywhere. The equivalent crack length from the circular hole is deduced as a function of the remote stress using the following algorithm. For an assumed length of equivalent crack l, solve for σ^{∞} and for the crack bridging law to the crack profile deduced from the elastic solution for a cracked body, Newman [42]. The cracked body is subjected to a remote stress, σ^{∞}, and crack face tractions T. At a critical length of equivalent crack, l_{cr}, the remote stress σ^{∞} attains a maximum value, designated σ_{cr}, and catastrophic failure occurs.

The model requires the knowledge of the unnotched strength, X_C^L, and the compressive in--plane fracture energy of the laminate, $\mathcal{G}_c$. The area under the curve of crack bridging stress versus overlap displacement – Figure 2.25 – represents the total energy $\mathcal{G}_c$ dissipated by fiber microbuckling in the axial plies, matrix plasticity in the off-axis plies and delamination:

$$\mathcal{G}_c = 2\int_0^{v_c} \sigma(v)\, dv \tag{2.16}$$

where v_c is the critical crack closing displacement on the crack traction - crack displacement curve.

For an orthotropic plate in plane stress, the fracture energy $\mathcal{G}_c$ is related to laminate elastic properties (E, G, v) and to fracture toughness K_c by the following formula:

$$\mathcal{G}_c = \left(\frac{1}{2}E_{xx}E_{yy}\right)^{\frac{1}{2}} \times \left[\left(\frac{E_{xx}}{E_{yy}}\right)^{\frac{1}{2}} - v_{xy} + \frac{E_{xx}}{2G_{xy}}\right]^{\frac{1}{2}} K_c^2 \tag{2.17}$$

The fracture toughness, K_c, is derived from a separate compressive kink (microbuckling) propagation experiment, wherein the in-plane fracture toughness $\left(K_c = Y\sigma\sqrt{\pi a}\right)$ of a laminate containing a sharpened long slit (= $2a$) is measured – see Chapter 4 for details on how to calculate K_c.

As a final note the following particularities of this crack bridging model are listed:

1. The model gives an accurate prediction of failure load and critical damage length for a range of hole sizes and **0° dominated laminates**;
2. **It is less accurate for laminates which are composed mainly of off-axis plies** (more than 80% of ±45° plies), because for these 45°-dominated laminates the damage at the edge of the hole is more diffuse in nature, and a cohesive zone representation of damage becomes less appropriate.

CHAPTER 3

NUMERICAL MODELS

This chapter will present the Numerical Models used to simulate the behavior of FRP under static loading. The first section introduces the general topic of composite materials modeling and it is based on **Maimí**'s PhD thesis [135]. The second section presents the continuum damage and the delamination numerical models used to simulate intralaminar and interlaminar damage, respectively, and their implementation in an ABAQUS® VUMAT subroutine. Finally, the third section presents **Catalanotti**'s [136] proposed full-3D failure criteria based on LaRC03/04 and its implementation in an ABAQUS® UVARM subroutine.

3.1 Composite Materials Modeling

Damage Modes in multilayered laminates

Consider an unnotched unidirectional lamina under a general plane stress state (σ_{11}, σ_{22} and σ_{12}). For certain plane stress states there is a limit load that the material can sustain. Plotting in a 3D stress surface (σ_{11}, σ_{22}, σ_{12}) the sequence of limit loads, it is possible to define a failure surface. The analytical representation of this surface is called the **failure criteria**. Stress states that are within the space delimited by this surface do not cause loss of structural integrity, whereas the stress states beyond the failure surface do. The first approach to correctly define the failure criteria is to identify the different **failure modes** of the material. For composite materials there are several failure modes, where "failure mode" is considered to be a combination of damage mechanisms which cause material failure.

Considering, without loss of generality, that the fibers of the unidirectional lamina are oriented

in direction 1 (Figure 3.1) there are five uniaxial tests which are possible to perform in order to fully characterize the mechanical behavior of CFRP: tension and compression in the fibers' direction ($\pm\sigma_{11}$) and perpendicular to that direction ($\pm\sigma_{22}$), and pure shear (σ_{12}). For each of these uniaxial tests the failure stresses are represented by X_T, X_C, Y_T, Y_C and S_L, respectively, and the strains are obtained by means of asset of constitutive laws. The constitutive laws can be reasonably well approximated by a **linear elastic behavior until failure** for loads applied in the **fiber direction** ($\pm\sigma_{11}$) and for **tensile transverse loads** ($\sigma_{22} > 0$) **but** for **compressive transverse loads** ($\sigma_{22} < 0$) and for **shear loads** ($\pm\sigma_{12}$) the material exhibits a **pronounced non-linearity** before failure [135], [137].

Experimental observations led to the conclusion that for unidirectional lamina under plane stress conditions there are **at least four failure modes** clearly identifiable. The fracture planes originated by each type of failure mode are shown in Figure 3.1 and the stress states that activate the respective failure mode are plotted in Figure 3.5.

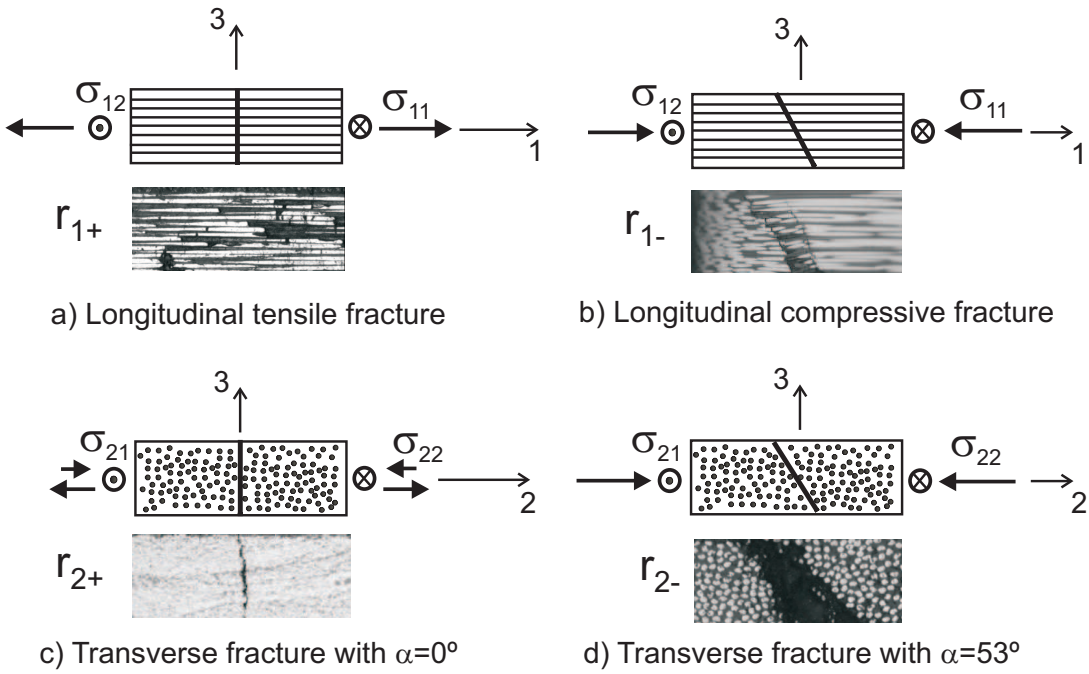

Figure 3.1: Fracture surfaces and corresponding internal variables.

- **(a) Longitudinal tensile fracture – Failure mode F_{FT}:**

  This is the simplest failure mode to identify due to the fact that FRP transfer most of the longitudinal tensile load through the fibers. In composites with a high fiber volume fraction or in which the resin has higher ultimate deformation than the fibers

(e.g., carbon fiber/epoxy composites), longitudinal failure begins with localized fiber failure in regions where they present defects. These failures increase the load of the neighboring fibers which is transferred to these fibers by shear between the interface and the matrix causing **matrix cracking** and fiber **pull-out** (debonding between fiber and matrix)[1]. Increasing the load will cause more damage to the fibers, eventually leading to overall structural failure.

Longitudinal tensile fracture occurs for both constituents and damage occurs in a plane with the normal defined by the vector $e_{F_{FT}} = (1, 0, 0)$.

- **(b) Longitudinal compressive fracture – Failure mode F_{FK}:**

  Longitudinal compressive failure is unquestionably the most complex failure mode identified in unidirectional lamina. Usually when these materials are subjected to compressive loads in the direction of the fibers there is the generation of a **kink band**, as shown in Chapter 2 (Figure 2.11). This failure mode should not be mistaken with the two most commonly identified fiber failure micromechanisms: **microbuckling** and **fiber crushing**; because the kink band failure mode is the (usually) observed failure phenomenon of the actual lamina, being (most likely) a combination of the microbuckling mechanism and the transferred shear stresses by the interface between matrix and fiber.

  Bai and Phoenix [83] presented an excellent review on kink band modeling which starts with the pioneering work of Rosen (in 1965) [51] and Argon (in 1972) [52], passes through the most relevant works in the field [53]-[68] and finishes with a proposed model [83].

  Rosen [51] was the first to analyze microbuckling in a systematic way as a viable failure mode. Microbuckling is a geometric instability of the fibers that causes a transverse displacement when a compressive load is applied, therefore, Rosen considered the classic model of a beam on an elastic foundation and modeled the composite as an infinite array of equi-spaced parallel bars with an elastic matrix in between. The author concluded that two distinct periodic modes could occur: an **extension mode**, typically observed in elastic polymer matrices with fiber volume fractions less than about 30%, and a **shear mode**, for fiber volume fractions greater than 30% – Figure 3.2(a).

[1] For ductile matrices plastic bands may also appear in addition to the referred failure mechanisms

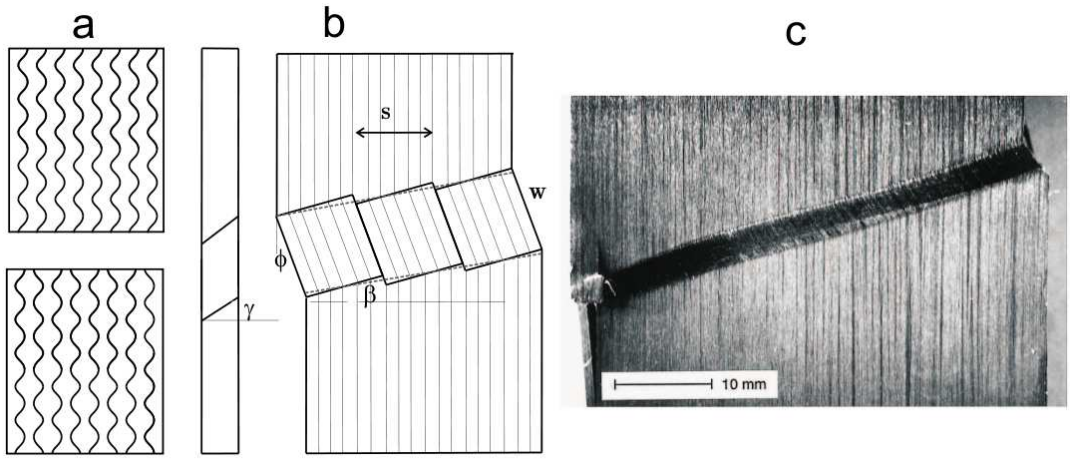

Figure 3.2: (a) Fiber microbuckling between an elastic matrix in shear mode (up) and in extension mode (down); (b) Kink band geometry; (c) Real kink band (after Vogler [65]). [135]

Rosen theoretically derived the critical collapse stress for these two microbuckling modes, unfortunately the predicted failure stresses are two to four times higher than those typically observed experimentally. Moreover this model does not explain the experimentally observed formation of kink bands (with a β rotation – Figure 3.2(b)) instead of the fiber microbuckling.

Argon [52] took a somewhat different approach. He considered that **matrix plastic yielding** and **initial fiber misalignment** from processing the material were the principal causes for kink band formation. Therefore, when the material is subjected to a compressive load, a shear stress appears between fiber and matrix that causes failure.

Subsequent research has mostly been based on various extensions of the microbuckling models of Rosen [51] to include inelastic and misalignment effects of Argon [52]. For instance, **Hahn and Williams** [55] and **Fleck *et al.*** [61] essentially combined the results of Rosen [51] and Argon [52] to obtain a critical compressive stress. More elaborate models were created and developed considering periodic or localized fiber misalignments inherited from processing as well as matrix inelasticity. In the previously cited [83] review, Bai and Phoenix recommend the work performed by Budiansky (1983) [54], Hahn and Williams (1986) [55], Waas *et al.* (1990) [56], Steif (1990) [57, 58], Ha and Nairn (1992) [59], Budiansky and Fleck (1993) [60] and Vogler and Kyriakides (1999) [65, 66]. The referred author of the review highlights the work of **Hahn and Williams** [55] and **Berbinau** *et al.* [67] which examined the microbuckling phenomenon from the point of view of the equilibrium of a single fiber in a yielding

matrix and undergoing bending prior to kink band formation. It was argued that a fiber could break at the point of maximum curvature, so the composite compressive failure strength could be related to **initial waviness**, **fiber volume fraction** and **fiber failure stress in bending**. **Steif** [57, 58] observed that the deflection of a bundle of slightly misaligned fibers until breakage occurred in two planes, which brought the fibers into a kinked configuration. Although his analysis was based in experimentally obtained kink band widths, a reasonable connection between fiber breaking strain and composite compressive stress was achieved.

In the referred work [57, 58], Steif also points out that the main difficulty to model the kink band geometry is to identify the key factors of the kink band phenomenon that at the time were not completely understood and still remain to be found. This is exactly the problem that researchers face when examining kink bands – many mechanical and geometric factors influence the threshold stress for compressive collapse and, considered together or separately, may trigger several possible failure modes.

On the one hand, **local fiber and matrix micromechanical features** that determine the critical failure stress remain yet to be explained and, most probably, the answer to this problem should be in micromechanical or even nanomechanical modeling. On the other hand, it is not enough to model the kinking of an isolated fiber or regularly deformed fiber arrays. It is necessary to consider mutual interaction of unequally deformed fibers in FRP laminae [56] and multi-layered FRPs.

In the particular case of **carbon fibers** it has been noted by several researchers [69]-[76] that there is a strong tendency for these fibers to fail first in a shear mode instead of by bending from microbuckling, which is more prevalent in glass fibers. This generates a slant failure surface and subsequent dislocation slip [83].

Finally, Bai and Phoenix [83] summarize the conclusions drawn by **Narayanan and Schadler** [77] from experimental tests on CFRP as follows: **carbon fiber** breaks were reported to occur before and during kink band formation and many had slanted failure surfaces suggesting **crushing** or **shear failure** occurs first. Thus, these authors envisioned a new failure mechanism whereby a small, slant-aligned sequence of fiber breaks develops in shear or crushing failures and triggers kink band formation through excessive overloading of neighbouring fibers to the point of bending and failure.

In conclusion, the kink band formation problem is very complex and is yet to be mod-

eled accurately. It is the result of several failure mechanisms and it depends not only of mechanical factors but also of geometric ones. Therefore, considering different fiber types, the failure mechanisms that trigger the kink band formation can be significantly different. For instance, for carbon fibers it appears that a shear mode and local fiber crushing preceeds the kink band formation, instead of microbuckling.

- **(c) Transverse fracture with $\alpha = 0°$ – Failure mode $F_{\alpha=0}$:**
  Under transverse tension ($\sigma_{22} > 0$) and in-plane shear (σ_{12}) FRP lamina fail transversely ($\alpha = 0°$). Considering the coordinate system of Figure 3.1, the normal vector to the failure plane is: $e_{F_{\alpha=0}} = (0, 1, 0)$.

  Under moderate transverse compression ($\sigma_{22} < 0$, low absolute values) and high in-plane shear (σ_{12}, high absolute values) it is experimentally observed that FRP lamina also fail transversely ($\alpha = 0°$). In fact, as the reader may have noticed, the behavior in transverse compression is very interesting: 1) there is a pronounced stress-strain non-linearity, as was already stated; 2) it is experimentally observed that the fracture angle varies with the intensity of the compressive and shear loads. This second point will be detailed in the next failure mode, $F_{\alpha\neq0}$.

- **(d) Transverse fracture with $\alpha \neq 0°$ – Failure mode $F_{\alpha\neq0}$:**
  It was also observed in experiments that increasing transverse compression results in an increase of the fracture plane angle α. **Puck *et al.*** [78, 79, 80] stated that: 1) for pure transverse compression tests α has the approximate value of $53° \pm 3°$; 2) if a shear stress is applied at the same time with a transverse compression stress, α decreases to approximately 40°; 3) if the shear stress is higher than the compressive stress then $\alpha = 0°$, as was referred in the previous failure mode. The normal vector to the fracture plane is $e_{F_{\alpha\neq0}} = (0, \cos\alpha, \sin\alpha)$.

  Koerber [137] observed experimentally the referred phenomenon of the fracture angle α variation with the applied transverse compression and shear, not only for static loading but also for dynamic loading. For the dynamic behavior the referred author used a high speed camera and was able to determine the fracture angle. The camera was not available at the time of the quasi-static tests but a great parallelism was observed so the behavior should be very similar between the quasi-static and dynamic tests resulting approximately in the same fracture angle for the same fiber orientation angle (θ). The

variation of α with the fiber orientation[2] θ is shown in Figure 3.3.

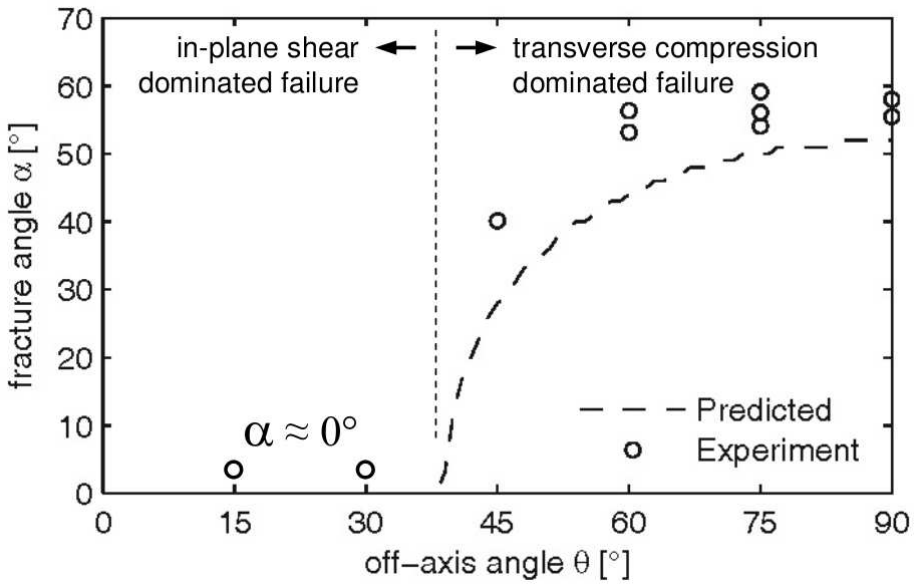

Figure 3.3: Experimentally observed dynamic fracture plane angle α for different fiber orientations obtained. The prediction was obtained by Catalanotti [136]. [138]

The figure clearly shows that for in-plane shear dominated failure the fracture angle is approximately 0°, whereas for transverse compression dominated failure the fracture angle is approximately 53°. Within the small range of $\theta = 40 - 55°$ the fracture angle α decreases from 53° to 0°. Therefore, the variation of the fracture angle can be roughly approximated by a step function (this will be used in the numerical model to improve computational efficiency). Figure 3.4 shows the quasi-static fractured specimens for different fiber orientations. It is clear that for off-axis angles of 15 and 30° the fracture angle α is nearly 0° and that for off-axis angles of 60 and 75° the fracture angle is approximately 53°. When the off-axis angle of the specimen is 45° the fracture angle is around 40°, very similar to the dynamic test results plotted in Figure 3.3.

Maimí [135] states that the mechanisms involved in this failure process can be explained by the same model used by Coulomb in the XVIII century for geomaterials. The failure is promoted by the shear stresses in the failure plane and by the friction produced by the normal stress to that plane, with the particularity that the friction coefficient in the direction of the fibers is different from the friction coefficient in the direction perpendicular to the fibers.

[2] Note that changing the specimen's fiber orientation and loading it longitudinally is a practical way of changing the intensity of the transverse compressive stress relatively to the shear stress

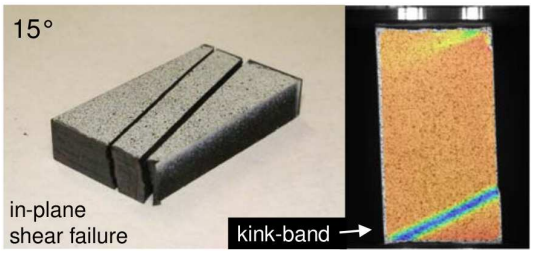

(a) For $\theta = 15°$ the fracture angle is $\alpha \approx 0°$

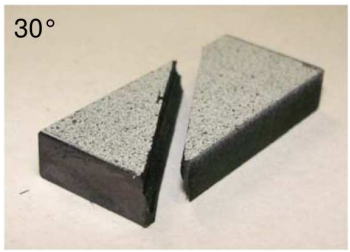

(b) For $\theta = 30°$ the fracture angle is $\alpha \approx 0°$

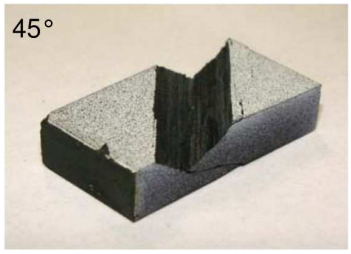

(c) For $\theta = 45°$ the fracture angle is $\alpha \approx 40°$

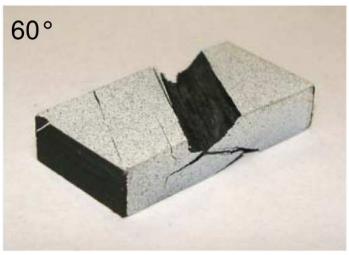

(d) For $\theta = 60°$ the fracture angle is $\alpha \approx 53°$

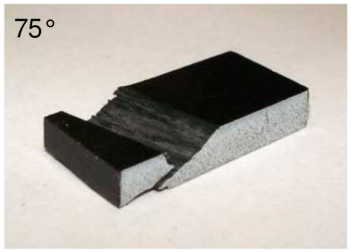

(e) For $\theta = 75°$ the fracture angle is $\alpha \approx 53°$

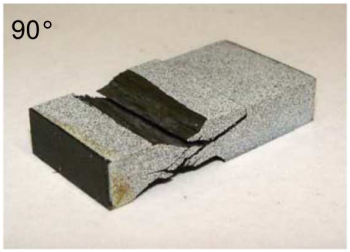

(f) For $\theta = 90°$ the fracture angle is $\alpha \approx 53°$

Figure 3.4: Specimens quasi-statically loaded in compression for different fiber orientations. The fracture angle α is measured from the normal to the top face and the fracture plane. [138]

In order to finish the explanation of the four failure modes observed experimentally, Figure 3.5 is presented. This figure relates the plane stress states with the referred failure modes (F_{FT}, F_{FK}, $F_{\alpha=0}$ and $F_{\alpha\neq0}$).

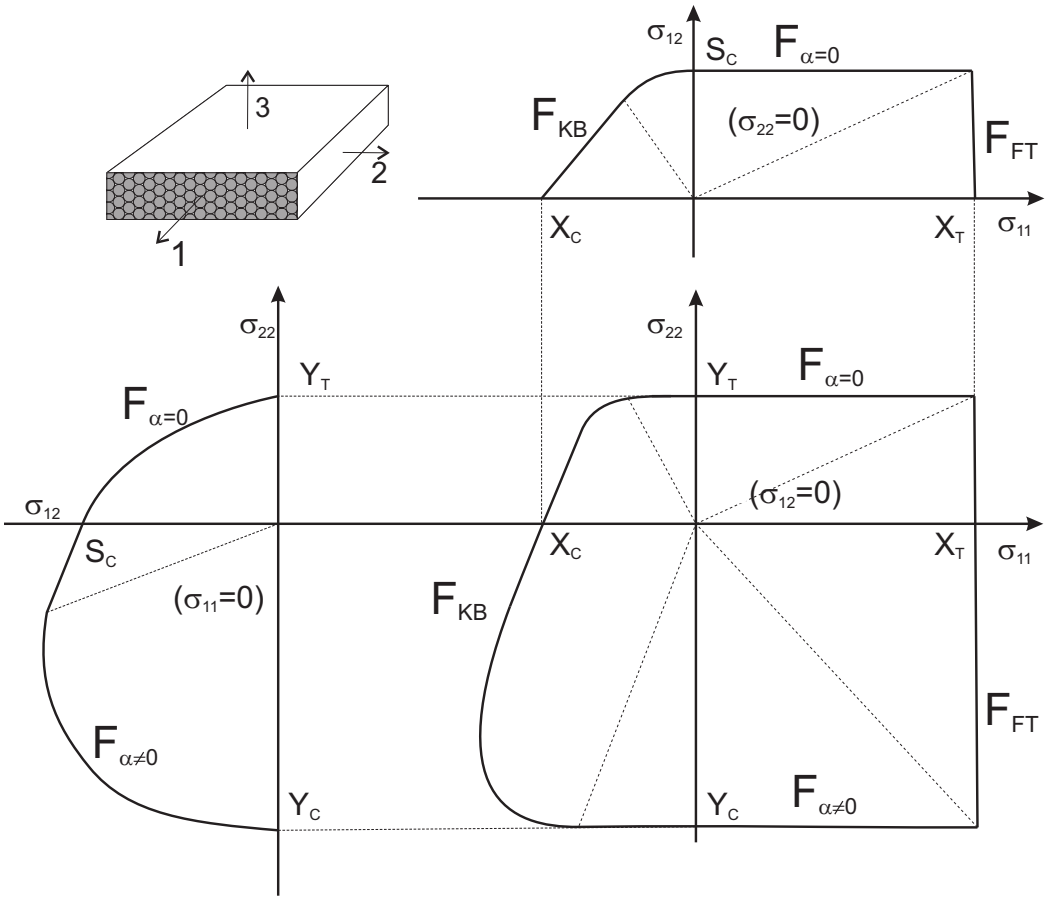

Figure 3.5: Fracture surfaces and corresponding internal variables. [135]

3.2 Numerical Model including Damage, Shear plasticity and Delamination

The envisaged numerical model for the prediction of damage and final fracture of notched and unnotched composite structures is based on a meso-mechanical representation of the laminate where **a single three-dimensional continuum element is used to represent the whole thickness of a ply**, and **cohesive elements or cohesive surfaces represent the interface between the plies**. The three-dimensional continuum elements should be able to represent ply failure mechanisms and the cohesive elements or cohesive surface to simulate delamination between the plies.

3.2.1 Ply (or intralaminar) damage – modeled by Continuum Damage Mechanics (CDM)

Continuum Damage Mechanics (CDM) is a methodology well suited for the simulation of damage evolution and ultimate failure of composites under general loads and boundary conditions for which no analytical solution is available. The quasi-three-Dimensional Continuum Damage Model (quasi-3D CDM) used here is based on previous work [124, 125], which developed a two-Dimensional Continuum Damage Model (2D CDM) for the prediction of the onset and evolution of intralaminar failure mechanisms and the collapse of structures manufactured in FRP laminates.

In resemblance with the 2D CDM, in the quasi-3D CDM the failure mechanisms occurring in the longitudinal and transverse directions of a ply are represented by a set of scalar damage variables. Crack closure effects under load reversal are taken into account by using damage variables that are established as a function of the sign of the components of the stress tensor. Damage activation functions based on the LaRC04 failure criteria are used to predict the different failure mechanisms occurring at the ply level.

The main aspects of the quasi-3D CDM used in this work are presented in the following points.

3.2.1.1 Introduction to damage description in the mesoscale

Physically, degradation of the material properties is the result of the initiation, growth and coalescence of microcracks or microvoids. Within the context of continuum mechanics, one

may model this process by introducing an internal damage variable which can be a scalar or a tensorial quantity [91].

The easiest way of describing damage is considering just one damage variable which affects all the constitutive tensor terms, after the pioneering work of Kachanov [85, 86]. The use of scalar damage models is common in constitutive modeling due to its simplicity, although they are not able to represent the macro-crack orientation of an evolving crack in the macroscale.

If the material is anisotropic, the number of independent damage variables that should be defined in order to maintain the principal directions unchanged is equal to the number of elastic constants of the material. Therefore, 5 damage variables have to be defined for a transversely isotropic material, 9 for an orthotropic material and 21 for a completely anisotropic material. This set of scalar variables which describe damage represent cracks oriented according to the material's preferential directions, not considering that load directions influence the crack orientations. This assumption is well suited for composite laminae because numerous experiments show that the cracks are generated in the fibers' transverse direction (matrix failure) or in the longitudinal direction (fiber failure), thus all possible directions are reduced mainly to two planes.

The most general way of relating the undamaged stiffness tensor C^0_{mnst} of a material with a general damaged state is by an eighth order tensor $M_{ijklmnst} = (I_{ijklmnst} - D_{ijklmnst})$ [87] (a tensor formed by 3^8 variables), where **I** is the identity matrix and **D** is the tensor formed by scalar damage variables.

$$C_{ijkl} = (I_{ijklmnst} - D_{ijklmnst})C^0_{mnst} \tag{3.1}$$

In order to reduce it to the formerly referred 21 independent parameters (for a completely anysotropic material) it is necessary to respect the compatibility condition and to consider the existence of a scalar function which respects the thermodynamic potential. Nevertheless, due to the great complexity and to the impossibility of determining the parameters for the eighth order tensor, these tensors are not used.

Simo and Ju [91] presented a review of some basic concepts of continuum damage mechanics that simplify the treatment of the constitutive damaged tensor, reducing it to a fourth order tensor (or less). Some hypothesis are formulated in order to relate kinematically the damaged

state with an effective space of the undamaged material (a fictitious space within the material that is considered to be equivalent to the physical space by the application of an hypothesis). In the effective space, the stresses ($\tilde{\sigma}$) and strains ($\tilde{\varepsilon}$) follow the initial elastic constitutive law, $\tilde{\sigma} = \mathbf{C}_0 : \tilde{\varepsilon}$. In the physical space, the nominal stresses (σ) and strains (ε) are obtained by defining a relation between them and the effective stresses and strains. There are **three main principles** that can be followed to define those relations: principle of strain equivalence; principle of stress equivalence and principle of energy equivalence. These principles are illustrated in Figure 3.6.

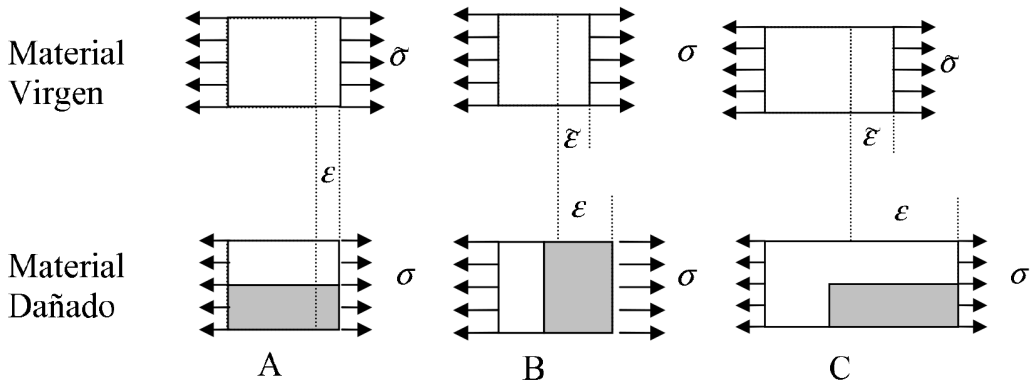

Figure 3.6: Hypothesis of (a) strain equivalence, (b) stress equivalence and (c) energy equivalence between the damaged physical space and the undamaged effective space. [135]

- **(a) Strain equivalence principle:**

  The strain associated with a damaged state under the applied stress (σ) is equivalent to the strain associated with the undamaged state under the effective stress ($\tilde{\sigma}$). From this it is possible to obtain the relation between the nominal stresses (σ) and the effective ones ($\tilde{\sigma}$):

$$\sigma = (\mathbf{I} - \mathbf{D}) : \tilde{\sigma} \qquad \text{and} \qquad \sigma = (\mathbf{I} - \mathbf{D}) : \mathbf{C}_0 : \varepsilon \tag{3.2}$$

- **(b) Stress equivalence principle:**

  The stress associated with a damaged state under the applied strain (ε) is equivalent to the stress associated with the undamaged state under the effective strain ($\tilde{\varepsilon}$). From this it is possible to obtain the relation between the nominal strains (ε) and the effective

ones ($\tilde{\varepsilon}$):

$$\tilde{\varepsilon} = (\mathbf{I} - \mathbf{D}) : \varepsilon \qquad \text{and} \qquad \sigma = \mathbf{C}_0 : (\mathbf{I} - \mathbf{D}) : \varepsilon \tag{3.3}$$

- **(c) Energy equivalence principle:**

  Helmholtz free energy density Ψ stored in the undamaged material under an effective strain is equivalent to the free energy density stored in the damaged material under a nominal strain. At the same time, the complementary free energy density $\bar{G}$ stored in the undamaged material under an effective stress is equivalent to the complementary free energy density stored in the damaged material under a nominal stress.

$$\Psi = \frac{1}{2}\tilde{\varepsilon} : \mathbf{C}_0 : \tilde{\varepsilon} \qquad \text{and} \qquad \bar{G} = \frac{1}{2}\tilde{\sigma} : \mathbf{C}_0^{-1} : \tilde{\sigma} = \frac{1}{2}\sigma : \mathbf{C}_0^{-1} : \sigma \tag{3.4}$$

  Resulting in the following constitutive relation:

$$\sigma = (\mathbf{I} - \mathbf{D}) : \mathbf{C}_0 : (\mathbf{I} - \mathbf{D})\varepsilon \tag{3.5}$$

The strain equivalence principle and the stress equivalence principle lead to non-symmetric stiffness matrices, which is thermodynamically inadmissible. However, the **energy equivalence principle leads to a symmetric stiffness matrix**. This is the main reason that justifies the use of the energy equivalence principle for the numerical model presented in this thesis.

So far, it was just introduced conceptually some of the basic formulations for continuum damage mechanics, but the actual constitutive relations were not specified. The above equivalence principles reduce the most general relation between the undamaged tensor and the damaged one to a fourth order tensor (or less). In the literature there are some models available which use fourth order tensors [90, 91, 92], but it is usual to consider that damage can be represented by second order symmetric tensors if it is considered that the material state can be represented by a set of orthogonal cracks defined by the orthonormal vectors ($\mathbf{n}_1$, $\mathbf{n}_2$, $\mathbf{n}_3$) that correspond to the principle directions of the second order tensor that describes damage. **For the numerical model** presented in this thesis a second order tensor $\mathbf{M} = (\mathbf{I} - \mathbf{D})$ is used to describe damage. Therefore, the corresponding scalar damage variables (d_1, d_2 and d_3) are

associated with the referred orthogonal directions. The relation between the effective and the nominal stresses can then be written as:

$$\sigma_{11} = (1 - d_1)\tilde{\sigma}_{11} \quad ; \quad \sigma_{22} = (1 - d_2)\tilde{\sigma}_{22} \quad ; \quad \sigma_{33} = (1 - d_3)\tilde{\sigma}_{33} \tag{3.6}$$

The shear stresses relations should not be defined in the same way because defining the relation $\sigma_{ij} = (I_{ik} - D_{ik})\tilde{\sigma}_{kj}$ results in a non-symmetric relation. Nevertheless, it is logic (and usual) to assume that the stresses in the ij plane are affected by the damage variables i and j (with $i \neq j$). Some examples to obtain the relation between the shear stress σ_{12} and the effective stress $\tilde{\sigma}_{12}$ that are commonly assumed are [93, 94]:

$$\begin{aligned} \sigma_{12} &= \sqrt{(1 - d_1)(1 - d_2)}\, \tilde{\sigma}_{12} \; ; \\ \sigma_{12} &= \frac{1}{2}\left[(1 - d_1) + (1 - d_2)\right] \tilde{\sigma}_{12} \; ; \\ \sigma_{12} &= 2\frac{(1 - d_1)(1 - d_2)}{2 - d_1 - d_2}\tilde{\sigma}_{12} \; , \end{aligned} \tag{3.7}$$

although none of these was used in the proposed model. [3]

These relations are the result of the **symmetrization** of the effective stress tensor. If the energy equivalence principle is applied, the resulting stiffness tensor is:

$$\mathbf{C} = \mathbf{M} : \mathbf{C}_0 : \mathbf{M} \tag{3.8}$$

with $\mathbf{M}$ being a matrix that can be expressed in the principle damage directions as:

$$\mathbf{M} = \begin{bmatrix} 1 - d_1 & 0 & 0 & 0 & 0 & 0 \\ 0 & 1 - d_2 & 0 & 0 & 0 & 0 \\ 0 & 0 & 1 - d_3 & 0 & 0 & 0 \\ 0 & 0 & 0 & 1 - d_4 & 0 & 0 \\ 0 & 0 & 0 & 0 & 1 - d_5 & 0 \\ 0 & 0 & 0 & 0 & 0 & 1 - d_6 \end{bmatrix} \tag{3.9}$$

[3] At the moment it is not important to define the relations between the effective and nominal shear stresses that were actually used in the model (from which it will result the relations between the independent and dependent damage variables) but to understand the concept that there are dependent and independent damage variables and to understand how they appear.

where, for instance, if it is considered one of the previously written assumptions to relate the effective $\tilde{\sigma}_{12}$ and nominal σ_{12} shear stresses, the corresponding term $M_{66} = (1-d_6)$ is defined by the respective relation:

$$\begin{aligned}(1-d_6) &= \sqrt{(1-d_1)(1-d_2)}\,; \\ (1-d_6) &= \frac{1}{2}\left[(1-d_1)+(1-d_2)\right]; \\ (1-d_6) &= 2\frac{(1-d_1)(1-d_2)}{2-d_1-d_2}\,,\end{aligned} \tag{3.10}$$

according to the type of symmetrization chosen.

With this example of possible relations between the effective ($\tilde{\sigma}_{12}$) and nominal (σ_{12}) shear stresses it is introduced the concept of dependent damage variable (d_6), where one or more variables are defined as a function of other (independent) damage variables. This reduces the number of damage laws that need to be defined for the model.

Having defined the second order tensor **M**, this general introduction to continuum damage mechanics applied to the mesoscale is finished. For a more detailed description the reader is advised to consult references [87]-[94]. In the next subsection, the constitutive model that was actually used, and also the simplifications assumed in order to make the model computationally efficient, will be described.

3.2.1.2 Constitutive model

The thermodynamics of irreversible processes is a general framework that can be used to formulate constitutive equations. It is a logical framework for incorporating observations and experimental results and a set of rules for avoiding incompatibilities. In this author's opinion, it is very interesting to understand the origin of the constitutive model instead of merely presenting it. For the reader that intends to understand how **Matzenmiller *et al.*** obtained the damaged stiffness tensor that was the origin of the complementary free energy used and modified by different authors (including Maimí *et al.* [124, 125]), and for the reader that wishes to understand the fundamental principles behind the constitutive models based on the thermodynamics of irreversible processes, a prescription of those theories is provided in **Appendix A**.

In this subsection, a constitutive damage model for laminated composites that has its foun-

dation in irreversible thermodynamics and that uses the LaRC04 failure criteria as damage activation functions, will be presented.

To establish a constitutive law, it is possible to define a scalar function corresponding to the complementary free energy density in the material. This function must be positive definite and it must be zero at the origin with respect to the free variables (the stresses) [89]. In Appendix A the ply complementary free energy density proposed by **Matzenmiller *et al.*** [100] is derived. This potential was obtained considering plane stress state. To obtain the potential for a 3D stress state it is necessary to generalize this expression. For instance, Ladevèze *et al.* [101]-[105] proposed several thermodynamic potentials similar to Matzenmiller's model. In some of these proposals the potential was generalized to 3D stress states. For this work, it was decided to generalize the 2D constitutive model defined in [124, 125] to a **transversely isotropic 3D constitutive model**.

The assumption of transverse isotropy is clearly erroneous, as proven in the preceding chapters. Nevertheless, this assumption greatly simplifies the generalization of the complementary free energy potential. If transverse isotropy is assumed $E_3 = E_2$, $G_{13} = G_{12}$, $\alpha_{33} = \alpha_{22}$ and $\beta_{33} = \beta_{22}$. This implies transverse coupling (the 2 and 3 terms).

The proposed definition for the ply **complementary free energy density**[4] potential is:

$$\begin{aligned}\bar{G} \;=\; & \frac{\sigma_{11}^2}{2(1-d_1)E_1} + \frac{1}{2E_2}\left[\frac{\sigma_{22}^2}{(1-d_2)} + \frac{\sigma_{33}^2}{(1-d_3)}\right] - \frac{\upsilon_{12}}{E_1}(\sigma_{22}+\sigma_{33})\sigma_{11} - \\ & -\frac{\upsilon_{23}}{E_2}\sigma_{22}\sigma_{33} + \frac{\sigma_{12}^2}{2(1-d_6)G_{12}} + \frac{\sigma_{13}^2}{2(1-d_5)G_{12}} + \frac{\sigma_{23}^2}{2(1-d_4)G_{23}} + \\ & + [\alpha_{11}\sigma_{11} + \alpha_{22}(\sigma_{22}+\sigma_{33})]\Delta T + [\beta_{11}\sigma_{11} + \beta_{22}(\sigma_{22}+\sigma_{33})]\Delta M \end{aligned} \quad (3.11)$$

where the damage variable d_1 is associated to the longitudinal direction, d_2 to the in-plane transverse direction, d_3 to the out-of-plane transverse direction, d_4 to plane 23 of Figure 3.1, d_5 to plane 13 and finally d_6 to plane 12. β_{11} and β_{22} are the coefficients of hygroscopic expansion in the longitudinal and transverse directions, respectively. ΔT and ΔM represent the variation of temperature and moisture content with respect to the corresponding reference values.

[4] The complementary free energy density $\bar{G}$ is defined as the symmetric of the Gibbs free energy density G: $\bar{G} = -G$.

Although there were six damage variables defined for the complementary free energy density of equation (3.11), they will not be considered all independent. Some simplifications will be made by considering that the stress components σ_{33}, σ_{13} and σ_{23} are very small compared to the remaining stresses. For this reason the failure modes previously described for **plane stress states** remain unchanged and the constitutive relation of σ_{13} can be considered linear elastic. Therefore, the damage variables directly associated with direction 1 and 2 are independent (d_1, d_2 and d_6) and the others (d_3, d_4, d_5) are defined as:

$$\begin{aligned} d_3 &= 1 - (1 - d_1)(1 - d_2) \\ d_4 &= d_6 \\ d_5 &= d_1 \end{aligned} \tag{3.12}$$

In order to guarantee the thermodynamic irreversibility of the dissipative processes (damage and plasticity), the increment of the complementary free energy ($\dot{\bar{G}}$) less the increment of the external work applied in the solid ($\dot{\sigma} : \varepsilon$) in constant deformation can not be negative:

$$\dot{\bar{G}} - \dot{\sigma} : \varepsilon \geq 0 \tag{3.13}$$

This inequality corresponds to the second principle of thermodynamics and must be respected by any constitutive model [89]. Applying the chain rule of derivation, it is possible to express $\dot{\bar{G}}$ as a function of the stress tensor (σ) and the internal variables ($d_1 ... d_6$ and ε_{ij}^p) which results in:

$$\left(\frac{\partial \bar{G}}{\partial \sigma} - \varepsilon\right) : \dot{\sigma} + \frac{\partial \bar{G}}{\partial \mathbf{d}} \cdot \dot{\mathbf{d}} + \frac{\partial \bar{G}}{\partial \varepsilon_{12}^p} \cdot \dot{\varepsilon}_{12}^p \geq 0 \tag{3.14}$$

In order to guarantee a positive dissipation of elastic energy, the entity within the parenthesis has to be null. Thus, the elastic deformations can be determined by the derivative of the complementary free energy in order to the stress tensor:

$$\varepsilon = \frac{\partial \bar{G}}{\partial \sigma} = \mathbf{H} : \sigma + \alpha \Delta T + \beta \Delta M \tag{3.15}$$

Considering linear elastic behavior, the lamina compliance tensor **H** can be represented as:

$$\mathbf{H} = \frac{\partial^2 \bar{G}}{\partial\sigma \bigotimes \partial\sigma} =$$

$$= \begin{bmatrix} \frac{1}{(1-d_1)E_1} & -\frac{\upsilon_{12}}{E_1} & -\frac{\upsilon_{12}}{E_1} & 0 & 0 & 0 \\ -\frac{\upsilon_{12}}{E_1} & \frac{1}{(1-d_2)E_2} & -\frac{\upsilon_{23}}{E_2} & 0 & 0 & 0 \\ -\frac{\upsilon_{12}}{E_1} & -\frac{\upsilon_{23}}{E_2} & \frac{1}{(1-d_3)E_2} & 0 & 0 & 0 \\ 0 & 0 & 0 & \frac{1}{(1-d_4)G_{23}} & 0 & 0 \\ 0 & 0 & 0 & 0 & \frac{1}{(1-d_5)G_{12}} & 0 \\ 0 & 0 & 0 & 0 & 0 & \frac{1}{(1-d_6)G_{12}} \end{bmatrix} \tag{3.16}$$

The closure of transverse cracks under load reversal, also known as the unilateral effect, is taken into account by defining four damage variables associated with longitudinal and transverse damage. To distinguish between the active and the passive damage variables, it is necessary to define the longitudinal and transverse damage modes as follows:

$$\begin{aligned} d_1 &= d_{1+}\frac{\langle\sigma_{11}\rangle}{|\sigma_{11}|} + d_{1-}\frac{\langle-\sigma_{11}\rangle}{|\sigma_{11}|} \\ d_2 &= d_{2+}\frac{\langle\sigma_{22}\rangle}{|\sigma_{22}|} + d_{2-}\frac{\langle-\sigma_{22}\rangle}{|\sigma_{22}|} \\ d_3 &= d_{3+}\frac{\langle\sigma_{33}\rangle}{|\sigma_{33}|} + d_{3-}\frac{\langle-\sigma_{33}\rangle}{|\sigma_{33}|} \end{aligned} \tag{3.17}$$

where $\langle x\rangle$ is the McCauley operator defined as $\langle x\rangle := (x + |x|)/2$.

The present model tracks damage caused by tensile loads (d_+) separately from the damage caused by compressive loads (d_-). Depending on the sign of the corresponding normal stress, a damage mode can be either active or passive.

The model also assumes that the shear damage variable (d_6) is not affected by the crack closure effect. Shear damage results from longitudinal and transverse cracks, which do not close under shear stresses (σ_{12}). Transverse cracks are influenced by transverse stresses (σ_{22}) producing the closure of cracks and a friction retention whereas longitudinal cracks produce the same effect under longitudinal stresses (σ_{11}) [96]. The effect of friction is neglected in the present model.

3.2.1.3 Damage activation functions – F_N

Determining the domain of elastic response under complex stress states is an essential component of an accurate damage model. It is assumed that the elastic domain is enclosed by four surfaces, o accounting for one damage mechanism: longitudinal and transverse fracture under tension and compression. Those surfaces are formulated by the damage activation functions based on the LaRC04 failure criteria.

The four damage activation functions, F_N, associated with damage in the longitudinal ($N = 1+, 1-$) and transverse ($N = 2+, 2-$) directions represented in Figure 3.1, are defined as:

$$\begin{aligned} F_{1+} &= \phi_{1+} - r_{1+} \leq 0 \quad ; \quad F_{1-} = \phi_{1-} - r_{1-} \leq 0 \\ F_{2+} &= \phi_{2+} - r_{2+} \leq 0 \quad ; \quad F_{2-} = \phi_{2-} - r_{2-} \leq 0 \end{aligned} \tag{3.18}$$

where the loading functions ϕ_N ($N = 1+, 1-, 2+, 2-$) depend on the strain tensor and material constants (elastic and strength properties). The elastic domain thresholds r_N ($N = 1+, 1-, 2+, 2-$) take an initial value of 1 when the material is undamaged, and they increase with damage. The elastic domain thresholds are the internal variables that describe damage in the present model and are related to the damage variables d_M ($M = 1+, 1-, 2+, 2-$, 6) by the damage evolution laws.

3.2.1.4 Elastic domain thresholds – r_N

The current values of the elastic domain thresholds r_N are obtained using the loading functions ϕ_N according to the following equations:

$$\begin{aligned} r_{1+} &= \max\left\{1, \max_{s=0,t}\left\{\phi_{1+}^s\right\}, \max_{s=0,t}\left\{\phi_{1-}^s\right\}\right\} \\ r_{1-} &= \max\left\{1, \max_{s=0,t}\left\{\phi_{1-}^s\right\}\right\} \\ r_{2+} &= \max\left\{1, \max_{s=0,t}\left\{\phi_{2-}^s\right\}, \max_{s=0,t}\left\{\phi_{2+}^s\right\}\right\} \\ r_{2-} &= \max\left\{1, \max_{s=0,t}\left\{\phi_{2-}^s\right\}\right\} \end{aligned} \tag{3.19}$$

To obtain these equations it is necessary to define the damage evolution. The evolution of the elastic domain thresholds r_N are mathematically expressed by the Kuhn-Tucker conditions:

$$\dot{r}_N \geq 0 \; ; \; F_N \leq 0 \; ; \; \dot{r}_N F_N = 0 \tag{3.20}$$

Without considering the viscous effects, the activation functions should be always non-positive. When the activation functions are negative the material response is elastic. Otherwise, when a stress state activates a failure criterion ($F_N = 0$), it is necessary to calculate the gradient of the respective loading function ($\dot{\phi}_N$) in order to determine whether the elastic domain thresholds (the internal variables) are evolving or not. If the loading function gradient $\dot{\phi}_N$ is non-positive then the material is being unloaded or at least is not being loaded, and the internal variables do not evolve. If the gradient $\dot{\phi}_N$ is positive then the elastic domain thresholds evolve and the consistency condition must be satisfied:

$$\dot{F}_N = \dot{\phi}_N - \dot{r}_N = 0 \tag{3.21}$$

Considering that the elastic domain thresholds depend exclusively on the damage variables (according to the damage evolution laws that will be presented further) and that the loading functions depend on the deformations, the constitutive model can be explicitly integrated [91, 92].

In the definition of the constitutive model it is necessary to define the evolution of the active and inactive elastic domain thresholds. The evolution of the active elastic domains results of the application of the consistency condition, equation (3.21), which means that it depends on the respective damage activation function F_N. However, it is also necessary to define the evolution of the inactive elastic domain thresholds. For the latter definition it is assumed that the elastic domain thresholds associated with the longitudinal and transverse damage are not coupled. Nevertheless, it is considered that the elastic domain thresholds for tension and compression are coupled.

Transverse load

The material resistance under a transverse load is almost exclusively dependent on the matrix behavior. When a transverse tensile load is applied (combined or not with shear) or a

moderate transverse compressive load combined with a high shear stress is applied and the respective damage activation function F_{2+} becomes zero (is activated), cracks perpendicular to the laminate plane appear (recall that the fracture angle α is zero for these loading conditions). If a compressive load is applied after the appearance of these perpendicular cracks, they close and do not affect the material response in any way: neither the respective elastic domain threshold r_{2-} neither the damage variable d_{2-} are affected.

However, matrix cracks with an angle $\alpha \approx 53°$ which appear with the application of compressive stresses have the same effect as perpendicular cracks ($\alpha = 0°$) when a tensile load is applied after. For this reason, the evolution of the tensile elastic domain threshold (r_{2+}) is dependent on both damage mechanisms.

Therefore, the evolution of the transverse elastic domain thresholds is given by:

$$\begin{aligned} &\text{Tension:} && \dot{r}_{2+} = \dot{\phi}_{2+} \quad \text{and} \quad \dot{r}_{2-} = 0 \\ &\text{Compression:} && \dot{r}_{2-} = \dot{\phi}_{2-} \quad \text{and} \quad \dot{r}_{2+} = \begin{cases} \dot{\phi}_{2-} & \text{if} \quad r_{2+} \leq r_{2-} \\ 0 & \text{if} \quad r_{2+} > r_{2-} \end{cases} \end{aligned} \tag{3.22}$$

Integrating explicitly:

$$\begin{aligned} r_{2+} &= \max\left\{1, \max_{s=0,t}\left\{\phi^s_{2-}\right\}, \max_{s=0,t}\left\{\phi^s_{2+}\right\}\right\} \\ r_{2-} &= \max\left\{1, \max_{s=0,t}\left\{\phi^s_{2-}\right\}\right\} \end{aligned} \tag{3.23}$$

Longitudinal load

Under longitudinal tension the failure plane generated is perpendicular to the direction of the fibers. If the load is reversed the damaged material is still capable of sustaining some stresses due to the crack closure but the stiffness suffers a decrease because the ruptured fibers lose the initial alignment and become incapable of transferring loads. Nevertheless, compressive damage initiation is defined by the matrix degradation which sets the fibers free, causing fiber instability [98, 99]. It is assumed that the necessary deformations for compressive damage initiation remain unchanged by the previously generated tensile damage.

Under longitudinal compressive loads, matrix cracks and fiber ruptures by kink band formation are produced, without a predefined damage orientation. When the loads are reversed, the

generated compressive damage remains active and the elastic domain increases.

Therefore, the evolution of the longitudinal elastic domain thresholds is defined by:

$$\begin{aligned} &\text{Tension:} && \dot{r}_{1+} = \dot{\phi}_{1+} \quad \text{and} \quad \dot{r}_{1-} = 0 \\ &\text{Compression:} && \dot{r}_{1-} = \dot{\phi}_{1-} \quad \text{and} \quad \dot{r}_{1+} = \begin{cases} \dot{\phi}_{1-} & \text{if} \quad r_{1+} \leq r_{1-} \\ 0 & \text{if} \quad r_{1+} > r_{1-} \end{cases} \end{aligned} \tag{3.24}$$

Integrating explicitly:

$$\begin{aligned} r_{1+} &= \max\left\{1, \max_{s=0,t}\left\{\phi_{1+}^{s}\right\}, \max_{s=0,t}\left\{\phi_{1-}^{s}\right\}\right\} \\ r_{1-} &= \max\left\{1, \max_{s=0,t}\left\{\phi_{1-}^{s}\right\}\right\} \end{aligned} \tag{3.25}$$

3.2.1.5 Loading functions – ϕ_N

In order to completely define the damage activation functions (F_N) it is necessary to define the loading functions (ϕ_N) and the elastic domain thresholds (r_N). In the previous section it was defined the elastic domain thresholds and it was concluded that they depend on the maximum value of the loading functions. Therefore, to completely define F_N it is necessary to show how the loading functions are calculated.

For the calculation of the various loading functions the present model uses the **LaRC04 criterion**, as already referred. The LaRC04 criterion is an evolution of the LaRC03 criterion in order to consider tridimensional stress states. Some damage mechanisms became more precisely described, in particular the kink band formation phenomenon. For complete detail about the LaRC03-04 failure criteria it is recommended to read the references [98, 99].

Note that at the moment it is important to show the four loading functions used in the numerical model and the corresponding variables which are necessary to calculate them but it will not be shown the origin of the expressions yet. Later in this work the expressions will be explained.

Longitudinal tensile fracture – ϕ_{1+}

The LaRC04 criterion for fiber tension is defined as:

$$\phi_{1+} = \frac{E_1}{X_T}\varepsilon_{11} = \frac{\tilde{\sigma}_{11} - \upsilon_{12}\tilde{\sigma}_{22}}{X_T} \tag{3.26}$$

where the effective stress tensor $\tilde{\sigma}$ is computed as $\tilde{\sigma} = \mathbf{H_0}^{-1} : \varepsilon$. $\mathbf{H_0}$ is the undamaged compliance tensor.

Longitudinal compressive fracture – ϕ_{1-}

The damage activation function used to predict damage under longitudinal compression ($\tilde{\sigma}_{11} < 0$) and in-plane shear (fiber kinking) is established as a function of the components of the stress tensor $\tilde{\boldsymbol{\sigma}}^{(m)}$ in a coordinate system (m) representing the fiber misalignment:

$$\phi_{1-} = \frac{\left\langle \left|\tilde{\sigma}_{12}^{(m)}\right| + \eta_L \tilde{\sigma}_{22}^{(m)} \right\rangle}{S_L} \tag{3.27}$$

where the coefficient of longitudinal influence can be approximated as:

$$\eta_L \approx -\frac{S_L \cos(2\alpha_0)}{Y_C \cos^2 \alpha_0} \tag{3.28}$$

with $\alpha_0 = 53°$. The components of the effective stress tensor in the coordinate system associated with the rotation of the fibers are calculated as:

$$\begin{aligned} \tilde{\sigma}_{22}^{(m)} &= \tilde{\sigma}_{11} \sin^2 \varphi_C + \tilde{\sigma}_{22} \cos^2 \varphi_C - 2\left|\tilde{\sigma}_{12}\right| \sin \varphi_C \cos \varphi_C \\ \tilde{\sigma}_{12}^{(m)} &= (\tilde{\sigma}_{22} - \tilde{\sigma}_{11}) \sin \varphi_C \cos \varphi_C + \left|\tilde{\sigma}_{12}\right| \left(\cos^2 \varphi_C - \sin^2 \varphi_C\right) \end{aligned} \tag{3.29}$$

The misalignment angle (φ_C) is determined using standard shear and longitudinal compression strengths, S_L and X_C, respectively:

$$\varphi_C = \arctan\left(\frac{1 - \sqrt{1 - 4\left(\frac{S_L}{X_C} + \eta_L\right)\frac{S_L}{X_C}}}{2\left(\frac{S_L}{X_C} + \eta_L\right)} \right) \tag{3.30}$$

Transverse fracture perpendicular to the mid-plane of the ply – ϕ_{2+}

Transverse matrix cracks perpendicular to the mid-plane of the ply, i.e., with $\alpha_0 = 0°$, are created by a combination of in-plane shear stresses and transverse tensile stresses, or in-plane

shear stresses and small transverse compressive stresses. These conditions are represented by the following failure criteria:

$$\phi_{2+} = \begin{cases} \sqrt{(1-g)\,\dfrac{\tilde{\sigma}_{22}}{Y_T} + g\left(\dfrac{\tilde{\sigma}_{22}}{Y_T}\right)^2 + \left(\dfrac{\tilde{\sigma}_{12}}{S_L}\right)^2} & \text{if} \quad \tilde{\sigma}_{22} \geq 0 \\ \dfrac{1}{S_L}\left\langle |\tilde{\sigma}_{12}| + \eta_L \tilde{\sigma}_{22} \right\rangle & \text{if} \quad \tilde{\sigma}_{22} < 0 \quad \text{and} \quad |\tilde{\sigma}_{12}| \gg 0 \end{cases} \tag{3.31}$$

where g is the fracture toughness ratio defined as: $g = \dfrac{\mathcal{G}_{2+}}{\mathcal{G}_6}$. The needed fracture toughnesses are determined experimentally (Chapter 4).

Transverse compressive fracture – ϕ_{2-}

The matrix failure criterion for transverse compressive stresses consists of a quadratic interaction between the effective shear stresses acting on the fracture plane:

$$\phi_{2-} = \sqrt{\left(\frac{\tilde{\tau}^T_{\text{eff}}}{S_T}\right)^2 + \left(\frac{\tilde{\tau}^L_{\text{eff}}}{S_L}\right)^2} \quad \text{if} \quad \tilde{\sigma}_{22} < 0 \tag{3.32}$$

where the effective stresses $\tilde{\tau}^T_{\text{eff}}$ and $\tilde{\tau}^L_{\text{eff}}$ are computed as:

$$\begin{aligned} \tilde{\tau}^T_{\text{eff}} &= \left\langle -\tilde{\sigma}_{22} \cos\alpha_0 \left(\sin\alpha_0 - \eta_T \cos\alpha_0 \cos\theta_s\right)\right\rangle \\ \tilde{\tau}^L_{\text{eff}} &= \left\langle \cos\alpha_0 \left(|\tilde{\sigma}_{12}| + \eta_L \tilde{\sigma}_{22} \cos\alpha_0 \sin\theta_s\right)\right\rangle \end{aligned} \tag{3.33}$$

with $\eta_T = \dfrac{-1}{\tan(2\alpha_0)}$ and $\theta_s = \arctan\left(\dfrac{-|\tilde{\sigma}_{12}|}{\tilde{\sigma}_{22}\sin(\alpha_0)}\right)$.

3.2.1.6 Damage evolution laws and numerical implementation

Strain-softening constitutive models that do not take into account the finite element discretization produce results that are mesh-dependent, i.e. the solution is non-objective with respect to the mesh refinement and the computed energy dissipated decreases with a reduction of the element size. An effective solution to assure objective solutions consists of using a characteristic length of the finite elements (l^*) in the definition of the constitutive model. As schematically

shown in Figure 3.7, the post-peak response of the material is scaled as a function of the element size to keep the computed energy dissipation independent of the size of the element, and equal to the material fracture energy.

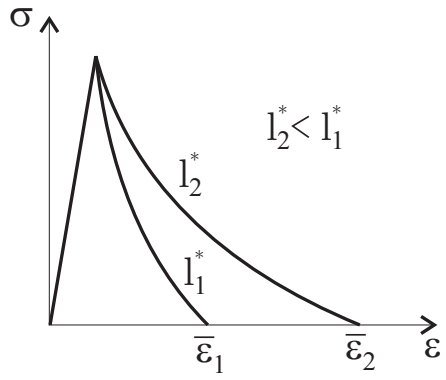

Figure 3.7: Scaling of constitutive model for different element sizes. [135]

The energetic regularization of the model proposed requires the fracture energies associated with the four fracture planes shown in Figure 3.1. These fracture energies were measured in the experimental program and are used in the damage evolution laws.

The exponential damage evolution laws proposed are expressed in the following general form:

$$\mathrm{d}_M = 1 - \frac{1}{f_N(r_N)} \exp\{A_M [1 - f_N(r_N)]\} f(r_K) \tag{3.34}$$

where the function $f_N(r_N)$ is selected to force the softening of the constitutive relation and it is taken as being independent of the material. The term $f(r_K)$ represents the coupling factor between damage laws and elastic threshold domains.

The regularization of the energy dissipated is performed by integrating the rate of energy dissipation for each failure mode. The energy dissipated in each failure mode must be independent of the element size, and must be equal to the fracture energy measured in the experiments:

$$\int_1^\infty \frac{\partial G}{\partial \mathrm{d}_M} \frac{\partial \mathrm{d}_M}{\partial r_M} dr_M = \frac{\mathcal{G}_M}{l^*}, \; M = 1+, 1-, 2+, 2-, 6 \tag{3.35}$$

Using (3.34) in (3.35), it is possible to numerically integrate the resulting equation and calculate the parameters A_M that assure a mesh-independent solution.

For more details about the damage laws derivation and the calculation of the necessary parameters it is advised to consult the references [124, 125, 135].

3.2.2 Shear plasticity

3.2.2.1 Behavior of composite materials under in-plane shear stresses

At the beginning of this Chapter it was stated that for a unidirectional lamina it is possible to perform five uniaxial tests: tension and compression in the fibers' direction ($\pm\sigma_{11}$) and perpendicular to that direction ($\pm\sigma_{22}$), and pure shear (σ_{12}). From these five tests it was experimentally observed that only two of them show **non-linearity**: when applying **compressive transverse loads** ($\sigma_{22} < 0$) or **shear loads** ($\sigma_{12} \neq 0$). Moreover, Koerber [137, 138] showed that the dynamic and quasi-static non-linear response of CFRP is significantly more pronounced for off-axis compression tests than for pure transverse compression tests. Figure 3.8 summarizes the results obtained by the referred author. In this figure it is possible to identify some curious behaviors of CFRP:

- Starting by the pure transverse compression test ("90° transverse compression"), it is clear to see that although the response of the composite material is non-linear, it is this particular stress-strain curve that is closer to a linear response;
- Observing the 75°, 60° and the "45° off-axis compression" response it can be seen that the **non-linearity is increasing significantly with the decrease of the fiber orientation angle**. Recall that for the off-axis tests there is a combination of transverse compression and shear. The closer the fibers' orientation angle is to the 45° the greater are the shear stresses when compared to the transverse compressive ones;
- Finally, if the fibers' orientation angle continues to decrease after passing by 45° the response approaches the linear case again. This can be concluded after comparing the "45° off-axis compression" test with the 30° and the latter with the "15° off-axis compression" test.

Therefore, from Figure 3.8 it is possible to conclude that the response of an unidirectional lamina subjected to shear loads is highly non-linear, whether for the pure transverse compression there is just a small non-linearity. This fact is of great interest for the numerical modeling of composite materials because if one pretends to enhance the model's computational efficiency there is the possibility of considering that plasticity occurs only when the material is subjected to shear loads.

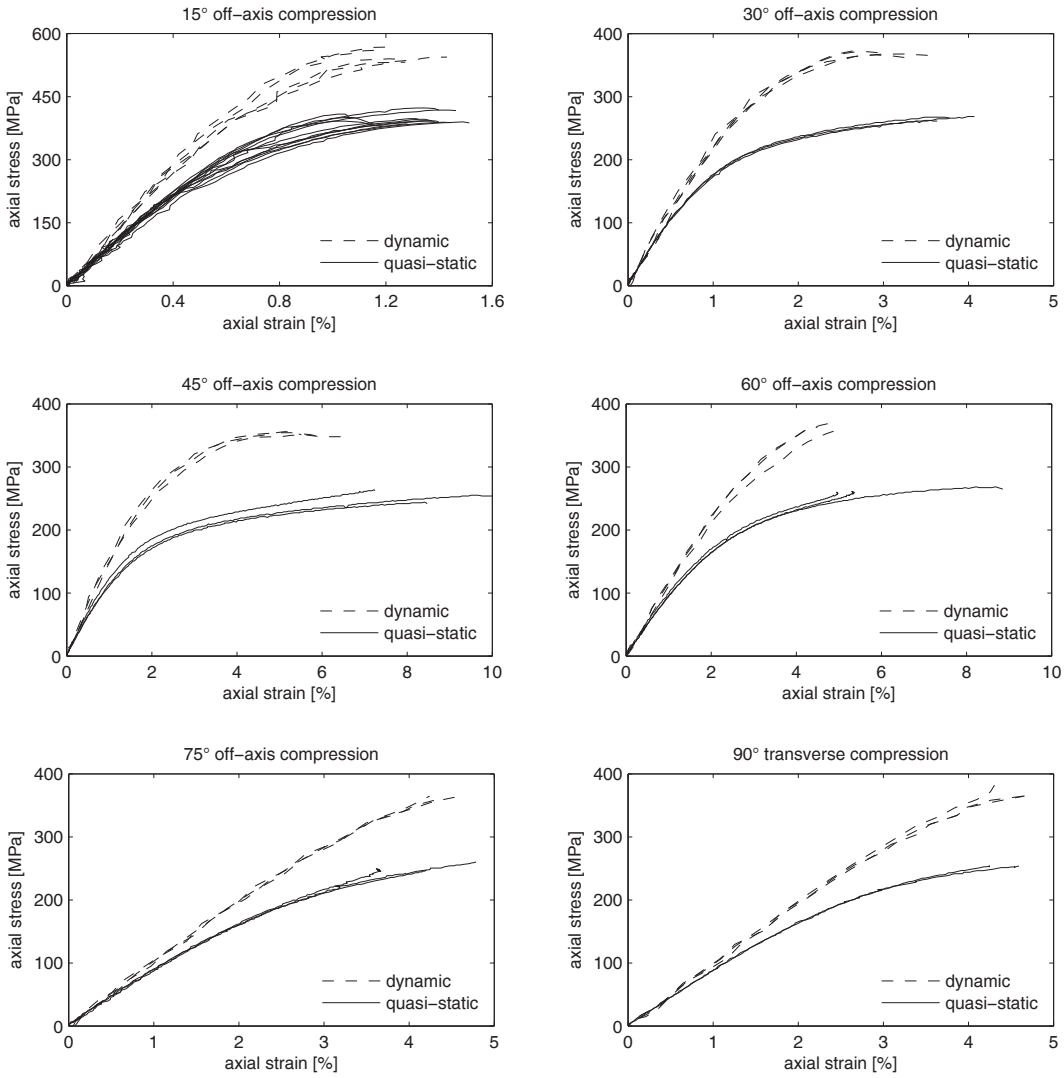

Figure 3.8: Individual comparison of quasi-static and dynamic axial stress-strain response for off-axis and transverse compression tests. Material: IM7/8552. [138]

3.2.2.2 Numerical model for shear plasticity

Since computational efficiency is extremely important for future commercial usage of the model, and having the experimental support that shear loads are more important than transverse compressive loads, a **plasticity model that only includes in-plane shear plasticity** was considered. Moreover, since there is no experimental data supporting that there is significant coupling between damage and plasticity for FRP, these two phenomena were modeled without interactions (uncoupled damage and plasticity). This greatly simplifies the model, once again increasing the computational efficiency and without losing accuracy.

The shear plasticity model here presented was proposed and described by Maimí [135]. Figure 3.9(a) shows a typical shear stress–shear strain response of a FRP. Observing the figure it is possible to see that after a brief linear-elastic phase the material follows a non-linear law. If the material is unloaded after achieving the non-linear phase it does not follow the same non--linear path back to the origin, which prevents the use of hyperelastic models. Instead, when unloading the path followed by the material's response is almost linear-elastic with a stiffness slightly lower then the one observed at the beginning of the loading case, leaving a permanent strain (γ_{12}^{p} or ε_{12}^{p}, depending of the notation used). As a final statement for describing the shear response, it is noted that the consecutive loading and unloading of FRP in shear causes hysteresis.

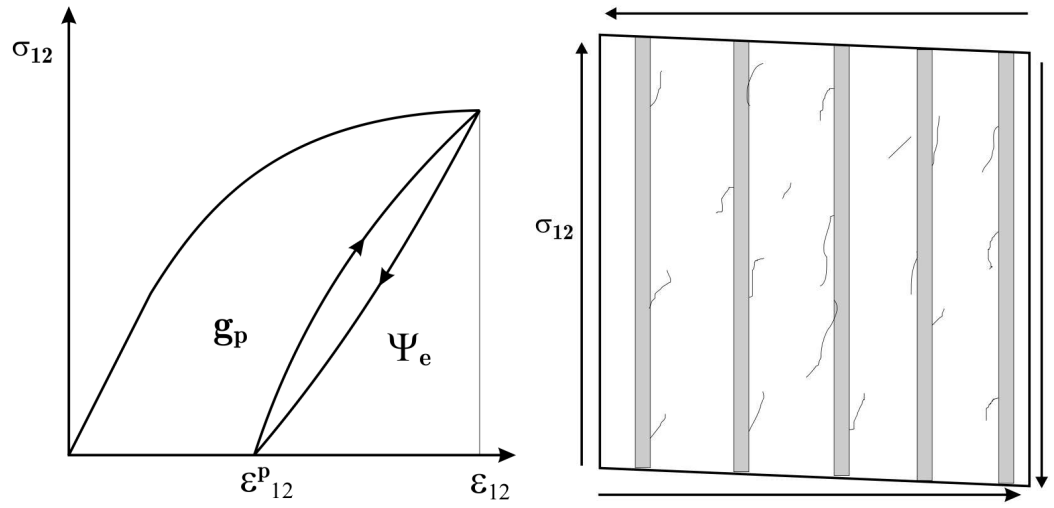

(a) Typical in-plane shear stress–shear strain response. (b) Schematic of matrix micro-cracking when subjecting the material to shear loads

Figure 3.9: (a) Non-linear in-plane shear response and (b) physical matrix behavior after non-linearity. [135]

Figure 3.9(b) provides some insight into the physical phenomena that can explain the non--linear behavior of FRP loaded in shear. When the material is subjected to shear loads the maximum principle stress appears for a 45° angle with the fibers' direction. Thus, in this direction microcracks start to appear in the matrix and at the interface between fiber and matrix. This causes the separation between matrix and fiber. Moreover, having microcracks in which the normal does not coincide with any of the maximum principle stresses' direction causes sliding between the two faces of the crack and, subsequently, friction. This friction along with the viscoelastic behavior of the matrix explains not only the previously referred permanent strain (γ_{12}^{p}) but also the hysteresis cycles. The presence of the microcracks between

fiber and matrix cause the stiffness to decrease (note that this type of damage is distributed to all volume). It is therefore concluded that the combination between the damage and the sliding processes causes energy dissipation (g_p, in Figure 3.9).

The shear plasticity model proposed by Maimí [135] that will be presented next does not consider the decrease in stiffness caused by the microcracking and the unloading process is considered linear-elastic without energy dissipation by hysteresis.

Friction model for shear behavior

Maimí [135] used a classical plasticity model [108, 109, 110] in order to consider the permanent strains of the material. As was already mentioned, the only component that will be considered to have permanent strains is the in-plane shear, γ_{12}.

A simple way of introducing the model is by making an analogy with a rheological system. Figure 3.10 shows the rheological model that is constituted by an **elastic system** with stiffness G_{12} (in the figure: right branch) and an **elasto-frictional system** (in the figure: left branch) connected in series. The elasto-frictional model consists of an elastic system with stiffness H' (in the figure: lower branch) connected in parallel with a frictional system with hardening (in the figure: upper branch), being $\sigma^0_{12}(\gamma^i_{12}, \varepsilon_{22})$ the yield stress. The yield stress establishes the limit between a pure elastic or an elasto-plastic behavior. Thus, if the upper branch applied stress ($\sigma^{(1)}_{12}$) is lower than the yield stress, $\left|\sigma^{(1)}_{12}\right| < \sigma^0_{12}(\gamma^i_{12}, \varepsilon_{22})$, the frictional model does not deform. The constitutive relation for the elastic element of the elasto-frictional system (lower branch) is: $\sigma^{(2)}_{12} = H'\gamma^p_{12}$; whether for the elastic element of the elastic system is: $\sigma_{12} = G_{12}\gamma^e_{12}$. The relation between the different stresses that act in the model is given by the equilibrium ($\sigma_{12} = \sigma^{(1)}_{12} + \sigma^{(2)}_{12}$) and between the strains by kinematics ($\gamma_{12} = \gamma^p_{12} + \gamma^e_{12}$). Obviously, both branches of the elasto-frictional system are subjected to the same strain (γ^p_{12}).

Summarizing the previous paragraph, the global system can have an elastic or elasto-plastic behavior. To distinguish between these two behaviors it is necessary to compare the stress applied to the upper branch ($\sigma^{(1)}_{12} = \sigma_{12} - \sigma^{(2)}_{12}$) of the elasto-frictional model and compare it with the yield stress:

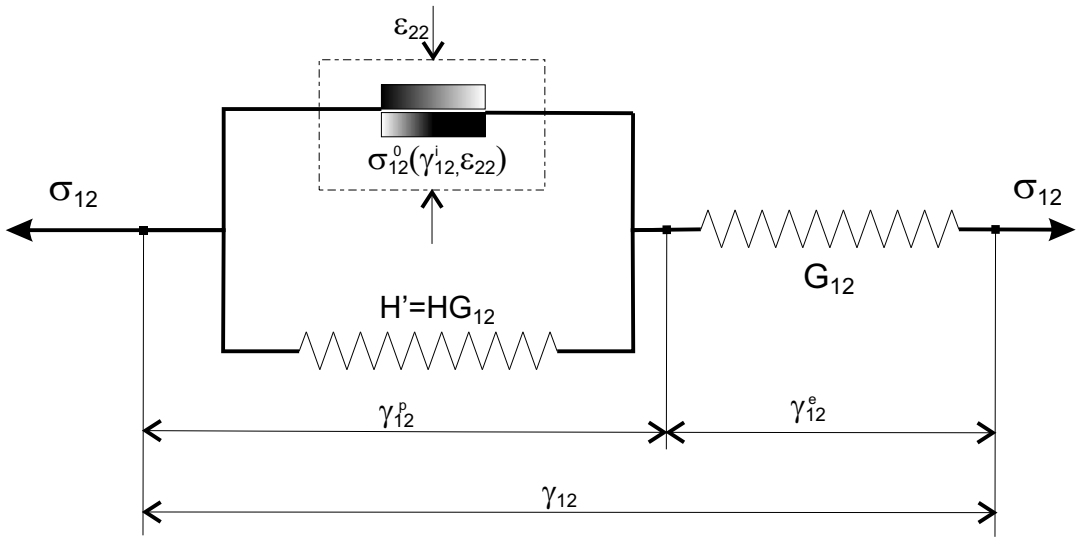

Figure 3.10: Elasto-frictional rheological model with hardening. [135]

$$\begin{aligned} &\text{Elastic behavior :} && \left|\sigma_{12} - H'\gamma_{12}^{p}\right| < \sigma_{12}^{0}(\gamma_{12}^{i},\, \varepsilon_{22}) \\ &\text{Elasto-plastic behavior :} && \left|\sigma_{12} - H'\gamma_{12}^{p}\right| = \sigma_{12}^{0}(\gamma_{12}^{i},\, \varepsilon_{22}) \end{aligned} \tag{3.36}$$

where the yield stress $\sigma_{12}^{0}(\gamma_{12}^{i},\, \varepsilon_{22})$ depends on the applied transverse stress (σ_{22}, or considering the constitutive law ε_{22}) and the internal variable of plastic hardening (γ_{12}^{i}). If one considers the following function:

$$\sigma_{12}^{0}(\gamma_{12}^{i},\, \varepsilon_{22}) = \gamma_{12}^{0} \log_2 \left(1 + \exp\left(-\mu\varepsilon_{22}\right)\right) + K'\gamma_{12}^{i} \tag{3.37}$$

Defining $H' = G_{12}H$ and $K' = G_{12}K$ one can write an equation that describes the elastic space of the material:

$$F_p = \left|\gamma_{12}^{e} - H'\gamma_{12}^{p}\right| - \left(\gamma_{12}^{0} \log_2 \left(1 + \exp\left(-\mu\varepsilon_{22}\right)\right) + K\gamma_{12}^{i}\right) \leq 0 \tag{3.38}$$

where the constants μ and γ_{12}^{0} adjust the surface. γ_{12}^{0} is the initial strain of the plastic process in a pure shear test, and $\mu \geq 0$ takes into account the transverse strain effect. The H and K parameters regulate the kinematic and isotropic hardening, respectively. **Appendix C** shows how γ_{12}^{0}, μ, H and K can be determined.

The plastic strain (γ_{12}^{p}) and isotropic hardening (γ_{12}^{i}) are internal variables of the model. The evolution law of the isotropic hardening variable is defined as:

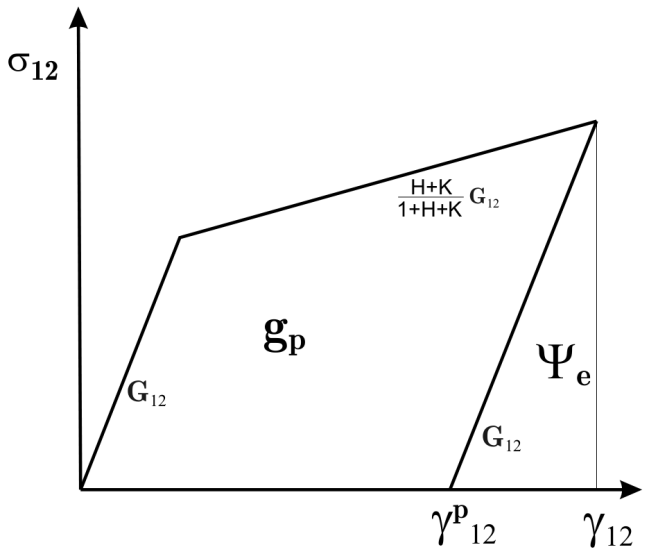

Figure 3.11: Shear stress–shear strain response of the model. [135]

$$\dot{\gamma}_{12}^{i} = \left|\dot{\gamma}_{12}^{p}\right| \tag{3.39}$$

The irreversible nature of the plastic process is expressed by the already mentioned[5] Kuhn--Tucker conditions:

$$\dot{\gamma}_{12}^{i} \geq 0 \; ; \; F_p \leq 0 \; ; \; \dot{\gamma}_{12}^{i} F_p = 0 \tag{3.40}$$

The determination of the plastic strains' evolution comes from the definition of the consistency condition: $\dot{F}_p = 0$.

Considering that the only scalar plastic variable is γ_{12}^{p} and that no permanent strains appear in the direction 22 ($\varepsilon_{22}^{p} = 0$) implies that it is not necessary to define an evolution potential. The consistency condition is enough to define the system's state. For more information about this subject the reader is referred to [108, 109, 110, 135]. Additionally, to check the thermodynamic consistency of this plastic model the reader is referred to the original work [135].

Model's integration and algorithm

If at a determined step time the in-plane shear strain exceeds the surface that defines the

[5] When defining the damage model.

elastic space, equation (3.38), the plastic variable has to increase. In order to determine this increment it is necessary to apply the consistency condition ($\dot{F}_p = 0$). At step time $n + 1$ the plastic variables have to obey the following relation:

$$F_p\left((\gamma_{12}^i)_{n+1},\ (\gamma_{12}^p)_{n+1}\right) = 0 \tag{3.41}$$

The plastic strains and the plastic hardening in step $n + 1$ can then be determined by:

$$\begin{aligned}\left(\gamma_{12}^i\right)_{n+1} &= \left(\gamma_{12}^i\right)_n + \Delta\left(\gamma_{12}^i\right)_{n+1} \\ \left(\gamma_{12}^p\right)_{n+1} &= \left(\gamma_{12}^p\right)_n + \Delta\left(\gamma_{12}^p\right)_{n+1} = \left(\gamma_{12}^p\right)_n + \Delta\left(\gamma_{12}^i\right)_{n+1} \operatorname{sign}\left\{(\gamma_{12})_{n+1} - (1+H)\left(\gamma_{12}^p\right)_n\right\}\end{aligned} \tag{3.42}$$

Resulting in an internal variable of hardening increment of:

$$\Delta\left(\gamma_{12}^i\right)_{n+1} = \frac{\left|(\gamma_{12})_{n+1} - (1+H)\left(\gamma_{12}^p\right)_n\right|}{1+K+H} - \frac{\left\{\gamma_{12}^0 \log_2\left[1+\exp\left(-\mu\,(\varepsilon_{22})_{n+1}\right)\right]\right\} + K\left(\gamma_{12}^i\right)_n}{1+K+H} \tag{3.43}$$

The integration process of the constitutive equation is summarized in the algorithm shown in Table 3.1.

Table 3.1: Computational algorithm.

1 - Having the system state of step n:

$$\left\{\left(\gamma_{12}^{p}\right)_{n},\ \left(\gamma_{12}^{p}\right)_{n}\right\}$$

2 - For the total strains in every integration point of step $n + 1$

$$\left\{(\gamma_{12})_{n+1},\ (\varepsilon_{22})_{n+1}\right\}$$

3 - Determine the elastic predictors

$$\left(\gamma_{12}^{p}\right)_{n+1}^{trial} = \left(\gamma_{12}^{p}\right)_{n},\quad \left(\gamma_{12}^{i}\right)_{n+1}^{trial} = \left(\gamma_{12}^{i}\right)_{n},\quad \left(\gamma_{12}^{e}\right)_{n+1}^{trial} = (\gamma_{12})_{n+1} - \left(\gamma_{12}^{p}\right)_{n}$$

$$\left(F_p\right)_{n+1}^{trial} = \left|\left(\gamma_{12}^{e}\right)_{n+1}^{trial} - H\left(\gamma_{12}^{p}\right)_{n+1}^{trial}\right| - \left[\gamma_{12}^{0}\log_2\left(1+\exp\left(-\mu\,(\varepsilon_{22})_{n+1}\right)\right) + K\left(\gamma_{12}^{i}\right)_{12}^{trial}\right]$$

4 - If $\left(F_p\right)_{n+1}^{trial} \leq 0 \quad \Rightarrow$ Elastic response: $(o)_{n+1} = (o)_{n+1}^{trial}$

Elseif $\left(F_p\right)_{n+1}^{trial} > 0 \quad \Rightarrow$ Elasto-plastic response:

$$\Delta\left(\gamma_{12}^{i}\right)_{n+1} = \frac{\left(F_p\right)_{n+1}^{trial}}{1+K+H}$$

$$\left(\gamma_{12}^{i}\right)_{n+1} = \left(\gamma_{12}^{i}\right)_{n} + \Delta\left(\gamma_{12}^{i}\right)_{n+1}$$

$$\left(\gamma_{12}^{p}\right)_{n+1} = \left(\gamma_{12}^{p}\right)_{n} + \Delta\left(\gamma_{12}^{i}\right)_{n+1}\,\text{sign}\left\{(\gamma_{12})_{n+1} - (1+H)\left(\gamma_{12}^{p}\right)_{n}\right\}$$

5 - Calculate the stresses

$$\sigma_{n+1} = \boldsymbol{C} : \varepsilon_{n+1}^{e}$$

3.2.3 Delamination (or interlaminar damage) – modeled by cohesive elements

The bond between each layer is simulated by means of the cohesive zone approach. In this approach, the fracture behavior (delamination) is lumped into a thin cohesive region representing the resin rich regions between layers. These resin rich regions are simulated by means of cohesive elements placed between each layer, as shown in Figure 3.12(a). The relative displacement of the two surfaces attached to the adjacent continuum elements that model the layers is a measure of the opening of the delamination crack. The opening is controlled by means of a bilinear cohesive constitutive relation, represented in Figure 3.12(b), that defines the delamination process.

In this work the cohesive elements were used without further improvements, therefore a brief description about this subject will be made. The complete formulation of the cohesive element used here is described by **González *et al.*** [127] in full detail.

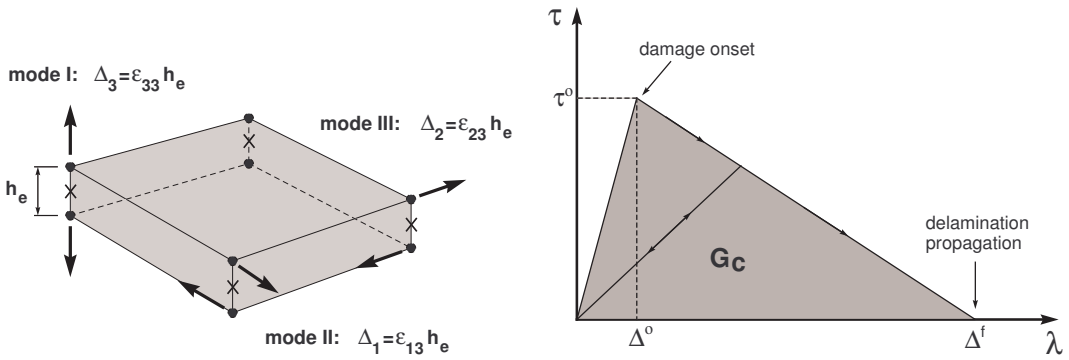

(a) Finite thickness cohesive element (b) Bilinear constitutive equation

Figure 3.12: Parameters of the cohesive element formulation in an explicit FE code. [127]

The free energy per unit surface of the interface is defined as:

$$\psi\left(\Delta_i, d\right) = \left(1-d\right)\psi^0\left(\Delta_i\right) - d\psi^0\left(\delta_{3i}\left\langle-\Delta_3\right\rangle\right) \quad i,j = 1,2,3 \tag{3.44}$$

where d is the scalar isotropic damage variable, Δ_i are the relative displacements, and δ_{ij} is the Kronecker delta.

The damage model has a unilateral behavior in mode I loading because negative values of the relative displacement in this mode, Δ_3, have no physical sense, i.e., a crack does not over-close. $\psi^0\left(\Delta\right)$ is a function of the relative displacement defined as:

$$\psi^0(\Delta_i) = \frac{1}{2}\Delta_i D^0_{ij}\Delta_j \quad i,j = 1,2,3 \tag{3.45}$$

where $D^0_{ij} = \delta_{ij}K$ is the undamaged stiffness tensor, wherein K is the scalar parameter defining the intact stiffness of the interface for each loading mode.

The cohesive constitutive equation is defined as:

$$\tau_i = \frac{\partial \psi}{\partial \Delta_i} = (1-d)\, D^0_{ij}\Delta_j - dD^0_{ij}\delta_{3j}\langle -\Delta_3\rangle \quad i,j = 1,2,3 \tag{3.46}$$

The thermodynamic consistency of the model is ensured by the positiveness of the energy dissipated by the damage process, i.e., $-\frac{\partial \psi}{\partial d}\dot{d} \geq 0$. The relative displacement vector, Δ, is the free variable of the system and d is the internal variable that ensures the irreversibility of the model, and whose value has to be evaluated at each time increment during the loading process.

The delamination propagation criterion is:

$$\mathcal{G}_c = \mathcal{G}_{Ic} + (\mathcal{G}_{IIc} - \mathcal{G}_{Ic})\left(\frac{\mathcal{G}_{II} + \mathcal{G}_{III}}{\mathcal{G}_I + \mathcal{G}_{II} + \mathcal{G}_{III}}\right)^{\eta} \tag{3.47}$$

where $\mathcal{G}_{Ic}$ and $\mathcal{G}_{IIc}$ are the fracture toughnesses in mode I and II, and $\mathcal{G}_I$, $\mathcal{G}_{II}$ and $\mathcal{G}_{III}$ are, respectively, the energy release rates in mode I, II and III. The shear loading modes II and III are coupled together in a single shear loading mode associated with the energy release rate $\mathcal{G}_{shear} = \mathcal{G}_{II} + \mathcal{G}_{III}$. The constitutive loading behaviors in mode II and III are considered the same and the fracture toughness $\mathcal{G}_{IIIc}$ is assumed to be equal to $\mathcal{G}_{IIc}$. This is a reasonable assumption since mode III loading is expected to play a minor role in most of the problems. Furthermore, in a FE formulation the distinction between these two loading modes is difficult to establish. The parameter η is found by least-square fit of the fracture toughness under different mixed-mode ratios.

The delamination propagation criterion can be expressed in terms of displacements by means of

$$\Delta^f = \frac{K_1\Delta^o_3\Delta^f_3 + \left(K_2\Delta^o_{shear}\Delta^f_{shear} - K_1\Delta^o_3\Delta^f_3\right)\mathcal{K}^{\eta}}{K_\beta\Delta^o} \tag{3.48}$$

with the parameter $\mathcal{K}$ expressed as

$$\mathcal{K} = \frac{K_2\beta}{K_2\beta + K_1(1-\beta)} \tag{3.49}$$

where β is the mixed-mode loading ratio defined as $\beta = \frac{\Delta_{shear}^2}{\langle\Delta_3\rangle + \Delta_{shear}^2}$. $\Delta_{shear} = \sqrt{\Delta_1^2 + \Delta_2^2}$ is the Euclidean norm of the relative displacements in mode II and III. Δ_3^o and Δ_{shear}^o are the onset relative displacements for pure mode I and shear mode, respectively. These are calculated by means of $\Delta_3^o = \frac{\tau_3^o}{K_1}$ and $\Delta_{shear}^o = \frac{\tau_1^o}{K_2}$, wherein τ_3^0 and τ_1^0 are the interface strengths for pure mode I and shear mode, respectively. $\Delta_3^f = \frac{2\mathcal{G}_{Ic}}{K_1\Delta_3^o}$ and $\Delta_{shear}^f = \frac{2\mathcal{G}_{IIc}}{K_2\Delta_{shear}^o}$ are the propagation relative displacements for pure mode I and shear mode, respectively.

The parameter Δ^o is the general relative displacement at damage onset, determined by means of the damage initiation criterion:

$$\Delta^o = \left\{ \frac{K_1\left(\Delta_3^o\right)^2 + \left(K_2\left(\Delta_{shear}^o\right)^2 - K_1\left(\Delta_3^o\right)^2\right)\beta^\eta}{K_\beta} \right\}^{\frac{1}{2}} \tag{3.50}$$

In equations (3.48) and (3.50), K_1, K_2 and K_β are the penalty stiffnesses, respectively, for the opening, shear and mixed modes, defined as:

$$K_1 = \frac{E_m}{h_c} \tag{3.51}$$

$$K_2 = \frac{G_m}{h_c} \tag{3.52}$$

$$K_\beta = K_1(1-\beta) + K_2\beta \tag{3.53}$$

where E_m is the Young's modulus and G_m is the shear elastic modulus of the cohesive layer (resin) material: $G_m = \frac{E_m}{2(1+\upsilon_m)}$. The thickness of the cohesive element is represented by h_c.

The correct implementation of a constitutive behavior for the continuum elements in ABAQUS® [126] requires the definition of the strain increment vector at each integration point. The cohesive strains are related with the relative displacements by: $\Delta_3 = h_c\varepsilon_{33}$ (mode I), $\Delta_1 = h_c(2\varepsilon_{13})$ (mode II) and $\Delta_2 = h_c(2\varepsilon_{23})$ (mode III).

Material Properties

The independent material properties required to completely define the cohesive model are:

- Elastic properties of the interface material, E_m and υ_m. These can be approximated using the ply material properties as $E_m \approx E_2$ and $\upsilon_m \approx \upsilon_{23}$.
- Interface strengths for pure mode I and shear modes (II and III), τ_3^0 and τ_1^0, which can be approximated as $\tau_3^0 \approx X_{2+}$ and $\tau_1^0 \approx X_6$.
- Interface fracture toughnesses for pure mode I and shear modes (II and III), $\mathcal{G}_{Ic} = \mathcal{G}_{2+}$ and $\mathcal{G}_{IIc} = \mathcal{G}_6$.
- The mode interaction parameter η, found by least-square fit of the experimental values of the fracture toughness under different mixed-mode ratios.

Therefore, except for the parameter η, the material properties required for the definition of the cohesive model are common to the ones required to define the intra-ply damage model. The value of the parameter η for IM7/8552, $\eta = 1.45$, was determined based on experimental data obtained from the Mixed-Mode Bending (MMB) test [127].

3.2.4 ABAQUS® VUMAT with Damage, Shear plasticity and Delamination

First of all, the reason that supports the implementation of the previously presented numerical model in a VUMAT subroutine (**Explicit code**) is quite simple to explain: Implicit codes have significant convergence problems when using models with damage and plasticity, especially if the structure has a complex geometry. On the contrary, with the Explicit code it is easier to obtain convergence although creating a good model that produces reliable results can be difficult because some parameters (like the variable mass scaling) can be difficult to manage by inexperienced users.

The objective of this section is to reveal the structure of the implemented VUMAT subroutine. All the topics that support the VUMAT algorithm were previously presented, although the damage evolution laws were not shown in detail. After reading the previous sections and observing the structure of the main program it is simple to implement the numerical model.

Maimí [134] wrote a user guide for the developed implicit numerical model for intralaminar damage and shear plasticity. Due to the great parallelism between the overall structure and theory behind the implicit model and the here presented explicit model, this section will have some points in common. For the case of the interlaminar damage (delamination), as was previously mentioned, the here presented numerical model uses **cohesive elements** and was created by González *et al.* [127]. The material properties needed for these elements have already been given, so no further presentation will be made (for further information the reader is advised to consult the original work).

Before continuing to present the structure of the VUMAT it is important to add some comments about the damage evolution laws and the shear plasticity model that were implemented, resulting in specific uniaxial responses that should be discussed.

The uniaxial stress-strain responses for different modes of failure are shown in Figure 3.13.

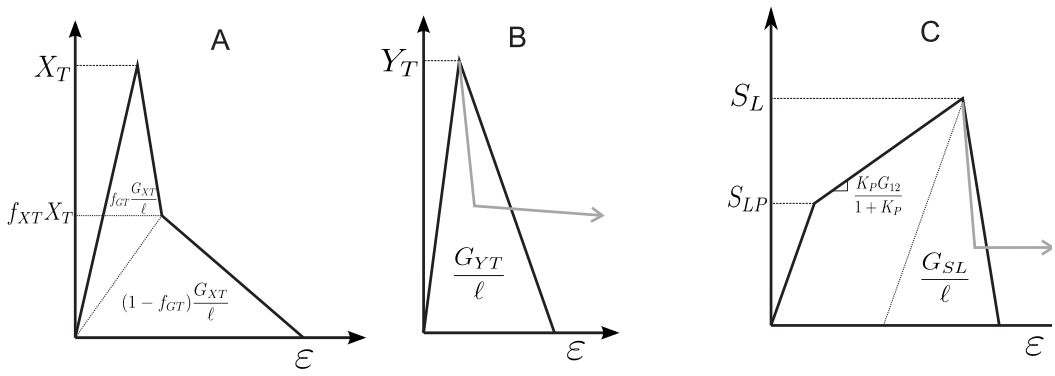

Figure 3.13: Uniaxial response (a) longitudinal tension or compression, (b) transverse tension or compression and (c) in-plane shear. [134]

Figure 3.13(a) represents the longitudinal stress-strain curve under tension or compression. Observing this figure it is possible to see that the response is linear-elastic until the initiation of damage, at the maximum tensile stress X_T or compressive stress X_C, and then the damage evolution law that was implemented was not of exponential form as was first proposed in the original work of Maimí *et al.* [124, 125]: **damage evolves according to a bi-linear softening law**. This was an update performed by the same authors because it is computationally more effective and it is believed to produce better results. This is the reason that explains why section 3.2.1.6 was presented very briefly: the exponential laws are not accurate for some failure modes, so the original papers [124, 125] for this point in particular were not used. Unfortunately, since the exponential laws used in this VUMAT were not created by the author of this thesis, it was decided not to publish the bi-linear laws used because they are still not published by their creators. Nevertheless, it is believed that these damage laws will be presented in a next publication of **Maimí** (*et al.*), so the interested reader should be alerted for this situation.

Although the evolution damage laws could not be presented, and still referring to Figure 3.13(a), it is interesting to explain the shape of the longitudinal laws. The break point for tension ($f_{XT}X_T$) is related with the moment when **fiber pull-out** starts to occur which leads to larger strains. For the compressive case, the break point ($f_{XC}X_C$) is related to the **formation of a kink band**, although for this case this point is more difficult to determine.

Figure 3.13(b) represents the transverse stress-strain curve under tension or compression. In this case, the softening law is linear because there is no failure mechanism (like in the longitudinal case) that physically supports the need of a bi-linear (or exponential) law.

Figure 3.13(c) represents the in-plane shear curve. The shear response is linear until S_{LP}, and the elasto-plastic response is activated thereafter. Relatively to the previous presentation of the shear plasticity model the only note that needs to be added is that in the VUMAT it was considered that the model has isotropic hardening only, resulting in $H = 0$ (see **Appendix C**). Therefore, the slope of the linear law for the elasto-plastic response is $\frac{K_p G_{12}}{1+K_p}$ (instead of $G_{12}\frac{H+K_p}{1+H+K_p}$).

For all responses the implemented model can perform a strength reduction due to the fact that the corresponding fracture toughness needs to be independent of the mesh size (finite element characteristic length, l): G_i/l, where $i = X_T$, Y_T or S_L. This will be explained in the following sub-section.

Maximum element size and strength reduction

Let's start by considering a large finite element. As was already mentioned, the fracture toughness is associated to the area of the element. Therefore, it is possible to write that the value of the fracture toughness per characteristic length is constant: G_i/l. If the element considered is large, then the area beneath the stress-strain curves (Figure 3.13) associated with the corresponding fracture toughness becomes a small value. If this happens, the slope/slopes of the softening law/laws will decrease sharply until, for a determined length, the constitutive response will have a "**snap-back**". Maimí [134] calculated the maximum element length that guarantees the correct energy dissipation for all damage modes:

$$l \leq \min\left\{\frac{2E_1G_{XT}}{X_T^2},\ \frac{2E_1G_{XC}}{X_C^2},\ \frac{2E_2G_{YC}}{Y_C^2},\ \frac{2E_2G_{YT}}{Y_T^2},\ \frac{2EG_{12}G_{SL}}{S_L^2}\right\} \tag{3.54}$$

Figure 3.14(a) illustrates a possible longitudinal tension strength reduction in order to guarantee the correct energy dissipation. Since the longitudinal softening law is bi-linear it is possible a partial snap-back. If the first segment have snap-back, in order to obey the inequality: $l \leq \frac{2E_1 f_{GT} G_{XT}}{X_T^2(1-f_{XT})^2}$, f_{XT} is increased as in Figure 3.14(b). On the other hand, if the snap-back occurs on the second segment the following inequality has to be respected: $lX_T^2 f_{XT}^2 + 2G_{XT}E_1(f_{XT}f_{GT} + f_{GT} - 1) \geq 0$, so f_{XT} is decreased as shown in Figure 3.14(c).

With the explanation of the damage evolution laws implemented and with all the theoretical

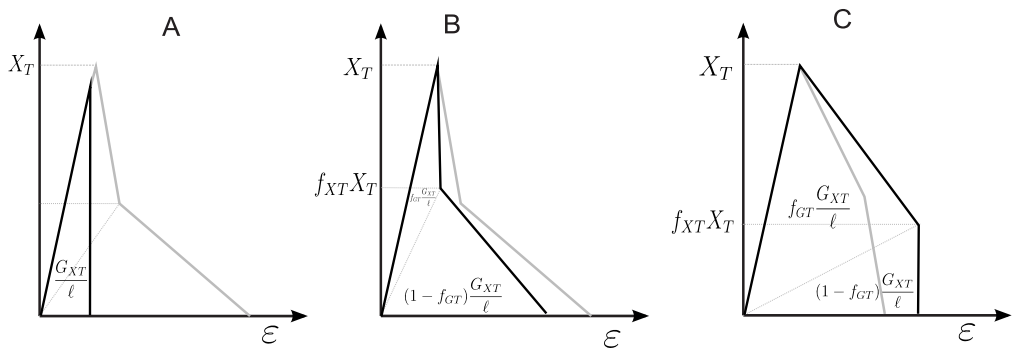

Figure 3.14: Strategies for strength reduction to guarantee a correct energy dissipation. [134]

introduction given in the previous sections, it is now possible to provide the main structure of the implemented VUMAT – Figure 3.15.

It should be stressed that the implemented VUMAT is based in a plane stress formulation. However, both shell and solid tridimensional elements can be used. In the latter case, it is assumed that each element represents a ply and the material is assumed to be transversely isotropic. Furthermore, as was already mentioned, it is assumed that the out of plane stress components are too small to promote damage, i.e., the damage is activated only by the in--plane stress components.

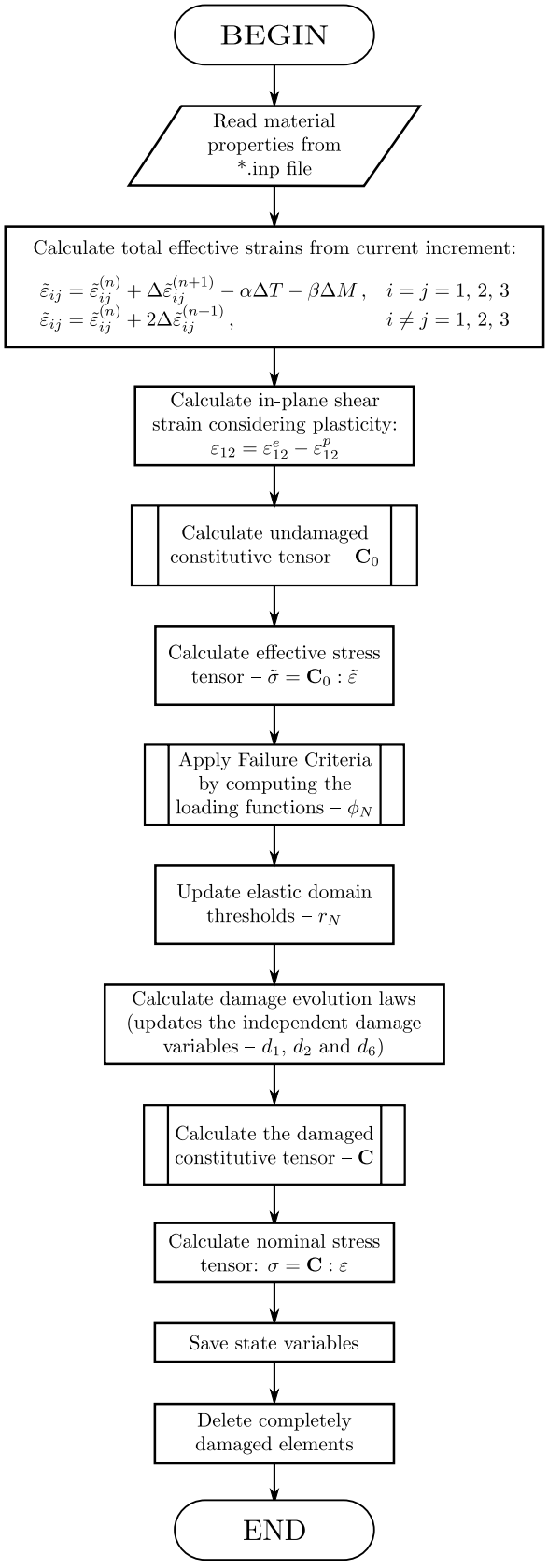

Figure 3.15: Flowchart of the VUMAT's **main program** for each time increment.

3.2.4.1 Input into ABAQUS/Explicit

Material properties

The material properties must be defined in the "jobname.inp" file using the following sequence of keywords:

*MATERIAL, NAME=[MAT_NAME]
*USER MATERIAL, CONSTANTS=27 (29)
E_1, E_2, G_{12}, υ_{12}, α_1, α_2, S_{LP}, K_P,
X_T, f_{XT}, X_C, f_{XC}, Y_T, Y_C, α_0, S_L,
G_{XT}, f_{GT}, G_{XC}, f_{GC}, G_{YT}, G_{YC}, G_{SL}, β_1,
β_2, ΔM, η, (υ_{23}), (t),
*DENSITY
ρ
*DEPVAR
11

The properties Y_T and S_L are *in situ* strengths. **Appendix B** was created in order to clarify the concept of *in situ* strength.

The number of material constants that need to be defined vary with the type of element: 27 for shell elements and 29 for tridimensional solid elements. Table 3.2 shows all the material constants that need to be defined and the corresponding definition. The only comment that needs to be added is about the "Longitudinal viscous parameter" (η). This parameter is important to aid in the convergence of Implicit analyses but it is not required for Explicit codes, therefore this function was deactivated (the user can put any value because this constant is not used).

Table 3.2: Input parameters required by the subroutine. 27 for shell elements and 29 for solid elements.

E_1	:	Longitudinal Young's modulus.
E_2	:	Transverse Young's modulus.
G_{12}	:	In-plane Shear modulus.
υ_{12}	:	Major Poisson's ratio.
α_1	:	Longitudinal thermal expansion coefficient.
α_2	:	Transverse thermal expansion coefficient.
S_{LP}	:	Shear stress that activates plastic flow. If $S_{LP} < 0$ is deactivated.
K_P	:	Shear incremental stiffness under plastic flow: $K_P > 0$.
X_T	:	Longitudinal tensile strength.
f_{XT}	:	Factor applied on X_T. $f_{XT}X_T$ is the longitudinal tensile strength at inflection point.
X_C	:	Longitudinal compressive strength.
f_{XC}	:	Factor applied on X_C. $f_{XC}X_C$ is the longitudinal compressive strength at inflection point.
Y_T	:	Transverse tensile strength.
Y_C	:	Transverse compressive strength.
α_0	:	Transverse compression fracture angle in radians (approx. 53°).
S_L	:	Shear strength.
G_{XT}	:	Fracture toughness for longitudinal tension.
f_{GT}	:	Proportion of G_{XT} dissipated by the first part.
G_{XC}	:	Fracture toughness for longitudinal compression.
f_{GC}	:	Proportion of G_{XC} dissipated by the first part.
G_{YT}	:	Fracture toughness transverse tension, mode I.
G_{YC}	:	Fracture toughness transverse compression.
G_{SL}	:	Fracture toughness in-plane shear, mode II.
β_1	:	Longitudinal hygroscopic expansion coefficient.
β_2	:	Transverse hygroscopic expansion coefficient.
ΔM	:	Variation in moisture content.
[η	:	Longitudinal viscous parameter.]
(υ_{23})	:	Transverse Poisson's ratio.
(t)	:	Ply thickness.

Initial conditions

The implemented VUMAT has a total of 18 state variables for the shell elements and 20 for the tridimensional solid elements – Table 3.3.

Table 3.3: State variables used by the implemented VUMAT subroutine.

STATEV(1)	r_{1+}: Longitudinal tension elastic domain threshold (fiber tension).
STATEV(2)	r_{2+}: Transverse tension elastic domain threshold (matrix tension).
STATEV(3)	r_{1-}: Longitudinal compression elastic domain threshold (fiber compression).
STATEV(4)	r_{2-}: Transverse compression elastic domain threshold (matrix compression).
STATEV(5)	γ_{12}^{p}: Shear plastic strain.
STATEV(6)	Shear hardening variable
STATEV(7)	Damage Index: 1:Matrix; 2:Fiber; 3:Fiber+matrix.
STATEV(8)	d_1: Longitudinal damage variable.
STATEV(9)	d_2: Transverse damage variable.
STATEV(10)	d_6: Shear damage variable.
STATEV(11)	Strength Reduction (5 digits). Each digit is an estimation of the strength reduction: X_T, X_C, Y_C, Y_T and S_L, respectively
STATEV(12)	g_f: Fiber dissipated energy ($g_f = g_1$)
STATEV(13)	g_m: matrix dissipated energy ($g_m = g_2 + g_6$)
STATEV(14)	ε_{11}: Longitudinal strain.
STATEV(15)	ε_{22}: Transverse strain (direction 22).
STATEV(16)	ε_{33}: Transverse strain (direction 33).
STATEV(17)	γ_{12}: In-plane shear strain.

For the case of **shell** elements:

STATEV(18)	Element status (1: Active; 0: Deleted).

For the case of **solid** elements:

STATEV(18)	γ_{23}: Shear strain (direction 23).
STATEV(19)	γ_{13}: Shear strain (direction 13).
STATEV(20)	Element status (1: Active; 0: Deleted).

Therefore, the model requires the definition of the initial values of the state variables. For instance, in the case of shell elements[6] the "jobname.inp" file must include the following

[6] If solid elements were to be use instead, the user needs to add two more zeros before the last state variable that has the value of 1.0 (the only state variable that needs to be initialized with a non-zero value is the "element status").

keywords:

```
*INITIAL CONDITIONS, TYPE=SOLUTION
ELSET, 0.0, 0.0, 0.0, 0.0, 0.0, 0.0, 0.0
0.0, 0.0, 0.0, 0.0, 0.0, 0.0, 0.0, 0.0
0.0, 0.0, 1.0
```

Where “ELSET” represents the group of elements for which for the constitutive model is defined by the VUMAT subroutine.

Thermal stresses

The constitutive model calculates the residual thermal stresses that result from the different coefficients of thermal expansion in the longitudinal and transverse directions. To enable the calculation of the thermal stresses, the user should define in the “jobname.inp” file the amplitude of the thermal step as follows:

```
*AMPLITUDE, NAME=[AMP_NAME], DEFINITION=TABULAR
0., 0., 1., 1.
```

The residual thermal stresses should be calculated in the initial step:

```
*TEMPERATURE, AMPLITUDE=[AMP_NAME]
NSET, ΔT
```

where “NSET” represents the group of nodes that belong to the elements in which the constitutive model is defined by the VUMAT subroutine, and ΔT is the balance between working and reference temperatures.

The following (mechanical) steps must include the following keyword:

```
*TEMPERATURE,
NSET, ΔT
```

3.2.4.2 ABAQUS/Explicit output

Energy variables

The elastic and dissipated energies are stored in the internal ABAQUS variable “ENER”.

State variables

As was already mentioned, the user subroutine has 18 or 20 state variables (according to the element type). The first four elastic domain thresholds are r_{1+}, r_{2+}, r_{1-} and r_{2-}. These are internal variables of the damage model. Before damage onset their values are smaller than 1.

The variables 5 and 6 are internal variables for the plastic model, γ^p_{12} and γ^i_{12}, respectively. They are historically related by $\dot{\gamma}^i_{12} = \left|\gamma^p_{12}\right|$, where γ^i_{12} is the classic isotropic hardening internal variable.

Variables 7 to 13 are for information only. Table 3.3 provides the information stored by each of these variables. The 11th state variable indicates if some strength reduction occurred. It is a 5 digit number, each digit indicates the percentage of strength reduction: $X_T X_C Y_C Y_T S_L$. For example, the number: 00129 indicates that Y_C has been reduced less then 10%, Y_T between 10% and 20% and S_L to a value greater then 80%.

Finally, variables 14 to 17 (in the case of shell elements) or 14 to 19 (in the case of solid elements) have the values of the strains. The 18th variable, for shell elements, and the 20th, for solid elements, represent the element status, giving information about what elements were deleted from the finite element mesh.

With this, the implemented VUMAT is completely described. The next section will present a new numerical model (absolutely independent from the here described VUMAT) that uses a new Failure Criteria for 3D stress states that was created by **Catalanotti** [136]. This model was created with a specific purpose that will be further explained in the next section.

3.3 Numerical Model with an improved Failure Criteria

In the previously presented numerical model that was implemented in an ABAQUS® VUMAT subroutine a 2D Failure Criteria was considered. This was the model used to predict the experimental results obtained in the experimental program that will be presented in Chapter 4. However, the generalization of the 2D Failure Criteria to a 3D Failure Criteria is greatly desirable. This section presents the generalization made by **Catalanotti** [136] and the subsequent implementation in an ABAQUS® UVARM subroutine.

It was previously stated that composite materials present different behavior in transverse tension, transverse compression, longitudinal tension, longitudinal compression and shear. It was concluded that the complete characterization of the different failure types implies the definition of at least four different failure criteria. Catalanotti [136] studied the accuracy of several failure criteria for each of the failure types considering different loading situations. The following sections present Catalanotti's proposed failure criteria for FRPs under 3D stress states.

3.3.1 Failure Criteria for 3D stress states

3.3.1.1 Matrix failure

The definition of the matrix failure criteria for a general stress state is based on the stresses in the fracture plane. The ideal failure criteria should be able to accurately predict material failure using as few mechanical properties as possible.

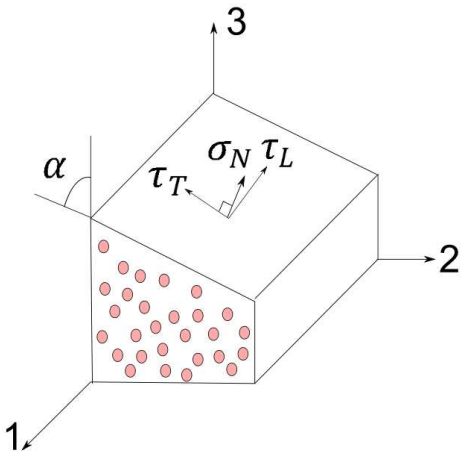

Figure 3.16: Components of the traction stress in the fracture plane. [136]

For a general stress state, the failure criteria is a function of the traction stress, t_n, acting on the fracture surface which can be expressed in the components σ_N, τ_T and τ_L as shown in Figure 3.16. For composite materials it is known in advance that the fracture plane will be parallel to the fibers direction which simplifies the definition of the plane to just one angle α. Therefore, for a general stress state described by the stress tensor **T**,

$$\mathbf{T} = \begin{bmatrix} \sigma_{11} & \sigma_{12} & \sigma_{13} \\ \sigma_{12} & \sigma_{22} & \sigma_{23} \\ \sigma_{13} & \sigma_{23} & \sigma_{33} \end{bmatrix} \tag{3.55}$$

and defining the normal to the fracture plane as $n = \begin{Bmatrix} 0 & \cos\alpha & \sin\alpha \end{Bmatrix}^T$, the traction stress t_n applied on the fracture plane is obtained by

$$t_n = T \cdot n = \begin{Bmatrix} \sigma_{12}\cos\alpha + \sigma_{13}\sin\alpha \\ \sigma_{22}\cos\alpha + \sigma_{23}\sin\alpha \\ \sigma_{23}\cos\alpha + \sigma_{33}\sin\alpha \end{Bmatrix} \tag{3.56}$$

Having defined the traction stress it is straightforward to calculate the stress components σ_N, τ_T and τ_L. The normal stress component, σ_N, is obtained as

$$\begin{aligned} \sigma_N &= t_n \cdot n = \begin{Bmatrix} \sigma_{12}\cos\alpha + \sigma_{13}\sin\alpha \\ \sigma_{22}\cos\alpha + \sigma_{23}\sin\alpha \\ \sigma_{23}\cos\alpha + \sigma_{33}\sin\alpha \end{Bmatrix} \cdot \begin{Bmatrix} 0 \\ \cos\alpha \\ \sin\alpha \end{Bmatrix} = \\ &= \sigma_{22}\cos^2\alpha + 2\sigma_{23}\cos\alpha\sin\alpha + \sigma_{33}\sin^2\alpha \end{aligned} \tag{3.57}$$

while the component in the transverse direction, τ_T, is given by

$$\tau_T = t_n \cdot \begin{Bmatrix} 0 \\ -\sin\alpha \\ \cos\alpha \end{Bmatrix} = -\sigma_{22}\sin\alpha\cos\alpha - \sigma_{23}\sin^2\alpha + \sigma_{23}\cos^2\alpha + \sigma_{33}\cos\alpha\sin\alpha \tag{3.58}$$

and finally, the component in the longitudinal direction, τ_L, is obtained as

$$\tau_L = t_n \cdot \left\{ \begin{array}{c} 1 \\ 0 \\ 0 \end{array} \right\} = \sigma_{12} \cos\alpha + \sigma_{13} \sin\alpha \tag{3.59}$$

As mentioned before, composite materials have different behavior in transverse tension and in transverse compression. Thus, it is not enough to use just one failure criteria to describe matrix failure. A failure criterion for matrix compression, $\sigma_N < 0$, and a failure criterion for matrix tension when $\sigma_N > 0$, were defined.

Before presenting the implemented failure criteria it is important to refer that the orientation of the fracture plane is obtained by calculating the maximum value of the failure criterion, i.e., the value of α that maximizes the failure criterion corresponds to the angle of the fracture plane. Catalanotti [136] based is search for the best failure criteria for each situation in the prediction of the fracture plane angle α for special cases where α is known. Using this approach the referred author was able to propose a new failure criterion for matrix tension.

Failure Criterion for Matrix Compression

The adopted failure criterion for matrix compression is a modification of the Puck and Shürmann's criterion proposed by **Dávila *et al.*** [81]. The modification was justified by the fact that under pure transverse compression ($\sigma_{22} \neq 0$ and $\sigma_{ij} = 0$) the obtained fracture angle for fiber reinforced plastics is equal to $\alpha_0 = 53 \pm 2°$, instead of the 45° obtained using the Mohr- -Coulomb criterion that Puck *et al.* [78] suggested to be used for predicting the orientation of the fracture plane. For the general case, the adopted failure criteria for matrix compression was

$$FI_{MC} = \left(\frac{\tau_L}{S_L - \eta_L \sigma_N} \right)^2 + \left(\frac{\tau_T}{S_T - \eta_T \sigma_N} \right)^2 \tag{3.60}$$

where S_L is the *in situ*[7] longitudinal shear strength, S_T is the *in situ* transverse shear strength, and η_L and η_T are the two slopes in the $\sigma_N - \tau_L$ and $\sigma_N - \tau_T$, respectively, when $\sigma_N = 0$ and are defined as

[7] **Appendix B** explains the concept of *in situ* strength.

$$\eta_L = -\frac{\partial \tau_L}{\partial \sigma_N}\bigg|_{\sigma_N=0} \qquad \eta_T = -\frac{\partial \tau_T}{\partial \sigma_N}\bigg|_{\sigma_N=0} \tag{3.61}$$

Failure Criterion for Matrix Tension

Catalanotti [136] proposed a new failure criterion for matrix tension:

$$FI_{MT} = \left(\frac{\tau_L}{S_L}\right)^2 + \left(\frac{\sigma_N}{Y_T}\right)^2 \tag{3.62}$$

In the referred work the author proves that the new failure criterion is able to predict the fracture plane angle for more loading cases than the previous criteria, namely:

- For $\sigma_{22} = Y_T$ and $\sigma_{ij} = 0$ the fracture plane angle is $\alpha = 0°$ and the Failure Index takes the value $FI_{MT} = 1$, in accordance to experimental results;
- For $\sigma_{33} = Y_T$ and $\sigma_{ij} = 0$ the fracture plane angle is $\alpha = 90°$ and the Failure Index takes the value $FI_{MT} = 1$, in accordance to experimental results;
- For $\sigma_{23} \neq S_L$ and $\sigma_{ij} = 0$ the fracture plane angle is $\alpha = 45°$ and the Failure Index takes the value $FI_{MT} = 1$ when $\sigma_{23} = S_L$, in accordance to experimental results;
- And finally, for $\sigma_{12} = S_L$ and $\sigma_{ij} = 0$ the fracture plane angle is $\alpha = 0°$ and the Failure Index takes the value $FI_{MT} = 1$, also in accordance to experimental results.

For further details about the presented results it is recommended to read the author's PhD thesis [136].

3.3.1.2 Fiber Failure

Fiber Tension Failure ($\sigma_{11} > 0$)

The implemented failure criterion for fiber tension failure was maintained the same as in LaRC03 suggested by Dávila *et al.* and presented before as:

$$FI_{FT} = \frac{E_1}{X_T}\epsilon_{11} \tag{3.63}$$

where E_1 is the elastic modulus in the longitudinal direction, X_T is the tensile strength and ε_{11} is the strain in the longitudinal direction.

Note that the influence of the transverse stress on the longitudinal strength of the fibers is being neglected.

Fiber Compression Failure – Kinking ($\sigma_{11} < 0$)

At the beginning of this chapter it was already mentioned that microbuckling and fiber kinking have been widely studied during the last 50 years, but despite all the efforts there is so far no full understanding about the physics and mechanics taking part in those phenomena. Moreover, there is no agreement yet between researchers on what differentiates them, as some authors consider kinking as a final result of microbuckling (hypothesis first suggested by Rosen [51]) while others argue that they are two independent failure modes (hypothesis first suggested by Argon [52]) [84].

The failure criterion presented here is based in Argon's approach [52] and the latter developments by Dávila *et al.* [81] and Pinho *et al.* [82], considering failure due to kinking as an independent mode. This approach considers that the formation of kink bands is triggered by **an initial misalignment of the fibers** which promotes shear stresses on the material that, by inducing moments, force the fibers to rotate more.

The generalization to a 3D stress state should improve significantly the prediction of failure by fiber kinking because it allows to calculate the kinking plane, which is not always parallel to the $1-2$ plane showed in Figure 3.17. A simple case where it was experimentally observed that the kinking plane occurs in the $1-3$ plane instead of the $1-2$ was already shown in Chapter 2: laminates loaded in compression which have 0° plies at the surface presented, for those plies, out-of-plane microbuckling (plane $1-3$) because in constrast with the 0° inner plies they don't have supporting plies that enforce them to fail by in-plane kink bands (plane $1-2$). Therefore, in a complex and general 3D stress state the kink band plane will be located in a plane obtained by a rotation around axis 1 – Figure 3.17(a).

In Figure 3.17(a) the kinking plane is highlighted. It shows the need to rotate the coordinate system $1-2-3$ around the axis 1 of an angle θ, obtaining the coordinate system $1^{(\theta)}-2^{(\theta)}-3^{(\theta)}$. The angle θ is a function of the local defects of the material because the kinking plane is

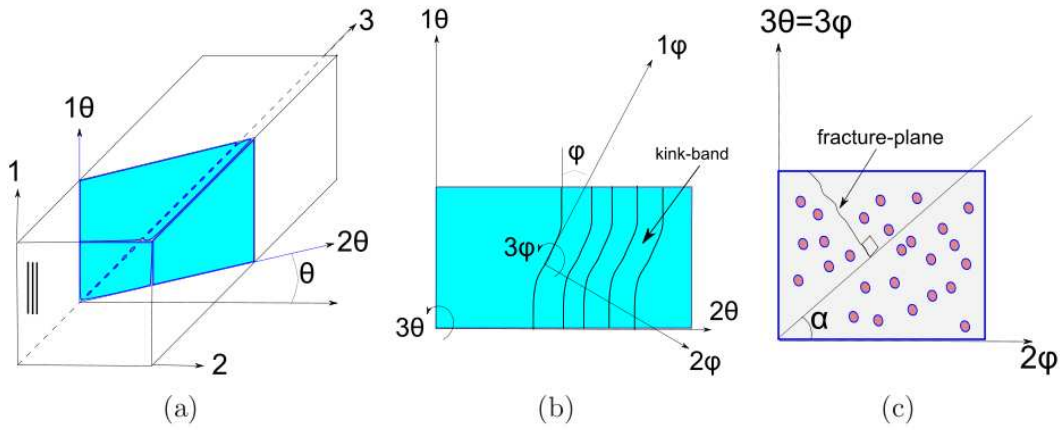

Figure 3.17: Coordinate systems used when fiber kinking occurs. (a) Fiber kinking plane – θ rotation (coordinate system: $1^{(\theta)} - 2^{(\theta)} - 3^{(\theta)}$); (b) Local kink-band formation – φ rotation (coordinate system: $1^{(\varphi)} - 2^{(\varphi)} - 3^{(\varphi)}$); (c) Transverse fracture – fracture plane α. [136]

triggered by these defects. However, if it is considered that the influence of the defects can be neglected **the angle θ can be reasonably approximated by calculating the maximum principal stress that acts on the transverse plane 2 – 3**, in this way θ is only a function of the stresses [136]. Catalanotti explained this by stating that if $\sigma_{23}^{(\theta)} \neq 0$ this would result in a movement perpendicular to the kinking plane contradicting the evidence that fibers kink on this plane. For this reason, using the Mohr's circle theory the angle θ can be obtained as,

$$tan(2\theta) = \frac{2\sigma_{23}}{\sigma_{22} - \sigma_{33}} \tag{3.64}$$

After defining the rotation angle θ it is necessary to define the stresses in the new coordinate system. Using the stress tensor previously defined in equation (3.55), the stress tensor $T^{(\theta)}$ in the new coordinate system after a rotation θ becomes,

$$T^{(\theta)} = R(\theta) \cdot T \cdot R(\theta)^T \tag{3.65}$$

where $R(\theta)$ is the rotation matrix, defined as:

$$R(\theta) = \begin{bmatrix} 1 & 0 & 0 \\ 0 & \cos\theta & \sin\theta \\ 0 & -\sin\theta & \cos\theta \end{bmatrix} \tag{3.66}$$

Thus, the stresses in the θ coordinate system are defined by:

$$\begin{aligned}
\sigma_{11}^{(\theta)} &= \sigma_{11} \\
\sigma_{22}^{(\theta)} &= \sigma_{22}\cos^2\theta + 2\sigma_{23}\cos\theta\sin\theta + \sigma_{33}\sin^2\theta \\
\sigma_{33}^{(\theta)} &= \sigma_{22}\sin^2\theta + 2\sigma_{23}\cos\theta\sin\theta + \sigma_{33}\cos^2\theta \\
\sigma_{12}^{(\theta)} &= \sigma_{12}\cos\theta + \sigma_{13}\sin\theta \\
\sigma_{23}^{(\theta)} &= -\sigma_{22}\sin\theta\cos\theta + \sigma_{33}\cos\theta\sin\theta + 2\sigma_{23}\left(\cos^2\theta - \sin^2\theta\right) \\
\sigma_{13}^{(\theta)} &= \sigma_{12}\sin\theta + \sigma_{13}\cos\theta
\end{aligned} \tag{3.67}$$

After finding the fiber-kinking plane and after expressing the stresses in that plane **it is necessary to proceed to another rotation**, this time to have the stresses in the misalignment frame. But first it is necessary to define the angle φ in order to calculate the stress tensor on the $1^{(\varphi)} - 2^{(\varphi)} - 3^{(\varphi)}$ coordinate system. The approach to calculate the misalignment angle φ could be the same used previously for 2D stress states (although in the 3D case new stress components appear related to the direction $3^{(\theta)}$). However, the already presented approach simplifies too much the calculation of the angle φ because it is obtained supposing that the material fails under pure axial compression ($\sigma_{11} = -X_C$ and $\sigma_{ij} = 0$), thus giving $\varphi = \varphi^C$ for all 2D stress states.

For calculating the angle φ Dávila *et al.* [81] used a combination of Argon's approach and LaRC02/03 failure criterion assuming a 2D stress state. Catalanotti [136] used exactly the same approach, so the angle φ is defined using strictly 2D stress components although the failure criterion for compression, which uses the angle φ, is generalized for a full 3D stress state. The author summarized the calculation of φ in the following manner:

The stresses in the local misalignment coordinate frame of Figure 3.18 are:

$$\begin{aligned}
\sigma_{11}^{(m)} &= \sigma_{11}\cos^2(\varphi) + \sigma_{22}\sin^2(\varphi) + 2\,|\sigma_{12}|\sin(\varphi)\cos(\varphi) \\
\sigma_{22}^{(m)} &= \sigma_{11}\sin^2(\varphi) + \sigma_{22}\cos^2(\varphi) - 2\,|\,\sigma_{12}|\sin(\varphi)\cos(\varphi) \\
\sigma_{12}^{(m)} &= (\sigma_{22} - \sigma_{11})\sin(\varphi)\cos(\varphi) + |\sigma_{12}|\left(\cos^2(\varphi) - \sin^2(\varphi)\right)
\end{aligned} \tag{3.68}$$

As already referred, the simplest stress case to model is to consider that the material fails under pure axial compression where the stresses take the values $\sigma_{11} = -X_C$, $\sigma_{22} = \sigma_{12} = 0$, and the misalignment angle comes defined as $\varphi = \varphi_C$. Supposing this stress state and substituting the

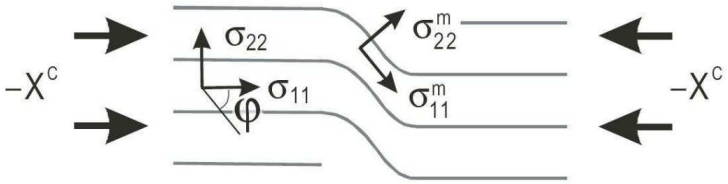

Figure 3.18: Stresses in the misalignment frame (2D). [136]

respective stress components in equation (3.68), the stresses in the misalignment frame are defined by:

$$\begin{aligned} \sigma_{11,C}^{(m)} &= -X_C \cos^2 \varphi_C \\ \sigma_{22,C}^{(m)} &= -X_C \sin^2 \varphi_C \\ \sigma_{12,C}^{(m)} &= X_C \sin \varphi_C \cos \varphi_C \end{aligned} \tag{3.69}$$

where φ_C is the already mentioned angle at the failure when a pure axial compression is applied.

Substituting these stresses in the LaRC02/03 failure criterion it becomes:

$$S_L = X_C \left(\sin \varphi_C \cos \varphi_C - \eta_L \sin^2 \varphi_C \right) \tag{3.70}$$

Equation (3.70) can be solved for φ_C obtaining

$$\varphi_C = \arctan \left(\frac{1 - \sqrt{1 - 4\left(\frac{S_L}{X_C} + \eta^L\right)\frac{S_L}{X_C}}}{2\left(\frac{S_L}{X_C} + \eta^L\right)} \right) \tag{3.71}$$

This was the equation previously presented in Section 3.2.1.5. Nevertheless, in order to calculate φ for a generic stress state the total misalignment angle can be thought as the sum of an **initial constant misalignment angle** φ_0 (that represents the manufacture defects and imperfections in the material) and a γ_m **angle that is originated by the shear loading applied** and depends on the shear constitutive law. For materials that exhibit linear elastic behavior in shear (as fiber reinforced polymers) the shear constitutive law is $\sigma_{12} = G_{12}\gamma_m$. Therefore, at failure under pure axial compression the angle γ_m becomes γ_{mC} and is defined as:

$$\gamma_{mC} = \frac{\sigma_{12,C}^{(m)}}{G_{12}} = \frac{\sin(\varphi_C)\cos(\varphi_C)X_C}{G_{12}} = \frac{\sin(2\varphi_C)X_C}{2G_{12}} \tag{3.72}$$

for less computational cost it can be considered the small angle approximation, $\gamma_{mC} \approx \frac{\varphi_C X_C}{G_{12}}$.

The initial misalignment angle can then be obtained as

$$\varphi_0 = \varphi_C - \gamma_{mC} \tag{3.73}$$

Finally, in order to obtain φ for a generic load case it is necessary to define γ_m because, as already stated [8],

$$\varphi = \varphi_0 + \gamma_m \tag{3.74}$$

where the strain γ_m is obtained solving the equation $\sigma_{12}^m = G_{12}\gamma_m$,

$$\gamma_m = \frac{\sigma_{12}^{(m)}}{G_{12}} = \frac{(\sigma_{22} - \sigma_{11})\sin\varphi\cos\varphi + |\sigma_{12}|\left(\cos^2\varphi - \sin^2\varphi\right)}{G_{12}} \tag{3.75}$$

Defining φ by equation (3.74) and assuming small angle approximation, equation (3.75) becomes

$$\gamma_m = \frac{(\sigma_{22} - \sigma_{11})(\varphi_0 + \gamma_m) + |\sigma_{12}|}{G_{12}} \tag{3.76}$$

Rearranging the equation,

$$\gamma_m = \frac{\varphi_0 G_{12} + |\sigma_{12}|}{G_{12} + \sigma_{11} - \sigma_{22}} - \varphi_0 \tag{3.77}$$

Therefore, the misalignment angle φ has been completely defined. The previous approach was deduced for 2D stress states, so for 3D stress states the stress components used for the calculation of γ_m have to be the ones obtained **after the θ-rotation**. Thus,

[8] In fact the misalignment angle φ is calculated by $\varphi = sgn[\sigma_{12}](\varphi_0 + \gamma_m)$, where $sgn[\sigma_{12}]$ is to extract the signal of the stress component σ_{12}.

$$\gamma_m = \frac{\varphi_0 G_{12} + \left|\sigma_{12}^{(\theta)}\right|}{G_{12} + \sigma_{11}^{(\theta)} - \sigma_{22}^{(\theta)}} - \varphi_0 \tag{3.78}$$

After the definition of the misalignment angle φ it is necessary to define the stress tensor in the misalignment frame. The rotation of the angle φ leads to the following stress tensor,

$$T^{(\varphi)} = R(\varphi) \cdot T \cdot R(\varphi)^T \tag{3.79}$$

where $R(\varphi)$ is the rotation matrix defined as:

$$R(\varphi) = \begin{bmatrix} \cos\varphi & \sin\varphi & 0 \\ -\sin\varphi & \cos\varphi & 0 \\ 0 & 0 & 1 \end{bmatrix} \tag{3.80}$$

Thus, the stresses in the misalignment frame can be expressed by

$$\begin{aligned}
\sigma_{11}^{(\varphi)} &= \sigma_{11}^{(\theta)} \cos^2\varphi + 2\sigma_{12}^{(\theta)} \cos\varphi \sin\varphi + \sigma_{22}^{(\theta)} \sin^2\varphi \\
\sigma_{22}^{(\varphi)} &= \sigma_{11}^{(\theta)} \sin^2\varphi - 2\sigma_{12}^{(\theta)} \cos\varphi \sin\varphi + \sigma_{22}^{(\theta)} \cos^2\varphi \\
\sigma_{33}^{(\varphi)} &= \sigma_{33}^{(\theta)} \\
\sigma_{12}^{(\varphi)} &= -\sin\varphi \cos\varphi \left(\sigma_{11}^{(\theta)} - \sigma_{22}^{(\theta)}\right) + 2\left(\cos^2\varphi - \sin^2\varphi\right)\sigma_{12}^{(\theta)} \\
\sigma_{23}^{(\varphi)} &= -\sigma_{13}^{(\theta)} \sin\varphi + \sigma_{23}^{(\theta)} \cos\varphi \\
\sigma_{13}^{(\varphi)} &= \sigma_{13}^{(\theta)} \cos\varphi + \sigma_{23}^{(\theta)} \sin\varphi
\end{aligned} \tag{3.81}$$

Finally, it is necessary to perform the matrix failure check using equations (3.60) and (3.62), respectively to obtain the Failure Index for Matrix Compression (FI_{MC}) and the Failure Index for Matrix Tension (FI_{MT}). In order to calculate these Failure Indexes it is necessary to define the components of the traction on the fracture plane, these components were already defined in equations (3.57), (3.59) and (3.58), except that this time the stress components of the stress tensor are related to the misalignment frame:

$$\begin{aligned}
\sigma_N^{(\varphi)} &= \sigma_{22}^{(\varphi)} \cos^2\alpha + 2\sigma_{23}^{(\varphi)} \cos\alpha \sin\alpha + \sigma_{33}^{(\varphi)} \sin^2\alpha \\
\tau_T^{(\varphi)} &= -\sigma_{22}^{(\varphi)} \sin\alpha \cos\alpha - \sigma_{23}^{(\varphi)} \sin^2\alpha + \sigma_{23}^{(\varphi)} \cos^2\alpha + \sigma_{33}^{(\varphi)} \cos\alpha \sin\alpha \\
\tau_L^{(\varphi)} &= \sigma_{12}^{(\varphi)} \cos\alpha + \sigma_{13}^{(\varphi)} \sin\alpha
\end{aligned} \tag{3.82}$$

To assess what is the applied Failure Index it is necessary to check if $\sigma_N^{(\varphi)}$ is either positive or negative. If $\sigma_N^{(\varphi)} < 0$ the Failure Index is given by:

$$FI_{KC} = \left(\frac{\tau_L^{(\varphi)}}{S_L - \eta_L \sigma_N^{(\varphi)}} \right)^2 + \left(\frac{\tau_T^{(\varphi)}}{S_T - \eta_T \sigma_N^{(\varphi)}} \right)^2 \tag{3.83}$$

while if $\sigma_N^{(\varphi)} > 0$ the Failure Index is

$$FI_{KT} = \left(\frac{\tau_L^{(\varphi)}}{S_L} \right)^2 + \left(\frac{\sigma_N^{(\varphi)}}{Y_T} \right)^2 \tag{3.84}$$

In conclusion, the Failure Index for Fiber Kinking will assume the value

$$FI_{FK} = \max \{ \max [FI_{KC}], \max [FI_{KT}] \} \tag{3.85}$$

where $\max [FI_{KC}]$ and $\max [FI_{KT}]$ are the maximum values of equations (3.83) and (3.84), respectively, as a function of α.

3.3.2 ABAQUS® UVARM with Failure Criteria for 3D stress states

First of all, it should be justified the choice of implementing the 3D Failure Criteria previously described in a UVARM subroutine. The industry, in general, and aerospace industry, in particular, are very interested in tools that can be applied to solve static and dynamic problems for large and complex structures without consuming too much time. Nowadays it is possible to model accurately the behavior of composite materials, although in a large number of cases the computation cost is extremely large because these kind of models should have the ability to predict intralaminar damage and delamination. The VUMAT previously presented is included in this kind of models that attempt to describe the material behavior as best as possible. On the contrary, the UVARM subroutine is different in a way that it just defines output quantities that are function of any element integration point variable available. Therefore, it is a very fast way of applying Failure Criteria to a linear elastic model, enabling the possibility of identifying "hot spots[9]" in the structure. This is very interesting for a vast majority of practical cases because with this approach it is possible to identify the areas with high stress concentrations in the structure and eventually if a more detailed analysis is needed it is possible to apply the complete (and costly) model, eg., the VUMAT previously described.

Based on the equations outlined above, the UVARM subroutine calculates the following parameters that can be used for post-processing:

Table 3.4: Parameters calculated by the subroutine.

UVARM(1)	FI_{MT}: Failure Index for transverse tensile failure (Matrix Tension)
UVARM(2)	FI_{MC}: Failure Index for transverse compressive failure (Matrix Compression)
UVARM(3)	FI_{FT}: Failure Index for longitudinal tensile failure (Fiber Tension)
UVARM(4)	FI_{FK}: Failure Index for longitudinal compressive failure (Fiber Kinking)
UVARM(5)	α_{MT}: Fracture angle (in degrees) for transverse tensile failure
UVARM(6)	α_{MC}: Fracture angle (in degrees) for transverse compressive failure

The following diagrams were created in order to present the implemented subroutine – Figures 3.19, 3.20 and 3.21.

[9] Stress concentration points.

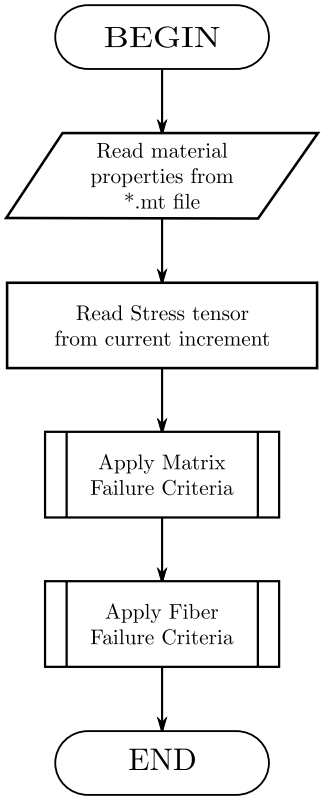

Figure 3.19: Flowchart of the **main program** – UVARM with 3D Failure Criteria.

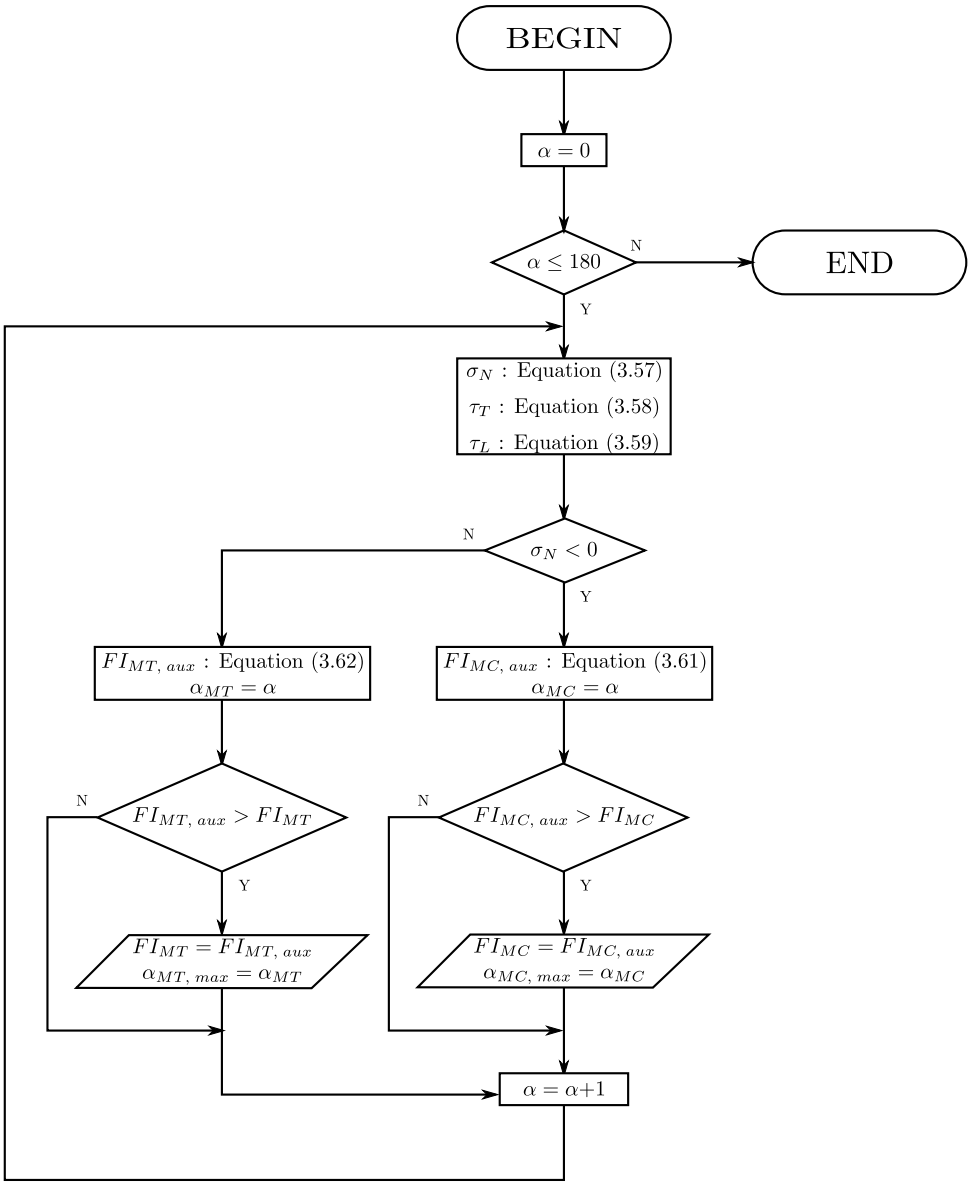

Figure 3.20: Flowchart of the function "**Apply Matrix Failure Criteria**".

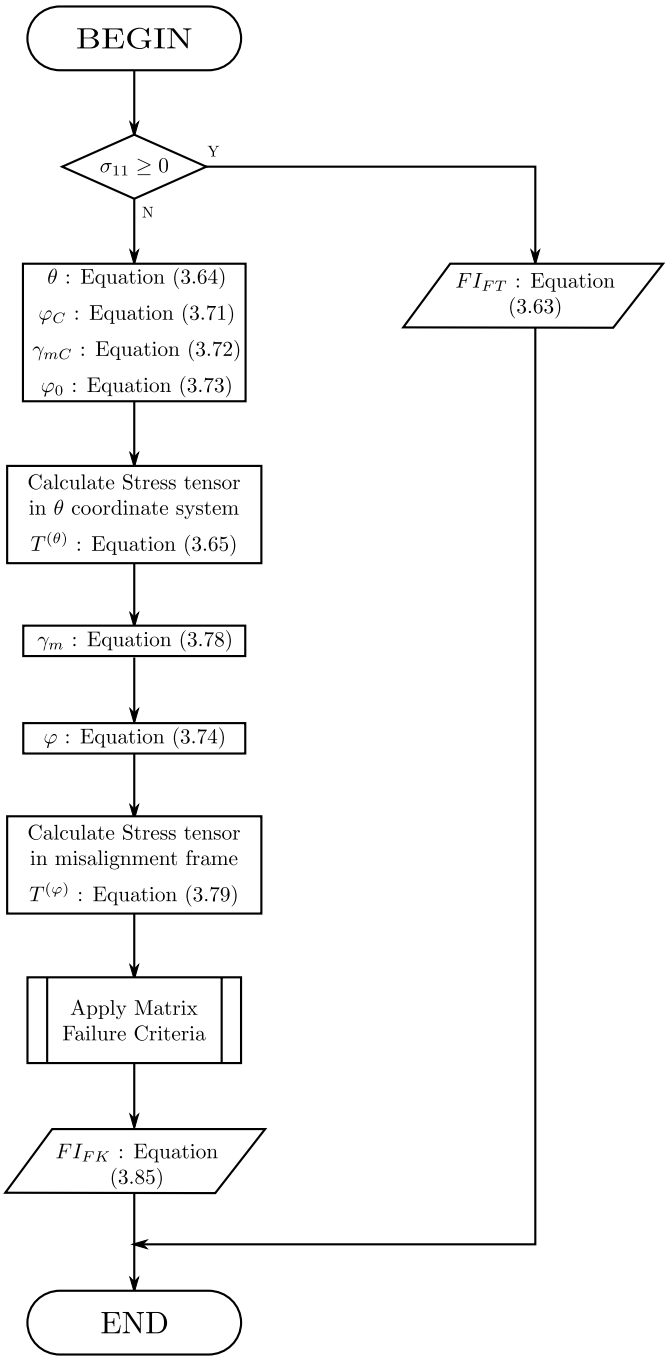

Figure 3.21: Flowchart of the function "**Apply Fiber Failure Criteria**".

In order to finish the presentation of the implemented UVARM it is important to show that the user must create not only the ABAQUS® **jobname.inp** file (where "jobname" can be any suitable name) but also a file with the name **jobname.mt** where the material properties are defined (the file must have the same name as the *.inp file that defines the model and must be placed in the same directory where the ABAQUS® input file is located).

The format of the file jobname.mt is shown in Table 3.5.

Table 3.5: Parameters calculated by the subroutine.

Line	Column					
	1	2	3	4	5	6
1	**					
2	3					
3	**					
4	MATERIAL					
5	**					
6	E_1	E_2	E_3	υ_{21}	υ_{31}	υ_{32}
7	**					
8	G_{12}	G_{23}	G_{31}	X_T	X_C	Y_T
7	**					
9	α_0	S_L	η_L			

The symbol ** means that the corresponding lines can be used to write comments. The name of the material (line 4) must be the same as the one given in the ABAQUS® **jobname.inp** file and must be written in CAPITALS. Lines 3 to 10 can be repeated for the definition of more than one materials. The following is an example of a file with the definition of three materials (this was the *.mt file used in Chapter 5 for analysis and validation of the UVARM subroutine).

```
** LaRC03 failure criteria: use 1 for proposed Failure Criteria (Catalanotti's PhD)
   1
** MAT. #1: IM7-8552-thin: thin embedded ply
   IM7-8552-THIN
** E1     , E2    , E3  , nu21 , nu31 , nu32
   171420., 9080., 9080., 0.017, 0.017, 0.4
** G12 , G23     , G31 , XT    , XC    , YT_is
   5290., 3242.9, 5290., 2323.5, 1200.1, 160.2
** alphao, SL_IS,  eta_L
   53.   , 130.2, 0.4
** MAT. #2: IM7-8552-thin: thin outer ply
   IM7-8552-THIN-OUTER
** E1     , E2    , E3  , nu21 , nu31 , nu32
   171420., 9080., 9080., 0.017, 0.017, 0.4
** G12 , G23     , G31 , XT    , XC    , YT_is
   5290., 3242.9, 5290., 2323.5, 1200.1, 101.4
** alphao, SL_IS, eta_L
   53.   ,  107., 0.4
** MAT. #3: IM7-8552-inner-2t: embedded ply with t=2*ply thickness
   IM7-8552-INNER-2T
** E1     , E2    , E3  , nu21 , nu31 , nu32
   171420., 9080., 9080., 0.017, 0.017, 0.4
** G12 , G23     , G31 , XT    , XC    , YT_is
   5290., 3242.9, 5290., 2323.5, 1200.1, 113.3
** alphao, SL_IS, eta_L
   53.   , 106.9, 0.4
```

The user must define consistent material properties in the **jobname.inp** file, and define six user output variables following the example shown below:

```
*Material, name=IM7-8552-THIN
*Elastic, type=ENGINEERING CONSTANTS
171420.,  9080.,  9080.,   0.32,   0.32,  0.487,  5290.,  5290.
 3242.9,
*User Output Variables
      6,
```

As stated above, in Chapter 5 two ABAQUS® models will be presented as examples of the use of the UVARM subroutine in the prediction of first ply failure of a quasi-isotropic Hexcel IM7/8552 $[90/0/\pm 45]_{3S}$ CFRP laminate with a central hole loaded, respectively, in tension and in compression.

CHAPTER 4

EXPERIMENTAL WORK

4.1 Material Selection and Characterization

The material selected for the present study was the IM7/8552, a unidirectional carbon fiber / epoxy prepreg with a nominal cured ply thickness of 0.125mm. It was supplied by Hexcel as a roll of pre-impregnated tape of epoxy matrix (8552) reinforced by continuous intermediate modulus unidirectional fibers (IM7). This is a high performance composite material for use in primary aerospace structures, it operates in environments up to 121°C.

The prepreg was cut into square sheets of 350mm × 350mm and laid up in a quasi-isotropic stacking sequence: $[90/0/\pm 45]_{3S}$ (total thickness: 3mm). The material was cured in a hot--press according to the manufacturer's specifications [111], with temperature stages of 110°C for 1h, followed by 180°C for 2h. A pressure of 7 bar was applied during the entire cure cycle.

The fiber volume fraction was measured using image processing techniques resulting in an average value of 59.1%. The coefficients of thermal expansion were measured using a dilatometer and the resulting values are $\alpha_{11} = -5.5 \times 10^{-6}$ /°C for the longitudinal direction, and $\alpha_{22} = 25.8 \times 10^{-6}$ /°C for the transverse direction. The elastic properties and strengths were measured using ASTM test standards [112, 113]. Five specimens were used for each test performed.

The mean measured values of the ply elastic properties are shown in Table 4.1. E_1 and E_2 are the longitudinal and transverse Young's modulus respectively, G_{12} is the shear modulus, and υ_{12} is the major Poisson's ratio. Table 4.1 also presents the standard used in each test, the standard deviation (STDV), and the coefficient of variation (CV).

Table 4.1: Measured ply elastic properties for IM7/8552.

Property	Standard	Mean value	STDV	CV (%)
E_1 (GPa)	Ref. [112]	171.42	2.38	1.39
E_2 (GPa)	Ref. [112]	9.08	0.09	1.03
G_{12} (GPa)	Ref. [113]	5.29	0.13	2.53
υ_{12}	Ref. [112]	0.32	0.02	6.18

The measured ply strengths are shown in Table 4.2. X_T and Y_T^{ud} are the longitudinal and transverse tensile strengths, respectively. X_C and Y_C are the longitudinal and transverse compressive strengths, respectively. S_L^{ud} is the in-plane shear strength.

Table 4.2: Measured ply strengths for IM7/8552.

Property	Standard	Mean value (MPa)	STDV (MPa)	CV (%)
X_T	Ref. [112]	2326.2	134.1	5.8
X_C	Ref. [114]	1200.1	145.7	12.1
Y_T^{ud}	Ref. [112]	62.3	5.3	8.5
Y_C	Ref. [114]	199.8	20.5	10.2
S_L^{ud}	Ref. [113]	92.3	0.6	0.7

The values of the transverse tensile strength (Y_T^{ud}) and of the in-plane shear strength (S_L^{ud}) measured in the test specimens correspond to the strengths of unconstrained unidirectional plies. The transverse tensile and shear strengths of constrained plies (in-situ strengths) are higher than those of an unidirectional ply and decrease when increasing the ply thickness. The in-situ strengths are calculated using models proposed by **Camanho *et al.*** [115], which are based on the mode I fracture toughness, $\mathcal{G}_{2+}$, and on the mode II fracture toughness, $\mathcal{G}_6$. In order to clarify the concept of in-situ strength and to know how these strengths were calculated, see **Appendix B**.

To measure the components of the fracture toughness, double cantilever beam (DCB) [116] and 4-point bending end notched flexure (4-ENF) [117] tests were performed. The measured components of the fracture toughness are shown in Table 4.3.

Table 4.3: Measured fracture energies for transverse fracture for IM7/8552 (kJ/m^2).

Property	Mean value	STDV	CV (%)
$\mathcal{G}_{2+}$	0.2774	0.0246	0.88
$\mathcal{G}_6$	0.7879	0.0803	10.19

Using a shear response factor of $\beta = 2.98 \times 10^{-8}\text{MPa}^{-3}$ and substituting the experimentally obtained values for the fracture toughness and ply elastic properties in equations (B.1) and (B.3), the in-situ strengths were calculated – Table 4.4.

Table 4.4: Calculated in-situ strengths for IM7/8552 (MPa).

Ply configuration	Y_T	S_L
Thin embedded ply	160.2	130.2
Thin outer ply	101.4	107.0
Thick ply	98.7	113.1

The shear strength in the transverse direction is calculated as:

$$S_T = Y_C \cos\alpha_0 \left(\sin\alpha_0 + \frac{\cos\alpha_0}{\tan 2\alpha_0} \right) \tag{4.1}$$

where α_0 is the fracture angle of a ply under pure transverse compression. For $\alpha_0 = 53°$, the shear strength in the transverse direction is calculated as $S_T = 75.3\text{MPa}$.

The continuum damage model also requires the fracture energies per unit surface for longitudinal failure, $\mathcal{G}_{1+}$ (tension) and $\mathcal{G}_{1-}$ (compression). **Pinho *et al.*** [118, 119] proposed to measure this energies using the Compact Tension (CT) and Compact Compression (CC) tests in cross-ply laminates. Unfortunately measuring these fracture energies is more complex than the previously referred properties. This will be evidenced in the next point of this work. Nevertheless, the CT and CC tests in cross-ply laminates were made for the IM7/8552 material and the results for the fracture energies per unit surface for longitudinal failure were obtained – Table 4.5.

Table 4.5: Preliminary measurements of fracture energies for longitudinal fracture, $\mathcal{G}_{1+}$ and $\mathcal{G}_{1-}$, for IM7/8552 (kJ/m^2).

Property	Mean value	STDV	CV (%)
$\mathcal{G}_{1+}$	118.0	6.1	7.6
$\mathcal{G}_{1-}$	82.3	2.2	2.1

It is important to highlight that these have to be considered **preliminary results** (specially for the compression case, as will be shown in the next point) because there were encountered similar problems to the ones reported by **Pinho *et al.*** in [119], even though it was used a more sophisticated method to measure the crack resistance curve: the **Digital Image Correlation**

(DIC) using a high speed camera.

At the same time that all the experimental work was being conducted (from the manufacturing process until the actual testing) the proposed numerical model was developed and implemented. Since this is a small time project (approximately 6 months) by the time that all the experimental work was done, the numerical model was ready. This way, **the numerical analysis had to use the preliminary measurements of the the fracture energies per unit surface for longitudinal failure**.

While the numerical analyses were running on FEUP's infrastructure for grid computing, a second batch of CT and CC tests was realized, this time using specimens with a bigger length (the next point will explain the reasons that were believed to lead to better results). Unfortunately, it took a significant amount of time to manufacture, test and (specially) to process all the data collected from the experiments, so the new results for $\mathcal{G}_{1+}$ became available almost at the deadline of the project, and no results for $\mathcal{G}_{1-}$ were obtained.

It should be noted that the measurement of $\mathcal{G}_{1+}$ and $\mathcal{G}_{1-}$ is very important for a correct numerical prediction of the material's behavior using ply properties, and as will be demonstrated further it is believed that they have great influence in the quality of the numerical model's predictions. Therefore, the fact that the available measures of the $\mathcal{G}_{1-}$ are still not reliable can affect the predictions in compression.

In order to summarize all the measured properties that were experimentally obtained and that are necessary for the numerical model, Table 4.6 was created.

Table 4.6: Summary of IM7/8552 ply properties measured by Camanho *et al.*. [23]

Density	1590 kg/m^3
Elastic Properties:	E_1=171.4 GPa; E_2=9.08 GPa; G_{12}=5.29 GPa; υ_{12}=0.32; υ_{23}=0.487
Ply Strengths (MPa):	X^T=2323.5 ; X^C=1200.1 ; Y^T=62.3 ; Y^C=199.8 ; S^L=92.3
Fracture Toughness (kJ/m^2):	$\mathcal{G}_{1+}$=118.0 $\mathcal{G}_{1-}$=82.3 $\mathcal{G}_{2+}$=0.28 $\mathcal{G}_6$=0.79

4.2 Compact Tension (CT) and Compact Compression (CC) tests

As previously referred, the continuum damage model requires the fracture energies per unit surface for longitudinal failure, $\mathcal{G}_{1+}$ (tension) and $\mathcal{G}_{1-}$ (compression). **Pinho *et al.*** [118, 119] proposed the CT and CC tests in cross-ply laminates to measure $\mathcal{G}_{1+}$ and $\mathcal{G}_{1-}$, respectively. Based on these tests, a new methodology to measure the crack resistance curves associated with fiber-dominated failure modes in polymer-matrix composites was used. This method was proposed by **Catalanotti *et al.*** and is described in [128].

Before presenting the experimental procedure, this author wants to express his gratitude to **Hannes Koerber** (PhD student, University of Porto) for the teaching and supervision of the manufacturing procedures of the cross-ply CC and CT specimens; and also to **Giuseppe Catalanotti** (PhD student, University of Porto) and Prof. **José Xavier** (Professor, UTAD) for their help in mounting the equipment and for explaining the principles of their new method to measure crack resistance curves.

The author of this thesis wants to clarify that the following presentation is related to a second set of CT and CC tests, which means that the results obtained for the fracture energies per unit surface for longitudinal failure that will be presented here were not the ones used in the numerical model (because they were obtained shortly before the project deadline). As already stated, the values of $\mathcal{G}_{1+}$ and $\mathcal{G}_{1-}$ that were used to run the numerical analyses to simulate the OHT and OHC tests were obtained in the preliminary CT and CC tests – values shown in Table 4.5.

Two additional notes should be taken:

- it was chosen to present only the experimental part of the CC and CT tests and it will not be presented the new method for the calculation of $\mathcal{G}_{1+}$ and $\mathcal{G}_{1-}$ because the latter is not a product of this thesis. For a detailed description of this interesting new method it is advised to read Catalanotti's article [128];

- the experimental procedure conducted for this work was used and described in the referred article and therefore the next 3 points are obviously common to both works (with minor modifications).

4.2.1 Configuration of the test specimens

The IM7/8552 pre-impregnated plies were laid-up in an $[90/0]_{8s}$ configuration and cured according to Hexcel's specifications. The resulting plates were cut using a diamond-coated disk to their nominal overall dimensions. The specimens were finally machined to their final geometry, shown in Figure 4.1a) for the CT specimen and b) for the CC specimen. Four small square plates made of the same laminate with the dimensions of $15 \times 15\text{mm}^2$ were bonded in the area of the holes for all the CC specimens (two square pieces per hole, in the upper and bottom faces of the specimen). The squares were bonded with Huntsman's Araldite 2011®, and were positioned in the center of the hole in a 45° direction (forming a lozenge), in order to create a quasi-isotropic area around the hole preventing the local plastification that was verified to occur at the first set of tests (in which the preliminary results were obtained). The holes were then drilled through the 2 square plates and the specimen. The holes for the load introduction pins shown in the same figures (the square plates are not represented) were cut using tungsten carbide drills while clamping the specimens between two sacrificial carbon--epoxy plates. This procedure prevents delamination at the entrance and exit of the drill.

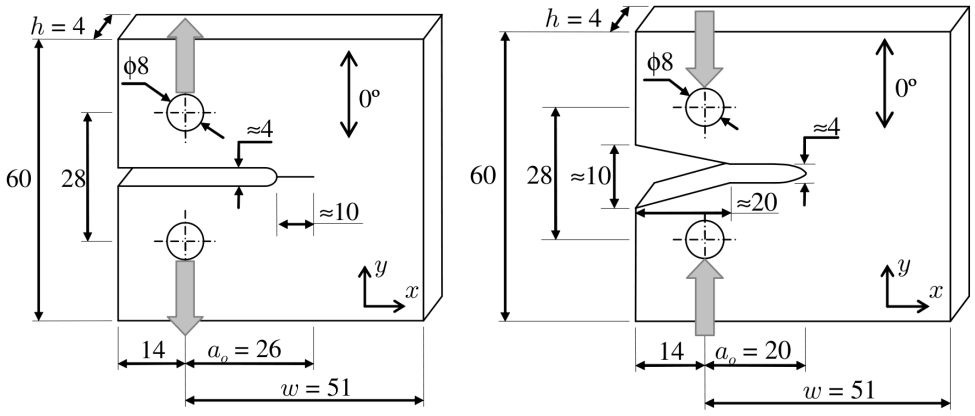

(a) Compact Tension (b) Compact Compression

Figure 4.1: Test specimen nominal dimensions (in mm) for the a) tensile and b) compressive fiber--breaking fracture toughness tests. [119]

The CT and CC tests were conducted using a servo-hydraulic MTS 312.31 test machine with a load capacity of 250kN. The tests were performed using a 100kN load cell and at controlled speed of 2mm/min. Figure 4.2 shows the set-up used during one CT tests. The test specimen was previously sprayed with a white and black ink to generate a random and contrasted distribution of granular spots, as required by the Digital Image Correlation (DIC) system. The

average size of the granular spots was suitable with regard to the resolution necessary for the measurement of the energy release rate.

Figure 4.2: Compact tension test specimen and Digital Image Correlation (DIC) system.

The single-camera ARAMIS digital image correlation software developed by GOM [129] was used. This measurement system is equipped with an 8-bit Baumer Optronic FWX20 camera (resolution of 1624×1236 pixels, pixel size of 4.4μm and sensor format of 1/1.8") coupled with a Schneider-Kreuznach Componar-S 50mm f/2.8 lens. For mobility and adaptability, the camera was mounted on a tripod, which was positioned facing the testing machine. In the set--up, the optical system was positioned perpendicular to the surface of the specimen mounted into the testing machine (Figure 4.2).

A laser pointer was used to facilitate the correct alignment. The working distance (defined between the specimen's surface and the support of the cameras) was set in the range of 0.8m. The lens was adjusted to be in focus with regard to the surface of interest, setting the lens aperture to $f/2.8$ in order to minimize the depth of field. The aperture of the lens was then closed ($f/11$) to improve the depth of field during testing. The shutter time was set to 1/20s, a value appropriate for the cross-head displacement rate used during testing (2mm/min), and the size of the camera unit cells (4.4μm). The light source was finally adjusted in order to guarantee an even illumination of the specimen's surface and to avoid over-exposition (i.e.,

the saturation of pixels over the field of view).

The region of interest was set to approximately 20×20mm^2, which defines a conversion factor of about 0.185mm.pixel^{-1}. In the digital image correlation method, the displacement field is measured by analyzing the geometrical deformation of the images of the surface of interest, recorded before and after loading. For this purpose, the initial (undeformed) image was mapped by square facets (subsets), within which an independent measurement of the displacement is calculated. Therefore, the facet size, on the plane of the object, will characterize the displacement spatial resolution. The facet step (i.e., the distance between adjacent facets) can also be set either for controlling the total number of measuring points over the region of interest, or for enhancing the spatial resolution by slightly overlapping adjacent facets. Typically, a larger facet size will improve the precision of the measurements but also will degrade the spatial resolution [130]. Thus, a compromise must be found according to the application to be handled. In this work, a facet size of 15×315pixels was chosen, attending to the size of the region of interest, the optical system (magnification) and the quality of the granulate (average speckle size) obtained by the spray paint. The facet step was also set to 15×15pixels to avoid statistically correlated measurements. The in-plane displacements were then numerically differentiated in order to determine the strain field needed for the calculation of the J-integral using the procedure previously presented.

4.2.2 Compact tension

A typical load-displacement relation obtained in the CT tests is shown in Figure 4.3. The load was measured using the 100kN load cell, and the displacement was measured using the linear variable differential transformer (LVDT) connected to the hydraulic actuator of the test machine.

Figure 4.3 shows that the load-displacement relation is linear up to approximately 80% of the peak load, and that crack propagation occurs in discrete jumps.

Figure 4.4 [1] shows the R-curve measured from the FEM post-processing of the test results method proposed by **Pinho *et al.*** [119] and were obtained by post-processing the displace-

[1] The legend of the vertical axis has an error in the original paper [128]: G_c units are kJ/m^2 instead of J/m^2. Figures 4.5 and 4.7 contain the same mistake.

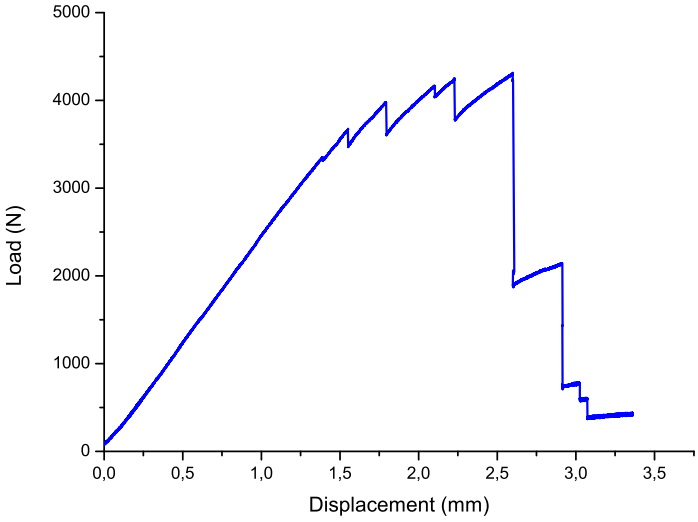

Figure 4.3: Load-displacement in a CT test specimen.

ment and strain fields measured by the DIC system.

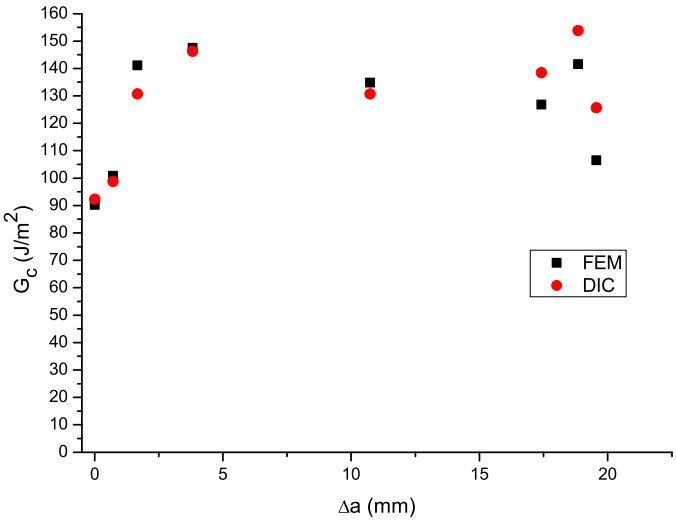

Figure 4.4: R-curves extracted from a CT specimen using FEM and DIC. [128]

Figure 4.4 shows a good correlation between the FEM and DIC data reduction methods. This means that the fracture process zone that bridges the crack has a minor effect on the displacement and strain fields in the regions where the Finite Element model computes the *J*-integral.

Figure 4.5 shows the R-curves obtained from the three CT tests. Figure 4.5 also shows the mean value of the fracture process zone, 3.4mm, and the mean value of the initial fracture toughness and the steady-state crack propagation fracture toughness, **97.8kJ/m^2** and **133.3kJ/m^2** respectively. These values are slightly lower than the mean values of the fracture toughness for initiation and steady-state propagation, 113.8kJ/m^2 and 146.7kJ/m^2 respectively, measured by Pinho [131] for the same material system.

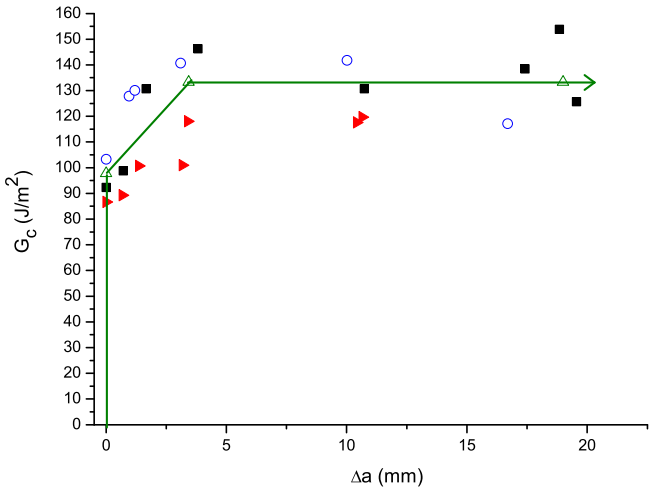

Figure 4.5: R-curves extracted from all CT specimens using DIC, and corresponding mean R-curve. Each symbol corresponds to one CT test. [128]

4.2.3 Compact compression

A typical load-displacement relation obtained from a CC test is shown in Figure 4.6.

Figure 4.7 shows the R-curve measured from the FEM post-processing of the test results obtained by the method proposed by Pinho *et al.* [119] and the R-curve obtained using the DIC data reduction procedure proposed in [128].

Figure 4.7 shows that the FEM-based solution yields unrealistically high values of the fracture toughness during the propagation of fiber kink bands. For 15mm of kink-band propagation the fracture toughness computed using the FEM is approximately twice that calculated using the DIC system. The reason for this fact is that the FEM-based calculation of the *J*-integral does not account for the contact and load transfer across the band of the kinked fibers. These

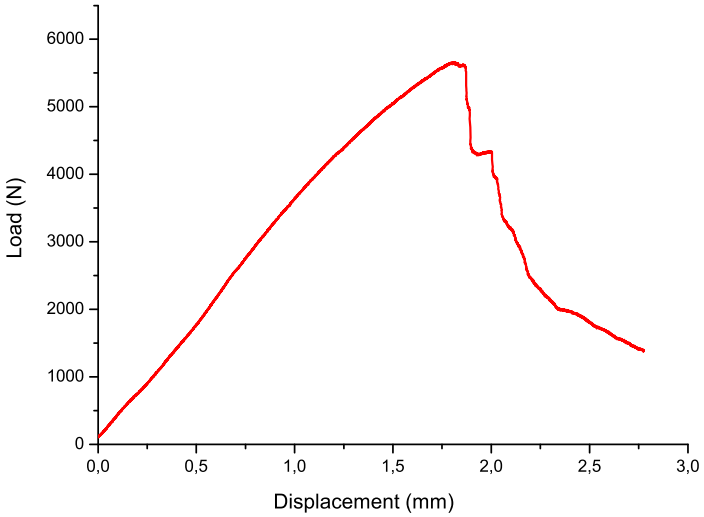

Figure 4.6: Load-displacement in a CC test specimen. [128]

effects clearly affect the displacement and strain fields along the contours of the J-integral computed using FEM. On the other hand, the DIC-based method uses the actual displacement and strain fields on the surface of the specimen, thus providing a more accurate R-curve. However, the contact stresses that are transferred along the kink band still pollute the data obtained using DIC because they introduce one additional term on the left hand side of the J-integral equation (for further detail, consult [128]).

Delamination associated with the propagation of the kink band from the initial notch was also observed in the CC tests. The presence of delamination **renders this test method unsuitable to measure the R-curve in compression** because there is another energy dissipating mechanism apart from those related to the kink band itself. In addition, the presence of delamination invalidates the assumptions of a two-dimensional crack, and of constant strain through the thickness of the laminate (assumption used in the J-integral equation). Delamination was also the reason why the DIC-based method could not detect the tip of the kink band for 2mm$\leq \Delta a \leq$ 11mm. The out-of-plane displacement of the delaminated plies renders the experimental determination of the displacement and strain fields impossible with just one camera. The delamination propagation stopped after 11mm of kink-band propagation, and the identification of its extremity was again possible.

In conclusion, the previously described test method seems to be well suited for determining the $\mathcal{G}_{1+}$ property by a Compact Tension (CT) test but is inadequate for measuring the $\mathcal{G}_{1-}$

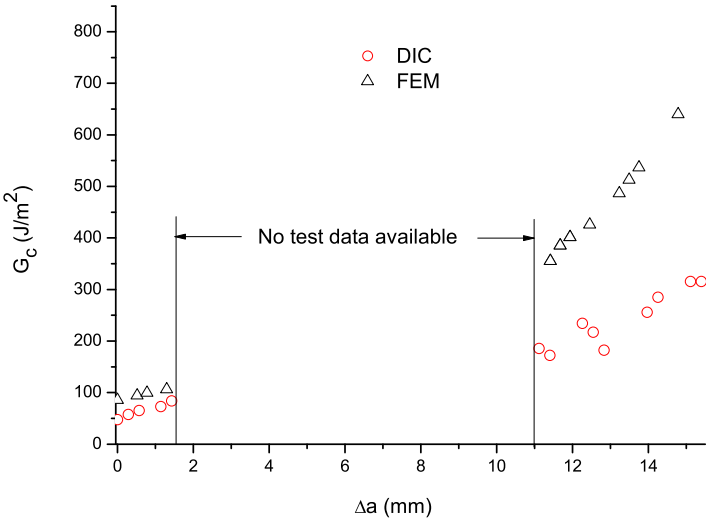

Figure 4.7: R-curves extracted from a CC specimen using FEM and DIC. [128]

property by performing a Compact Compression (CC) test. The up-to-date value of $\mathcal{G}_{1+}$ to be considered in the next analyses is 133kJ/m^2 instead of the 118kJ/m^2 used. However, the value of $\mathcal{G}_{1-}$ that was obtained in a previous CC test (that revealed localized plasticity around the holes and that had a small stable propagation area) is not reliable and further research is necessary to measure a more accurate fracture energy per unit surface for longitudinal compression failure (the currently used value was 82.3kJ/m^2, as was already referred in the previous section).

4.3 Measurement of the Laminate's Fracture Toughness (for the BFS criterion)

The **laminate's fracture toughness is only necessary in this work for the BFS analytical method** for compressive failure prediction (presented in Chapter 2). None of the numerical models previously presented (Chapter 3) needs laminate properties, on the contrary, only ply properties are used.

A series of tests was performed on center-cracked compression and tension specimens to calculate the fracture toughness, K_c and K_t, respectively. The material used was the IM7/8552. These tests are very simple to perform:

1. Two specimens were manufactured for each of the tension and compression tests. The specimens tested in tension had the following nominal dimensions: width – W = 45.0mm, gauge section length – L = 90.0mm, thickness – t = 3.0mm, and center-crack length – $2a$ = 15.0mm. The nominal dimensions of the compression specimen were: width – W = 45.0mm, gauge section length – L = 52.0mm, thickness – t = 3.0mm, and center- -crack length – $2a$ = 15.0mm;

2. After manufacturing the four specimens, they were loaded until failure and the specimens' failure loads were obtained.

Before presenting the calculations of the fracture toughness it is referred that **Soutis and Fleck** [132] showed that the fractured toughness of the T800/924C, with $[(\pm 45/0_2)_3]_S$ lay-up, is independent of the center-crack size. Therefore, for the quasi-isotropic laminate used in the OHC and OHT tests ($[90/0/\pm 45]_{3S}$) the fracture toughness was also considered independent of the crack length, which decreases the number of specimens that need to be tested (only one length of the center-crack was tested).

The test results are listed in Table 4.7, and Figure 4.8 shows a post-failure picture of one specimen for each test type.

Table 4.7: Fracture toughness test results. Material: IM7/8552.

Type of test	Specimen ref.	Failure stress (MPa)
Tension	T1	283.3
	T2	302.0
Compression	C1	198.0
	C2	193.0

(a) Specimen for determining the fracture toughness in tension, K_t.

(b) Specimen for determining the fracture toughness in compression, K_c.

Figure 4.8: Post-failure pictures of the specimens used for determining the fracture toughness in tension and in compression.

After measuring the failure stresses for each test type the fracture toughness is determined by:

$$K_{c,t} = \sigma_{c,t}^{\infty} \sqrt{\pi a} \sqrt{\sec \frac{\pi a}{W}} \tag{4.2}$$

where $\sigma_{c,t}^{\infty}$ is the failure stress in tension (t) or compression (c), a is the center-crack semi--length and W is the laminate width.

Therefore, substituting the real dimensions of the specimens, the fracture toughness in tension and in compression is determined – Table 4.8

Table 4.8: Fracture toughness test results. Material: IM7/8552.

Type of test	Specimen ref.	Fracture toughness, $K_{c,t}$ (MPa. $\sqrt{\text{m}}$)	Average $K_{c,t}$ value (MPa. $\sqrt{\text{m}}$)
Tension	T1	61.0	63.0
	T2	65.0	
Compression	C1	42.6	42.1
	C2	41.6	

Finally, according to Soutis and Fleck [132], the energy release rate for tension ($\mathcal{G}_t^L$) and for compression ($\mathcal{G}_t^L$) are related with the respective stress intensity factor K_t and K_c by:

$$\mathcal{G}_{t,c}^{L} = \lambda K_{t,c}^{2} \tag{4.3}$$

where for plane stress loading, λ is given by **Paris *et. al*** [133]

$$\lambda = \left(\frac{a_{11}a_{22}}{2}\right)^{1/2}\left[\left(\frac{a_{22}}{a_{11}}\right)^{1/2} + \frac{2a_{12}+a_{66}}{2a_{11}}\right]^{1/2} \tag{4.4}$$

$$[a] = \begin{bmatrix} a_{11} & a_{12} & 0 \\ a_{21} & a_{22} & 0 \\ 0 & 0 & a_{66} \end{bmatrix} = \begin{bmatrix} \frac{1}{E_{11}} & -\frac{\upsilon_{12}}{E_{11}} & 0 \\ -\frac{\upsilon_{12}}{E_{11}} & \frac{1}{E_{22}} & 0 \\ 0 & 0 & \frac{1}{G_{12}} \end{bmatrix} \tag{4.5}$$

Substituting the laminates properties the energy release rates become:

$$\mathcal{G}_{\mathbf{t}}^{\mathbf{L}} = \mathbf{61.5\,kJ/m^2} \quad ; \quad \mathcal{G}_{\mathbf{c}}^{\mathbf{L}} = \mathbf{27.5\,kJ/m^2} \tag{4.6}$$

4.4 Open-Hole Compression test

Compressive tests of notched composite laminates were performed to quantify the size effect and to obtain experimental data to validate the analytical and numerical models. Quasi-isotropic laminates were manufactured in Hexcel IM7/8552 CFRP with a stacking sequence of $[90/0/\pm 45]_{3S}$.

Before performing the tests in notched composites, the mean value of the unnotched compressive strength of the laminate, $X_C^{\mathrm{L}} = 532.6$MPa, was measured using five test specimens. The corresponding mean value of the failure strain was $9940\mu\varepsilon$.

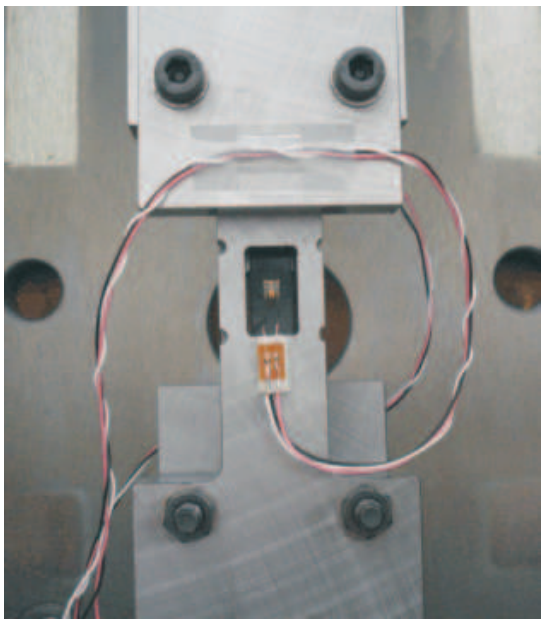

Figure 4.9: Test rig for the OHC specimen.

The notched test specimens were machined using a procedure that prevents delaminations in the regions close to the insertion point and the exit of the drill bit. Sacrificial frontal and backing plates were used to clamp the specimens during the drilling process. All test specimens were machined to class 1 hole quality and no damage was observed in a sample of test specimens inspected using X-rays.

Four different specimens, with hole diameters d=2, 3, 4, 5mm and with a width-to-diameter ratio (w/d) equal to 6, were tested. A MTS servo-hydraulic machine was used following the ASTM D 6484/D 6484M-04 standard [120] according to the test matrix shown in Table 4.9.

Three specimens were tested for each geometry.

Table 4.9: Open-hole compression test matrix.

Specimen ref.	D (mm)	W (mm)	W/D
OHC1	2	12	6
OHC1a	3	18	6
OHC2	4	24	6
OHC2a	5	30	6

One of the OHC1 specimens was instrumented with two strain gages in the positions schematically shown in Figure 4.10 with $d_s = 2.5$mm.

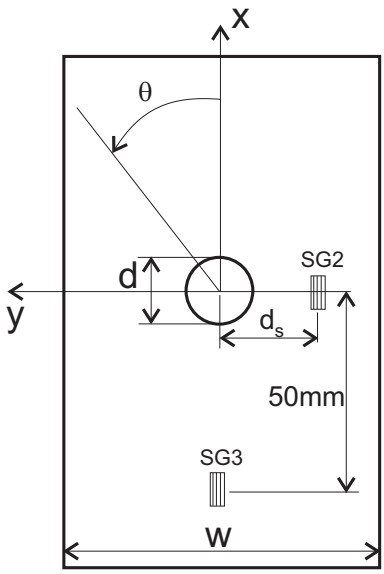

Figure 4.10: Strain gages positioning on the OHC specimen.

The remote failure stress is defined using the failure load measured in the tests ($\overline{P}$) and the measured values of the specimen thickness (t_L) and width (W) as: $\overline{\sigma}^{\infty} = \dfrac{\overline{P}}{W\,t_L}$. The remote failure stresses obtained for the different geometries are summarized in Table 4.10.

Table 4.10: Results of open-hole compression tests.

Hole diameter (mm)	$\overline{\sigma}^{\infty}$(MPa)	STDV (MPa)	CV(%)
2	383.1	18.3	4.8
3	372.9	4.6	1.2
4	365.2	4.8	1.3
5	353.7	2.4	0.7

Figure 4.11 shows the measured relation between the remote stress and the specimen strain measured using the strain gage. The observation of this figure leads to the conclusion that the material has a linear-elastic constitutive behavior.

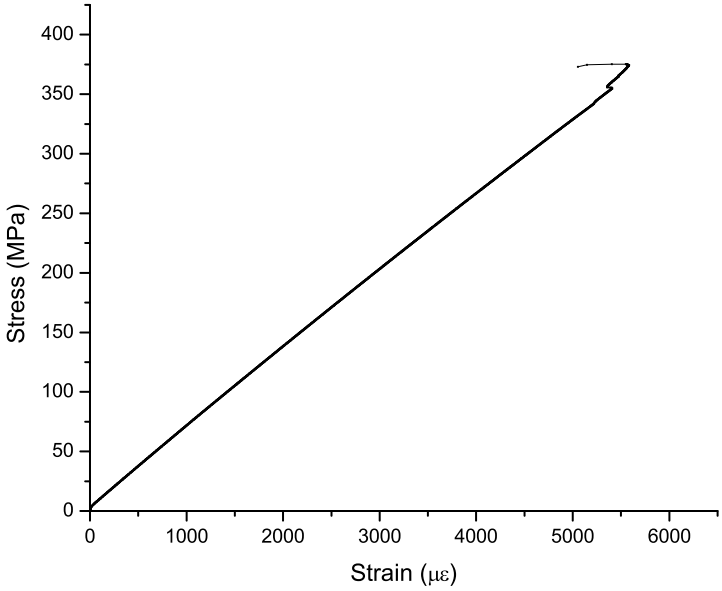

Figure 4.11: Stress-strain curve for the OHC1 specimen.

Figure 4.12 presents the mean values of the failure stresses for the different specimen sizes tested.

From Table 4.10 and Figure 4.12 it is concluded that this laminate with an open-hole presents a hole size effect when subjected to compression, although the decrease in strength is not as significant as the observed in the OHT case. The OHC specimens' strength decreased approximately 7.7% when the in-plane dimensions were scaled by a factor of 2.5.

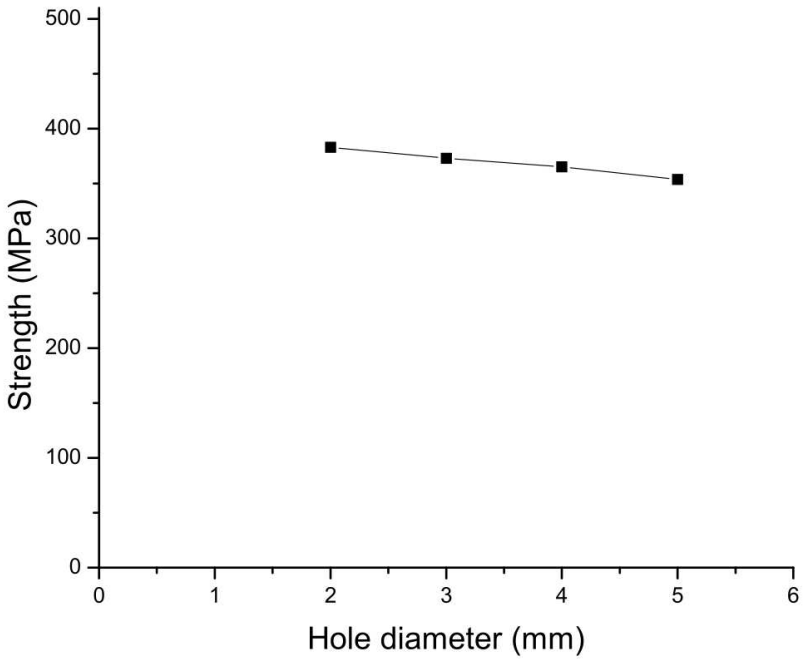

Figure 4.12: Hole size effect in OHC specimens.

CHAPTER 5

ANALYTICAL & NUMERICAL MODELS' ANALYSIS & VALIDATION

In this Chapter it will be made an analysis to the accuracy of the previously presented analytical and numerical methods in predicting the tensile and compressive strength of advanced CFRP for the two most important quasi-static tests performed by aerospace companies: Open--Hole Tension and Compression.

In the first section it will be made a comparison between the different Analytical methods that were described earlier and the experimental results. The second section will start by presenting the validation process of the Numerical model implemented in an ABAQUS® VUMAT subroutine, and subsequently it will present the comparison between the numerical results obtained and the same experimental data considered in the first section.

A third section was added showing the results obtained when applying the 3D Failure Criteria to a linear elastic lamina with an open-hole. Two examples (OHT and OHC) were considered in order to illustrate the practical interest of using the ABAQUS® UVARM subroutine.

5.1 Analytical methods

The analytical methods previously described in Chapter 2 and Section 2.2 were applied to predict the **Open-Hole Tensile and Compressive strength** (the models should be able to predict size effects). The first section of Chapter 2 listed a large amount of experimental results with particular emphasis to OHT and OHC tests. Any of the referred experimental data could be used to assess the accuracy of the analytical methods. It was decided to use the "in-

-house" experimental data collected by **Camanho *et al.*** [23], Table 2.6, and the experimental data obtained with the experimental work performed for this thesis and presented in Chapter 4, Table 4.10.

For simplicity, the mean average tensile and compressive strength obtained in both experimental programs will be presented again:

Table 5.1: Results of Open-Hole Tension [23] and Compression tests. Material: IM7/8552; Width to Diameter ratio: 6.

	Open-Hole Tension	Open-Hole Compression
Hole diameter (mm)	$\overline{\sigma}_t^{\infty}$(MPa)	$\overline{\sigma}_c^{\infty}$(MPa)
2	555.7	383.1
3	–	372.9
4	480.6	365.2
5	–	353.7
6	438.7	–
8	375.7	–
10	373.7	–

5.1.1 Application

It was seen that Equation (2.9) provides the **LEFM** (Linear Elastic Fracture Mechanics) **prediction** for the notched strength of the laminate when all the in-plane dimensions are scaled. This method is extremely simple to apply but leads to inaccurate predictions [23]. One just needs to consider the average failure stress measured in the specimens for a hole diameter within the range of the available diameters (thus, for the OHT it was considered the $d = 6$mm, and for the OHC the $d = 3$mm) and then replace the corresponding values in Equation (2.9). However, due to the fact that this method produces inaccurate predictions and since it were considered several (more advanced) analytical methods this method was not plotted in the figures that summarize all the predictions.

Then, let's start by considering the **Inherent Flaw Model** (IFM) or Waddoups model. Equation (2.13) provides the inherent flaw model prediction of the notched strength. If one considers the specimen with a 6mm hole diameter for predicting the remaining failure stresses of

the OHT test, and the specimen with a 3mm hole diameter for the OHC test, it is possible to calculate the length of the inherent flaw for each of these cases. Using the respective measured mean failure stresses in Equation (2.13), the length of the inherent flaw is calculated as $a = 1.28$mm for the OHT, and $a = 1.56$mm for the OHC. Therefore, after determining the parameter a and knowing the unnotched tensile and compressive strength of the laminate, $X_T^L = 845.1MPa$ and $X_C^L = 532.7MPa$, it is possible to predict the failure stresses for the remaining hole diameters for both tests by applying once again Equation (2.13).

The **Point-Stress Model** (PSM) prediction of the size effect is performed using equation (2.5). This method was applied with two different approaches. In one approach it is considered that the ultimate failure occurs when the stress at a given distance from the hole boundary, r_{ot} or r_{oc}, reaches the unnotched strength of the laminate, $X_T^L = 845.1$MPa and $X_C^L = 532.7$MPa. In the other approach the point stress model uses the ply stresses and strengths, so that it is not necessary to measure the strength for every different laminate. Thus, two characteristic distances are obtained with the first approach by using the measured mean failure stress in the respective tension and compression specimens (tension: $d = 6$mm; compression: $d = 3$mm), and other two characteristic distances come from the same analysis but this time considering the ply mean failure stress (PSM applied to the 0° plies). Using the laminates properties (PSM – laminate), the characteristic distances calculated were $r_{ot} = 0.84$mm (tension case) and $r_{ot} = 0.98$mm (compression case). Considering the 0° ply properties (PSM – 0° plies) the characteristic distances obtained were $r_{ot} = 0.75$mm and $r_{oc} = 1.45$mm. These values of the characteristic distances are used to predict the strength of the other specimens.

Finally, it was used the **Budiansky-Fleck-Soutis** (BFS) compressive criterion. This is a more advanced analytical method that was **specifically developed for OHC tests**. Nevertheless, the method was applied to the OHT test in order to evaluate what kind of performance should be expected for the BFS criterion when applied to this test[1]. **Sutcliffe *et al.*** [139] created an interesting PC software design tool to quickly predict the failure strength of FRP for some predefined geometries: **Composite Compressive Strength Modeller** (CCSM). This software was used[2] exclusively to determine the OHC and OHT compressive and tensile strength, respectively.

[1] Again, it is referred that this method was developed **only** for the compressive case!

[2] The author of this thesis wishes to express his gratitude towards Prof. Sutcliffe for sharing the CCSM computer software.

Next section shows the predictions of the normalized strength as a function of the hole diameter obtained using the different models.

5.1.2 OHT analytical predictions

Table 5.2 and Figure 5.1 summarize the results obtained for the OHT test.

Table 5.2: Comparison between the Analytical and Experimental OHT strength results.

Spec. ref.	**Experim.** [MPa]	**PSM** (laminate) [MPa]	Diff. [%]	**PSM** (0° plies) [MPa]	Diff. [%]	**IFM** [MPa]	Diff. [%]	**BFS** [MPa]	Diff. [%]
OHT11	555.7	639.7	15.1	645.7	16.2	627.8	13.0	616.5	10.9
OHT10	480.6	505.7	5.2	501.2	4.3	505.8	5.2	560.5	16.6
OHT3	438.7	438.7	0.0	438.7	0.0	438.7	0.0	510.7	16.4
OHT6	375.7	400.7	6.7	398.1	6.0	398.3	6.0	470.9	25.3
OHT9	373.7	376.6	0.8	380.2	1.7	371.8	-0.5	440.2	17.8

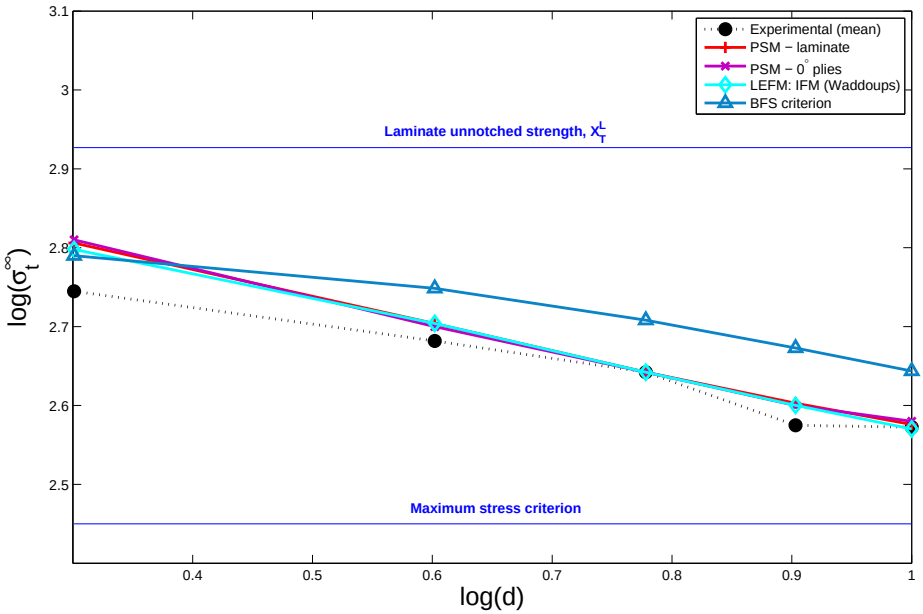

Figure 5.1: Analytical predictions of size effects in CFRP plates with an open-hole loaded in tension. $w/d = 6$.

It can be observed that the **BFS** criterion clearly is not suited for OHT strength prediction. This was expected due to the fact that this model was developed exclusively for the com-

pression case. The error obtained in the prediction for the specimen with the smallest hole diameter was 10.9% and for the largest one was 17.8%. The maximum error calculated was 25.3% (d = 8mm). Obviously these results are completely unacceptable.

Apart from the BFS criterion, the remaining two methods (the **PSM** and **LEFM-IFM**) can predict with reasonable accuracy the size effect law of notched composite laminates in tension. The point stress and inherent flaw models are particularly accurate for specimens with hole diameters close to the diameter used to calculate the characteristic distance (PSM) and the length of the inherent flaw. For specimens with small hole diameters, the predictions lose accuracy. Therefore, to accurately predict the notched strength of laminates these models require the calculation of the characteristic distance and length of inherent flaw for different geometries, and the definition of an extrapolation procedure to define the values of these parameters for other geometries. It should also be noted that the basic equation used in the inherent flaw model, equation (2.13), is only valid when finite width effects are negligible, which is the case of the specimens tested. For smaller ratios between the specimen width and hole diameter, the inherent flaw model should be modified.

Analyzing the two **PSM** model variations, it is concluded that the application of the point stress method to the 0° plies does not lead to an accuracy loss. This is interesting because it permits the usage of PSM without the need of measuring the tensile strength for every laminate. Nevertheless, it should be noted that this is only valid for laminates in which the fiber fracture of the 0° plies leads to the laminate failure. If other failure modes contribute to the global laminate failure (for instance, delamination) the method loses accuracy.

The **Maximum Stress Criterion** for longitudinal tensile failure is unable to predict size effects and always underpredicts the strength of notched laminates. For a hole diameter of 2 mm, the application of the maximum stress criterion results in an error of -49.1%. The error associated with the strength of materials approach is even larger when using a failure criterion for transverse (matrix) cracking, which occurs before fiber fracture, or failure criteria that are unable to distinguish fiber and matrix failure modes [23].

5.1.3 OHC analytical predictions

For the OHC case, the predictions are presented in Table 5.3 and Figure 5.2.

Table 5.3: Comparison between the Analytical and Experimental OHC strength results.

Spec. ref.	**Experim.** [MPa]	**PSM** (laminate) [MPa]	Diff. [%]	**PSM** (0° plies) [MPa]	Diff. [%]	**IFM** [MPa]	Diff. [%]	**BFS** [MPa]	Diff. [%]
OHC1	383.1	421.5	10.0	407.9	6.5	414.7	8.2	392.6	2.5
OHC1a	372.9	372.9	0.0	372.9	0.0	372.9	0.0	376.7	1.0
OHC2	365.2	337.6	-14.1	343.1	-6.1	340.5	-6.8	360.9	-1.2
OHC2a	353.7	311.6	-11.9	318.4	-10.0	315.4	-10.8	345.7	-2.3

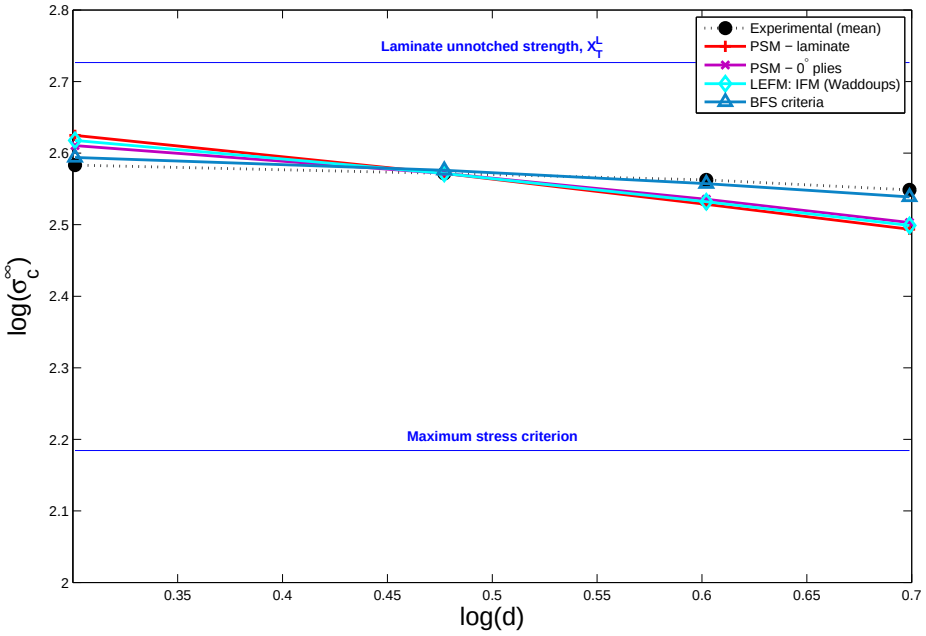

Figure 5.2: Analytical predictions of size effects in CFRP plates with an open-hole loaded in compression. $w/d = 6$.

The **BFS** compressive failure criterion prediction is impressive. The maximum error obtained was 2.5% for the smallest specimen. When this model was presented, it was mentioned that it gives an accurate prediction of the failure load for **0° dominated laminates**, like the one used in the experimental work. If the laminates are composed manly of off-axis plies, since the damage at the edge of the hole is more diffuse in nature, the model loses accuracy. So, although the BFS model is not a general method of predicting the FRPs' compressive strength, it is well suited for various laminates.

Figure 5.2 also shows that the **PSM** and **LEFM-IFM** originate quite similar predictions,

similarly to what was observed for the tension case. These models can predict with reasonable accuracy the compressive strength. It is noted that the PSM applied to the 0° plies produces better results than the PSM applied to the laminate and even than the IFM model. This fact supports the accuracy observed in the the BFS model because it highlights the importance of the 0° fibers' fracture in the whole laminate failure.

Once again, the **Maximum Stress Criterion** revealed unable to accurately predict the strength of notched laminates.

5.2 ABAQUS® VUMAT numerical model

After implementing the numerical model with damage, shear plasticity and delamination in an ABAQUS® VUMAT subroutine, the validation process was initiated. Next section will briefly present that process and the subsequent section will show the subroutine's results for the prediction of the laminate's strength.

5.2.1 Validation

The complete validation procedure of a complex numerical model is a long process. The following is a preliminary procedure and not a complete demonstration of the subroutine's capabilities for all kinds of geometries and loads. Nevertheless, the successful accomplishment of these preliminary tests is imperative. The test consisted in running the subroutine in order to obtain the **uniaxial response** for a single element model subjected to:

- Longitudinal Tension and Compression;
- Transverse Tension and Compression;
- In-plane Shear.

Figure 3.13 (Chapter 3) showed the expected results that one should obtain when using the VUMAT for each loading case. Figure 5.3 presents the longitudinal stress-stain curve for (a) compression and (b) tension. The response is linear-elastic until damage evolves according to a bi-linear law, exactly as the theoretical curve of Figure 3.13(a).

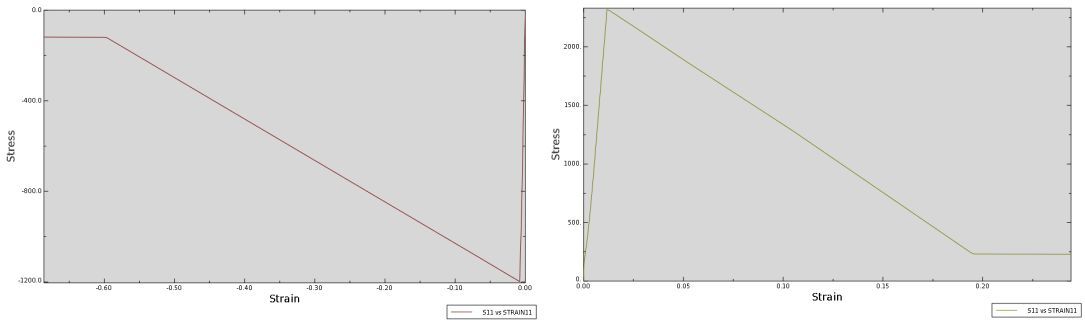

(a) Longitudinal compression (b) Longitudinal tension

Figure 5.3: Uniaxial response of a single shell element: longitudinal direction.

Figure 5.4 shows the transverse stress-strain curve under (a) compression and (b) tension. Observing these figures it is possible to conclude that the softening law for transverse matrix failure has the correct shape: linear (as was previously presented by Figure 3.13(b) in Chapter 3).

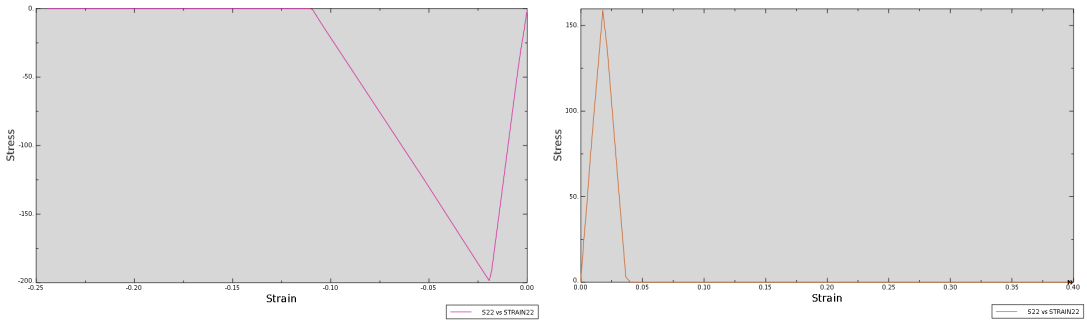

(a) Transverse compression (b) Transverse tension

Figure 5.4: Uniaxial response of a single shell element: transverse direction.

Finally, the in-plane shear curve obtained with the implemented VUMAT is shown in Figure 5.5. As expected, the response is linear until S_{LP}, where elasto-plastic response is activated, and then (after the ply strength is exceeded) damage evolves according to a linear softening law. The slope of the softening law is determined to dissipate the correct energy, i.e. the area under the stress-strain curve is the corresponding fracture toughness divided by the finite element characteristic length: G_C/l. [134]

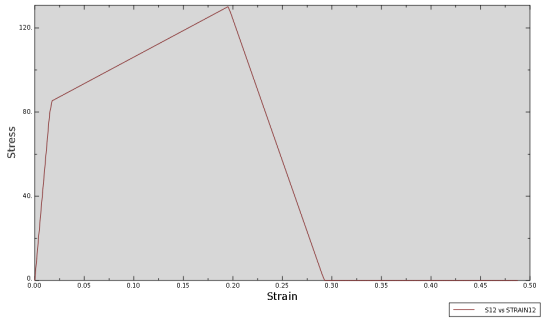

Figure 5.5: Uniaxial response of a single shell element: shear direction.

The VUMAT subroutine is available for **shell elements** and for **3D elements**, therefore it was performed the validation for both types of elements: S4R (4 noded shell element with reduced integration) and C3D8R (8 noded continuum element with reduced integration). It were already shown the results for the shell element in Figures 5.3, 5.4 and 5.5. The results obtained for the 3D element were the same, so there is no need to repeat the figures.

A final note concerning the results of the validation process should be added. The second slope of the longitudinal response is almost horizontal – Figure 5.3. The reason for this is explained by the values of the material properties that were chosen. The value that was chosen for the start point of the second linear curve was very small (just 10% of the longitudinal tension strength, X_T) which is a very low value. On the other hand, the fracture toughness in longitudinal direction used was deliberately high, which implies that the second slope of the linear curve has to be very small in order to guarantee the correct energy dissipation (that has to be independent from the size of the element). This was a way of assuring that the bi-linear law was clearly visible.

5.2.2 Pre-processing the ABAQUS® models of the OHT & OHC specimens

To avoid further enlargement of this thesis, specific details of the pre-processing process will not be addressed. Two models were created for each specimen geometry:

1. **Non-Structured mesh**: this model uses one **3D solid element per ply thickness** that simulate intralaminar damage and plasticity using the VUMAT subroutine previously described, and **3D cohesive elements within each ply** simulating the resin rich part that separates each ply (these elements were 0.01mm thick). The cohesive elements were formulated by **Gonzalez et al.** [127]. It is called a "non-structured mesh" due to the fact that the elements are not oriented according to the fibers' direction, which means that the elements have all the same orientation;

2. **Structured mesh**: this model uses the same 3D element and subroutine for intralaminar simulation but a **cohesive surface** was used instead of 3D cohesive elements. An ABAQUS® 6.8.3 default cohesive surface was chosen. The usage of a cohesive surface enables the possibility of orienting the 3D solid elements according to the fibers orientation. On one hand this is expected to improve the numerical predictions, on the other hand creating a structured mesh has the disadvantage of consuming much more time[3] (specially if one does not use a powerful pre-processor). ABAQUS' necessary parameters for the ABAQUS cohesive surface that were used are: '**Elegibility=Original Contacts**' to restrict cohesive behavior to only those nodes of the slave surface that are

[3] The author wants to acknowledge Dr. Claudio Lopes for his huge support in the creation of the structured mesh.

in contact with the master surface at the start of a step; '**Type=Uncoupled**' to uncouple the traction-separation behavior which means that pure normal separation by itself does not give rise to cohesive forces in the shear directions, and that pure shear slip with zero normal separation does not give rise to any cohesive forces in the normal direction. The properties considered were [140]: $K_{nn} = K_{ss} = K_{tt} = 1e6$. The Damage Initiation criterion considered was based on the maximum nominal stress criterion for cohesive elements (properties used [140]: 62.3MPa for the Maximum nominal stress in the normal-only mode; 92.3MPa for the Maximum nominal stress in the first shear direction; and 92.3MPa for the Maximum nominal stress in the second shear direction). The Damage Evolution was defined using fracture energies, a linear softening law and the fracture energy was specified as a function of the mode mix by means of the Benzeggagh-Kenane mixed mode fracture criterion (properties used are listed in Chapter 4: 0.28 kJ/m^2 for the Normal mode fracture energy; 0.79 kJ/m^2 for the Shear mode fracture energy for failure in the first shear direction; and 0.79 kJ/m^2 for the Shear mode fracture energy for failure in the first shear direction).

Figure 5.6 shows the non-structured mesh and geometry of one of the open-hole specimens that was used.

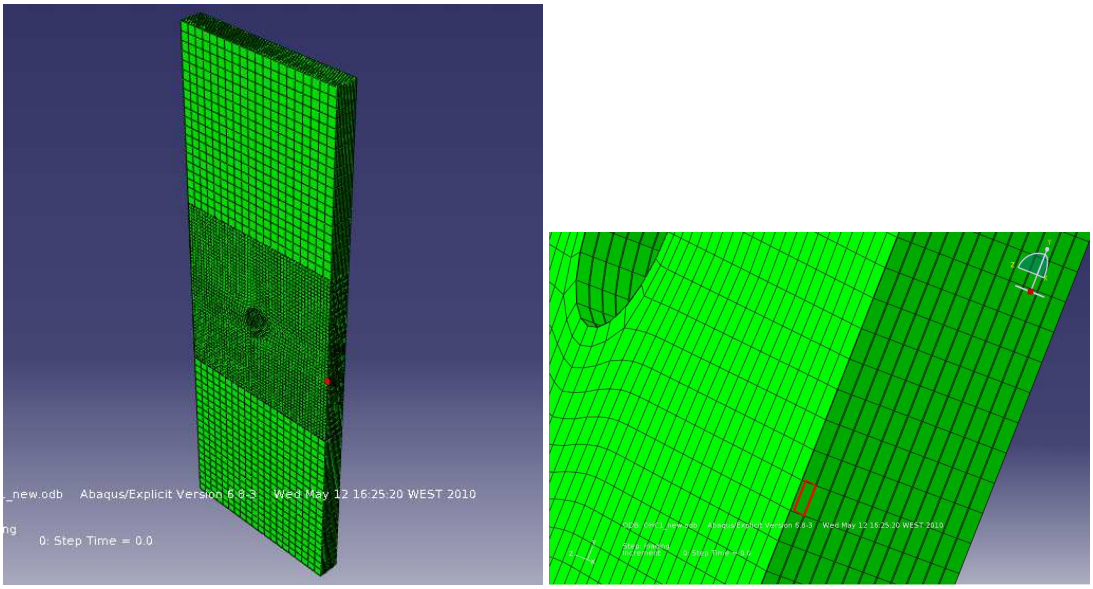

(a) Entire specimen (one 3D cohesive element is highlighted).

(b) Close-up of the highlighted cohesive element.

Figure 5.6: ABAQUS open-hole model: Non-Structured mesh.

In order to illustrate the concept of structured mesh the following figures are presented:

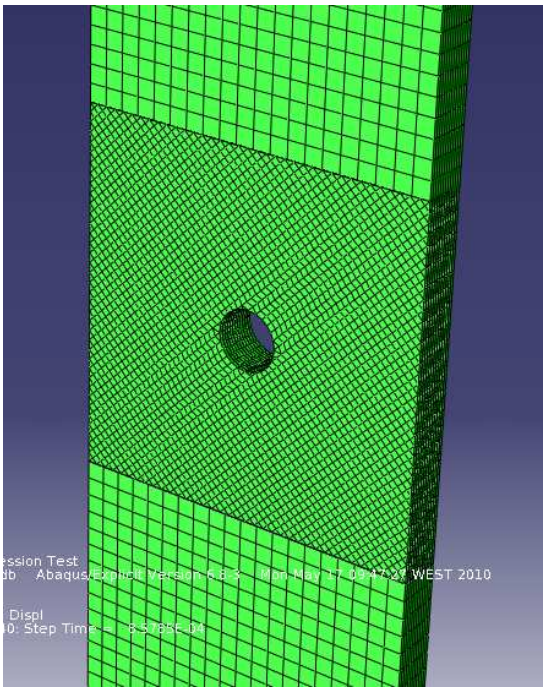

(a) Entire specimen (In the picture: the upper layer corresponds to a 45° ply).

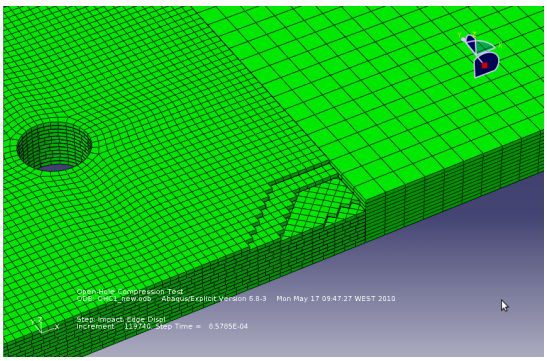

(b) Detail showing the 1st four plies.

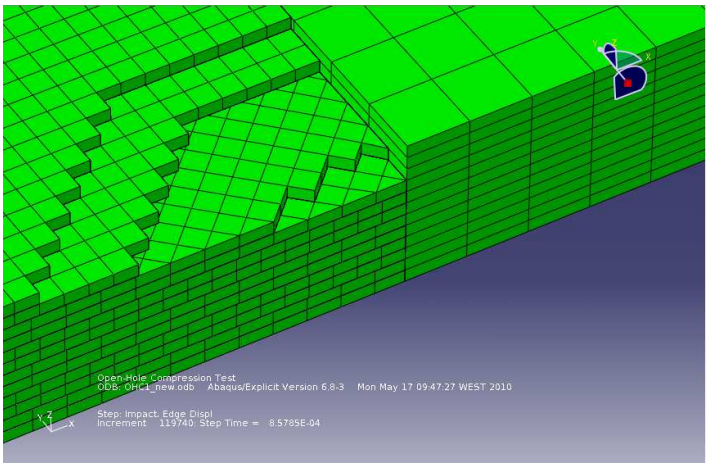

(c) Close-up of the detail. From top to bottom: 90°, 0° and ±45°.

Figure 5.7: ABAQUS open-hole model: Structured mesh.

The remaining details of the pre-processing will be omitted. As a final note, it is referred that the specimen was loaded defining the velocity at one of the ends, and it was clamped at the other end. A smooth first step for the velocity was considered in order to avoid dynamic loading (recall that the model was applied in an Explicit code).

5.2.3 OHT test: VUMAT's numerical predictions

Table 5.4 and Figure 5.8 summarize the results obtained for the prediction of the tensile strength of the OHT test.

Table 5.4: Comparison between the Numerical and Experimental OHT strength results.

Specimen ref.	Experimental (MPa)	Numerical (Non-Structured) (MPa)	Diff. (%)	Numerical (Structured) (MPa)	Diff. (%)
OHT11	555.7	560.7	0.9	566.1	1.0
OHT10	480.6	491.5	2.3	473.2	-1.5
OHT3	438.7	433.9	-1.1	432.2	-1.5
OHT6	375.7	416.5	10.9	399.1	6.2
OHT9	373.7	395.6	5.9	388.6	4.0

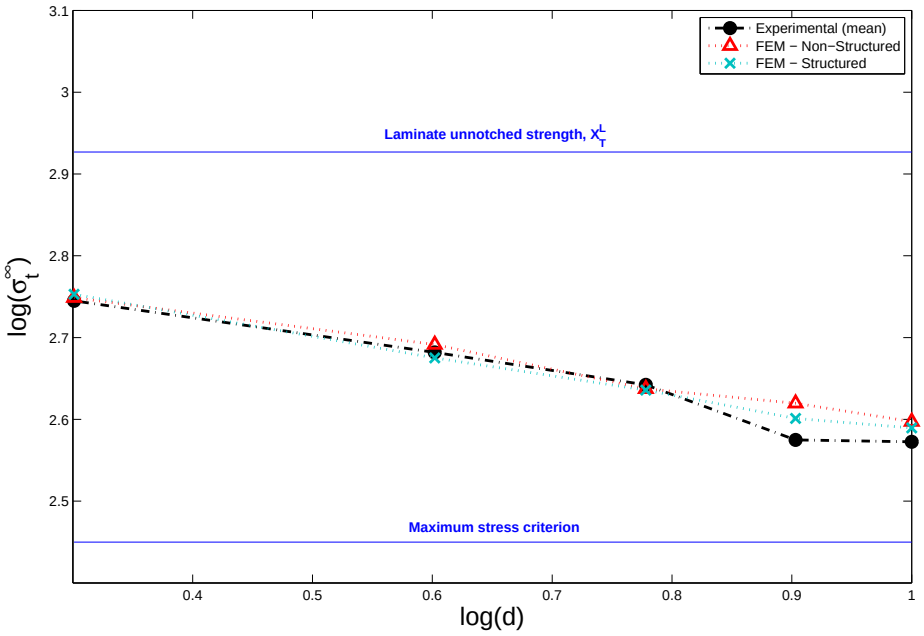

Figure 5.8: Numerical predictions of size effects in CFRP plates with an open-hole loaded in tension. $w/d = 6$.

It is observed that the numerical model can accurately predict the tensile strength of all the OHT specimens for both types of meshes, except for the OHT6 (d = 8mm) which has a sharp drop. This could be more critical if the prediction for the OHT9 was inaccurate, which is not the case. More importantly, the structured mesh predicts a bigger decrease for the strength of

the OHT6 specimen, following the real experimental behavior.

These results are encouraging for two reasons:

1. The strength prediction is very accurate;
2. The usage of a time consuming and more complex mesh (Structured) did not result in a big improvement in the accuracy because the latter was already good. These are obviously good news for a possible future usage of the code in practical design problems.

The first step to assess the quality of the numerical model in OHT strength prediction is completed. However, an exceptional model has to be able to predict not only the peak load but also the damage onset and evolution. At this particular point the experimental program was not useful due to the unpractical geometry of the test rig and the consequent inaccessibility to follow the damage progression. Nevertheless, in the next pictures it will be shown the damage progression for the 3 types of plies present in the laminate: 90°, 0° and 45°.

90° layer

For the 90° layer the damage (d_2) initiates at approximately 60% of the peak load. Then, there is damage propagation until the damage reaches values near 1 at the peak load. Shortly after the peak load the damage starts to progress from the edges due to the free edge effect. There is no significant difference between the results obtained with the Non-Structured and Structured meshes, which was expectable due to the fact that at 90° (and 0°) the structured mesh has the same orientation of the non-structured one. Figure 5.9 and 5.10 show the damage evolution for the OHT11 non-structured and structured meshes, respectively.

0° layer

For the 0° layer it is important to check two damage variables: d_1 and d_2. The first is obviously needed to check for fiber rupture and fiber pull-out. The second, to check if there is matrix cracking and fiber splitting. However, to avoid an overflow of pictures the d_2 ones will not be presented because no significant matrix cracking and fiber splitting were found. Figure 5.11 (non-structured) and Figure 5.12 (structured) present the damage onset and evolution in the longitudinal direction. It is interesting to observe that for the case of the 0° plies shortly after

the peak load is reached the laminae fails. This is in accordance with the fact that for this laminate the role played by the 0° layers is extremely important.

45° layer

For the 45° plies it is necessary to check the d_6 damage variable for the Non-Structured mesh (because it is not oriented with the direction of the fibers) and d_1 or d_2 for the Structured mesh. The observation of Figure 5.13 (non-structured) and Figure 5.14 (structured) leads to the conclusion that the 45° layers play a smaller role in the damage propagation. For the Structured case it is just presented the d_2 variable because the d_1 was not activated, meaning that the 45° plies failed by matrix cracking and delamination, instead of fiber rupture (which is expected to happen in reality).

It is curious to verify that even for the case of the 45° layers the difference between the results obtained with the Structured mesh and the Non-Structured is small.

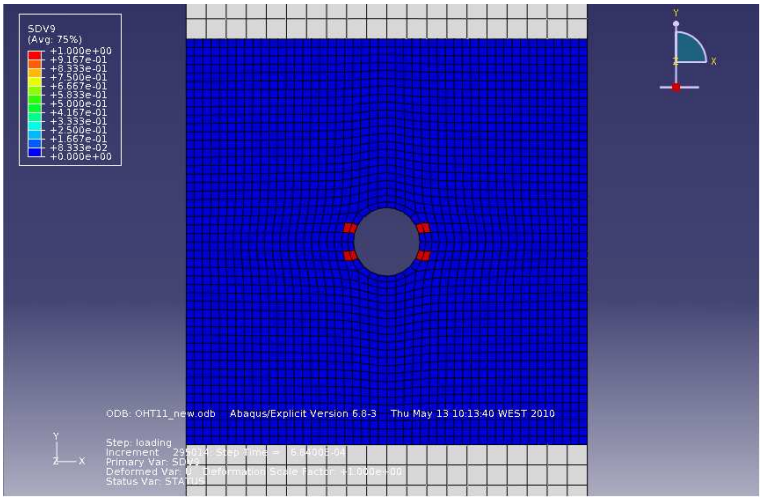

(a) Damage initiation at ≈ 60% of the peak load.

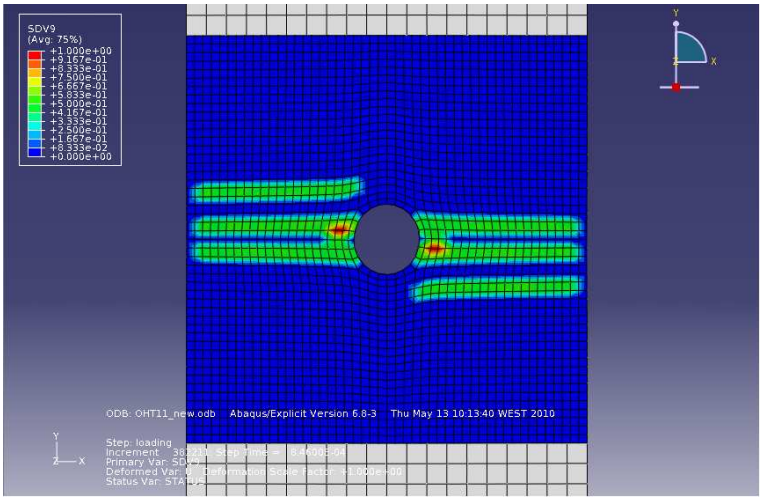

(b) Damage at the peak load.

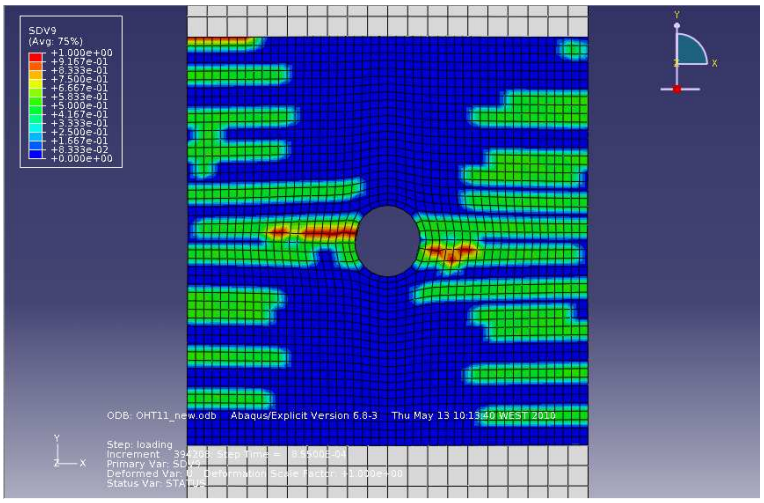

(c) Damage shortly after the peak load (note the free edge effect).

Figure 5.9: Non-Structured mesh: d_2 Damage onset and propagation for the top 90° ply.

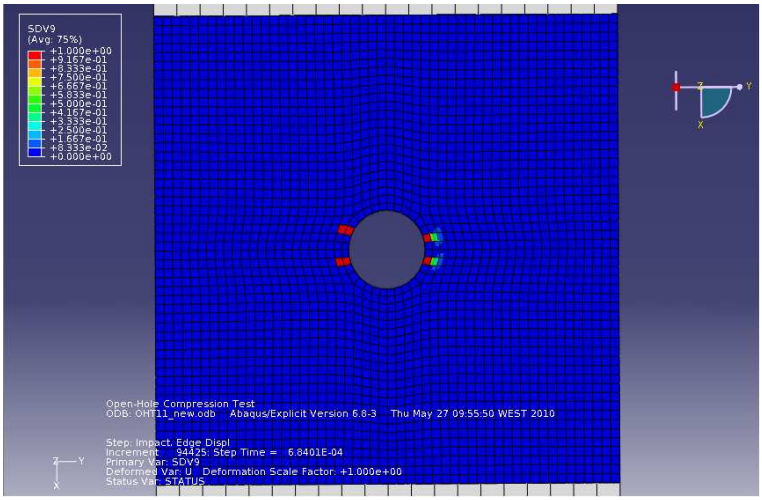

(a) Damage initiation at ≈ 60% of the peak load.

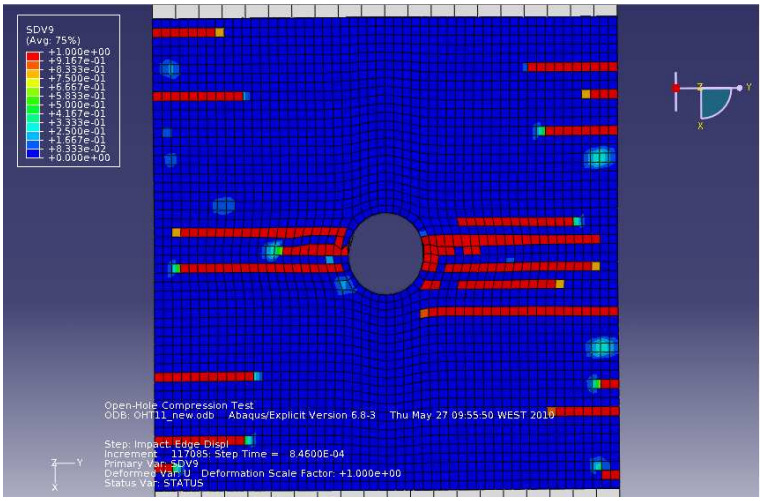

(b) Damage at the peak load.

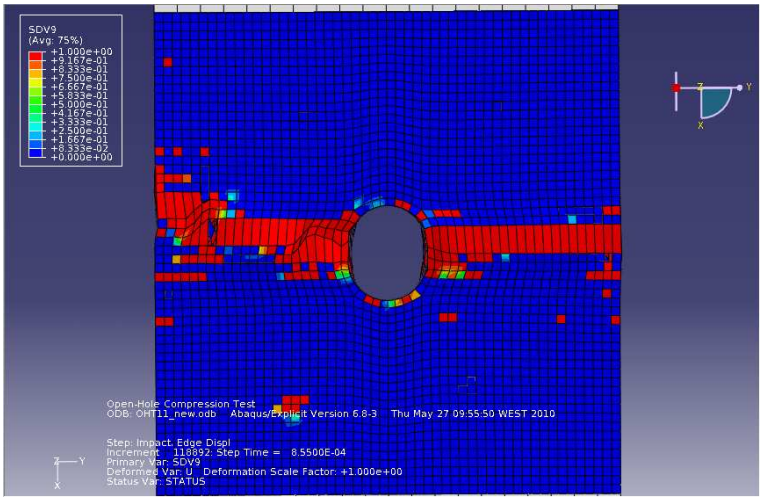

(c) Damage shortly after the peak load (note the free edge effect).

Figure 5.10: Structured mesh: d_2 Damage onset and propagation for the top 90° ply.

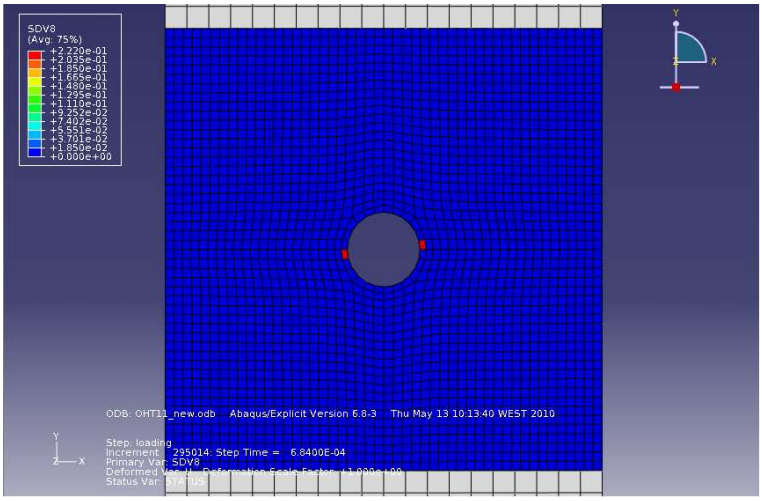

(a) Damage initiation at ≈ 60% of the peak load.

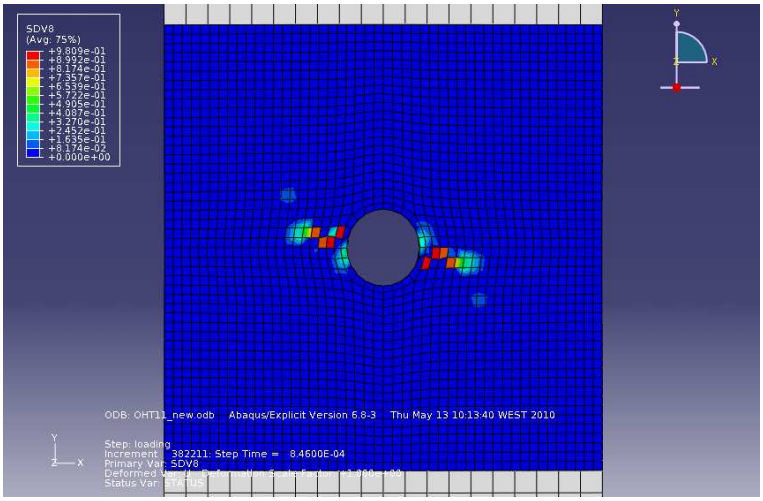

(b) Damage at the peak load.

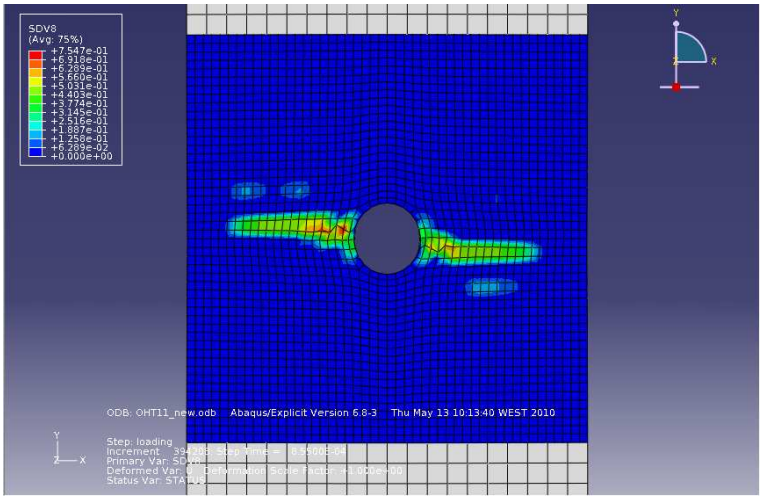

(c) Damage shortly after the peak load.

Figure 5.11: Non-Structured mesh: d_1 Damage onset and propagation for a 0° ply.

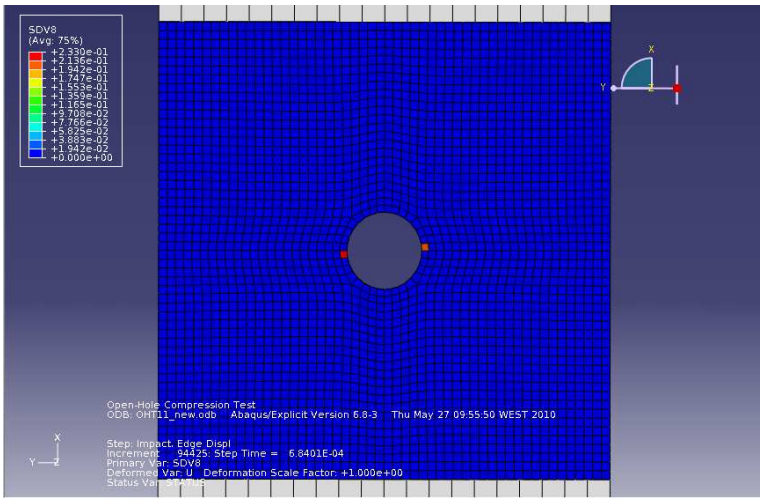

(a) Damage initiation at ≈ 60% of the peak load.

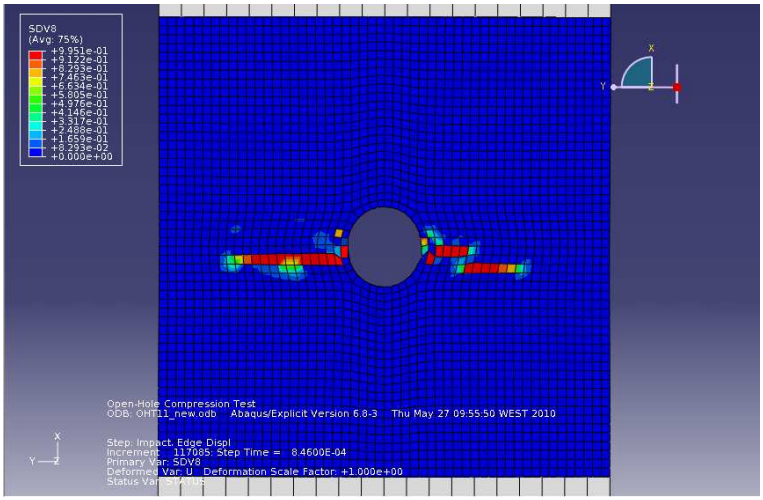

(b) Damage at the peak load.

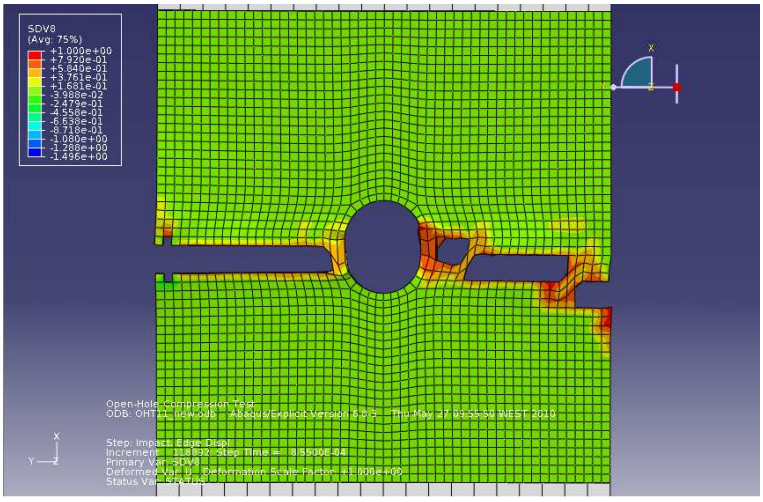

(c) Damage shortly after the peak load.

Figure 5.12: Structured mesh: d_1 Damage onset and propagation for a 0° ply.

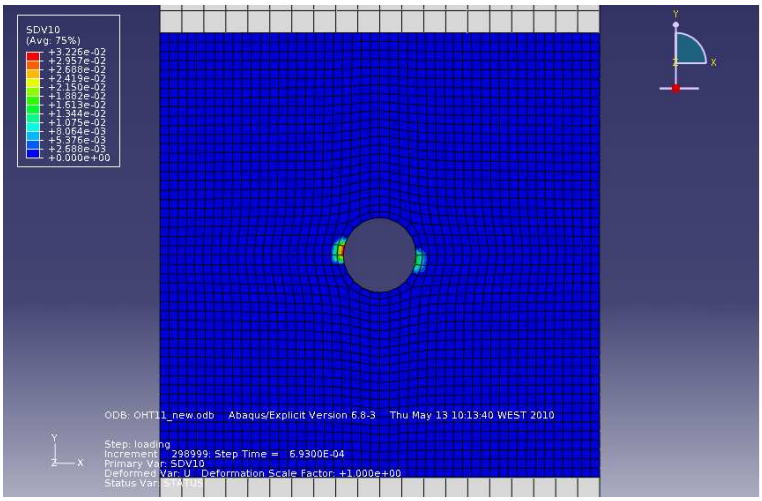

(a) Damage initiation at ≈ 60% of the peak load.

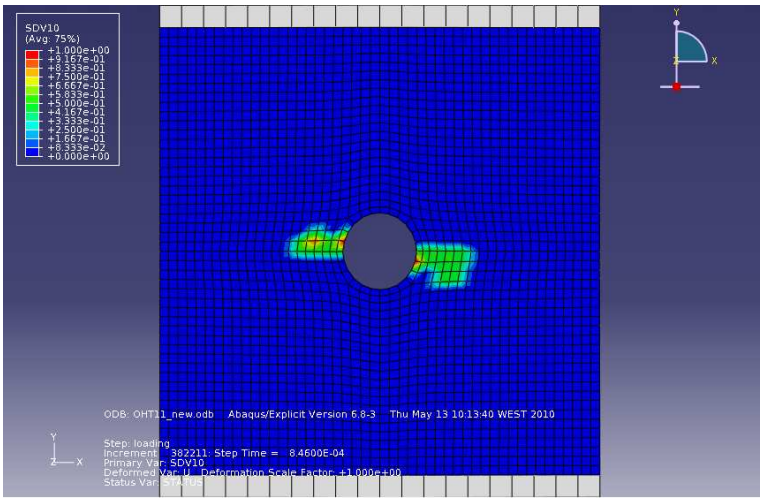

(b) Damage at the peak load.

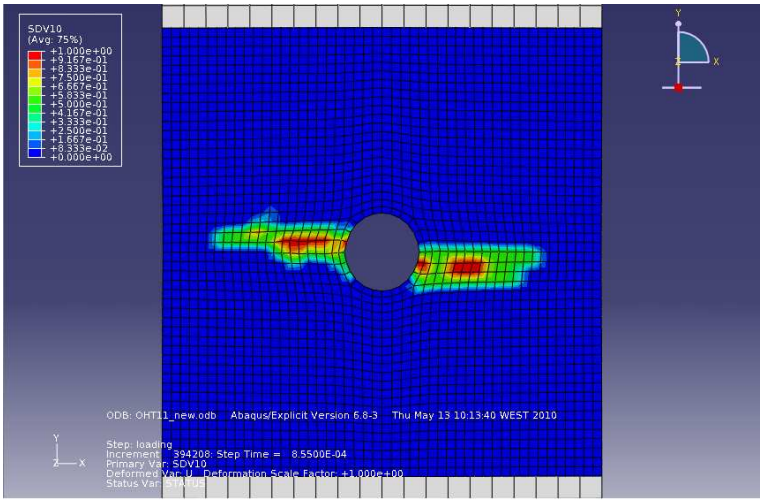

(c) Damage shortly after the peak load.

Figure 5.13: Non-Structured mesh: d_6 Damage onset and propagation for a 45° ply.

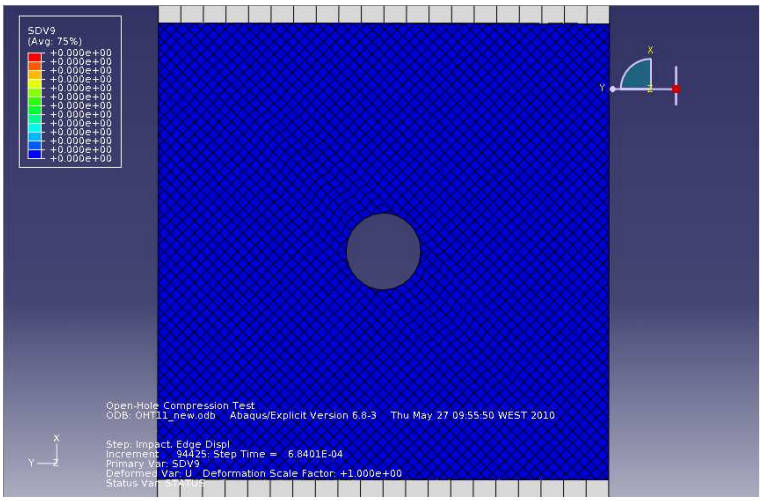

(a) No damage initiation at ≈ 60% of the peak load.

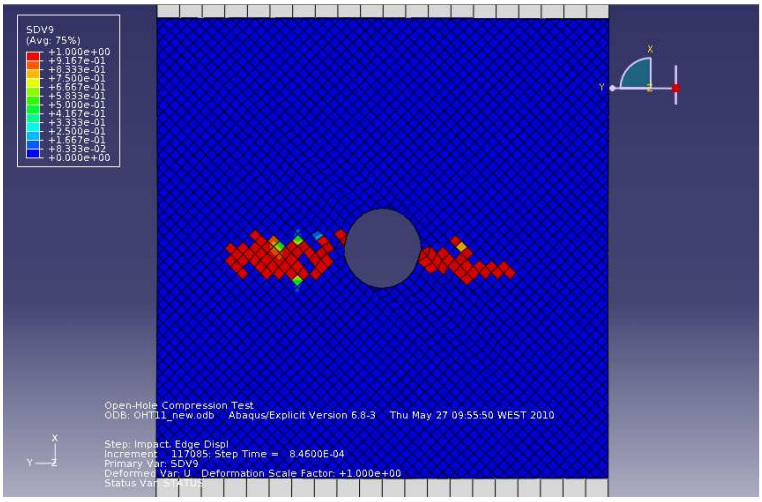

(b) Damage at the peak load.

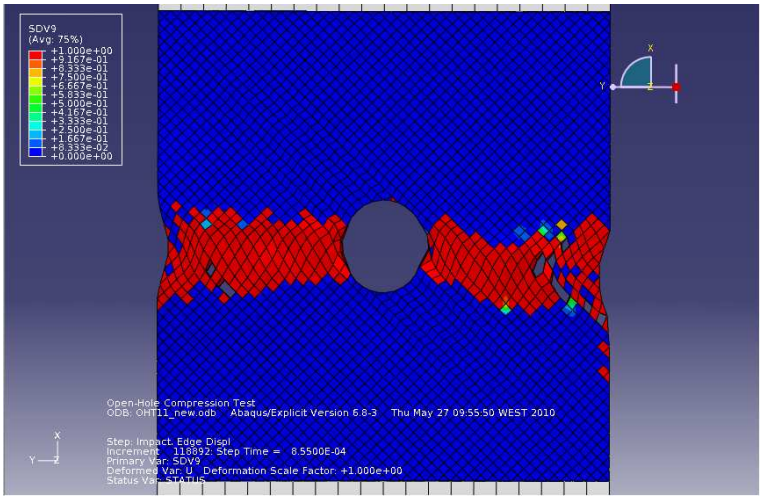

(c) Damage shortly after the peak load.

Figure 5.14: Structured mesh: d_2 Damage onset and propagation for a 45° ply.

5.2.4 OHC test: VUMAT's numerical predictions

Table 5.5 and Figure 5.15 summarizes the results obtained for the prediction of the compressive strength of the OHC test.

Table 5.5: Comparison between the Numerical and Experimental OHC strength results.

Specimen ref.	Experimental (MPa)	Numerical (Non-Structured) (MPa)	Diff. (%)	Numerical (Structured) (MPa)	Diff. (%)
OHC1	383.1	438.6	14.5	439.3	14.7
OHC1a	372.9	434.2	16.4	430.3	15.4
OHC2	365.2	393.1	7.6	411.2	12.6
OHC2a	353.7	381.2	7.8	401.4	13.5

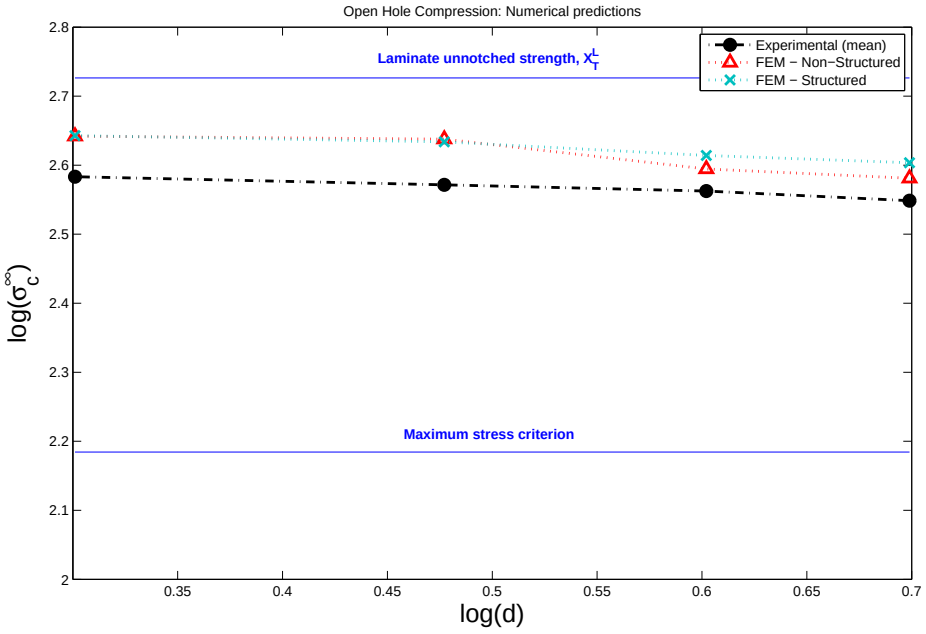

Figure 5.15: Numerical predictions of size effects in CFRP plates with an open-hole loaded in compression. $w/d = 6$.

The compressive strength predictions are less accurate than the tensile ones. For the Non--Structured mesh the maximum error is 16.4% for the OHC1a (d = 3mm) and the minimum is 7.6% for the OHC2 (d = 4mm). It is interesting to observe that the numerical predictions approach the correct solution in a consistent way, meaning that the error is around 15% for the 2 smaller specimens and around 8% for the bigger ones. This is, obviously, a better trend

than a “peak/valley” prediction.

Considering the Structured mesh the situation is quite interesting. The predictions have an off-set of approximately 14% compared to the experimental data. It is desirable to follow the trend of the real results.

These results are better than what might seem at a first observation if one reminds some important details:

1. Generally, the compressive strengths are more difficult predict because the damage mechanisms are more complex (particularly the kink band formation in the 0° plies);

2. There are not many measurements of the ply’s fracture energy per unit surface for longitudinal failure in compression, $\mathcal{G}_{1-}$, because the tests developed to its measurement, to this author’s knowledge, are not yet accurate. In Chapter 4 it was stated that the $\mathcal{G}_{1-}$ used for the IM7/8552 material was 82.3kJ/m^2, but this was considered an unreliable measurement. The second “in-house” attempt to measure the same property revealed inconclusive. No data was found in scientific articles about this subject. **This way it is believed that the primary problem in the numerical predictions should not be related to the code itself but with the measurement of the input property $\mathcal{G}_{1-}$.**

Before showing the damage initiation and propagation in each type of laminae of the laminate it is highlighted that, once again, the usage of a Structured mesh did not reveal a major improvement in the predictions. Nevertheless, it is possible that the Structured mesh produces better predictions because it was obtained the same trend of the experimental data (with an off-set). On the contrary, the Non-Structured mesh revealed better accuracy but not the same trend, which probably means that, when the $\mathcal{G}_{1-}$ is more accurately measured, the predictions of the Structured mesh will be better.

Despite what was previously stated, it was not concluded if the Structured mesh should or should not be used. On one hand, it produced marginally better results for the OHT case and managed to give the same trend of the OHC experimental data, on the other hand, it takes more time to do the pre-processing of the model and the subsequent improvement in accuracy is small.

90° layer

In the compression case, the damage (d_2) initiation occurs at approximately 77% of the peak load, for the 90° layer (instead of the approx. 60% obtained for tension). Then, the remaining behavior is somewhat similar to the one observed for the tension case. There is no significant difference between the results obtained with the Non-Structured and Structured meshes, which was expectable due to the fact that at 90° (and 0°) the structured mesh has the same orientation of the non-structured one. Figure 5.16 and 5.17 show the damage evolution for the OHC1 non-structured and structured meshes, respectively.

0° layer

For the 0° layer it is important to check two damage variables: d_1 and d_2. The first is obviously needed to check for kink band formation. The second, to check if there is matrix cracking. No significant matrix cracking was found. Figure 5.18 and Figure 5.19 present the damage onset and evolution in the longitudinal direction. It is interesting to observe that for the case of the 0° plies the damage initiates early (33% of the peak load for the Non-Structured mesh and 37% for the Structured). Again, there is great parallelism between the Non-Structured and Structured meshes.

45° layer

For the 45° plies it is necessary to check the d_6 damage variable for the Non-Structured mesh and d_1 or d_2 for the Structured mesh. The observation of Figure 5.20 and Figure 5.21 leads to the conclusion that the 45° layers play a more important role in damage propagation for the compression case than the one observed for the tension case. A relevant change from the tension test is observed for the Structured mesh, in which the d_1 variable becomes active and the d_2 inactive (the opposite of what was observed in OHT). This means for the 45° plies it is predicted that the latter will fail by fiber rupture (not by matrix cracking or delamination).

Nevertheless, it was again verified that even for the case of the 45° layers the difference between the results obtained with the Structured mesh and the Non-Structured is small. Although, it is only possible to predict the actual damage mechanism using the Structured mesh (because it is known if it is the d_1 or the d_2, or both variables that are activated).

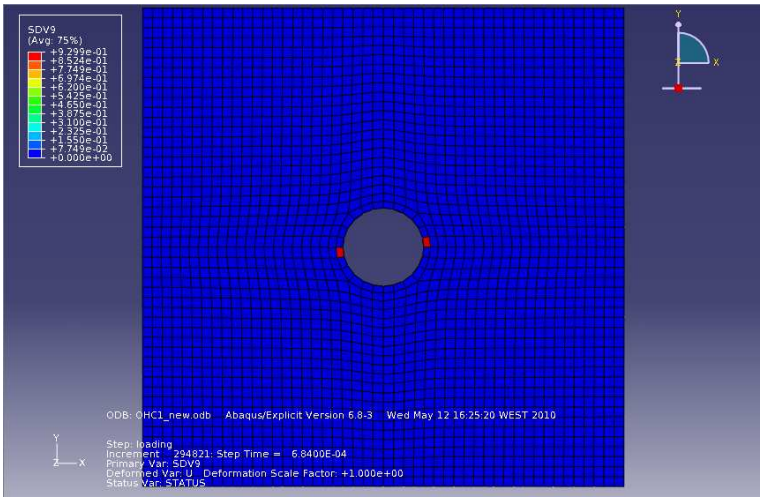

(a) Damage initiation at ≈ 77% of the peak load.

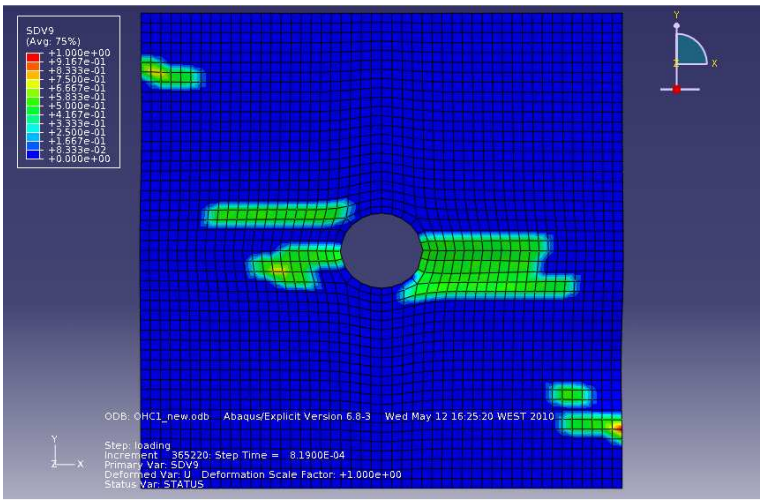

(b) Damage at the peak load.

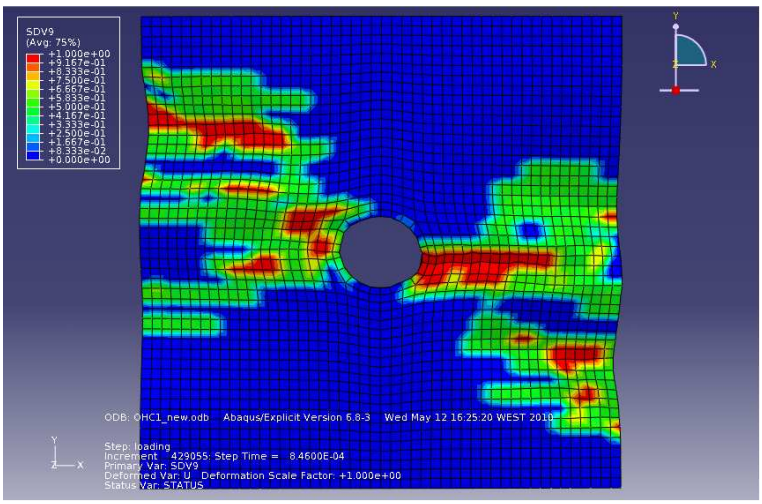

(c) Damage shortly after the peak load.

Figure 5.16: Non-Structured mesh: d_2 Damage onset and propagation for the top 90° ply.

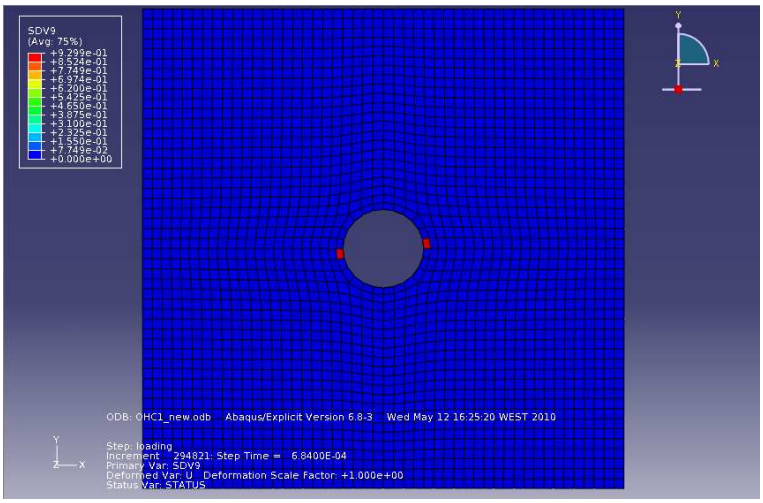

(a) Damage initiation at ≈ 77% of the peak load.

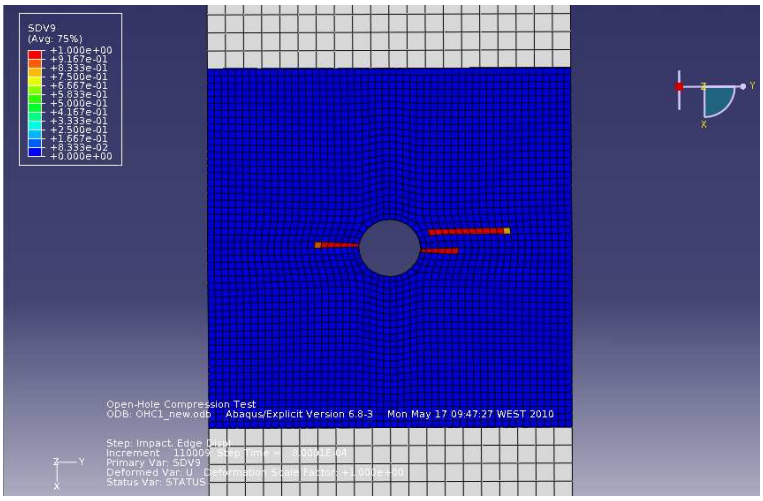

(b) Damage at the peak load.

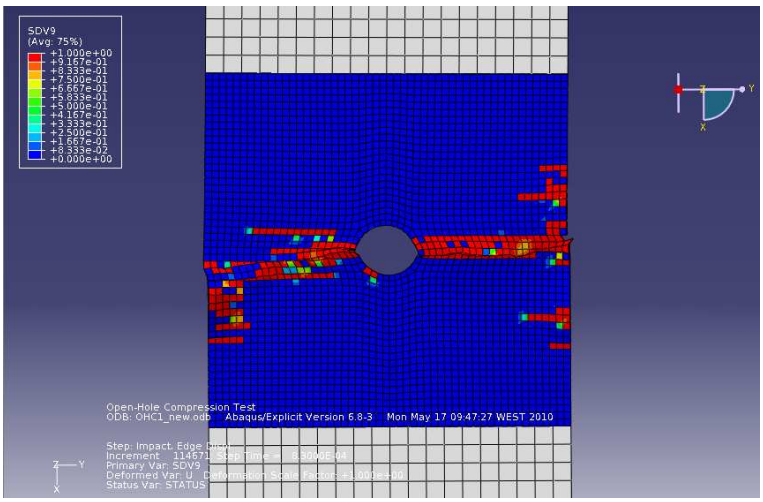

(c) Damage shortly after the peak load.

Figure 5.17: Structured mesh: d_2 Damage onset and propagation for the top 90° ply.

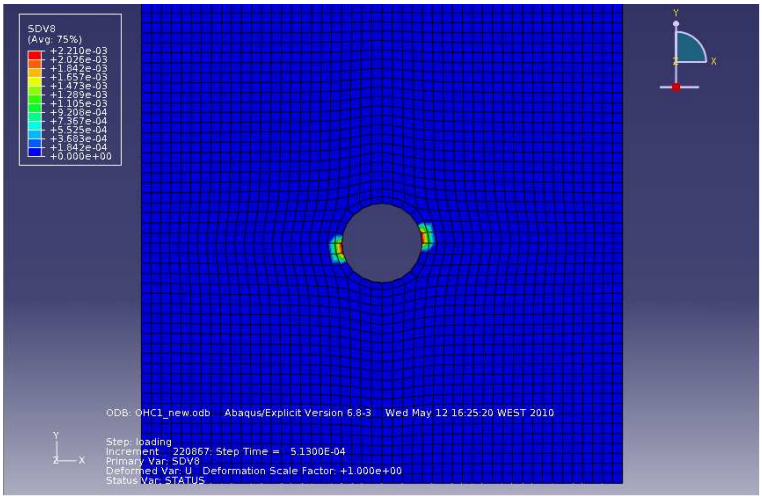

(a) Damage initiation at ≈ 33% of the peak load.

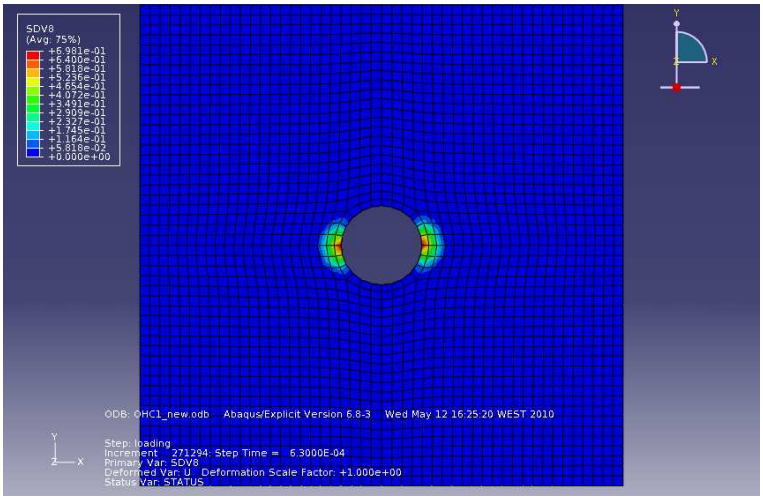

(b) Damage at ≈ 60% of the peak load.

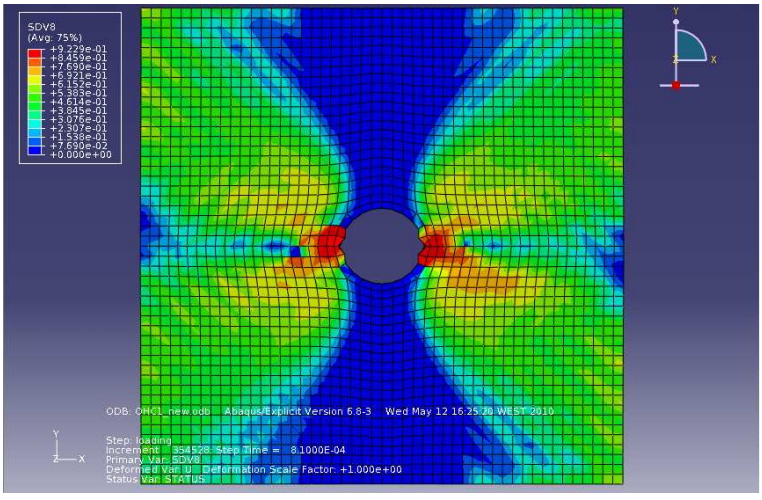

(c) Damage at the peak load.

Figure 5.18: Non-Structured mesh: d_1 Damage onset and propagation for a 0° ply.

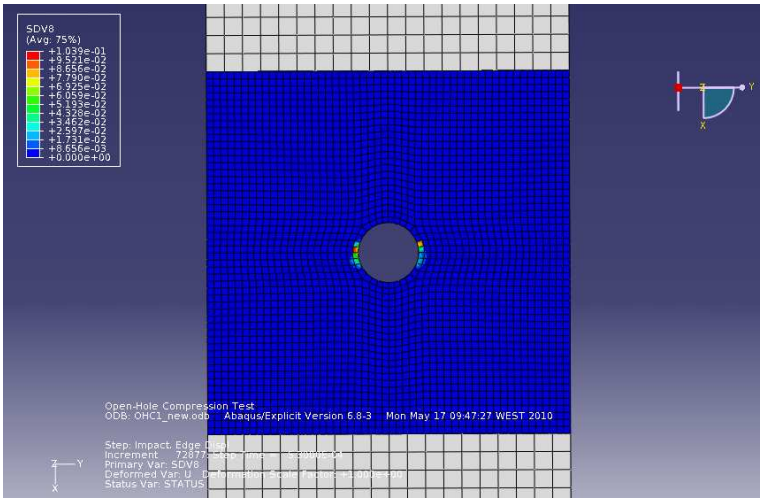

(a) Damage initiation at ≈ 37% of the peak load.

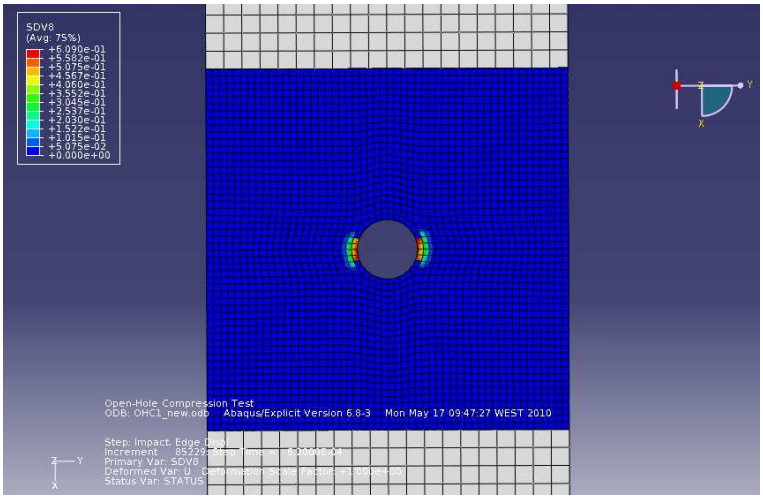

(b) Damage at ≈ 60% load.

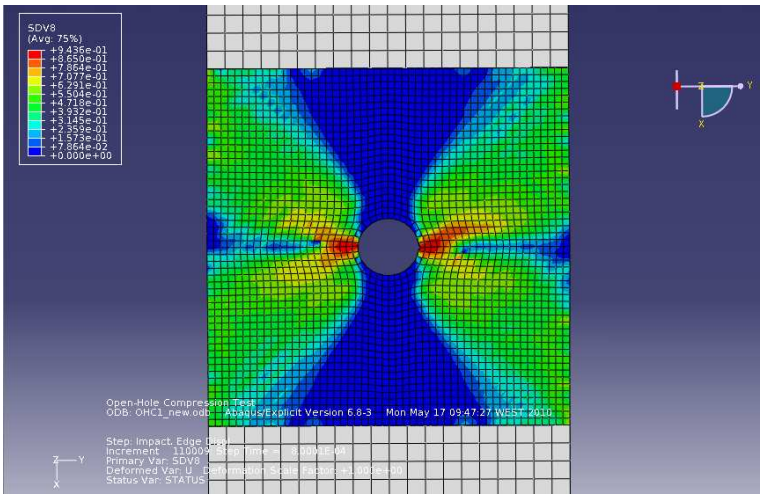

(c) Damage at the peak load.

Figure 5.19: Structured mesh: d_1 Damage onset and propagation for a 0° ply.

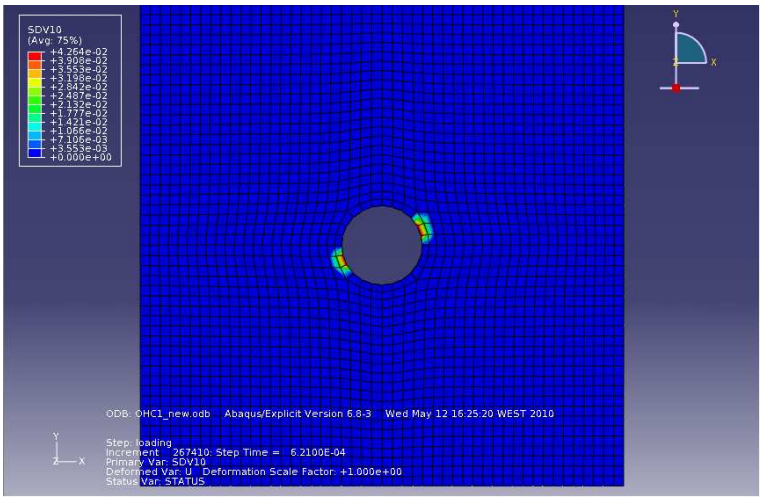

(a) Damage initiation at ≈ 60% of the peak load.

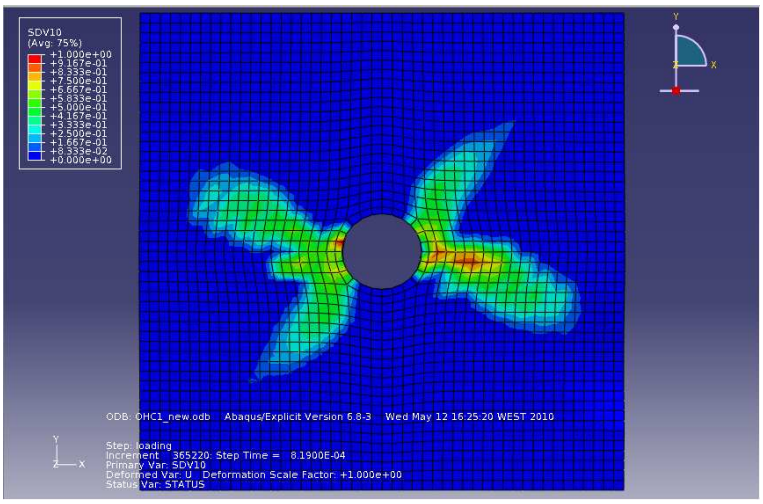

(b) Damage at the peak load.

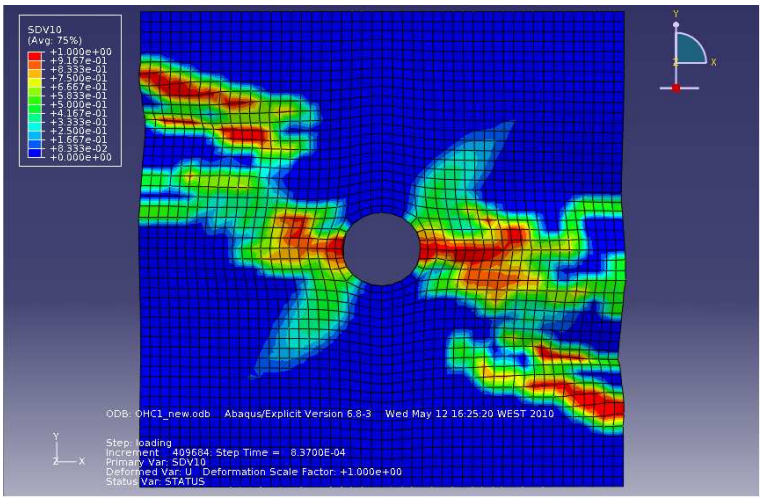

(c) Damage shortly after the peak load.

Figure 5.20: Non-Structured mesh: d_6 Damage onset and propagation for a 45° ply.

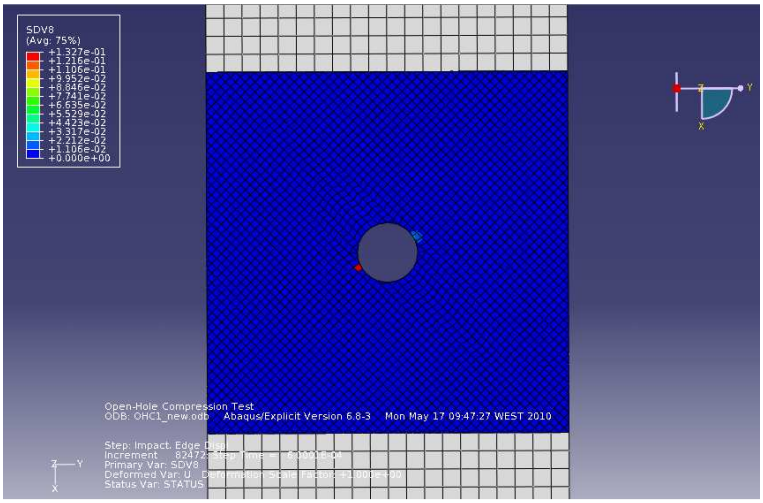

(a) No damage initiation at ≈ 55% of the peak load.

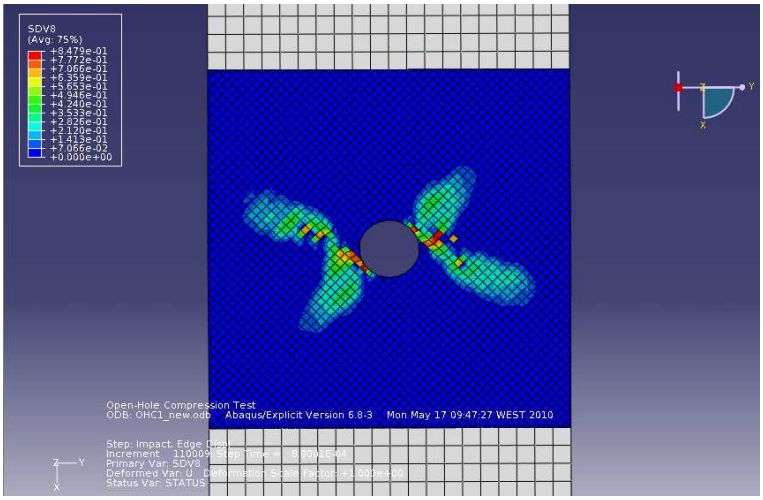

(b) Damage at the peak load.

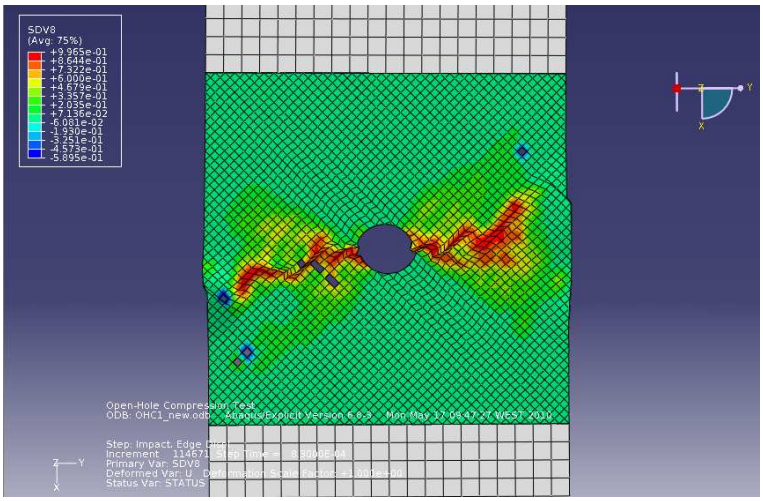

(c) Damage shortly after the peak load.

Figure 5.21: Structured mesh: d_1 Damage onset and propagation for a 45° ply.

5.2.5 Off-axis tension test of an unidirectional laminate (45°)

The last numerical model created to test the accuracy of the VUMAT numerical model was an off-axis tension test of an unidirectional laminate with the fibers oriented 45° relatively to the direction of the load. The experimental work was performed by **Cros** [141], using the IM7/8552 material. The specimen dimensions are shown in Figure 5.22.

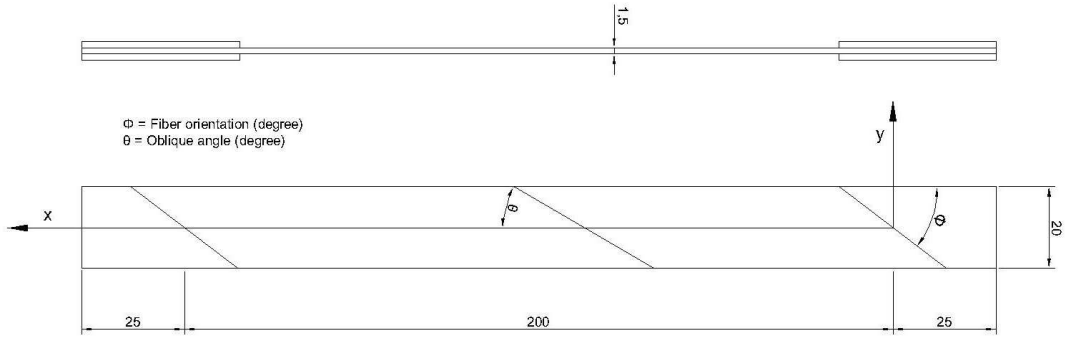

Figure 5.22: Off-axis specimen dimensions. $\theta = 45°$ and $\phi = 54°$. [141]

The experimental results that were obtained are quite interesting. The first specimen tested **failed at one of the end tabs**, with the failure stress of **80.0MPa**. The second and third specimens that were tested failed by the middle length with failure stresses of **103.0MPa** and **101.3MPa**, respectively. A post-failure examination showed that near the end tabs of the 2nd and 3rd specimens **the adhesive that was used to bond the tabs to the specimens went over the tab's edge**, which caused **a stress relieve** and consequently **increased the tensile strength** of the specimen (the failure surface did not occur at the end tabs). This is shown in Figure 5.23, where it can be seen that the edges of the tabs of the specimens which failed at the middle length are "shining" due to the adhesive excess.

The numerical model was created defining the end tabs without the excessive adhesive that relieves the stresses in that area. Therefore, the expected prediction for the tensile strength is 80.0MPa[4]. A Structured mesh was used in this numerical model. Table 5.6 provides the numerical prediction and the error that was obtained (for the specimen without excessive adhesive).

[4] It is important to state that it is not statistically viable to use just one measurement. Nevertheless, due to the fact that this experimental work finished in the last week conceded to write this thesis, there was not the possibility of performing more tests. This way, **the comparison between the numerical prediction and the experimental result presented in this section has to be considered preliminary**.

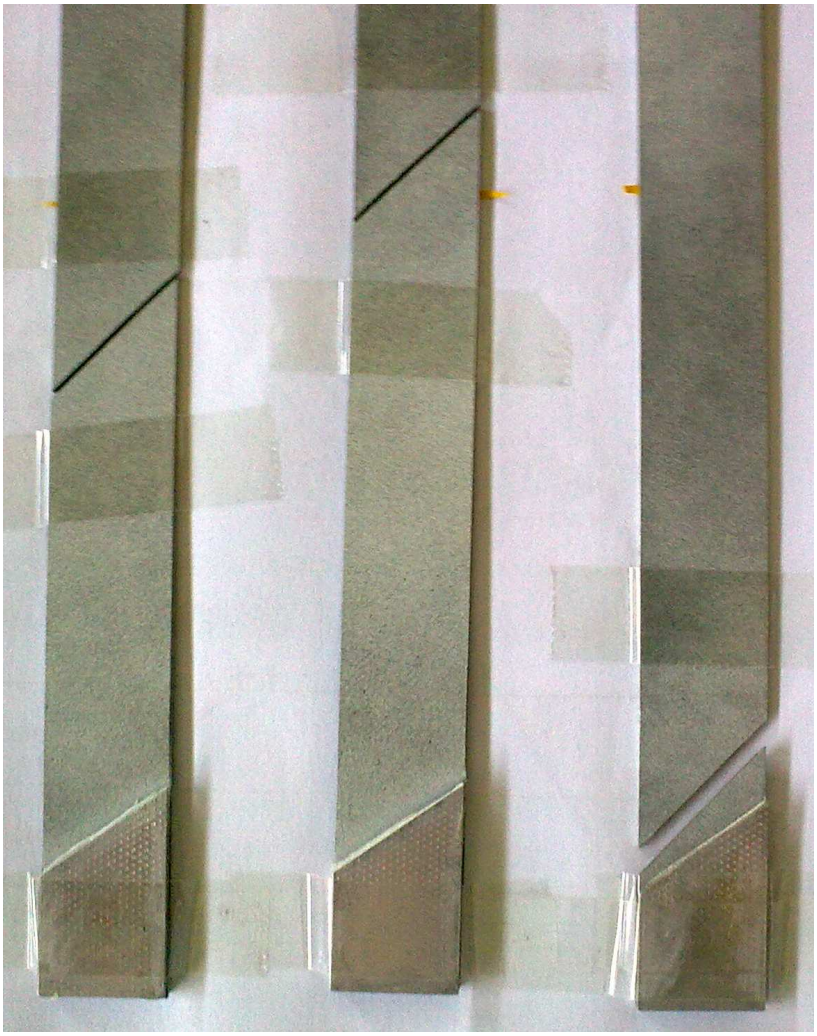

Figure 5.23: Fracture surfaces of the 3 off-axis specimens tested. [141]

Table 5.6: Comparison between the Numerical and Experimental Off-axis (45°) tensile strength results. Experimental work performed by Cros [141]. Material: IM7/8552.

Specimen ref.	Failure Mode	Exper. Fail. Stress $\overline{\sigma}_t^{\infty}$ (MPa)	Numerical Fail. Stress $\overline{\sigma}_t^{\infty}$ (MPa)	Diff. (%)
OA1	45° fracture surface near the end tabs	80.0	81.5	1.9
OA2	45° fracture surface at middle length	103.2	–	–
OA3	45° fracture surface at middle length	101.3	–	–

Figure 5.24 compares the real fractured surface of the OA1 specimen with the numerical prediction. It is concluded that the prediction is in perfect agreement.

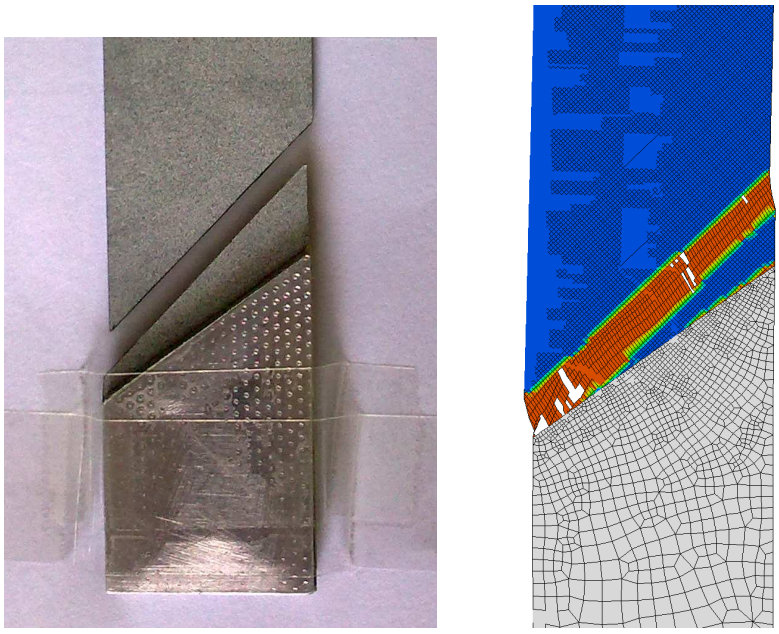

(a) Real fractured surface of the OA1 specimen.

(b) Predicted fracture surface by the ABAQUS VUMAT model.

Figure 5.24: Comparison between the experimentally and the numerically obtained fracture surfaces.

5.3 ABAQUS® UVARM numerical model

In this section it will be shown the advantage of using an UVARM subroutine in order to obtain the "hot-spots" of a structure. The Failure Criteria implemented in the UVARM subroutine is more advanced than the ones used by the VUMAT. Therefore, the UVARM should predict the stress concentrations more accurately. Figure 5.25 shows the damage initiation in an OHT specimen and Figure 5.26 in a OHC.

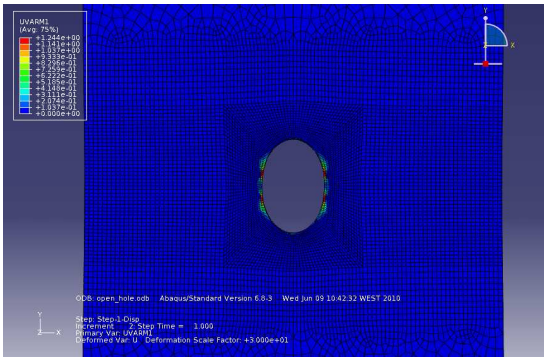

(a) 90° outer ply's Failure Index for Matrix Tension: FI_{MT}.

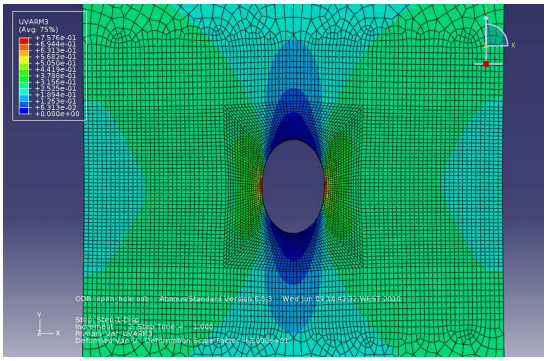

(b) 90° outer ply's Failure Index for Fiber Tension: FI_{FT}.

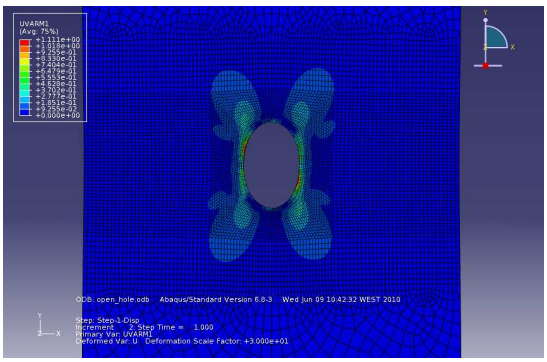

(c) 0° ply's Failure Index for Matrix Tension: FI_{MT}.

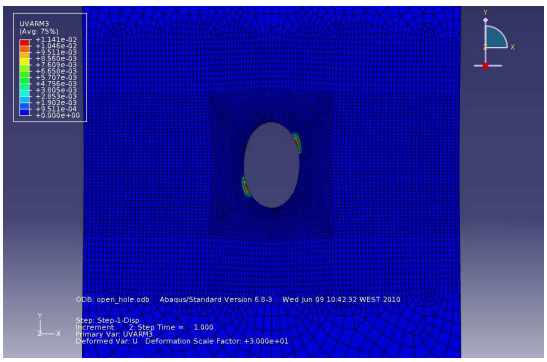

(d) 0° ply's Failure Index for Fiber Tension: FI_{FT}.

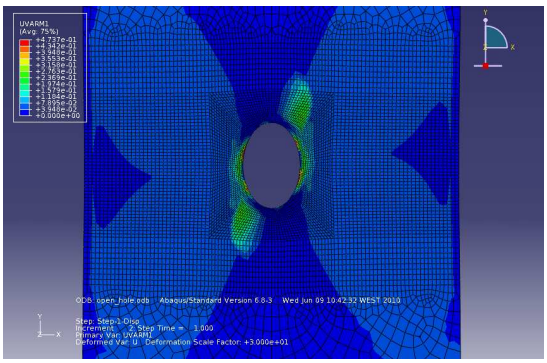

(e) 45° ply's Failure Index for Matrix Tension: FI_{MT}.

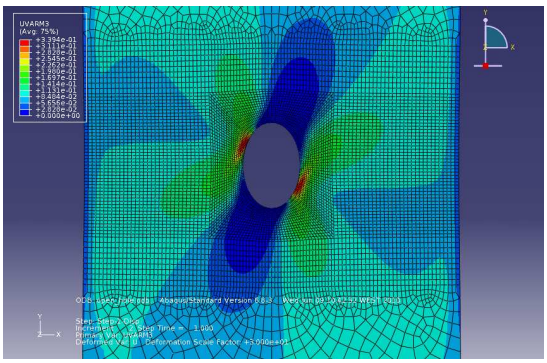

(f) 45° ply's Failure Index for Fiber Tension: FI_{FT}.

Figure 5.25: OHT stress concentrations.

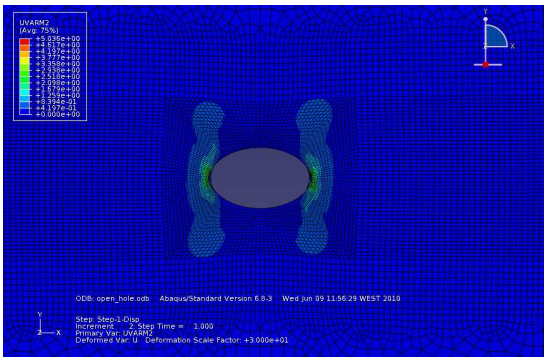

(a) 90° outer ply's Failure Index for Matrix Compression: FI_{MC}.

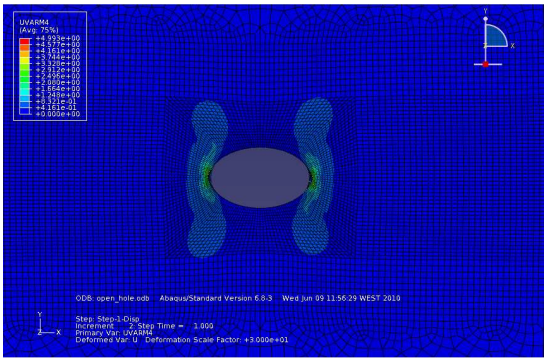

(b) 90° outer ply's Failure Index for Fiber Kinking: FI_{FK}.

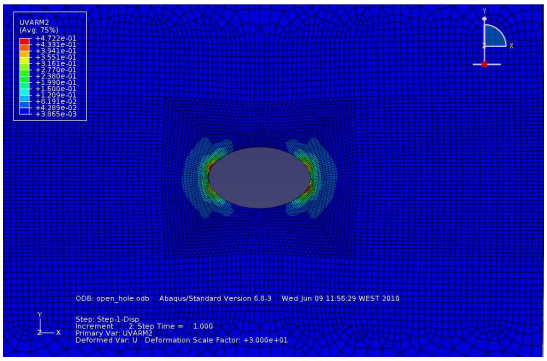

(c) 0° ply's Failure Index for Matrix Tension: FI_{MC}.

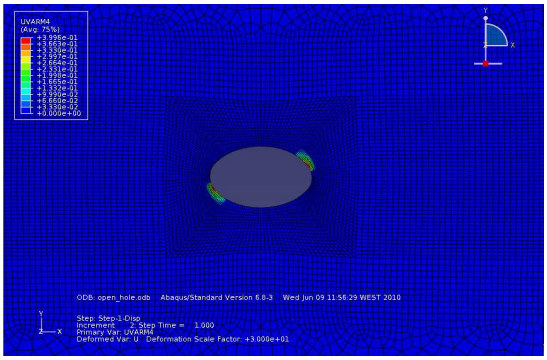

(d) 0° ply's Failure Index for Fiber Tension: FI_{FK}.

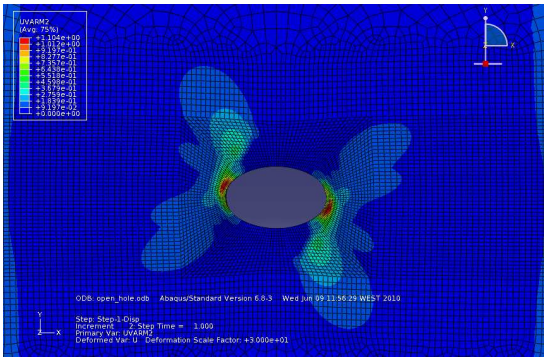

(e) 45° ply's Failure Index for Matrix Tension: FI_{MC}.

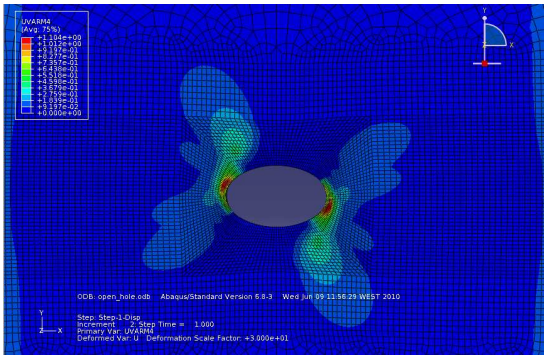

(f) 45° ply's Failure Index for Fiber Tension: FI_{FK}.

Figure 5.26: OHC stress concentrations.

It is observed that damage initiates for the 0° plies at the top right and bottom left of the hole, and for the 45° plies in the top left and bottom right of the hole. This is exactly what is expectable:

- For the +45° plies the damage should begin transversely to the fibers direction because the fibers are the primary constituent that gives resistance to the laminae.
- For the 0° plies, and having in mind that the adjacent layers to these plies are the 90° and

the 45° plies, the damage should initiate in the hole edge which as the 45° orientation because of the higher stresses transmitted by the 45° adjacent ply.

It is concluded that the application of a 3D Failure Criteria to the same OHT and OHC problems leads to more accurate damage onset predictions. Moreover, the fact that the referred criteria was applied in an UVARM subroutine makes it extremely fast to run different analyses and quickly identify the stress concentrations present in the structure.

CHAPTER 6

CONCLUSIONS

In this Chapter it is intended to summarize the main conclusions of the thesis. It was not intended to analyze in a detailed manner the numerous experimental, analytical and numerical results, due to the fact that this part of the work is interpreted by this author as a general conclusion. For specific details, the reader is referred to the remaining parts of the thesis.

6.1 Experimental observations

An extensive review on the experimental data was carried in this work (Chapter 2), in which it was possible to understand that there are numerous factors (such as material's nature, stacking sequence, geometry, load, etc.) that contribute differently to the composite material's failure. The main failure mechanisms identified in advanced composite materials are: fiber **pull-out** (in tension; extensive sub-critical damage), fiber **brittle fracture** (in tension; little sub-critical damage), **kink band formation and propagation** (in compression; extensive sub-critical damage), fiber **crushing** (in compression; little sub-critical damage), **delamination** (in tension and compression; ply debonding, usually causing premature failure), **matrix cracking** (in tension and compression; this failure mechanism is related to the initiation and growth of cracks within the matrix) and fiber **splitting** (in tension and compression; results from matrix cracks that propagate in the direction parallel to the fibers' orientation causing the separation of the fibers). These failure mechanisms combined can lead to different failure modes (also known as failure types), which usually have the designation of the principal failure mechanism that was in their respective origin.

However, since there are many failure mechanisms and even more factors that trigger them,

the analysis of the fracture of composite materials is complex. In a general way, it was observed that:

- **Unnotched** unidirectional (UD) and multidirectional (MD) specimens **in tension** exhibited a **clear volume effect**, with the tensile strength decreasing when the volume increases. However, a **small thickness effect** was observed, although some combination of factors can lead to strength variations (it was observed that for certain lay-ups the strength increases when the thickness increases, due to the free edge effect). It was also showed that the scaling technique (sublaminate- or ply-level scaling) may significantly influence the size effect;

- **Unnotched** UD and MD specimens **in compression** showed **significantly less size effects** than the specimens loaded in tension, for all scaling techniques (volume, in-plane dimensions or thickness variation);

- **OHT** specimens show a **clear hole size effect** (in-plane dimensions size effect). The thickness effect can be meaningful if a change in the failure mode occurs: usually, a change to a delamination type of failure (this change can be explained by different factors, probably the most important is the thickness scaling technique – ply-level scaling can cause sharp decreases in strength). Otherwise, the thickness effect is negligible. The volume effect (as the product of in-plane dimensions and thickness) exists;

- **OHC** specimens present a **clear hole size effect**, although (generally) it is **smaller than** the hole size effect observed for the **OHT** specimens. The **thickness effect is negligible**, unless for ply-level scaled specimens (as was verified with the remaining types of specimens). Thus, the volume effect exists but it is mainly due to the in-plane dimensions variation (similarly to what was stated in the OHT case).

In conclusion, in-plane dimensions variation is clearly the most important type of size effect for composite materials. The thickness is negligible most of the times, although it is proven that the ply-level scaling technique (usually) affects severely the strength of the material. Moreover, it can be generally concluded that size effects are more pronounced in tension than in compression.

6.2 Analytical models

It was demonstrated that the present analytical models are not sufficiently accurate for predicting advanced composite material's strength under general geometries, lay-ups and loading conditions. There is an honorable exception: the **BFS compressive criterion**. This criterion predicts very accurately the failure load for the OHC test, **as long as the failure is dominated by the** 0° **fibers**. For the remaining cases the model is not suited.

6.3 Numerical models

Meso-mechanical numerical models were used and developed in this thesis. The first model included **Damage**, **Shear plasticity** and **Delamination**, and was implemented in an **ABAQUS® VUMAT**. It was proven to be well suited for **predicting the strength** and the **failure modes** of the open-hole specimens. Moreover, the VUMAT model is applicable (with good accuracy) to off-axis tests, although more numerical analyses need to be performed to confirm this applicability.

The great advantage of the numerical model previously presented is that it is meso-mechanically based, meaning that the material is being modeled at the laminae level. This avoids the use of laminate properties, that need to be measured for each lay-up and component size.

A final comment about the VUMAT: the accuracy of the model in predicting the OHC strength can be improved because it is dependent of the longitudinal fracture energy in compression, which was revealed to be difficult to measure. So far, this was the only problem encountered in the model, being an external factor and not a formulation problem. Nevertheless, the computational cost of the model is very high and this should be an issue to account for in further improvements.

There was another numerical model developed to respond to the high computational cost of the VUMAT model: the **UVARM**. This model is based only in advanced 3D failure criteria that are applied to each integration point. The result is a very fast analysis that defines the stress concentrations points of the structure. This by itself can be enough to design some components or can be the first step of the design (the second step consists of applying more advanced models in the local area where the stress concentrations are located).

CHAPTER 7

FUTURE WORK

There are several aspects that can be further improved. However, there are 4 main improvements that should be highlighted:

1. The discovery of a way of measuring accurately the Longitudinal Fracture Energy of composite materials under compressive loads;
2. The formulation and implementation of full **3D Damage Laws**;
3. The implementation in the VUMAT of the **3D Failure Criteria** included in the UVARM;
4. The significant improvement of the **Plasticity Model**, not only in order to describe more accurately the shear plasticity, but also in order to describe the transverse compression non-linearity;

REFERENCES

[1] Wisnom, M.R.. *Size effects in the testing of fibre-composite materials*. Compos Sci Technol. 1999; 59:1937-57.

[2] Wisnom, M.R., Khan, B., Hallet, S.R.. *Size effects in unnotched tensile strength of unidirectional and quasi-isotropic carbon/epoxy composites*. Composite Structures. 2008; 84:21-28.

[3] Bullock, R.E.. *Strength ratios of composite materials in flexure and in tension*. J Compos Mater. 1974; 8:200-6.

[4] Hitchon, J.W., Phillips, D.C.. *The effect of specimen size on the strength of cfrp*. Composites. 1978; 9:119-24.

[5] Jackson, K.E., Kellas, S.. *Effect of specimen size on the tensile strength of geometrically scaled* $[+\theta_n/-\theta_n/90_{2n}]_S$ *composite laminates*. In: US Army Symposium on Solid Mechanics, Plymouth MA, August 1993.

[6] Wisnom, M.R., Atkinson, J.A.. *Reduction in tensile and flexural strength of unidirectional glass fibre-epoxy with increasing specimen size*. Compos Struct. 1997; 38:405-12.

[7] Jackson, K.E., Kellas, S., Morton, J.. *Scale effects in the response and failure of fiber reinforced composite laminates loaded in tension and in flexure*. J Compos Mater. 1992; 26:2674-705.

[8] Cunningham, M.E., Schoulz, S.V., Toth, J.M.. *Effect of the end tab design on tension specimen stress concentrations*. In: Recent advances in composites in the United States and Japan, ASTM STP 864. 1985; p.p. 263-62.

[9] Hojo, M., Sawada, Y., Miyairi, H.. *Influence of clamping method on tensile properties of unidirectional CFRP in* 0° *and* 90° *directions - round robin activity for international standardization in Japan*. Composites. 1994; 25:786-96.

[10] Wisnom, M.R., Maheri, M.R.. *Tensile strength of unidirectional carbon fibre-epoxy from tapered specimens*. In: Second European conference on composites testing and standardization, Hamburg, 1994. p.p. 239-47.

[11] O'Brien, T.K.. *Characterization of delamination onset and growth in a composite laminate*. In: Reifsnider KL, editor. Damage in composite materials ASTM STP 775. 1982; p.p. 140-67.

[12] Johnson, D.P., Morton, J., Kellas, S., Jackson, K.. *Scaling effects in sublaminate-level scaled composite laminates*. AIAA J. 1998; 36:441-7.

[13] Bing, Q., Sun, C.T.. *Specimen size effect in off-axis compression tests of fiber composites*. Composites Part B: Engineering. 2008; 39:20-26.

[14] Soutis, C., Lee, J.. *Scaling effects in notched carbon fibre/epoxy composites loaded in compression*. Journal of Materials Science. 2008; 43(20):6593-98.

[15] Lee, J., Soutis, C.. *Measuring the notched compressive strength of composite laminates: Specimen size effects*. Composites Science and Technology. 2008; 68(12):2359-66.

[16] Wisnom, M.R., Hallet, S.R., Soutis, C.. *Scaling Effects in Notched Composites*. Journal of Composite Materials. 2010; 44(2):195-210.

[17] Soutis, C., Curtis, P.T., Fleck, N.A.. *Compressive failure of notched carbon fibre composites*. Proc. R. Soc. Lond. A.. 1993; 440:241-56.

[18] Lee, J., Soutis, C.. *Thickness effect on the compressive strength of T800/924C carbon fibre-epoxy laminates*. Composites: Part A. 2005; 36:213-27.

[19] Camponeschi, E.T.. *Compression testing of thick-section composite materials*. Composite materials: fatigue and fracture (third volume), ASTM STP 1110. Philadelphia, PA: American Society for Testing and Materials. 1991; 439-56.

[20] Daniel, I.M., Hsiao H.M.. *Is there a thickness effect on compressive strength of unnotched composite laminates?* Int J Fract. 1999; 95(Special issue):143-58.

[21] Hsiao, H.M., Daniel, I.M., Wooh, S.C.. *A new compression test methods for thick composites*. J Compos Mater. 1995; 29(13):1789-806.

[22] Garala, H.J.. *Experimental evaluation of graphite/epoxy composite cylinders subjected to external hydrostatic compressive loading*. Proceedings, 1987 Spring Conference on Experimental Mechanics, Society for Experimental Mechanics, Bethel, CT, 1987; 948-51.

[23] Camanho, P. P., Maimí, P. and Dávila, C. G.. *Prediction of Size Effects in Notched Laminates using Continuum Damage Mechanics*. Composites Science and Technology. 2007; 67:2715-27.

[24] Green, B.G., Wisnom, M.R., Hallet, S.R.. *An experimental investigation into the tensile strength scaling of notched composites*. Composites: Part A. 2007; 38:867-78.

[25] Daniel, I.M., Rowlands, R.E., Whiteside, J.B.. *Effects of material and stacking sequence on behavior of composite plates with holes*. Experimental mechanics. 1974; 14(1):1.

[26] de Morais, A.. *Open-hole tensile strength of quasi-isotropic laminates*. Composites science and technology. 2000; 60(10):1997

[27] Ogihara, S., Takeda, N., Kobayashi, S., Kobayashi, A.. *Experimental characterization of microscopic damage progress in quasi-isotropic CFRP laminates: effect of interlaminar-toughened layers*. Advanced composite materials. 1998; 7(2):183.

[28] Lagace, P.A.. *Notch sensitivity and stacking sequence of laminated composites*. In: Whitney JM, editor. Composite materials: testing and design (seventh conference), ASTM STP 893. Philadelphia: 1986. p.p 161-76.

[29] O'Higgins, R.M.. *Experimental and numerical study of the open-hole tensile strength of carbon/epoxy composites*. Mechanics of composite materials. 2004; 40(4):264.

[30] Halet, S., Jiang, W., Wisnom, M.R.. *The effect of stacking sequence on thickness scaling of tests on open-hole tensile composite specimens*. 48th AIAA/ASME/AHS/ASC Structures, Structural Dynamics, and Materials Conference. 23-26 April 2007, Honolulu, Hawai.

[31] Vaidya, R.S., Klug, J.C., Sun, C.T.. *Effect of ply thickness on fracture of notched composite laminates*. AIAA J. 1998; 36:81-8.

[32] Green, B.G.. *The effect of size on the tensile strength of composite laminates containing circular holes*. Ph.D. thesis, University of Bristol (2006).

[33] Iarve, E.V., Mollenhauer, D., Whitney, T.J., Kim, R.. *Strength prediction in composites with stress concentrations: classical Weibul and critical failure volume methods with micromechanical considerations*. J Mater Sci. 2006; 41:6610-21.

[34] Wisnom, M.R., Hallett, S.R.. *The role of delamination in strength, failure mechanism and hole size effect in open hole tensile tests on quasi-isotropic laminates*. Composites: Part A. 2009; 40:335-42.

[35] Awerbuch, J., Madhuka, M.S.. *Notched strength of composite laminates: predictions and experiments - a review*. J Reinf Plast Compos. 1985; 4:3-159.

[36] Kortschot, M.T., Beaumont, M.F., Ashby, P.W.R.. *Damage mechanics of composite materials; III. Prediction of damage growth and notched strength*. Compos Sci Technol. 1991; 40:147-65.

[37] Lagace, P.A.. *Notch sensitivity and stacking sequence of laminated composites*. In: Whitney JM, editor. Composite materials: testing and design (seventh conference), ASTM STP 893, Philadelphia: 1986. p.p. 161-76.

[38] Vaidya, R.S., Klug, J.C., Sun, C.T.. *Effect of ply thickness on fracture of notched composite laminates*. AIAA J. 1998; 36:81-8.

[39] Abou-Khalil, D.. *Failure of Open Hole Tensile Composite Plates: Numerical Investigation*. Master Project, Imperial College London (2008).

[40] Open hole tensile strength of polymer composite laminates, ASTM D 5766/D 5766M-02a, American Society for Testing and Materials (ASTM), West Conshohocken, PA, U.S.A.

[41] Guynn, E.G., Bradley,W.L., Elber, W.. *Micromechanics of compression failures in open hole composite plates*. Composite Materials: Fatigue and Fracture, ASTM STP 1012. 1989; 118-36.

[42] Newman, J.C.. *A nonlinear fracture mechanics approach to the growth of small cracks. Behavior of short cracks on airframe components*. AGARD Conf. Proc., France 1982.

[43] Tada, H., Paris, P.C., Irwin, G.R.. *The stress analysis of cracks handbook*. St. Louis, MO: Del Research Corporation, 1973.

[44] Lee, J., Soutis, C.. *Scaling effects in notched composites (SINCS) - Investigation of scaling effects on static and fatigue compressive behaviour*. Report of The University of Sheffield. July 2006.

[45] Lessard, L.B., Chang, F.. *Damage tolerance of laminated composites containing an open hole and subjected to compressive loadings: Part II-Experiment*. Journal of Composite Materials. 1991; 25:44-64.

[46] Suemasu, H., Takahashi, H., Ishikawa, T.. *On failure mechanisms of composite laminates with an open hole subjected to compressive load*. Composites Science and Technology. 2006; 66:634-41.

[47] Iarve, E., Pagano, N.J.. *Singular full-field stresses in composite laminates with an open hole*. Int J Solids Struct. 2001; 38:1-28.

[48] Iarve, E.. *Spline variational three dimensional stress analysis of laminated composite plates with open holes*. Int J Solids Struct. 1996; 33(14):2095-118.

[49] Soutis, C., Fleck, N.A., Smith, P.A.. *Failure prediction technique for compression loaded carbon fibre-epoxy laminate with open holes*. Journal of Composite Materials. 1991; 33:1476-98.

[50] Soutis, C.. *Compressive behaviour of composites – Report 94*. Rapra Review Reports. 1997; 8(10):17-19.

[51] Rosen, V.W.. *Mechanics of composite strenghening*. Fibre Composite Materials, American Society of Materials, Metals Park, Ohio. 1965; p.p. 37-75.

[52] Argon, A.S.. *Fracture of composites*. Treatise on Materials Science and Technology, Academy Press, New York 1972.

[53] Greszczuk, L.B.. *On failure modes of unidirectional composites under compressive loading*. In: Proc. 2nd USA-USSR Sump. on Fracture of Composite Materials. Martinus Nijhoff, The Hague, NL, 1982. pp. 231-44.

[54] Budiansky, B.. *Micromechanics*. Comput. Struct.. 1983; 16:3-12.

[55] Hahn, H.T., Williams, J.G.. *Compression failure mechanisms in unidirectional composites*. Composite Materials Testing and Design. STP 893. ASTM, Philadelphia, PA, 1986; pp. 115-39.

[56] Waas, A.M., Babcock, C.D., Knauss, W.G.. *A mechanical model for elastic fiber microbuckling*. J. Appl. Mech.. 1990; 57:138-49.

[57] Steif, P.S.. *A model for kinking in fiber composites – I. Fiber breakage via microbuckling*. Int. J. Solids Struct.. 1990; 26:549-61.

[58] Steif, P.S.. *A model for kinking in fiber composites – II. Kink band formation*. Int. J. Solids Struct.. 1990; 26:563-9.

[59] Ha, J.B., Nairn, J.A.. *Compression failure mechanisms of single-ply, unidirectional, carbon-fiber composites*. SAMPE Quart.. 1992; 23:29-36.

[60] Budiansky, B., Fleck, N.A.. *Compressive failure of fibre composites*. J. Mech. Phys. Solids.. 1993; 41:183-211.

[61] Fleck, N.A., Deng, L., Budiansky, B.. *Prediction of kink band width in compressed fiber composites*. ASME J. Appl. Mech.. 1995; 62:329â37.

[62] Schultheisz, C.R., Waas, A.M.. *Compressive failure of composites, part I: testing and micromechanical theories*. Progress Aerospace Science. 1996; Volume 32.

[63] Waas, A.M., Schultheisz, C.R.. *Compressive failure of composites, part II: Experimental studies*. Prog. Aerosp. Sci.. 1996; 32:43-78.

[64] Chaudhuri, R.A., Xie, M., Garala, H.. *Stress singularity due to kink band weakening a unidirectional composite under compression*. J. Compos. Mater.. 1996; 30:672-91.

[65] Vogler, T.J., Kyriakides, S.. *On the axial propagation of kink bands in fiber composites: Part I experiments*. Int. J. Solids Struct.. 1999; 36:557-74.

[66] Vogler, T.J., Kyriakides, S.. *On the axial propagation of kink bands in fiber composites: Part II analysis*. Int. J. Solids Struct.. 1999; 36:575-95.

[67] Berbinau, P., Soutis, C., Guz, I.A.. *Compressive failure of* 0° *unidirectional carbon-fibre-reinforced plastics (cfrp) laminates by fibre microbuckling*. Compos. Sci. Technol.. 1999; 59:1451-5.

[68] Yerramalli, C.S., Waas, A.M.. *A non-dimensional number to classify composite compressive failure*. J. Appl. Mech.. 2004;71:402-8.

[69] Hawthorne, H.M., Teghtsoonian, E.. *Axial compression fracture in carbon fibres*. J. Mater. Sci.. 1975; 10:41-51.

[70] Hahn, H.T., Sohi, M.M.. *Buckling of a fiber bundle embedded in epoxy*. Comp. Sci. Technol.. 1986; 27:25-41.

[71] Oshawa, T., Miwa, M., Kawade, M., Tsushima, E.. *Axial compressive strength of carbon fiber*. J. Appl. Poly. Sci.. 1990; 39:1733-43.

[72] Boll, D.J., Jensen, R.M., Cordner, L., Bascom, W.D.. *Compressive behavior of single carbon filaments embedded in an epoxy polymer*. J. Compos. Mater.. 1990; 24:208-19.

[73] Shioya, M., Nakatani, M.. *Compressive strength of single carbon fibres and composite strands*. Comp. Sci. Technol.. 2000; 60:219-29.

[74] Schorr, D.. *Compressive failure mechanisms of single filament carbon fiber reinforced composites*. Senior Thesis, Department of Materials Science and Engineering, Cornell University (2001).

[75] Goutianos, S., Peijs, T., Galiotis, C.. *Mechanisms of stress transfer and interface integrity in carbon/epoxy composites under compression loading part I: Experimental investigation*. Int. J. Solids Struct.. 2002; 39:3217-31.

[76] Goutianos, S., Peijs, T., Galiotis, C.. *Mechanisms of stress transfer and interface integrity in carbon/epoxy composites under compression loading part II: Numerical approach*. Int. J. Solids Struct.. 2003; 40:5521-38.

[77] Narayanan, S., Schadler, L.S.. *Mechanism of kink-band formation in graphite/epoxy composites: a micromechanical experimental study*. Compos. Sci. Technol.. 1999; 59:2201-13.

[78] Puck, A., Schürmann, H.. *Failure analysis of FRP laminates by means of physically based phenomenological models*. Composites Science and Technology. 1998; 58:1045-67.

[79] Puck, A., Kopp, J., Knops, M.. *Guidelines for the determination of the parameters in puck's action plane strength criterion*. Composites Science and Technology. 2002; 62:371-8.

[80] Puck, A., Schürmann, H.. *Failure analysis of FRP laminates by means of physically based phenomenological models*. Composites Science and Technology. 2002; 62:1633-62.

[81] Dávila, C.G., Camanho, P.P., Rose, C.A.. *Failure criteria for FRP laminates*. Journal of Composite Materials. 2005; 39(4):323-345.

[82] Pinho, S.T., Iannucci, L., Robinson, P.. *Physically-based failure models and criteria for laminated fibre-reinforced composites with emphasis on fibre kinking: Part I: Development*. Composites Part A. 2006; 37:63-73.

[83] Bai, J., Phoenix, S.L.. *Compressive failure model for fiber composites by kink band initiation from obliquely aligned, shear-dislocated fiber breaks*. Int J Solids and Struct. 2005; 42:2089-128.

[84] Pimenta, S.. *Micromechanics of kink-band formation*. MSc thesis, Faculty of Engineering, University of Porto and Imperial College London (2008).

[85] Kachanov, L.M.. *Time of the rupture process under creep conditions*. Izvestia Akademii Nauk SSSR. Otdelenie Tekhnicheskich Nauk. 1958; 8:26-31.

[86] Kachanov, L.M.. *Rupture time under creep conditions*. International Journal of Fracture. 1999; 37:xi-xviii.

[87] Cauvin, A., Testa, R.B.. *Damage mechanics: basic variables in continuum theories*. International Journal of Solids and Structures. 1999; 36:747-61.

[88] Camanho, P.P.. *Computational methods in fracture mechanics and damage*. Lecture Notes (2006).

[89] Malvern, L.E.. *Introduction to the mechanics of a Continuous Medium*. Prentice-Hall, Englewood Cliffs (1969).

[90] Ortiz, M.. *A constitutive theory for inelastic behaviour of concrete*. Mech. Mater.. 1985; 4:67-93.

[91] Simo, J.C., Ju J.W.. *Strain and stress-based continuum damage models-I. Formulation*. International Journal of Solids and Structures. 1986; 23(7):821-40.

[92] Simo, J.C., Ju J.W.. *Strain and stress-based continuum damage models-II. Computational aspects*. International Journal of Solids and Structures. 1986; 23(7):841-69.

[93] Cordebois J.P., Sidoroff F.. *Anisotropie élastique induite par endommagment. Comportement mécanique des solides anisotropes*. CNRS. 1979; 295:796-74.

[94] Jirásek, M.. *Numerical modeling of deformation and failure of materials*. Lecture Notes (2000).

[95] Lemaitre, J., Chaboche, J.-L.. Mechanics of solid materials. Cambridge University Press, Cambridge (1990).

[96] Chaboche, J.-L., Maire, J.F.. *A new micromechanics based CDM model and its application to CMC's*. Aerospace Sci. Technol.. 2002; 6:131-45.

[97] Baker, G.. *Thermodynamics in solid mechanics: a commentary*. Phil. Trans. R. Soc. A. 2005; 363:2465-77.

[98] Dávila, C.G., Camanho, P.P., Rose, C.A.. *Failure criteria for FRP laminates*. Journal of Composite Materials. 2005; 39:323-45.

[99] Pinho, S.T., Dávila, C.G., Camanho, P.P., Ianucci, L., Robinson, P.. *Failure models and criteria for FRP under in-plane or three-dimensional stress states including shear non-linearity*. NASA/TM-2003-213530 (2004).

[100] Matzenmiller, A., Lubliner, J., Taylor, R.L.. *A constitutive model for anisotropic damage in fiber-composites*. Mechanics of Materials. 1995; 20:125-52.

[101] Ladevèze, P., Allix, O., Deü, J-F., Lévêque, D.. *A mesomodel for localisation and damage computation in laminates*. Computer Methods in Applied Mechanics and Engineering. 2000; 183:105-22.

[102] Gasser, A., Ladevèze, P., Peres, F.. *Damage modelling for a laminated composite*. Materials Science and Engineering. 1998; A250:249-55.

[103] Ladevèze, P., Allix, O., Douchin, B., Lévêque, D.. *A computational method for damage intensity prediction in a laminated composite structure*. Computational Mechanics, new trends and applications. (1998) CIMNE.

[104] Ladevèze, P., Lubineau, G.. *On a damage mesomodel for laminates: micro-meso relationships, possibilities and limits*. Composites Science and Technology. 2001; 61:2149-58.

[105] Ladevèze, P., Lubineau, G.. *An enhanced mesomodel for laminates based on micromechanics*. Composites Science and Technology. 2002; 32:533-41.

[106] Coleman, B.D., Noll, W.. *The thermodynamics of elastic materials with heat conduction and viscosity*. Arch. Rat. Mech. Anal.. 1963; 13:167-78.

[107] Lubliner, J.. *On the thermodynamic foundations of non-linear solid mechanics*. Int. J. Nonlinear Mech.. 1972; 7:237-54.

[108] Lubliner, J.. *Plasticity theory*. Macmillan publishing, New York. 1990.

[109] Simo, J.C., Hughes, T.J.R.. *Computational inelasticity*. Mechanics and Materials, Springer-Verlag. 1997.

[110] Oliver, X., Agelet de Saracíbar, C.. *Mecànica de medis continus per a enginyers*. Edicions UPC. 2003.

[111] http://www.hexcel.com/NR/rdonlyres/B99A007A-C050-4439-9E59-828F539B03A4/0/HEXPLY85528PPA4.pdf

[112] Standard test method for tensile properties of polymer matrix composite materials, ASTM D 3039/D 3039M-00, American Society for Testing and Materials (ASTM), West Conshohocken, PA, U.S.A.

[113] Standard test method for in-plane shear response of polymer matrix composite materials by test of a ±45° laminate, ASTM D 3518/3518M-94, American Society for Testing and Materials (ASTM), West Conshohocken, PA, U.S.A.

[114] Standard test method for compressive properties of unidirectional or cross-ply fiber-resin composites, ASTM D 3410-87, American Society for Testing and Materials (ASTM), West Conshohocken, PA, U.S.A.

[115] Camanho, P.P., Dávila, C.G., Pinho, S.T., Iannucci, L. and Robinson, P.. *Prediction of in-situ strengths and matrix cracking in composites under transverse tension and in-plane shear*. Composites-Part A. 2006; 37:165-76.

[116] Standard test methods for mode I interlaminar fracture toughness of unidirectional fiber-reinforced polymer matrix composites, ASTM D 5528-01, American Society for Testing and Materials (ASTM), West Conshohocken, PA, U.S.A.

[117] Martin, R., Elms, T. and Bowron, S.. *Characterization of mode II delamination using the 4ENF*. Proceedings of the 4th European Conference on Composites: Testing and Standardisation, Lisbon, 1998.

[118] Pinho, S.T.. *Modelling failure of laminated composites using physically-based failure models*. Ph.D Thesis, Department of Aeronautics, Imperial College London, U.K. (2005).

[119] Pinho, S.T., Robinson, P. and Iannucci, L.. *Fracture toughness of the tensile and compressive fibre failure modes in laminated composites*. Composites Science and Technology. 2006; 66:2069-79.

[120] Standard test method for open-hole compressive strength of polymer matrix composite laminates, ASTM D6484 / D6484M - 09, American Society for Testing and Materials (ASTM), West Conshohocken, PA, U.S.A.

[121] Whitney, J.M. and Nuismer, R.J.. *Stress fracture criteria for laminated composites containing stress concentrations*. Journal of Composite Materials. 1974; 8:253-65.

[122] Yamada, S.E. and Sun, C.T.. *Analysis of laminate strength and its distribution*. Journal of Composite Materials. 1978; 12:275-84.

[123] Waddoups, M.E.; Eisenmann, J.R. and Kaminski, B.E.. *Macroscopic fracture mechanics of advanced composite materials*. Journal of Composite Materials. 1971; 5:446-54.

[124] Maimí, P., Camanho, P.P., Mayugo, J.A. and Dávila, C.G.. *A continuum damage model for composite laminates: part I - constitutive model*. Mechanics of Materials. 2007; 39(10):897-908.

[125] Maimí, P., Camanho, P.P., Mayugo, J.A. and Dávila, C.G.. *A continuum damage model for composite laminates: part II - computational implementation and validation*. Mechanics of Materials. 2007; 39(10):909-19.

[126] ABAQUS 6.8 User's Manual, ABAQUS Inc., Pawtucket, RI, U.S.A. (2008).

[127] Gonzalez, E.V., Maimí, P., Turon, A., Camanho, P.P., Renart, J.. *Simulation of delamination by means of cohesive elements using an explicit finite element code*. Computers, Materials and Continua. 2009; 9:51-92.

[128] Catalanotti, G., Camanho, P.P., Xavier, J., Dávila, C.G., Marques, A.T.. *Measurement of resistance curves in the longitudinal failure of composites using digital image correlation*. Composites Science and Technology. 2010 (submitted).

[129] GOM International AG, Bremgarterstrasse 89B, CH-8967 Widen, Switzerland.

[130] Lecompte, D., Smits, A., Bossuyt, S., Sol, H., Vantomme, J., Van Hemelrijck, D., Habraken, A.M.. *Quality assessment of speckle patterns for digital image correlation*. Optics and Lasers in Engineering. 2006; 44:1132-45.

[131] Pinho, S.T., Private communication to Catalanotti, G.. 2009.

[132] Soutis, C., Fleck, N.A.. *Static compression failure of carbon fibre T800/924C composite plate with a single hole*. Journal of Composite Materials. 1990; 24:536-58.

[133] Paris, P.C., Sih, G.C.. *Stress analysis of cracks. Fracture toughness testing and its applications*. ASTM STP. 1965; 381:30-83.

[134] Maimí, P.. *User material damage model for laminated composites*. User Guide.

[135] Maimí, P.. *Modelización constitutiva y computacional del daño y la fractura de materiales compuestos*. Tesis doctoral, Dept. D'Enginyeria Mecânica I de la Construcció Industrial, Universitat de Girona, Spain (2006).

[136] Catalanotti, G.. PhD thesis (to be concluded), Faculty of Engineering, University of Porto (2010).

[137] Koerber, H.. PhD thesis (to be concluded), Faculty of Engineering, University of Porto (2010).

[138] Koerber, H., Xavier, J.C., Camanho, P.P.. *High strain rate characterisation of unidirectional carbon-epoxy IM7-8552 in transverse compression and in-plane shear using digital image correlation*. Mechanics of Materials. 2010; submitted for publication.

[139] Sutcliffe, M.P.F., Xin, X.J., Fleck, N.A., Curtis, P.T.. *Composite Compressive Strength Modeller*. Engineering Department, Cambridge University, Cambridge, CB2 1PZ, U.K.; Structural Materials Centre, DERA Farnborough, GU14 0LW, U.K.. 1999 (website: http://www2.eng.cam.ac.uk/ mpfs/ccsmsumm.html).

[140] Lopes, C.S.. Private communication. 2010.

[141] Cros, Q.. MSc thesis (to be concluded), Faculty of Engineering, University of Porto (2010).

[142] Parvizi, A., Garrett, K., Bailey, J.. *Constrained cracking in glass fibre-reinforced epoxy cross-ply laminates*. Journal of Material Science. 1978; 13:195-201.

[143] Dvorak, G.J., Laws, N.. *Analysis of progressive matrix cracking in composite laminates II. first ply failure*. Journal of Composite Materials. 1987; 21:309-29.

Appendix A

Constitutive Modeling – Bases

A.1 Matzenmiller Model: a first definition of the complementary free energy density for FRP

Matzenmiller *et al.* [100] introduced some very important concepts and relations for constitutive modeling of anisotropic damage in FRP. Two of the most important aspects of the Matzenmiller's model, in this author's opinion, are:

1. the *derivation of the damaged stiffness tensor* $\boldsymbol{C}$, because it preceded the definition of the complementary free energy density that is of particular importance to formulate the constitutive equations based on the thermodynamics of irreversible processes;

2. the use of the concept *passive damage*.

The authors considered that the orthotropic nature of the mechanical response was maintained at all states of damage in order to treat the lamina as a homogenized continuum in plane stress. This assumption permits the modeling of damage by two arrays of parallel cracks that are orthogonal to each other. This means that the orientation of each crack-array is given by the direction of the fibers and their orthogonal direction – the authors called this the **orthogonal crack arrays assumption**. For each crack orientation there is a damage variable associated, d_1 is related to the fibers direction and d_2 to the transverse direction.

The orthogonal crack arrays assumption leads to the relation of the effective normal stresses $\tilde{\sigma}_{11}$ and $\tilde{\sigma}_{22}$ with the respective d_1 and d_2 damage variables, in the classical sense of CDM. The authors also considered that the shear stresses were associated to a damage parameter d_6 that was independent from the other two (d_1 and d_2), which differs from the model developed

by Maimí *et al.* [124, 125] that was presented in Chapter 3. A simple relationship between effective stresses ($\tilde{\sigma}$) and nominal stresses (σ) holds:

$$\tilde{\boldsymbol{\sigma}} = \boldsymbol{M}\boldsymbol{\sigma} \tag{A.1}$$

where $\boldsymbol{M}$ is the damage operator and is postulated by the authors as

$$\boldsymbol{M} = \begin{bmatrix} 1-d_1 & 0 & 0 \\ 0 & 1-d_2 & 0 \\ 0 & 0 & 1-d_6 \end{bmatrix} \tag{A.2}$$

It should be noticed that the two parameters d_1 and d_2 assume different values for tension (d_{1+} and d_{2+}) and compression (d_{1-} and d_{2-}) in order to account for the closure of transverse cracks under load reversal, also known as unilateral effect[1] (see Chapter 3). In contrast, d_6 is independent of the sign of the shear stress σ_{12}.

After postulating the damage operator $\boldsymbol{M}$ the authors were able to define the damaged stiffness $\boldsymbol{C}$ of the material. It was assumed that the constitutive law was linear between the stresses and strains and that the influence of damage on the elastic response may be described by the damage variables $\boldsymbol{d}$. The components of the constitutive tensor were represented as functions of the damage variables $\boldsymbol{d}$ and the material parameters of the undamaged lamina (instead of taking the elasticity constants themselves as unknowns, like in [90]). Therefore, in accordance with the assumption of the orthogonal crack arrays, the constitutive tensor $\boldsymbol{C}(\boldsymbol{d})$ was derived by **physical arguments** and information of the dependencies between effective elastic properties and individual damage variables.

To obtain $\boldsymbol{C}$ the authors started defining the compliance relationship $\boldsymbol{H}$ because this way is easier to relate the material parameters to the mechanical response in the privileged axes. One important aspect to refer is that this relationship was actually defined using the strain equivalence principle, although it generates an inadmissible unsymmetrical constitutive tensor. The compliance relationship for orthotropic elasticity in plane stress is recalled in terms of the effective stresses $\tilde{\boldsymbol{\sigma}}$:

[1] By discriminating the damage variables by the sign of the respective stress the authors used the concept of passive damage.

$$\boldsymbol{\varepsilon} = \boldsymbol{H}_0\tilde{\boldsymbol{\sigma}} \quad , \quad \boldsymbol{H}_0 = \begin{bmatrix} \frac{1}{E_1} & -\frac{\upsilon_{21}}{E_1} & 0 \\ -\frac{\upsilon_{12}}{E_2} & \frac{1}{E_2} & 0 \\ 0 & 0 & \frac{1}{G_{12}} \end{bmatrix} \quad , \quad \boldsymbol{\varepsilon} = \begin{bmatrix} \varepsilon_{11} \\ \varepsilon_{22} \\ 2\varepsilon_{12} \end{bmatrix} \tag{A.3}$$

with E_1, E_2, G_{12}, υ_{21} and υ_{12} as the elasticity parameters of the undamaged lamina. Positive definiteness of $\boldsymbol{H}_0$ requires: $\upsilon_{21}\upsilon_{12} < 1$.

From equations (A.1) and (A.2) results: $\boldsymbol{\varepsilon} = \boldsymbol{H}_0\boldsymbol{M}\boldsymbol{\sigma} \rightarrow \boldsymbol{H}(\boldsymbol{d}) = \boldsymbol{H}_0\boldsymbol{M}$. However, the final form of the compliance tensor for the damaged lamina, $\boldsymbol{H}(\boldsymbol{d})$, is obtained after **adjusting**[2] the Poisson's ratios $\upsilon_{21}(\boldsymbol{d})$ and $\upsilon_{12}(\boldsymbol{d})$ in order to turn them unaffected by the damage variables:

$$\begin{aligned} \boldsymbol{H}(\boldsymbol{d}) = & \begin{bmatrix} \frac{1}{(1-d_1)E_1} & -\frac{\upsilon_{21}}{(1-d_2)E_1} & 0 \\ -\frac{\upsilon_{12}}{(1-d_1)E_2} & \frac{1}{(1-d_2)E_2} & 0 \\ 0 & 0 & \frac{1}{(1-d_6)G_{12}} \end{bmatrix} \\ & \Downarrow \\ \boldsymbol{H}(\boldsymbol{d}) = & \begin{bmatrix} \frac{1}{(1-d_1)E_1} & -\frac{\upsilon_{21}}{E_1} & 0 \\ -\frac{\upsilon_{12}}{E_2} & \frac{1}{(1-d_2)E_2} & 0 \\ 0 & 0 & \frac{1}{(1-d_6)G_{12}} \end{bmatrix} \end{aligned} \tag{A.4}$$

Its inverse always exists as long as the damage variables are less than one ($d_i < 1$),

$$\boldsymbol{C}(\boldsymbol{d}) = \frac{1}{\Upsilon}\begin{bmatrix} (1-d_1)E_1 & (1-d_1)(1-d_2)\upsilon_{21}E_2 & 0 \\ (1-d_1)(1-d_2)\upsilon_{12}E_1 & (1-d_2)E_2 & 0 \\ 0 & 0 & \Upsilon(1-d_6)G_{12} \end{bmatrix} \tag{A.5}$$

with $\Upsilon = 1 - (1-d_1)(1-d2)\upsilon_{12}\upsilon_{21} > 0$

and $\boldsymbol{H}_0$ is positive definite.

[2] This adjustment was justified exclusively with experimental observations and therefore has no mathematical basis.

Although it might seem to some that this model is not very elegant, it serves as basis for many other models (including the one presented in Chapter 3) that seem a lot more elegant and completely mathematically based. In fact, most of the models defined in the framework of the thermodynamics of irreversible processes start with the definition of the complementary free energy density G, and many of these are greatly inspired by the Matzenmiller's constitutive model derived complementary free energy density:

$$G = \frac{1}{2E_1}\left(\frac{\langle\sigma_{11}\rangle^2}{1-d_{1+}} + \frac{\langle-\sigma_{11}\rangle^2}{1-d_{1-}}\right) - \frac{\upsilon_{12}\sigma_{22}\sigma_{11}}{E_1} + \frac{1}{2E_2}\left(\frac{\langle\sigma_{22}\rangle^2}{1-d_{2+}} + \frac{\langle-\sigma_{22}\rangle^2}{1-d_{2-}}\right) + \frac{\sigma_{12}^2}{2G_{12}(1-d_6)} \tag{A.6}$$

Examples of models that use a similar complementary free energy density to this are: the Ladevèze *et al.* models [101]-[105] and the model presented in Chapter 3 [124, 125].

A.2 Thermodynamic bases for constitutive models

As already referred, thermodynamics of irreversible processes offers a good framework to formulate constitutive models. This section intends to give some basic concepts about thermodynamics and its value in nonlinear solid mechanics. When dynamical processes are being dealt with, that involve time evolution of strain (and stress), heat generation, conduction and dissipation to neighboring domains, an analysis of the relevant systems becomes a powerful tool [97].

An excellent review on this subject is presented by Baker [97]. This article will be summarized here (without being continuously referenced).

A.2.1 Equilibrium thermodynamics (thermostatics)

Thermodynamics, in resemblance with other type of analysis, also uses equilibrium as a starting point. Equilibrium thermodynamics is a subject that is more familiar to undergraduate students, and its application to solid mechanics is trivial.

a) Energy

In any nonlinear dynamic system there will be a potential energy of the applied actions, V, and kinetic energy of the dynamical system, K; everything else is internal energy, U. The total energy of a system is written as

$$\Pi = K + V + U \tag{A.7}$$

As is also of the readers knowledge, the change in total energy between two thermodynamic states is

$$\Pi(\varepsilon_2) - \Pi(\varepsilon_1) = Q + W \tag{A.8}$$

where Q is the exchange of heat and W is the work.

It is also possible to consider the change in energy due to an infinitesimal transformation as: $\mathrm{d}\Pi = \mathrm{d}Q + \mathrm{d}W$, where $\mathrm{d}Q$ and $\mathrm{d}W$ are contributions to elementary heat and work, respectively.

Energy is defined as a function of a set of **independent state variables**. it is then appropriate to consider the differential increment in total energy as a chain of partial derivative terms, each with respect to a state variable. Each of the terms must then represent a contribution (or component) of elementary heat or work.

b) Thermodynamic potential and forces

The concepts of thermodynamic potential and thermodynamic force are cornerstones for applying thermodynamics to damage and plasticity models (or any other type of nonlinear solid mechanics models). **Thermodynamic potentials** are quantities from which all characteristics of the system can be deduced. An example of a thermodynamic potential is the complementary free energy defined by equation (A.6). A thermodynamic potential is defined as a function of a set of independent state variables, of which *damage* and *plastic strain* are of particular interest for this work. Associated with this set of independent state variables, there is a set of dependent variables, called **thermodynamic forces** (also known as thermodynamic properties). If one writes energy as a function of some general state variables, $\Pi = \tilde{\Pi}(\chi_0, \chi_1, \ldots)$, then the chain rule yields

$$\mathrm{d}\Pi = \frac{\partial \Pi}{\partial \chi_0}\mathrm{d}\chi_0 + \frac{\partial \Pi}{\partial \chi_1}\mathrm{d}\chi_1 + \ldots \tag{A.9}$$

where $\frac{\partial \Pi}{\partial \chi_j}$ are the thermodynamic forces[3] associated with each independent state variable χ_j.

c) Entropy

From basic thermodynamic courses it is known that the change in entropy, S, from one state ϵ_1 to another state ϵ_2 is represented, in its most general form, as:

$$S(\epsilon_2) - S(\epsilon_1) = \int_{t_1}^{t_2} \oint_s \frac{\mathrm{d}q}{T} \mathrm{d}s\mathrm{d}t\,, \tag{A.10}$$

where dq is the inward normal heat flux, T is the temperature and s is the boundary coordinate.

The second law of thermodynamics recognizes that heat and work are not equivalent because mechanical energy can be completely converted to thermal energy, but thermal energy can only be partially converted to mechanical energy during any cyclic process. Thus, there is dissipation in between.

As is also known, entropy is the appropriate state variable governing internal energy, associated with the transfer of heat. The elementary exchange of heat is thus,

$$\mathrm{d}Q = \frac{\partial U}{\partial S}\mathrm{d}S = T\mathrm{d}S \tag{A.11}$$

The latter comes from equation (A.10), so it can be deduced that:

$$T = \frac{\partial U}{\partial S} \tag{A.12}$$

In other words, temperature is the thermodynamic force associated with the state variable of entropy.

d) Enthalpy and free energy

Here the crucial concept of free energy will be introduced. Free energy is defined by a Legendre transformation, being the difference between internal energy U and the exchanged heat TS:

$$\Psi = U - TS \tag{A.13}$$

Then, by simple differentiation, noting that U depends on S but not on T:

$$S = -\frac{\partial \Psi}{\partial T} \tag{A.14}$$

[3] For example, for the complementary free energy defined by (A.6) it is possible to define $Y_j = \frac{\partial G}{\partial d_j}$ as the thermodynamic forces associated to the damage variables.

The consequence is that temperature becomes the independent variable of the free energy, being entropy its thermodynamic force.

In the study of solids the form of free energy defined by equation (A.13) is known as **Helmholtz free energy**, and is a very important thermodynamic potential. It is well known that the **internal energy for solids** is a function of entropy S, strain ε and other independent state variables (like damage d and plastic strains ε^p): $U = \tilde{U}(S, \varepsilon, d, \ldots)$, therefore the Helmholtz free energy is a function of strain ε, temperature and the other independent state variables: $\Psi(\varepsilon, T, d, \ldots) = U(S, \varepsilon, d, \ldots) - TS$. Moreover, it is also known that the internal energy is related to the stresses and strains of the solid by $\sigma = \frac{\partial U}{\partial \varepsilon}$, thus,

$$\sigma = \frac{\partial \Psi}{\partial \varepsilon} \tag{A.15}$$

Another important definition is the **Gibbs free energy** $G(\sigma, T, d, \ldots)$ because in some cases it is more interesting to define the free energy as a function of the stresses instead of the strains:

$$G(\sigma, T, d, \ldots) = \sigma : \varepsilon - U(S, \varepsilon, d, \ldots) + TS \tag{A.16}$$

It is clear from equations (A.13) and (A.16) that Ψ and G (taken per unit volume) form complementary energies

$$\Psi + G = \sigma : \varepsilon \tag{A.17}$$

from which the duality of constitutive description follows:

$$\sigma = \frac{\partial \Psi}{\partial \varepsilon} \leftrightarrow \varepsilon = \frac{\partial G}{\partial \sigma}. \tag{A.18}$$

A.2.2 Non-equilibrium thermodynamics

The issue in non-equilibrium thermodynamics is how to deal with systems that are changing, in the thermodynamic sense. There are three main approaches. The classical approach looks to a thermodynamic process as a series of thermostatic equilibrium, the second uses the rational theory of Coleman and Noll [106] and the third uses the theory of internal variables [107]. In non-equilibrium thermodynamics there is a very important assumption: temperature and entropy can still be used for non-equilibrium processes.

Usually, this subject is presented using specific intrinsic variables (per unit mass) or alternatively per unit volume. Baker used entities per unit volume but in this presentation it was

chosen to use specific variables. Let's start by writing the Helmholtz form of free energy and the internal energy per unit mass as ψ and u, respectively, as well as the entropy per unit mass s. Then, the Helmholtz energy is $\psi = u - Ts$. The important result for our purposes then derives from the time derivative of this Legendre transformation

$$\dot{\psi} = \dot{u} - s\dot{T} - T\dot{s} \tag{A.19}$$

where the term $T\dot{s}$ is actually the rate of heat exchange, and $s\dot{T}$ can be considered a kind of "thermodynamic momentum".

a) Dissipation

For a reversible process, the change in entropy is due only to the input of the heat to the system. By contrast, for an **irreversible process** (intrinsic changes to material structure, for example) the change in entropy results from (pure) heat input and irreversibilities that occur (e.g., damage). Then, for an isothermal process, it is possible to write the following inequality

$$S(\epsilon_2) - S(\epsilon_1) - \frac{\mathrm{d}Q}{T} \geq 0 \tag{A.20}$$

where dQ is the heat received across all boundaries during the transformation. The so called **Claussius inequality** for deformable solids is obtained by applying the divergence theorem (Gauss' theorem) to the equation (A.10):

$$T\dot{s} \geq r - T\nabla\left[\frac{\mathbf{q}}{T}\right], \tag{A.21}$$

where r is an internal point heat source per unit volume, and $\mathbf{q}$ is the heat flux. The difference is **dissipation** Ξ, which consists of mechanical and thermal dissipation (namely plasticity and damage).

To balance the inequality equation (A.21), it is possible to add Ξ and re-write the equation as

$$\Xi = T\dot{s} - r + T\nabla\left[\frac{\mathbf{q}}{T}\right] \geq 0 \tag{A.22}$$

with Ξ being always a non-negative entity.

The last term in equation (A.22) can be subdivided in two terms that represent two different kinds of dissipation: mechanical dissipation (Ξ_{mech}) and thermal dissipation (Ξ_{therm}):

$$\Xi_{mech} \equiv T\dot{s} - r + \nabla\mathbf{q} \geq 0 \qquad ; \qquad \Xi_{therm} \equiv -\mathbf{q} \cdot \frac{\nabla T}{T} \geq 0 \tag{A.23}$$

Nevertheless, it was already referred that the experimentally obtained variables in a mechanical problem are the strains (ε), stresses (σ) and absolute temperature (T), plus the plastic strains (ε^p) and damage (d). If the first principle of thermodynamics is re-written as:

$$\rho\dot{u} = \sigma : \dot{\varepsilon} + \rho r - \nabla\mathbf{q} \tag{A.24}$$

Then the mechanical dissipation Ξ_{mech} is defined as:

$$\Xi_{mech} \equiv \sigma : \dot{\varepsilon} + \rho(T\dot{s} - \dot{u}) \geq 0 \tag{A.25}$$

However, in a thermodynamical problem it is difficult to define the internal energy $u(\varepsilon, s, \chi_j, \ldots)$ because it depends on the value of entropy. Thus, considering the previously defined Helmholtz energy, $\psi(\varepsilon, T, \chi_j, \ldots) = u(S, \varepsilon, \chi_j, \ldots) - Ts$, and substituting its derivative, $\dot{\psi} = \dot{u} - \dot{T}s - T\dot{s}$, in equation (A.25) then:

$$\Xi_{mech} \equiv \sigma : \dot{\varepsilon} - \rho(\dot{\psi} - \dot{T}s) \geq 0 \tag{A.26}$$

Re-writing the variation of the free energy as function of its arguments

$$\dot{\psi} = \frac{\partial\psi}{\partial\varepsilon} : \dot{\varepsilon} + \frac{\partial\psi}{\partial T}\dot{T} + \frac{\partial\psi}{\partial\boldsymbol{\chi}}\dot{\boldsymbol{\chi}} \tag{A.27}$$

where $\boldsymbol{\chi}$ represents the other independent state variables (namely damage and plasticity).

This way, the mechanical dissipation can be written as

$$\Xi_{mech} \equiv \left(\sigma - \rho\frac{\partial\psi}{\partial\varepsilon}\right) : \dot{\varepsilon} - \rho\left(\frac{\partial\psi}{\partial T} + s\right)\dot{T} - \rho\frac{\partial\psi}{\partial\boldsymbol{\chi}} : \dot{\boldsymbol{\chi}} \geq 0 \tag{A.28}$$

Being the strain and absolute temperature the free variables, in order to avoid the mechanical dissipation to become negative:

$$\sigma = \rho\frac{\partial\psi}{\partial\varepsilon} \quad ; \quad s = -\frac{\partial\psi}{\partial T}\,, \tag{A.29}$$

expressions that were already obtained by a different approach.

From these results:

$$\Xi_{mech} \equiv -\rho\frac{\partial\psi}{\partial\boldsymbol{\chi}} : \dot{\boldsymbol{\chi}} = \boldsymbol{Y} : \dot{\boldsymbol{\chi}} \geq 0 \tag{A.30}$$

where $\boldsymbol{Y}$ are the thermodynamic forces associated to the internal variables $\dot{\boldsymbol{\chi}}$ of the Helmholtz energy. As previously referred, the thermodynamic forces indicate the variation of the free energy with the evolution of the internal variables.

As a final note, it is stated that instead of using the Helmholtz energy to obtain the stresses and the mechanical dissipation, it could be used the Gibbs free energy $G(\sigma, T, \chi)$ leading to the result:

$$\Xi_{mech} \equiv \left(-\rho\frac{\partial G}{\partial \sigma} + \varepsilon\right) : \dot{\sigma} - \rho\left(\frac{\partial G}{\partial T} + s\right)\dot{T} - \rho\frac{\partial G}{\partial \chi} : \dot{\chi} \geq 0 \tag{A.31}$$

The state laws derived with the Gibbs free energy are:

$$\varepsilon = -\rho\frac{\partial G}{\partial \sigma} \quad ; \quad s = -\frac{\partial G}{\partial T} \quad ; \quad \boldsymbol{Y}\frac{\partial G}{\partial \chi}. \tag{A.32}$$

Appendix B

In-situ Strengths

The in-situ effect was originally detected by **Parvizi *et al.*** [142] after performing tensile tests on cross-ply glass fiber reinforced plastics. It is characterized by **higher transverse tensile** and **shear strengths** of a ply when it is constrained by plies with different fiber orientations in a laminate, compared with the strength of the same ply in an unidirectional laminate. The in-situ strength depends on the number of plies clustered together and on the fiber orientation of the constraining plies.

Dvorak and Laws [143] performed experiments where the relation between the in-situ transverse tensile strength[1] Y_T and the total number of 90° plies clustered together ($2n$) was measured. The results were obtained for the CFRP T300/944 and are presented in Figure B.1.

Accurate in-situ strengths are necessary for many stress-based failure criteria, in order to predict matrix cracking in constrained plies. One of the failure criteria that uses the in-situ strengths was presented in Chapter 3. Therefore, it is imperative to show how the in-situ strengths can be calculated.

Camanho *et al.* [115] proposed a model for the calculation of the in-situ strengths, which makes the simplifying assumption that the fiber orientation of the constraining layers does not affect their value. The closed-form solutions to predict the in-situ strengths proposed in this model were used to calculate the inputs of the numerical model.

The tensile transverse in-situ strengths are given by [115]:

[1] The in-situ transverse tensile strength could be symbolized by Y_T^{is}, but in this work it will be omitted the superscript "is". Therefore, both of the Y_T and S_L properties that will appear throughout the entire work are in-situ strengths.

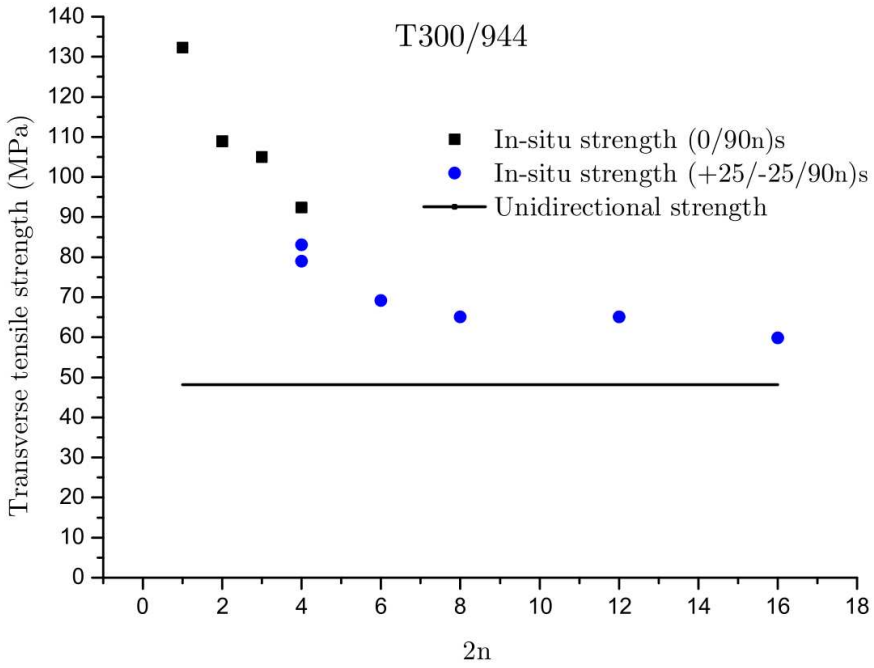

Figure B.1: In-situ effect in laminated composites. [143]

$$\begin{aligned} \text{For a thin embedded ply:} \quad & Y_T = \sqrt{\frac{8\mathcal{G}_{2+}}{\pi t \Lambda_{22}^0}} \\ \text{For a thin outer ply:} \quad & Y_T = 1.79\sqrt{\frac{\mathcal{G}_{2+}}{\pi t \Lambda_{22}^0}} \\ \text{For a thick ply:} \quad & Y_T = 1.12\sqrt{2}Y_T^{\text{ud}} \end{aligned} \tag{B.1}$$

where Y_T^{ud} is the tensile transverse strength measured in an unidirectional test specimen, t is the ply thickness, $\mathcal{G}_{2+}$ is the mode I fracture toughness, and Λ_{22}^0 is defined as:

$$\lambda_{22}^0 = 2\left(\frac{1}{E_2} - \frac{\upsilon_{21}^2}{E_1}\right) \tag{B.2}$$

The in-situ shear strengths are obtained as [115]:

$$S_L = \sqrt{\frac{\left(1+\beta\phi G_{12}^2\right)^{1/2} - 1}{3\beta G_{12}}} \tag{B.3}$$

where β is the shear response factor, and the parameter ϕ is defined according to the configu-

ration of the ply:

$$\begin{aligned} \text{For a thin embedded ply:} \quad & \phi = \frac{48\mathcal{G}_6}{\pi t} \\ \text{For a thin outer ply:} \quad & \phi = \frac{24\mathcal{G}_6}{\pi t} \\ \text{For a thick ply:} \quad & \phi = \frac{12\left(S_L^{\text{ud}}\right)^2}{G_{12}} + 18\beta\left(S_L^{\text{ud}}\right)^4 \end{aligned} \tag{B.4}$$

where S_L^{ud} is the shear strength measured in an unidirectional test specimen, and $\mathcal{G}_6$ is the mode II fracture toughness.

Appendix C

Parameters for the Shear plasticity Model

The necessary parameters (besides the elastic parameters) for the elasto-plastic model defined in Chapter 3 are a total of four. Two are necessary to determine the initial surface that defines the elastic space and the other two to determine its evolution. The in-plane shear strain γ_{12}^{0} represents the beginning of the non-linear behavior in a pure shear test, and μ is a parameter that has into account the transverse stresses (σ_{22}) at the beginning of the non-linear behavior. It is possible to determine μ by realizing an in-plane shear stress–shear strain test with a constant transverse stress applied and measuring the beginning of the non-linear behavior (γ_{12}^{1} in Figure C.1).

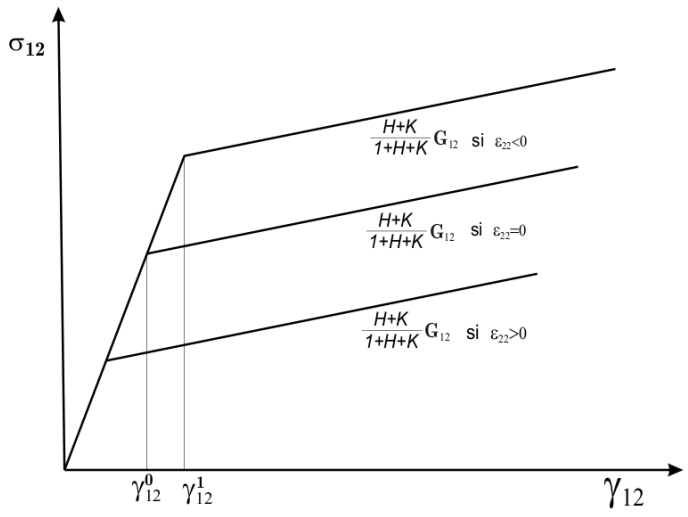

Figure C.1: In-plane shear stress–shear strain response varying the transverse stress (σ_{22}). [135]

After measuring γ_{12}^{0} and γ_{12}^{1}, the μ parameter comes defined as:

$$\mu = -\frac{E_2}{\sigma_{22}} \log\left[\exp\left(log(2)\frac{\gamma_{12}^1}{\gamma_{12}^0}\right) - 1\right] \tag{C.1}$$

The parameters H and K can be determined by a test including a load/unload cycle – Figure C.2.

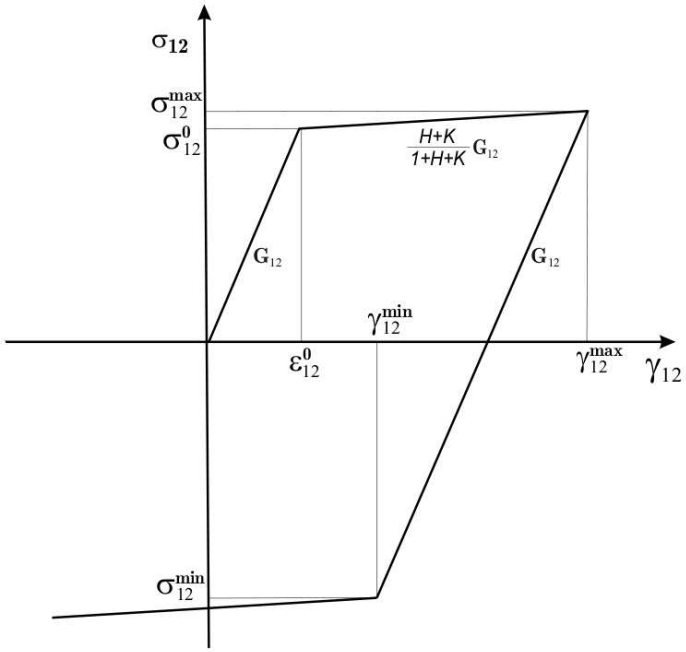

Figure C.2: In-plane shear stress–shear strain response including load/unload cycle. [135]

Consider that the material is loaded beyond the linear phase and that the non-linear phase is modeled as a linear law with slope: $G_{12}^T = \frac{\sigma_{12}^{max} - G_{12}\gamma_{12}^0}{\gamma_{12}^{max} - \gamma_{12}^0} = G_{12}\frac{H+K}{1+H+K}$. Once a maximum strain (γ_{12}^{max}) is reached the load is reversed. The unloading process is considered to be elastic until the point where the plastic process begins, γ_{12}^{min}. Then, it is possible to write the following:

$$\begin{aligned} K &= \frac{1 - \left(G_{12}^T - 1\right)R}{2\left(G_{12} - G_{12}^T\right)} \\ H &= R + K - 1 \end{aligned} \tag{C.2}$$

where R is defined as: $R = 1 + H - K = \frac{\gamma_{12}^{min} - \gamma_{12}^0}{\gamma_{12}^{max} - \sigma_{12}^{max}/G_{12}}$.

As a final note, if $\sigma_{12}^{max} = \sigma_{12}^{min}$ then the model has isotropic hardening, resulting $H = 0$.